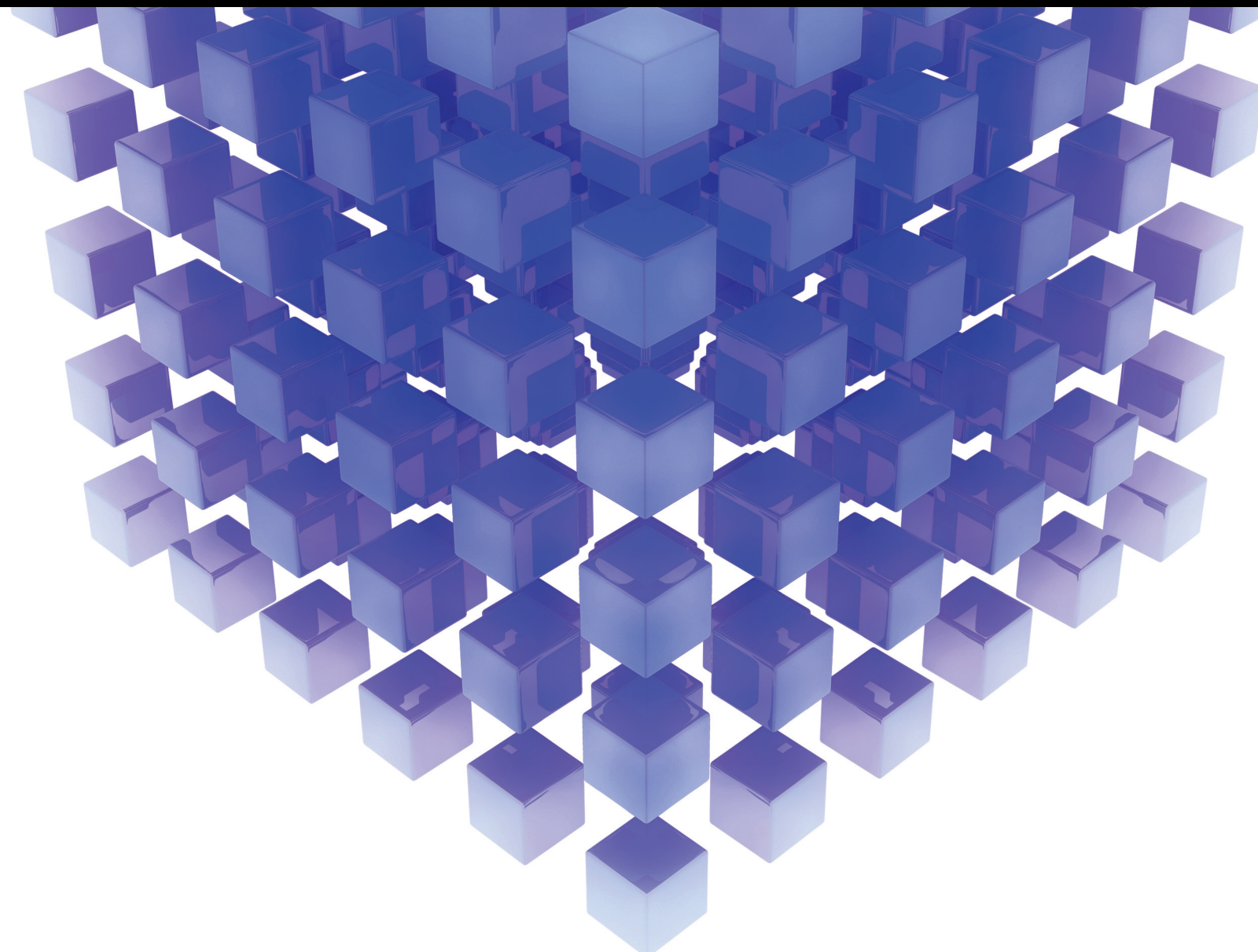


Mathematical Problems in Engineering

Chaotic Oscillators: Theory, Experiment, Control, and Applications 2021

Lead Guest Editor: Viet-Thanh Pham

Guest Editors: Sundarapandian Vaidyanathan, Adel Ouannas, and
Giuseppe Grassi





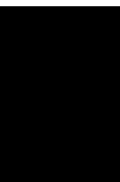
**Chaotic Oscillators: Theory, Experiment,
Control, and Applications 2021**

Mathematical Problems in Engineering

**Chaotic Oscillators: Theory,
Experiment, Control, and Applications
2021**

Lead Guest Editor: Viet-Thanh Pham


Guest Editors: Sundarapandian Vaidyanathan, Adel
Ouannas, and Giuseppe Grassi



Copyright © 2021 Hindawi Limited. All rights reserved.

This is a special issue published in “Mathematical Problems in Engineering.” All articles are open access articles distributed under the Creative Commons Attribution License, which permits unrestricted use, distribution, and reproduction in any medium, provided the original work is properly cited.

Chief Editor

Guangming Xie , China

Academic Editors

Kumaravel A , India
Waqas Abbasi, Pakistan
Mohamed Abd El Aziz , Egypt
Mahmoud Abdel-Aty , Egypt
Mohammed S. Abdo, Yemen
Mohammad Yaghoub Abdollahzadeh
Jamalabadi , Republic of Korea
Rahib Abiyev , Turkey
Leonardo Acho , Spain
Daniela Addessi , Italy
Arooj Adeel , Pakistan
Waleed Adel , Egypt
Ramesh Agarwal , USA
Francesco Aggogeri , Italy
Ricardo Aguilar-Lopez , Mexico
Afaq Ahmad , Pakistan
Naveed Ahmed , Pakistan
Elias Aifantis , USA
Akif Akgul , Turkey
Tareq Al-shami , Yemen
Guido Ala, Italy
Andrea Alaimo , Italy
Reza Alam, USA
Osamah Albahri , Malaysia
Nicholas Alexander , United Kingdom
Salvatore Alfonzetti, Italy
Ghous Ali , Pakistan
Nouman Ali , Pakistan
Mohammad D. Aliyu , Canada
Juan A. Almendral , Spain
A.K. Alomari, Jordan
José Domingo Álvarez , Spain
Cláudio Alves , Portugal
Juan P. Amezcua-Sanchez, Mexico
Mukherjee Amitava, India
Lionel Amodeo, France
Sebastian Anita, Romania
Costanza Arico , Italy
Sabri Arik, Turkey
Fausto Arpino , Italy
Rashad Asharabi , Saudi Arabia
Farhad Aslani , Australia
Mohsen Asle Zaem , USA

Andrea Avanzini , Italy
Richard I. Avery , USA
Viktor Avrutin , Germany
Mohammed A. Awadallah , Malaysia
Francesco Aymerich , Italy
Sajad Azizi , Belgium
Michele Bacciocchi , Italy
Seungik Baek , USA
Khaled Bahlali, France
M.V.A Raju Bahubalendruni, India
Pedro Balaguer , Spain
P. Balasubramaniam, India
Stefan Balint , Romania
Ines Tejado Balsera , Spain
Alfonso Banos , Spain
Jerzy Baranowski , Poland
Tudor Barbu , Romania
Andrzej Bartoszewicz , Poland
Sergio Baselga , Spain
S. Caglar Baslamisli , Turkey
David Bassir , France
Chiara Bedon , Italy
Azeddine Beghdadi, France
Andriette Bekker , South Africa
Francisco Beltran-Carbajal , Mexico
Abdellatif Ben Makhlof , Saudi Arabia
Denis Benasciutti , Italy
Ivano Benedetti , Italy
Rosa M. Benito , Spain
Elena Benvenuti , Italy
Giovanni Berselli, Italy
Michele Betti , Italy
Pietro Bia , Italy
Carlo Bianca , France
Simone Bianco , Italy
Vincenzo Bianco, Italy
Vittorio Bianco, Italy
David Bigaud , France
Sardar Muhammad Bilal , Pakistan
Antonio Bilotta , Italy
Sylvio R. Bistafa, Brazil
Chiara Boccaletti , Italy
Rodolfo Bontempo , Italy
Alberto Borboni , Italy
Marco Bortolini, Italy

Paolo Boscariol, Italy
Daniela Boso , Italy
Guillermo Botella-Juan, Spain
Abdesselem Boulkroune , Algeria
Boulaïd Boulkroune, Belgium
Fabio Bovenga , Italy
Francesco Braghin , Italy
Ricardo Branco, Portugal
Julien Bruchon , France
Matteo Bruggi , Italy
Michele Brun , Italy
Maria Elena Bruni, Italy
Maria Angela Butturi , Italy
Bartłomiej Błachowski , Poland
Dhanamjayulu C , India
Raquel Caballero-Águila , Spain
Filippo Cacace , Italy
Salvatore Caddemi , Italy
Zuowei Cai , China
Roberto Caldelli , Italy
Francesco Cannizzaro , Italy
Maosen Cao , China
Ana Carpio, Spain
Rodrigo Carvajal , Chile
Caterina Casavola, Italy
Sara Casciati, Italy
Federica Caselli , Italy
Carmen Castillo , Spain
Inmaculada T. Castro , Spain
Miguel Castro , Portugal
Giuseppe Catalanotti , United Kingdom
Alberto Cavallo , Italy
Gabriele Cazzulani , Italy
Fatih Vehbi Celebi, Turkey
Miguel Cerrolaza , Venezuela
Gregory Chagnon , France
Ching-Ter Chang , Taiwan
Kuei-Lun Chang , Taiwan
Qing Chang , USA
Xiaoheng Chang , China
Prasenjit Chatterjee , Lithuania
Kacem Chehdi, France
Peter N. Cheimets, USA
Chih-Chiang Chen , Taiwan
He Chen , China
























Kebing Chen , China
Mengxin Chen , China
Shyi-Ming Chen , Taiwan
Xizhong Chen , Ireland
Xue-Bo Chen , China
Zhiwen Chen , China
Qiang Cheng, USA
Zeyang Cheng, China
Luca Chiapponi , Italy
Francisco Chicano , Spain
Tirivanhu Chinyoka , South Africa
Adrian Chmielewski , Poland
Seongim Choi , USA
Gautam Choubey , India
Hung-Yuan Chung , Taiwan
Yusheng Ci, China
Simone Cinquemani , Italy
Roberto G. Citarella , Italy
Joaquim Ciurana , Spain
John D. Clayton , USA
Piero Colajanni , Italy
Giuseppina Colicchio, Italy
Vassilios Constantoudis , Greece
Enrico Conte, Italy
Alessandro Contento , USA
Mario Cools , Belgium
Gino Cortellessa, Italy
Carlo Cosentino , Italy
Paolo Crippa , Italy
Erik Cuevas , Mexico
Guozeng Cui , China
Mehmet Cunkas , Turkey
Giuseppe D'Aniello , Italy
Peter Dabnichki, Australia
Weizhong Dai , USA
Zhifeng Dai , China
Purushothaman Damodaran , USA
Sergey Dashkovskiy, Germany
Adiel T. De Almeida-Filho , Brazil
Fabio De Angelis , Italy
Samuele De Bartolo , Italy
Stefano De Miranda , Italy
Filippo De Monte , Italy

José António Fonseca De Oliveira
Correia , Portugal
Jose Renato De Sousa , Brazil
Michael Defoort, France
Alessandro Della Corte, Italy
Laurent Dewasme , Belgium
Sanku Dey , India
Gianpaolo Di Bona , Italy
Roberta Di Pace , Italy
Francesca Di Puccio , Italy
Ramón I. Diego , Spain
Yannis Dimakopoulos , Greece
Hasan Dinçer , Turkey
José M. Domínguez , Spain
Georgios Dounias, Greece
Bo Du , China
Emil Dumic, Croatia
Madalina Dumitriu , United Kingdom
Premraj Durairaj , India
Saeed Eftekhari Azam, USA
Said El Kafhali , Morocco
Antonio Elipse , Spain
R. Emre Erkmen, Canada
John Escobar , Colombia
Leandro F. F. Miguel , Brazil
FRANCESCO FOTI , Italy
Andrea L. Facci , Italy
Shahla Faisal , Pakistan
Giovanni Falsone , Italy
Hua Fan, China
Jianguang Fang, Australia
Nicholas Fantuzzi , Italy
Muhammad Shahid Farid , Pakistan
Hamed Faruqi, Iran
Yann Favennec, France
Fiorenzo A. Fazzolari , United Kingdom
Giuseppe Fedele , Italy
Roberto Fedele , Italy
Baowei Feng , China
Mohammad Ferdows , Bangladesh
Arturo J. Fernández , Spain
Jesus M. Fernandez Oro, Spain
Francesco Ferrise, Italy
Eric Feulvarch , France
Thierry Floquet, France

Eric Florentin , France
Gerardo Flores, Mexico
Antonio Forcina , Italy
Alessandro Formisano, Italy
Francesco Franco , Italy
Elisa Francomano , Italy
Juan Frausto-Solis, Mexico
Shujun Fu , China
Juan C. G. Prada , Spain
HECTOR GOMEZ , Chile
Matteo Gaeta , Italy
Mauro Gaggero , Italy
Zoran Gajic , USA
Jaime Gallardo-Alvarado , Mexico
Mosè Gallo , Italy
Akemi Gálvez , Spain
Maria L. Gandarias , Spain
Hao Gao , Hong Kong
Xingbao Gao , China
Yan Gao , China
Zhiwei Gao , United Kingdom
Giovanni Garcea , Italy
José García , Chile
Harish Garg , India
Alessandro Gasparetto , Italy
Stylianos Georgantzinou, Greece
Fotios Georgiades , India
Parviz Ghadimi , Iran
Ştefan Cristian Gherghina , Romania
Georgios I. Giannopoulos , Greece
Agathoklis Giaralis , United Kingdom
Anna M. Gil-Lafuente , Spain
Ivan Giorgio , Italy
Gaetano Giunta , Luxembourg
Jefferson L.M.A. Gomes , United Kingdom
Emilio Gómez-Déniz , Spain
Antonio M. Gonçalves de Lima , Brazil
Qunxi Gong , China
Chris Goodrich, USA
Rama S. R. Gorla, USA
Veena Goswami , India
Xunjie Gou , Spain
Jakub Grabski , Poland

Antoine Grall , France
George A. Gravvanis , Greece
Fabrizio Greco , Italy
David Greiner , Spain
Jason Gu , Canada
Federico Guarracino , Italy
Michele Guida , Italy
Muhammet Gul , Turkey
Dong-Sheng Guo , China
Hu Guo , China
Zhaoxia Guo, China
Yusuf Gurefe, Turkey
Salim HEDDAM , Algeria
ABID HUSSANAN, China
Quang Phuc Ha, Australia
Li Haitao , China
Petr Hájek , Czech Republic
Mohamed Hamdy , Egypt
Muhammad Hamid , United Kingdom
Renke Han , United Kingdom
Weimin Han , USA
Xingsi Han, China
Zhen-Lai Han , China
Thomas Hanne , Switzerland
Xinan Hao , China
Mohammad A. Hariri-Ardebili , USA
Khalid Hattaf , Morocco
Defeng He , China
Xiao-Qiao He, China
Yanchao He, China
Yu-Ling He , China
Ramdane Hedjar , Saudi Arabia
Jude Hemanth , India
Reza Hemmati, Iran
Nicolae Herisanu , Romania
Alfredo G. Hernández-Díaz , Spain
M.I. Herreros , Spain
Eckhard Hitzer , Japan
Paul Honeine , France
Jaromir Horacek , Czech Republic
Lei Hou , China
Yingkun Hou , China
Yu-Chen Hu , Taiwan
Yunfeng Hu, China
Can Huang , China
Gordon Huang , Canada
Linsheng Huo , China
Sajid Hussain, Canada
Asier Ibeas , Spain
Orest V. Iftime , The Netherlands
Przemyslaw Ignaciuk , Poland
Giacomo Innocenti , Italy
Emilio Insfran Pelozo , Spain
Azeem Irshad, Pakistan
Alessio Ishizaka, France
Benjamin Ivorra , Spain
Breno Jacob , Brazil
Reema Jain , India
Tushar Jain , India
Amin Jajarmi , Iran
Chiranjibe Jana , India
Łukasz Jankowski , Poland
Samuel N. Jator , USA
Juan Carlos Jáuregui-Correa , Mexico
Kandasamy Jayakrishna, India
Reza Jazar, Australia
Khalide Jbilou, France
Isabel S. Jesus , Portugal
Chao Ji , China
Qing-Chao Jiang , China
Peng-fei Jiao , China
Ricardo Fabricio Escobar Jiménez , Mexico
Emilio Jiménez Macías , Spain
Maolin Jin, Republic of Korea
Zhuo Jin, Australia
Ramash Kumar K , India
BHABEN KALITA , USA
MOHAMMAD REZA KHEDMATI , Iran
Viacheslav Kalashnikov , Mexico
Mathiyalagan Kalidass , India
Tamas Kalmar-Nagy , Hungary
Rajesh Kaluri , India
Jyottheswara Reddy Kalvakurthi, India
Zhao Kang , China
Ramani Kannan , Malaysia
Tomasz Kapitaniak , Poland
Julius Kaplunov, United Kingdom
Konstantinos Karamanos, Belgium
Michal Kawulok, Poland

Irfan Kaymaz , Turkey
Vahid Kayvanfar , Qatar
Krzysztof Kecik , Poland
Mohamed Khader , Egypt
Chaudry M. Khalique , South Africa
Mukhtaj Khan , Pakistan
Shahid Khan , Pakistan
Nam-Il Kim, Republic of Korea
Philipp V. Kiryukhantsev-Korneev ,
Russia
P.V.V Kishore , India
Jan Koci , Czech Republic
Ioannis Kostavelis , Greece
Sotiris B. Kotsiantis , Greece
Frederic Kratz , France
Vamsi Krishna , India
Edyta Kucharska, Poland
Krzysztof S. Kulpa , Poland
Kamal Kumar, India
Prof. Ashwani Kumar , India
Michal Kunicki , Poland
Cedrick A. K. Kwuimy , USA
Kyandoghere Kyamakya, Austria
Ivan Kyrchei , Ukraine
Márcio J. Lacerda , Brazil
Eduardo Lalla , The Netherlands
Giovanni Lancioni , Italy
Jaroslaw Latalski , Poland
Hervé Laurent , France
Agostino Lauria , Italy
Aimé Lay-Ekuakille , Italy
Nicolas J. Leconte , France
Kun-Chou Lee , Taiwan
Dimitri Lefebvre , France
Eric Lefevre , France
Marek Lefik, Poland
Yaguo Lei , China
Kauko Leiviskä , Finland
Ervin Lenzi , Brazil
ChenFeng Li , China
Jian Li , USA
Jun Li , China
Yueyang Li , China
Zhao Li , China































Zhen Li , China
En-Qiang Lin, USA
Jian Lin , China
Qibin Lin, China
Yao-Jin Lin, China
Zhiyun Lin , China
Bin Liu , China
Bo Liu , China
Heng Liu , China
Jianxu Liu , Thailand
Lei Liu , China
Sixin Liu , China
Wanquan Liu , China
Yu Liu , China
Yuanchang Liu , United Kingdom
Bonifacio Llamazares , Spain
Alessandro Lo Schiavo , Italy
Jean Jacques Loiseau , France
Francesco Lolli , Italy
Paolo Lonetti , Italy
António M. Lopes , Portugal
Sebastian López, Spain
Luis M. López-Ochoa , Spain
Vassilios C. Loukopoulos, Greece
Gabriele Maria Lozito , Italy
Zhiguo Luo , China
Gabriel Luque , Spain
Valentin Lychagin, Norway
YUE MEI, China
Junwei Ma , China
Xuanlong Ma , China
Antonio Madeo , Italy
Alessandro Magnani , Belgium
Toqeer Mahmood , Pakistan
Fazal M. Mahomed , South Africa
Arunava Majumder , India
Sarfraz Nawaz Malik, Pakistan
Paolo Manfredi , Italy
Adnan Maqsood , Pakistan
Muazzam Maqsood, Pakistan
Giuseppe Carlo Marano , Italy
Damijan Markovic, France
Filipe J. Marques , Portugal
Luca Martinelli , Italy
Denizar Cruz Martins, Brazil

Francisco J. Martos , Spain
Elio Masciari , Italy
Paolo Massioni , France
Alessandro Mauro , Italy
Jonathan Mayo-Maldonado , Mexico
Pier Luigi Mazzeo , Italy
Laura Mazzola, Italy
Driss Mehdi , France
Zahid Mehmood , Pakistan
Roderick Melnik , Canada
Xiangyu Meng , USA
Jose Merodio , Spain
Alessio Merola , Italy
Mahmoud Mesbah , Iran
Luciano Mescia , Italy
Laurent Mevel , France
Constantine Michailides , Cyprus
Mariusz Michta , Poland
Prankul Middha, Norway
Aki Mikkola , Finland
Giovanni Minafò , Italy
Edmondo Minisci , United Kingdom
Hiroyuki Mino , Japan
Dimitrios Mitsotakis , New Zealand
Ardashir Mohammadzadeh , Iran
Francisco J. Montáns , Spain
Francesco Montefusco , Italy
Gisele Mophou , France
Rafael Morales , Spain
Marco Morandini , Italy
Javier Moreno-Valenzuela , Mexico
Simone Morganti , Italy
Caroline Mota , Brazil
Aziz Moukrim , France
Shen Mouquan , China
Dimitris Mourtzis , Greece
Emiliano Mucchi , Italy
Taseer Muhammad, Saudi Arabia
Ghulam Muhiuddin, Saudi Arabia
Amitava Mukherjee , India
Josefa Mula , Spain
Jose J. Muñoz , Spain
Giuseppe Muscolino, Italy
Marco Mussetta , Italy

Hariharan Muthusamy, India
Alessandro Naddeo , Italy
Raj Nandkeolyar, India
Keivan Navaie , United Kingdom
Soumya Nayak, India
Adrian Neagu , USA
Erivelton Geraldo Nepomuceno , Brazil
AMA Neves, Portugal
Ha Quang Thinh Ngo , Vietnam
Nhon Nguyen-Thanh, Singapore
Papakostas Nikolaos , Ireland
Jelena Nikolic , Serbia
Tatsushi Nishi, Japan
Shanzhou Niu , China
Ben T. Nohara , Japan
Mohammed Nouari , France
Mustapha Nourelfath, Canada
Kazem Nouri , Iran
Ciro Núñez-Gutiérrez , Mexico
Włodzimierz Ogryczak, Poland
Roger Ohayon, France
Krzysztof Okarma , Poland
Mitsuhiro Okayasu, Japan
Murat Olgun , Turkey
Diego Oliva, Mexico
Alberto Olivares , Spain
Enrique Onieva , Spain
Calogero Orlando , Italy
Susana Ortega-Cisneros , Mexico
Sergio Ortobelli, Italy
Naohisa Otsuka , Japan
Sid Ahmed Ould Ahmed Mahmoud , Saudi Arabia
Taoreed Owolabi , Nigeria
EUGENIA PETROPOULOU , Greece
Arturo Pagano, Italy
Madhumangal Pal, India
Pasquale Palumbo , Italy
Dragan Pamučar, Serbia
Weifeng Pan , China
Chandan Pandey, India
Rui Pang, United Kingdom
Jürgen Pannek , Germany
Elena Panteley, France
Achille Paolone, Italy

George A. Papakostas , Greece
Xosé M. Pardo , Spain
You-Jin Park, Taiwan
Manuel Pastor, Spain
Pubudu N. Pathirana , Australia
Surajit Kumar Paul , India
Luis Payá , Spain
Igor Pažanin , Croatia
Libor Pekař , Czech Republic
Francesco Pellicano , Italy
Marcello Pellicciari , Italy
Jian Peng , China
Mingshu Peng, China
Xiang Peng , China
Xindong Peng, China
Yuexing Peng, China
Marzio Pennisi , Italy
Maria Patrizia Pera , Italy
Matjaz Perc , Slovenia
A. M. Bastos Pereira , Portugal
Wesley Peres, Brazil
F. Javier Pérez-Pinal , Mexico
Michele Perrella, Italy
Francesco Pesavento , Italy
Francesco Petrini , Italy
Hoang Vu Phan, Republic of Korea
Lukasz Pieczonka , Poland
Dario Piga , Switzerland
Marco Pizzarelli , Italy
Javier Plaza , Spain
Goutam Pohit , India
Dragan Poljak , Croatia
Jorge Pomares , Spain
Hiram Ponce , Mexico
Sébastien Poncet , Canada
Volodymyr Ponomaryov , Mexico
Jean-Christophe Ponsart , France
Mauro Pontani , Italy
Sivakumar Poruran, India
Francesc Pozo , Spain
Aditya Rio Prabowo , Indonesia
Anchasa Pramuanjaroenkij , Thailand
Leonardo Primavera , Italy
B Rajanarayan Prusty, India

Krzysztof Puszynski , Poland
Chuan Qin , China
Dongdong Qin, China
Jianlong Qiu , China
Giuseppe Quaranta , Italy
DR. RITU RAJ , India
Vitomir Racic , Italy
Carlo Rainieri , Italy
Kumbakonam Ramamani Rajagopal, USA
Ali Ramazani , USA
Angel Manuel Ramos , Spain
Higinio Ramos , Spain
Muhammad Afzal Rana , Pakistan
Muhammad Rashid, Saudi Arabia
Manoj Rastogi, India
Alessandro Rasulo , Italy
S.S. Ravindran , USA
Abdolrahman Razani , Iran
Alessandro Reali , Italy
Jose A. Reinoso , Spain
Oscar Reinoso , Spain
Haijun Ren , China
Carlo Renno , Italy
Fabrizio Renno , Italy
Shahram Rezapour , Iran
Ricardo Rianza , Spain
Francesco Riganti-Fulginei , Italy
Gerasimos Rigatos , Greece
Francesco Ripamonti , Italy
Jorge Rivera , Mexico
Eugenio Roanes-Lozano , Spain
Ana Maria A. C. Rocha , Portugal
Luigi Rodino , Italy
Francisco Rodríguez , Spain
Rosana Rodríguez López, Spain
Francisco Rossomando , Argentina
Jose de Jesus Rubio , Mexico
Weiguo Rui , China
Rubén Ruiz , Spain
Ivan D. Rukhlenko , Australia
Dr. Eswaramoorthi S. , India
Weichao SHI , United Kingdom
Chaman Lal Sabharwal , USA
Andrés Sáez , Spain

Bekir Sahin, Turkey
Laxminarayan Sahoo , India
John S. Sakellariou , Greece
Michael Sakellariou , Greece
Salvatore Salamone, USA
Jose Vicente Salcedo , Spain
Alejandro Salcido , Mexico
Alejandro Salcido, Mexico
Nunzio Salerno , Italy
Rohit Salgotra , India
Miguel A. Salido , Spain
Sinan Salih , Iraq
Alessandro Salvini , Italy
Abdus Samad , India
Sovan Samanta, India
Nikolaos Samaras , Greece
Ramon Sancibrian , Spain
Giuseppe Sanfilippo , Italy
Omar-Jacobo Santos, Mexico
J Santos-Reyes , Mexico
José A. Sanz-Herrera , Spain
Musavarah Sarwar, Pakistan
Shahzad Sarwar, Saudi Arabia
Marcelo A. Savi , Brazil
Andrey V. Savkin, Australia
Tadeusz Sawik , Poland
Roberta Sburlati, Italy
Gustavo Scaglia , Argentina
Thomas Schuster , Germany
Hamid M. Sedighi , Iran
Mijanur Rahaman Seikh, India
Tapan Senapati , China
Lotfi Senhadji , France
Junwon Seo, USA
Michele Serpilli, Italy
Silvestar Šesnić , Croatia
Gerardo Severino, Italy
Ruben Sevilla , United Kingdom
Stefano Sfarra , Italy
Dr. Ismail Shah , Pakistan
Leonid Shaikhet , Israel
Vimal Shanmuganathan , India
Prayas Sharma, India
Bo Shen , Germany
Hang Shen, China

Xin Pu Shen, China
Dimitri O. Shepelsky, Ukraine
Jian Shi , China
Amin Shokrollahi, Australia
Suzanne M. Shontz , USA
Babak Shotorban , USA
Zhan Shu , Canada
Angelo Sifaleras , Greece
Nuno Simões , Portugal
Mehakpreet Singh , Ireland
Piyush Pratap Singh , India
Rajiv Singh, India
Seralathan Sivamani , India
S. Sivasankaran , Malaysia
Christos H. Skiadas, Greece
Konstantina Skouri , Greece
Neale R. Smith , Mexico
Bogdan Smolka, Poland
Delfim Soares Jr. , Brazil
Alba Sofi , Italy
Francesco Soldovieri , Italy
Raffaele Solimene , Italy
Yang Song , Norway
Jussi Sopanen , Finland
Marco Spadini , Italy
Paolo Spagnolo , Italy
Ruben Specogna , Italy
Vasilios Spitas , Greece
Ivanka Stamova , USA
Rafał Stanisławski , Poland
Miladin Stefanović , Serbia
Salvatore Strano , Italy
Yakov Strelniker, Israel
Kangkang Sun , China
Qiuqin Sun , China
Shuaishuai Sun, Australia
Yanchao Sun , China
Zong-Yao Sun , China
Kumarasamy Suresh , India
Sergey A. Suslov , Australia
D.L. Suthar, Ethiopia
D.L. Suthar , Ethiopia
Andrzej Swierniak, Poland
Andras Szekrenyes , Hungary
Kumar K. Tamma, USA



Yong (Aaron) Tan, United Kingdom
Marco Antonio Taneco-Hernández , Mexico
Lu Tang , China
Tianyou Tao, China
Hafez Tari , USA
Alessandro Tasora , Italy
Sergio Teggi , Italy
Adriana del Carmen Téllez-Anguiano , Mexico
Ana C. Teodoro , Portugal
Efstathios E. Theotokoglou , Greece
Jing-Feng Tian, China
Alexander Timokha , Norway
Stefania Tomasiello , Italy
Gisella Tomasini , Italy
Isabella Torricollo , Italy
Francesco Tornabene , Italy
Mariano Torrisi , Italy
Thang nguyen Trung, Vietnam
George Tsiatas , Greece
Le Anh Tuan , Vietnam
Nerio Tullini , Italy
Emilio Turco , Italy
Ilhan Tuzcu , USA
Efstratios Tzirtzilakis , Greece
FRANCISCO UREÑA , Spain
Filippo Ubertini , Italy
Mohammad Uddin , Australia
Mohammad Safi Ullah , Bangladesh
Serdar Ulubeyli , Turkey
Mati Ur Rahman , Pakistan
Panayiotis Vafeas , Greece
Giuseppe Vairo , Italy
Jesus Valdez-Resendiz , Mexico
Eusebio Valero, Spain
Stefano Valvano , Italy
Carlos-Renato Vázquez , Mexico
Martin Velasco Villa , Mexico
Franck J. Vernerey, USA
Georgios Veronis , USA
Vincenzo Vespri , Italy
Renato Vidoni , Italy
Venkatesh Vijayaraghavan, Australia

Anna Vila, Spain
Francisco R. Villatoro , Spain
Francesca Vipiana , Italy
Stanislav Vitek , Czech Republic
Jan Vorel , Czech Republic
Michael Vynnycky , Sweden
Mohammad W. Alomari, Jordan
Roman Wan-Wendner , Austria
Bingchang Wang, China
C. H. Wang , Taiwan
Dagang Wang, China
Guoqiang Wang , China
Huaiyu Wang, China
Hui Wang , China
J.G. Wang, China
Ji Wang , China
Kang-Jia Wang , China
Lei Wang , China
Qiang Wang, China
Qingling Wang , China
Weiwei Wang , China
Xinyu Wang , China
Yong Wang , China
Yung-Chung Wang , Taiwan
Zhenbo Wang , USA
Zhibo Wang, China
Waldemar T. Wójcik, Poland
Chi Wu , Australia
Qihong Wu, China
Yuqiang Wu, China
Zhibin Wu , China
Zhizheng Wu , China
Michalis Xenos , Greece
Hao Xiao , China
Xiao Ping Xie , China
Qingzheng Xu , China
Binghan Xue , China
Yi Xue , China
Joseph J. Yame , France
Chuanliang Yan , China
Xinggang Yan , United Kingdom
Hongtai Yang , China
Jixiang Yang , China
Mijia Yang, USA
Ray-Yeng Yang, Taiwan

Zaoli Yang , China
Jun Ye , China
Min Ye , China
Luis J. Yebra , Spain
Peng-Yeng Yin , Taiwan
Muhammad Haroon Yousaf , Pakistan
Yuan Yuan, United Kingdom
Qin Yuming, China
Elena Zaitseva , Slovakia
Arkadiusz Zak , Poland
Mohammad Zakwan , India
Ernesto Zambrano-Serrano , Mexico
Francesco Zammori , Italy
Jessica Zangari , Italy
Rafal Zdunek , Poland
Ibrahim Zeid, USA
Nianyin Zeng , China
Junyong Zhai , China
Hao Zhang , China
Haopeng Zhang , USA
Jian Zhang , China
Kai Zhang, China
Lingfan Zhang , China
Mingjie Zhang , Norway
Qian Zhang , China
Tianwei Zhang , China
Tongqian Zhang , China
Wenyu Zhang , China
Xianming Zhang , Australia
Xuping Zhang , Denmark
Yinyan Zhang, China
Yifan Zhao , United Kingdom
Debao Zhou, USA
Heng Zhou , China
Jian G. Zhou , United Kingdom
Junyong Zhou , China
Xueqian Zhou , United Kingdom
Zhe Zhou , China
Wu-Le Zhu, China
Gaetano Zizzo , Italy
Mingcheng Zuo, China

Contents

Numerical Approximation of Blast Loads on Confined Dry-Stacked Masonry Wall

Muhammad Ishfaq, Azmat Ullah, Awais Ahmed, Sarfraz Ali, Syed Muhammad Ali, Marjan Uddin , and Khan Shahzada 





Research Article (13 pages), Article ID 2394931, Volume 2021 (2021)

Generalized Ulam–Hyers–Rassias Stability Results of Solution for Nonlinear Fractional Differential Problem with Boundary Conditions

A. Naimi, B. Tellab, Y. Altayeb , and A. Moumen




Research Article (11 pages), Article ID 7150739, Volume 2021 (2021)

Four-Scroll Hyperchaotic Attractor in a Five-Dimensional Memristive Wien Bridge Oscillator: Analysis and Digital Electronic Implementation

Gabin Jeatsa Kitio, Cyrille Ainamon, Karthikeyan Rajagopal , Léandre Kamdjeu Kengne , Sifeu Takougang Kingni , and Justin Roger Mboupda Pone 



Research Article (21 pages), Article ID 4820771, Volume 2021 (2021)

Numerical Analysis of Stratified and Slug Flows

Saliha Nouri, Zouhaier Hafsia , Salah Mahmoud Boulaaras , Ali Allahem , Salem Alkhalaf, and Baowei Feng




Research Article (9 pages), Article ID 8418008, Volume 2021 (2021)

On Behavior of the Periodic Orbits of a Hamiltonian System of Bifurcation of Limit Cycles

Amor Menaceur, Mohamed Abdalla , Sahar Ahmed Idris , and Ibrahim Mekawy






Research Article (6 pages), Article ID 1952706, Volume 2021 (2021)

A Note on Small Amplitude Limit Cycles of Liénard Equations Theory

Yassine Bouattia, Djalil Boudjem , Ammar Makhoulouf, Sulima Ahmed Zubair , and Sahar Ahmed Idris 


Research Article (6 pages), Article ID 3101000, Volume 2021 (2021)

FPGA Realization and Lyapunov–Krasovskii Analysis for a Master-Slave Synchronization Scheme Involving Chaotic Systems and Time-Delay Neural Networks

J. Perez-Padron , C. Posadas-Castillo , J. Paz-Perez , E. Zambrano-Serrano , and M. A. Platas-Garza 

Research Article (17 pages), Article ID 2604874, Volume 2021 (2021)

Circuit Implementation Synchronization between Two Modified Fractional-Order Lorenz Chaotic Systems via a Linear Resistor and Fractional-Order Capacitor in Parallel Coupling

Juan Liu, Xuefeng Cheng, and Ping Zhou 

Research Article (8 pages), Article ID 6771261, Volume 2021 (2021)

Research Article

Numerical Approximation of Blast Loads on Confined Dry-Stacked Masonry Wall

Muhammad Ishfaq,¹ Azmat Ullah,¹ Awais Ahmed,¹ Sarfraz Ali,³ Syed Muhmmad Ali,¹ Marjan Uddin ,² and Khan Shahzada ¹

¹Department of Civil Engineering, University of Engineering & Technology, Peshawar, Pakistan

²Department of Basic Sciences, University of Engineering & Technology, Peshawar, Pakistan

³Wits Mining Institute (WMI), University of the Witwatersrand, Johannesburg, South Africa

Correspondence should be addressed to Marjan Uddin; marjan@uetpeshawar.edu.pk and Khan Shahzada; khanshahzada@uetpeshawar.edu.pk

Received 14 September 2021; Revised 15 November 2021; Accepted 7 December 2021; Published 30 December 2021

Academic Editor: Viet-Thanh Pham

Copyright © 2021 Muhammad Ishfaq et al. This is an open access article distributed under the Creative Commons Attribution License, which permits unrestricted use, distribution, and reproduction in any medium, provided the original work is properly cited.

This research intends to numerically study the out-of-plane behaviour of confined dry-stacked masonry (CDSM) walls against blast loading. CDSM is a mortarless interlocking masonry system consisting of Hydraform blocks laid in stretcher bond with reinforced concrete (RC) confining elements. A nonlinear numerical model is developed using advanced finite element hydrocode ANSYS-Autodyn to study the response of CDSM walls subjected to explosive loads. Four different test cases using a charge weight of 4 kg, 8 kg, 12 kg, and 16 kg of Wabox explosive are investigated numerically. The results obtained from numerical simulation are validated with the experimental tests results. The numerical results are found in good agreement with the experimental results. The ability of the numerical model is studied to correctly predict the pressure-time history in pressure gauges installed on walls and compared with experimental data. Peak incident overpressures obtained in these numerical tests ranged from 240 to 1000 kPa. Likewise, the damage patterns obtained from the numerical simulations are compared with available experimental results which show a satisfactory agreement. This study helps to check the response of CDSM structures against blast load which can be used for the construction of blast resisting design of buildings.

1. Introduction

Terrorism, after 9/11 in Pakistan, has become a devastating and extremely harmful phenomenon. The human losses are more than 70,000 and with economic cost of more than \$68 billion [1]. Terrorists mostly hit government lifeline structures such as educational institutes, healthcare facilities, police and army installations, and government infrastructures by bomb blasts which are mainly built from masonry [2]. In these scenarios, the performance of masonry walls is very critical for the structural integrity of buildings. It is very challenging to study experimentally the effects of blast load on structures due to numerous input parameters, limited financial resources, time constraints, and safety considerations. Therefore, the best alternative for such type of costly experiments is an efficient computer software and codes such as ANSYS-Autodyn [3].

Besides conventional masonry, a new masonry system of mortarless interlocking blocks, which is also known as dry-stack masonry, has recently been introduced in Pakistan. The typical shape of dry-stack masonry blocks (Hydraform blocks) and their masonry assemblage is shown in Figure 1. If this masonry system is confined by reinforced concrete (RC) beam and columns, then it is termed as confined dry-stack masonry (CDSM) system. The CDSM system was found to be more ductile and reliable in strength for lateral loads [4]. The structural strength and integrity of this masonry system depend on interlocking system of blocks between masonry units. The interlocking mechanism provides stability, self-alignment, and levelling to the walls. Hydraform blocks are manufactured from mixture of soil with at least 22% clay, 10% sand, and 6.7% cement by weight mixed using a cement mixer. Approximately, 10% water is added to



FIGURE 1: (a) Hydraform block. (b) Assemblage of dry-stacking Hydraform blocks.

the mixture to achieve the desired consistency for block pressing and after seven days of curing, it is used in constructing walls [5]. The construction process in this type of masonry is simplified and highly economically competitive due fast track construction and very effective where skilled labor is expensive and even unavailable. Being a sustainable building material, it is more energy efficient compared to traditional clay-bricks which require three times more energy per square metre (406 kg of CO₂ emission) than Hydraform blocks (119 kg of CO₂ emission) [6].

The numerical modelling of CDSM walls is complex and computationally expensive. The analysis complexity reasons are modelling of the nonlinear behaviour of an RC confining frame, modelling of the nonlinear behaviour of a dry-stacked masonry panel, and modelling the interaction between frame and masonry [7].

Several researchers in the past have studied the blast load phenomenon on various structures numerically and experimentally such as Luccioni et al. [8] who conducted a numerical study to analyse the structural failure of the reinforced concrete building under the blast load. The results were compared with actual buildings that were damaged in terrorist attacks. In another study [9], the same researcher performed numerical analysis of blast load using hydrocodes and compared the results with empirical models with a good correlation. Theobald and Nurick [10] performed numerical and experimental study to investigate the performance of tube-core claddings under blast loads. A numerical model was developed in computer program ABAQUS/Explicit for numerical simulations which shows satisfactory correlation with experimental response. Thiagarajan et al. [11] conducted numerical and experimental study to investigate the performance of doubly reinforced concrete slabs against the blast loads. They employed the commercial program LS-DYNA for numerical simulations, and their numerical and experimental results were matched with a good agreement. Wu et al. [12] conducted a 3D and 2D numerical study by using commercial software Autodyn3D for the analysis of infilled masonry in RC frame structures subjected to ground excitations induced by blast waves. After comparison of results, they concluded that 3D analysis captured the real response of the structures. Ghaderi et al. [13] in 2015 used ABAQUS as numerical analyses tools to represent unreinforced brick masonry walls strengthened with 1.5 mm thick FRP strips fixed in various formations and subjected to a blast load based on scale-distance parameter. Finally, they

observed more damage to wall as the scale-distance decreased. Scaled distance (z) is parameter used for the intensity level of blast load as defined by equation (1), established by Hopkinson and Crazz [14], which relate charge weight of equivalent TNT (W) and standoff distance (R).

$$z = \frac{R}{\sqrt[3]{W}} \quad (1)$$

Alsayed et al. [15] in 2016 carried out blast load tests on block masonry wall specimen confined by a frame of reinforced concrete. They conducted five tests of various charge size and standoff displacements in the field. In conclusion, they found that the numerical results, obtained from ANSYS-Autodyn, best matched for the blast load parameters such as arrival time, peak incident, and peak reflected overpressures and therefore, the numerical techniques are the valid way to analyse the walls against blast load. Edri and Yankelevsky [16] in 2018 considered a new analytical model for the dynamic response in terms of time-displacement history of one-way arching URM walls under blast loads. Their SDOF model predictions have shown good agreement after comparisons with experimental test results. Michaloudis and Gebbeken [17] in 2019 presented in their study a modelling strategy appropriate for masonry walls subjected to far-field and contact detonations blasts to capture the local damage and debris formation. They adopted a derived material model for brick masonry from a concrete model which was already tested under blast load. Their proposed model shows good performance and combines the advantages of fully Lagrangian approaches and Smoothed Particle Hydrodynamic (SPH) approach. The delivered numerical results of the model were in good agreement with the result of experimental studies. It is concluded from abovementioned discussion that most of the recent research studies have focused on the performance evaluation of conventional masonry and RC structures while research on CDSM structures performance against blast load is limited.

The aim of this research study is to develop a 3D finite element model to systematically study the out-of-plane behaviour of CDSM wall against blast load. A full-scale CDSM wall was developed in ANSYS-Autodyn and tested against the blast loads generated from Wabox explosive. The numerical simulations were performed for different test cases. Finally, the results obtained from numerical analysis

were compared with the data obtained from experimental tests conducted by Ullah [18] on the same masonry wall.

2. Description of CDSM Test Wall

The considered test model in this research is a CDSM wall shown in Figure 2, which is representative of typical masonry buildings constructed in Pakistan. The CDSM wall tested in the field by Ullah [18] and the same wall was modelled in the ANSYS-Autodyn. The CDSM wall panel is 7 ft (2.134 m) tall, 7 ft (2.134 m) wide, 8 inch (200 mm) thick confined by confining elements of 8 inch \times 8 inch (200 mm \times 200 mm) with typical 4-#4 (4 ϕ 12 mm) steel longitudinal reinforcement and #3 (ϕ 10 mm) rings provided at 6 inch (150 mm) center-to-center distance. All the steel rebars used in the wall specimen are tested and are of 40,000 psi (420 MPa) strength. Concrete cylinder specimens were casted during construction of test wall and tested for compressive strength after 28 days of curing. On average, compressive strength of 3000 psi (20.70 MPa) was obtained for ordinary concrete. The Hydraform blocks available in the local market of size 8 inch \times 8 inch \times 4 inch (200 mm \times 200 mm \times 100 mm) have been used to construct wall specimens. The gross area compressive strength of Hydraform block is 1940 psi (13.25 MPa) whereas based on shoulder area it is 1240 psi (8.50 MPa). As the stress transfer in dry-stacking condition is only through shoulders of the block, masonry prisms tested in the laboratory by applying load on the shoulders and the compressive strength of masonry were calculated as 730 psi (5.00 MPa). The Elastic Modulus from prism test was calculated as 606,660 psi (4182.77 MPa). All the test results are adopted from the research study of Hafeez [19]. The cement mortar with mix proportion of (1 : 6) has been used in the construction of starter course of the masonry walls.

3. Description of Testing Setup

Wabox (TNT equivalent = 1.1) explosive is used in this research study for blasting which is a nitroglycerine-based dynamite manufactured by WA Nobel PVT Ltd. Rawalpindi, Pakistan. The charge of Wabox explosive is situated 3 ft (915 mm) above the ground at a distance of 12 ft (3.66 m) from the wall as shown in Figure 3. Three pressure gauges G-01, G-02, and G-03 are installed on the windward face of the wall. The pressure gauges are installed to measure the incident overpressures on the face of the wall.

Four blast tests on the same CDSM wall, namely, blast tests #1, #2, #3, and #4, with varying charge weight were conducted in field by Ullah [18] carried out in Risalpure (Nowshera), Pakistan, and the same tests were modelled in ANSYS-Autodyn for calibration. In these tests, the wall was subjected to four blast load tests with increasing level of intensity and scale-distance parameter has been used for intensity level measurement; details are listed in Table 1.

4. Material Models for Simulations

ANSYS-Autodyn is a hydrocode which uses fundamental law of physics such as law of conservation of mass,

momentum, and energy in the form of partial differential equations (PDEs). These governing PDEs including initial and boundary conditions are used to predict the response of the system materials for large deformation in nonlinear dynamic problem. The mathematical relationships between density, pressure, internal energy, stresses, and strains are required for this analysis. These relationships are equation of state (EOS), strength constitutive model, and failure criteria for each material component. The following subsections provide the details of the material models and parameters used for numerical analysis.

4.1. Material Model for Air. In this study, the strength models and failure criteria models are not required as it is air blast and these parameters are usually required in undermining blast experiment. The following equation of state (EOS), as given by equation (2), is used for the air as it was assumed that the surrounded air is an ideal gas.

$$p = (\gamma - 1)\rho e. \quad (2)$$

Here, p is the pressure, γ is the constant of adiabatic process, which is estimated to be 1.4 for ideal gas, ρ is the specific mass, and e is the specific internal energy of the air. The parameters values of ideal gas EOS are listed in Table 2, which are adopted from ANSYS-Autodyn material library.

4.2. Material Model for Wabox Explosive. The Jones-Wilkins-Lee (JWL) [20] equation of state is formulated for the modelling of Wabox explosive material. JWL equation of states correlates chemical properties such as energy, volume, and pressure of high energy explosive products. The JWL equation of state in mathematical form is given by

$$p = A \left(1 - \frac{\omega}{R_1 V} \right) e^{R_1 V} + B \left(1 - \frac{\omega}{R_2 V} \right) e^{R_2 V} + \frac{\omega e}{V}, \quad (3)$$

where A , B , R_1 , R_2 , ω are derived empirical constants which have different values for different explosive materials, V define the expansion of the detonating materials, and e is the specific energy at detonation stage.

The input parameters values of the JWL equation of state used for Wabox explosive (TNT equivalent = 1.1) are taken from Abbas et al. [21] and remaining properties are available in ANSYS-Autodyn which are summarised in Table 3. In this study, the Eulerian solver (multimaterial) was employed for modelling both air and explosive material.

4.3. Material Model for Reinforced Concrete. In this study, the Riedel-Hiermaier-Thoma (RHT) material model of Riedel et al. [22], implemented in ANSYS-Autodyn, has been used for reinforced concrete. This model is extensively used for concrete and brittle materials to predict their response under blast load. In the RHT model for concrete, the two basic parameters, compressive strength (f_c) and tensile strength (f_t) obtained from uniaxially loaded cylinder test, are required. The remaining parameters of concrete are derived from these parameters. The concrete strength in

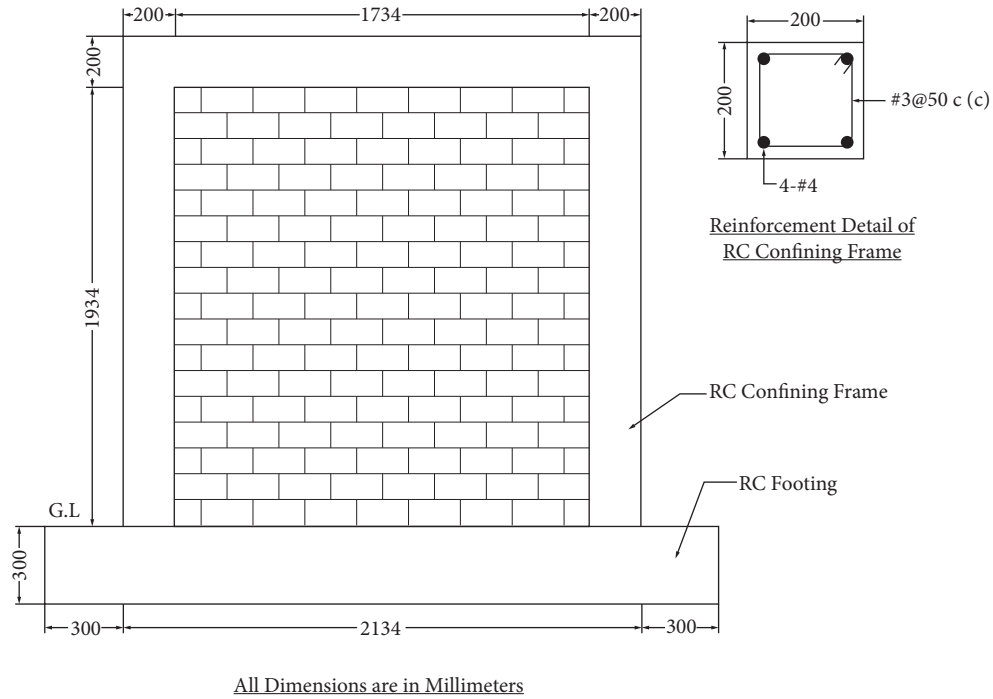


FIGURE 2: Geometric description of test model wall with dimensions and reinforcement detail of RC confining frame.

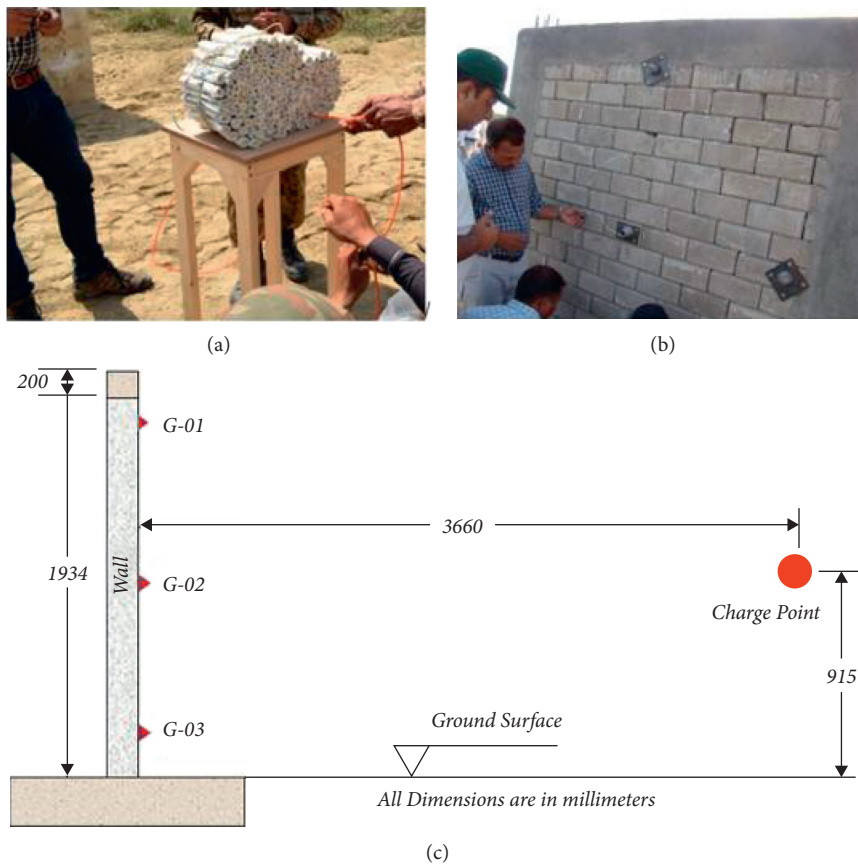


FIGURE 3: Detail of explosive and pressure sensors for field tests. (a) Wabox explosive. (b) Installation of pressure sensors [18]. (c) Geometrical description of test setup.

TABLE 1: Detail of parameters for blast load tests.

	Test 1	Test 2	Test 3	Test 4
Wabox charge mass (kg)	4	8	12	16
Standoff distance (m)	3.66	3.66	3.66	3.66
Charge height (m)	0.91	0.91	0.91	0.91
Scaled distance (m/kg ^{1/3})	2.23	1.77	1.55	1.41

TABLE 2: Material model parameter values for air (equation of state: ideal gas).

EOS parameter	Value
Reference density, ρ (kg/m ³)	1.225
Heat capacity ratio, γ	1.4
Adiabatic constant	0.0
Pressure shift	0.0
Ref. temp. (K)	288.2
Spec. heat (J/kg K)	717.6
Initial internal energy (kJ/kg)	2.0E+5

TABLE 3: Material model parameter values for Wabox explosive (equation of state: JWL).

EOS parameter	Value
Reference density, ρ (kg/m ³)	1.42E+3
State variable, A (MPa)	609.7E+3
State variable, B (MPa)	12.9E+3
State variable, R_1	4.5
State variable, R_2	1.4
State variable, w	0.2
Velocity of wave, v (m/s)	8.2E+3
Specific energy, e (MJ/m ³)	9.0E+3
Initial pressure, p (MPa)	28.0E+3

RHT is controlled by three strength failure surfaces: initial surface also called elastic limit surface, failure surface, and postfailure surface (residual surface) as shown in Figure 4. In this model, high tensile strength of concrete has been adopted to incorporate the tensile strength of mild steel reinforcement bars based on the study of Luccioni et al. [8]. Therefore, modified properties of reinforced concrete, as listed in Table 4, have been used.

Based on the hydrostatic behaviour of porous concrete the RHT model utilizes the p - α equation of state (EOS) model of Herrmann [23]. EOS is a function that mathematically correlates hydrostatic pressure, specific volume, and internal energy. This equation of state model is adopted in this research to capture the key global response of the wall. The input parameter values, that define the p - α equation of state, are adopted from ANSYS-Autodyn materials library which are listed in Table 4.

4.4. Material Model for Dry-Stack Masonry. In numerical modelling, masonry walls can be modelled using either micro- or macromodel. Micromodel is distinctive simulation of masonry while macromodel is a homogenized simulation. In this study, homogenized macromodel is used

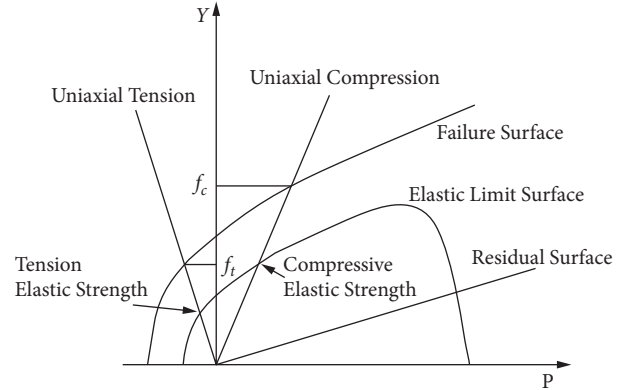


FIGURE 4: Failure surfaces of RHT concrete model.

for masonry wall to characterize Hydraform blocks and joints properties [24–28]. The use of macromodelling for masonry substantially optimises the computational time and cost for simulation. Therefore, it can be efficiently employed when microscopic response is not important like in case of extreme loads [29]. In this study, dry-stack masonry was modelled as homogenous low-strength concrete as the wall is constructed from concrete Hydraform blocks. The mechanical properties of Hydraform blocks and dry-stack masonry are taken from Hafeez [19] and the remaining input parameters are adopted from ANSYS-Autodyn material library which are listed in Table 5.

5. Finite Element Model Parts

The finite element model was developed in the software which is composed of CDSM wall and air volume by the wall. Due to symmetry, only half of the physical air domain and wall was modelled to reduce the computation costs. The model for CDSM wall is developed with three different Lagrangian parts, i.e., RC footing, confining elements, and dry-stack masonry wall. The 8-noded hexahedral solid elements of size 50 mm have been used in all three Lagrangian parts. Figure 5 illustrates the finite element meshing grid of the model, pressure gauge's location, and detonation. In this model, a fixed boundary condition was adopted by using unbreakable connection between the confining frame and footing, whereas stress-criteria based breakable connections were assumed between the masonry and confining frame. The details of input parameters for breakable connection are listed in Table 6.

The surrounded air part of the model was modelled as Eulerian, ideal gas. A three-dimensional (3D) domain of cuboid-shaped was created for surrounded air. The sizes of surrounded air domain are $4.22 \times 2.40 \times 2.20$ m. The element dimension for air volume is used as 25 mm which is an optimised size based on mesh convergence studies.

6. Erosion Criteria

As per the study carried out by researcher [32, 33], the elements of the reinforced concrete confining frame were

TABLE 4: Material properties for confining reinforced concrete (state equation: p - α , strength model: RHT).

EOS parameter	Value	Strength parameter	Value
Initial density, ρ_o (kg/m ³)	2.3E+3	Compressive strength, f_c (MPa)	21.0
Reference density, ρ_o (kg/m ³)	2.75E+3	Tensile strength, f_t (MPa)	10.0
Porous sound speed (m/s)	2.75E+3	Failure surface constant, A_c	1.60
Initial compaction, O_c (MPa)	23.3	Failure surface exponent, N_c	0.61
Solid compaction, O_s (MPa)	6.0E+3	Parameter, Q_o	0.68
Compaction exponent, n_c	3.0	Parameter, Q_1	0.011
Bulk modulus, K (MPa)	35.2E+3	Fractured constant, B_c	1.60
State variable, A_2 (MPa)	39.5E+3	Fractured exponent, M_c	0.61
State variable, A_3 (MPa)	9.0E+3	Damage parameter, D_1	0.04
State variable, B_o	1.22	Damage parameter, D_2	1.00
State variable, B_1	1.22	Failure strain (minimum), ϵ_f	0.01
State variable, T_1 (MPa)	35.2E+3	Shear modulus fraction	0.13
State variable, T_2 (MPa)	0.0	Principal tensile stress (MPa)	10.0
Reference temperature (K)	300.0	Fracture energy, G_f (J/m ²)	100.0
Specific heat (J/kg K)	654.0	Erosion parameter	Strain
		Erosion limit	0.50

TABLE 5: Material properties used for dry-stack masonry (state equation: p - α , strength model: RHT).

Strength parameter	Value
Compressive strength, f_c (kPa)	5.0E+3
Tensile strength, f_t (kPa)	400
Principal tensile stress (kPa)	400
Elastic modulus, E (MPa)	4.2E+3
Softening criteria	Nil
Erosion parameter	Strain
Erosion limit	0.02

Remaining properties are the same as used for reinforced concrete.

permitted to erode from the system when the level of geometric strain (instantaneous) reaches 0.5. But dry-stack masonry geometric strain (instantaneous) of 0.02 was assumed as a criterion for the erosion of wall elements. These erosion models are adopted in ANSYS-Autodyn to avoid extreme and impractical deformation of mesh or grid system and also to model the fragmentation of wall parts.

7. Blast Analysis in ANSYS-Autodyn

The blast load analysis of the CDSM wall in ANSYS-Autodyn was performed in two phases. The first phase, which is a one-dimension (1D) analysis, simulates the early-stage time expansion of blast wave in 1D using radial symmetry. This expansion of pressure wave continues until it hits the reflecting boundary. In the second phase, the output of the 1D analysis is then transferred to the 3D domain which is created independently. In this study, the explosive material is installed at 0.92 m above the ground surface. Therefore, it is considered as air blast and ground shocks are ignored due to its negligible effects.

7.1. 1D ANSYS-Autodyn Analysis. In 1D analysis, the expansion of blast wave, generated after the explosive detonation of material in the surrounding air, was first modelled and simulated. The problem in this stage can be treated as one-dimensional (1D) due to spherical symmetry, and a

wedge is defined for the problem domain. The wedge geometric dimensions are specified on the basis of mass of explosive material and standoff distance. The finite element model of the wedge for the blast test of 16 kg Wabox at 3.66 m standoff distance is shown in Figure 6. The inner radius of the wedge is kept equal to 1 mm to avoid the zero thickness of the element at the origin. However, when this correction is employed, it reduces the weight of the explosive material, but its effect is insignificant due to small percentage reduction. The wedge model is filled with explosive material and surrounding air. The dimension of the elements in wedge is taken as 2 mm for achieving the desired level of accuracy and less computational time [34].

The output of this 1D analysis was later remapped in 3D domain of the model which was developed separately. The 3D domain of the model represents the wall with occupied air volume. This remapping technique reduces drastically the computational time and cost of the analysis. Figure 6 shows the plot of pressure contours at the end of the 1D analysis for 16 kg Wabox at 3.66 m standoff distance. The 1D blast analysis was carried out for four different scaled distances covering different charge weight of blast tests.

7.2. 3D ANSYS-Autodyne Analysis. The 1D analyses results were remapped onto the 3D domain already modelled with wall and surrounded air, separately. During remapping process, the center position of explosive charge from wall, that is, its standoff distance and height from ground, is defined in the remap dialogue box of ANSYS-Autodyn. In 3D analysis, fully coupled simulation was assumed between Lagrangian parts and air. The pressure waves at the start of the 3D analysis for 12 kg Wabox test are shown in Figure 7. All the foundation element nodes were assigned zero translational velocities which simulates fixed boundary condition for the wall at ground level. In ANSYS-Autodyn, Eulerian boundaries adopt reflecting boundary condition by default unless the specified boundary condition is assigned. Therefore, flow-out boundary condition was first defined in ANSYS-Autodyn and then assigned to the outer surfaces of

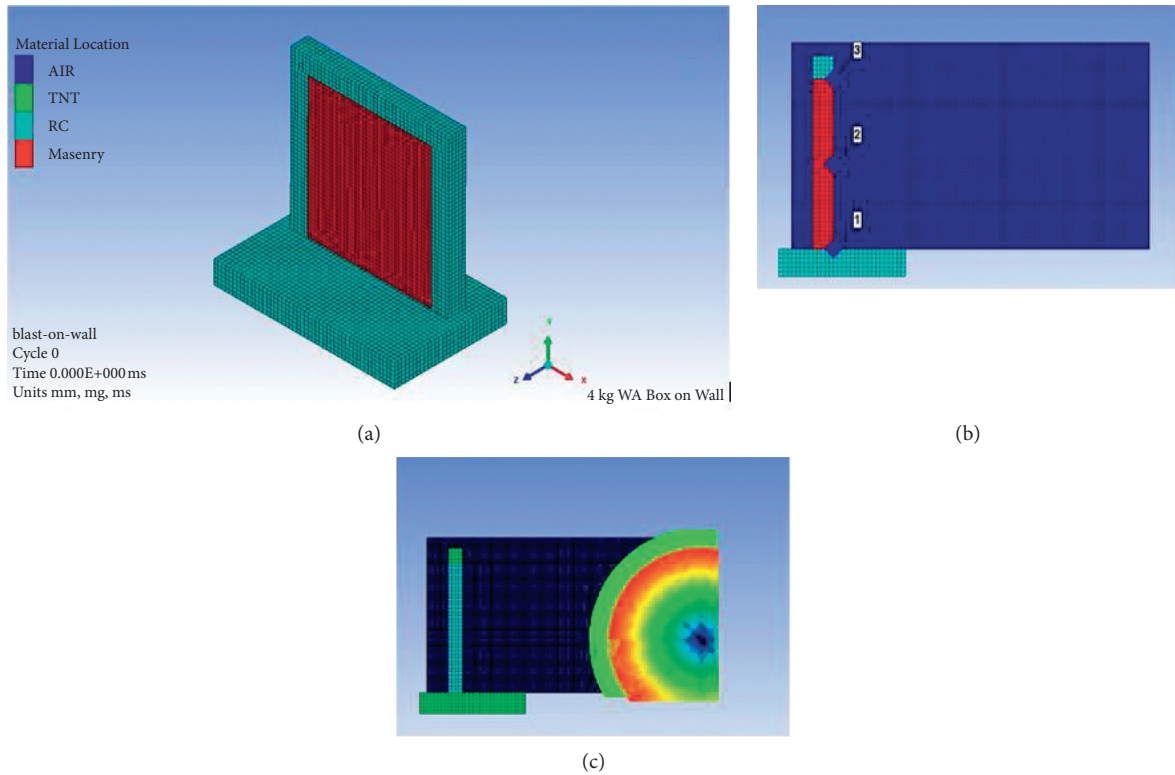


FIGURE 5: (a) Finite element (FE) model of the test specimen with meshing; (b) wall section enclosed in air domain with added pressure gauges; (c) explosive material detonation.

TABLE 6: Breakable connection failure parameter detail [30, 31].

Connection	Compressive strength (S_n)	Shear strength (S_s)
Wall and confining element interface	$S_n = S_s/3.1$	$S_s = 0.62\sqrt{\min(f'_c, f'_m)}$ (MPa) whereas f'_c = confining concrete compressive strength f'_m = dry-stack masonry compressive strength

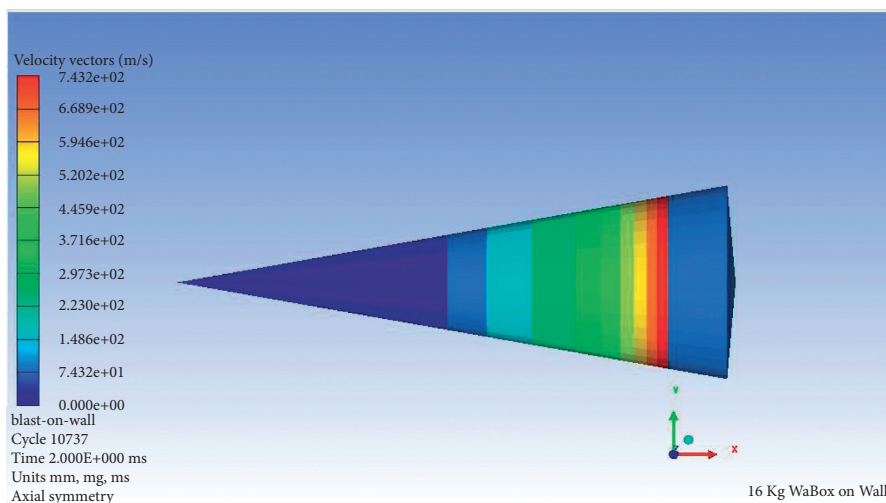


FIGURE 6: Pressure contours in 1D wedge filled with Wabox explosive and air.

all air domain. The flow-out boundary condition allows the exit of pressure waves from 3D air domain outer surfaces without reflection of pressure waves back to the domain [35].

Moreover, the terminal time for the analysis was kept as 50.0 ms for the blast traveling time between detonation point and wall. For the complete analysis and response

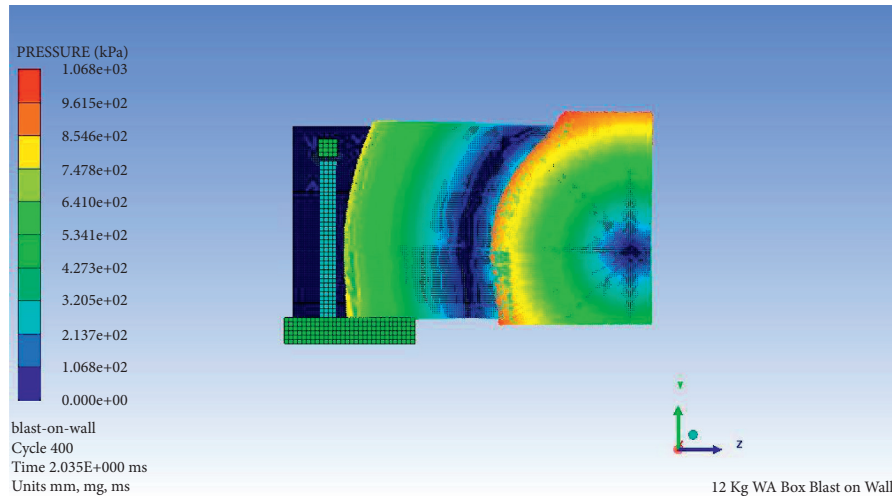


FIGURE 7: Pressure contours in 3D air domain after remapping from 1D output.

investigation of the wall specimen, this time is considered enough and appropriate.

8. Results and Discussion

A total of four charge weights detonations were simulated, of 4 kg, 8 kg, 12 kg, and 16 kg of Wabox explosive material. Furthermore, the gauge installed at mid locations was considered for pressure-time history as per availability of the experimental data. The analysis of explosive detonation and CDSM response was carried out using software ANSYS-Autodyn. The comparison of the results obtained from ANSYS-Autodyn was made with experimental data from Azmatullah [18] for pressure-time history and damage pattern which will be discussed in the coming sections.

8.1. Pressure-Time History. The pressure-time history comparisons between the experimental data and numerical simulation resulting from 4 kg, 8 kg, 12 kg, and 16 kg Wabox explosive detonation are shown in Figure 8. Minor discrepancies have been observed in Figure 8 between the numerical simulation and experimental graphs. Experimental graphs of pressure-time history display some roughness in curves while smooth pressure profile has been obtained from the numerical simulation. Moreover, the pressure peaks and arrival time do not match by small margin. These minor differences are mainly due to the reflection effects of blast waves from ground, which can be detected by pressure sensors installed on the wall. These minor reflections were not considered in the ANSYS-Autodyn model. However, there is still a general agreement between the pressure profiles of the numerical simulation and experimental tests. This validates that the numerical simulation in ANSYS-Autodyn is a reliable alternative for blast load tests on structures. From these graphs a comparison of incident overpressure and arrival time is illustrated in the coming subsections. The results were also calibrated with empirical model developed by Kingery-Bulmarsh [36] for incident overpressure and arrival time. The

Kingery-Bulmarsh equations have also been automated in the computer program CONWEP used for analysis of blast load.

8.1.1. Comparison of Peak Incident Overpressure. The summary of incident peak overpressure for different scaled distances obtained from ANSYS-Autodyn, experimental tests by Ullah [18], and Kingery-Bulmarsh model is given in Table 7 and is also plotted in Figure 9.

It is observed from Figure 9 that pressure variation trend for the three different model is nearly the same. The incident pressure values are also in close range except for the near field blast ($z = 1.41 \text{ m/kg}^{1/3}$).

8.1.2. Comparison of Arrival Time. Summary of results in terms of arrival time obtained from ANSYS-Autodyn, experimental tests, and Kingery-Bulmarsh empirical model is listed in Table 8.

The results comparison chart, as illustrated in Figure 10, displays the variation in arrival time values. However, the arrival time obtained from all three sources still shows a good correlation with slight variation which can be ignored for such type of large deformation or strain phenomenon.

8.2. Damage Pattern of Wall. The validation of the ANSYS-Autodyn 3D results with the experimental tests conducted by Ullah [18] was carried out through damage or failure pattern. The failure pattern is based on the damage level contours obtained from numerical analysis at the end of each simulation which shows damage zones of the specimen. The numerical values for damage level contour ranges from 0.0 to 1.0 which represents no damage and full damage, respectively. The failure pattern obtained from the numerical simulation shows a good correlation with the experimental results as illustrated in the coming sections.

8.2.1. Damage Pattern of Blast Test #1. In the first blast test, the CDSM wall was subjected to a blast of 4 kg explosive of Wabox at an altitude of 0.92 m and standoff distance of

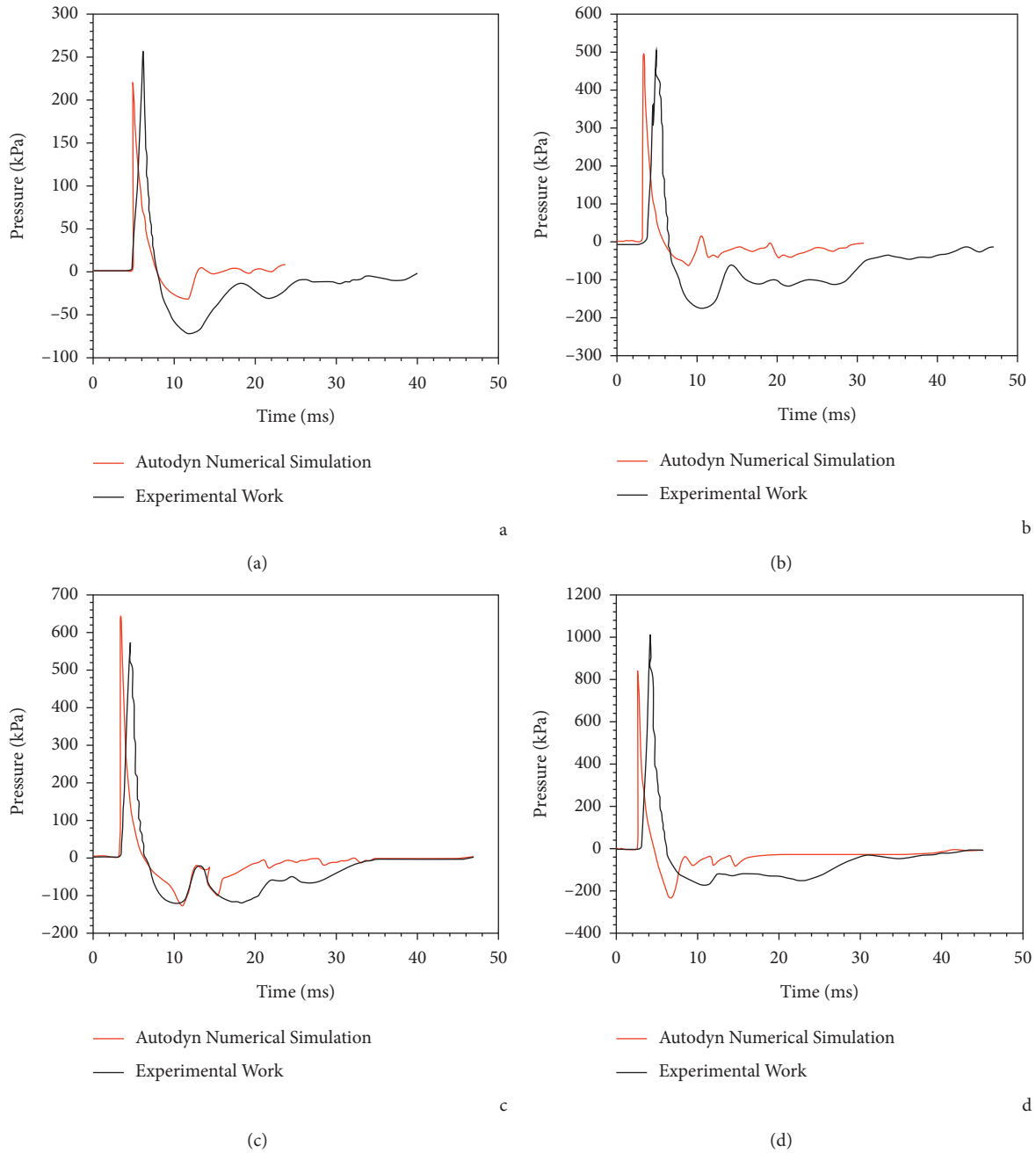


FIGURE 8: Pressure-time history comparison for (a) 4 kg Wabox Blast; (b) 8 kg Wabox Blast; (c) 12 kg Wabox Blast; (d) 16 kg Wabox Blast.

TABLE 7: Summary of results of peak incident overpressure for wall specimen.

Test case	Scaled distance, $z = R/\sqrt[3]{W_e}$ (m/kg ^{1/3})	Numerical peak incident overpressure (kPa)	Experimental peak incident overpressure (kPa)	Kingery-Bulmash peak incident overpressure (kPa)
1	2.23	240	260	221
2	1.77	490	498	375
3	1.55	630	590	512
4	1.41	895	1015	638

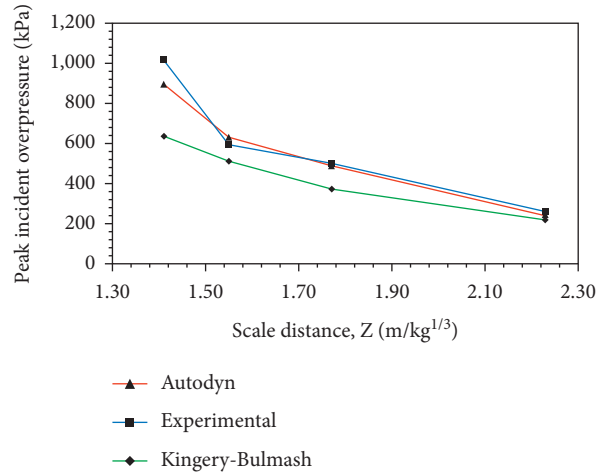


FIGURE 9: Peak incident overpressure comparison for different blast tests.

TABLE 8: Results summary of blast arrival time.

Test case	Scaled distance, $z = R/\sqrt[3]{W_e}$ (m/kg ^{1/3})	Numerical peak incident overpressure (ms)	Experimental peak incident overpressure (ms)	Kingery-Bulmash peak incident overpressure (ms)
1	2.23	3.97	4.00	3.41
2	1.77	3.25	3.50	2.79
3	1.55	2.85	2.55	2.48
4	1.41	2.50	2.45	2.28

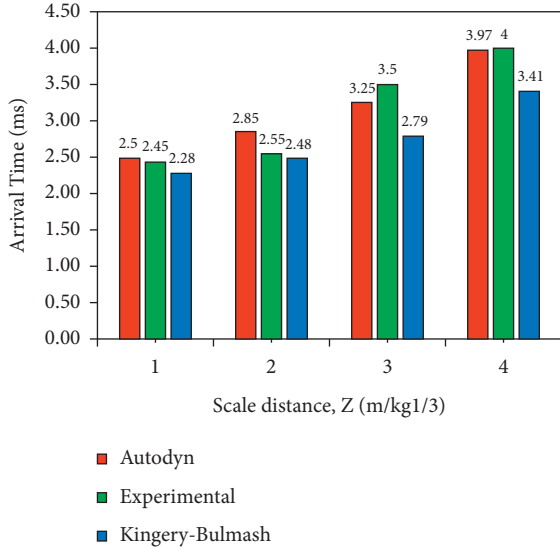


FIGURE 10: Arrival time comparison for different blast tests.

3.66 m. This blasting test of scaled distance, 2.23 m/kg^{1/3}, was of very low intensity; therefore, no damage has been observed to the wall as shown in Figure 11. After that, higher level intensity blast has been applied to the same wall specimen in the second blast which was named as blast test (#2).

8.2.2. *Damage Pattern after Blast Test #2.* It was found that for wall after 8 kg Wabox Blast (scaled distance of 1.77 m/kg^{1/3}) minor cracked are observed at the interface of the

masonry and confining frame as shown in Figure 12, which confirms the experimental result. The damage was minor; therefore, the same wall was used for the third blast test.

8.2.3. *Damage Pattern after Blast Test #3.* Further damage was observed and the cracks between confining element and masonry interface were increased after 12 kg (scaled distance of 1.55 m/kg^{1/3}) blast. However, for the wall specimen with increased intensity level of blast load, the wall was still intact, and no global failure has been observed. This result also shows a good comparison with the experimental results as shown in Figure 13.

8.2.4. *Damage Pattern after Blast Test #4.* In the final 16 kg Wabox explosion (scaled distance of 1.41 m/kg^{1/3}), the CDSM wall was completely damaged due to joint failure of the confining elements. The experienced damage level was high due to the debonding of the confining elements and blocks of the wall. This result also shows good conformance with the experimental test as shown in Figure 14. Although the left joint of the confining frame is intact, the right side joint failed by stress concentration which may be due to poor construction.

Based on the above simulations, a decent correlation has been attained between the obtained damage patterns of numerical analysis and field experiments of all four blast tests on the CDSM wall. This shows the validity of the numerical modelling analyses in capturing the real behaviour of CDSM wall exposed to blast loads.

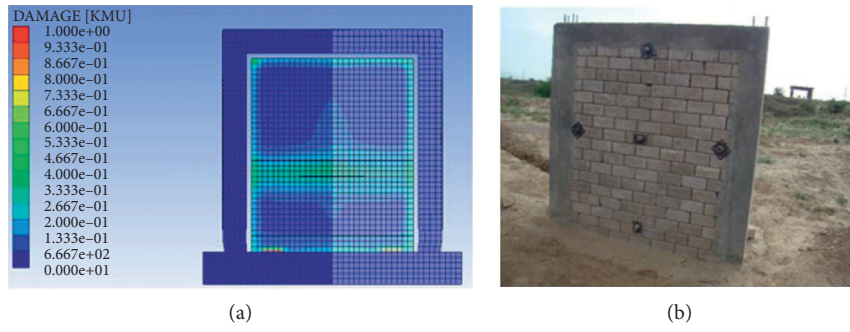


FIGURE 11: Damage pattern comparison for 4 kg Wabox Blast: (a) numerical results; (b) experimental results.

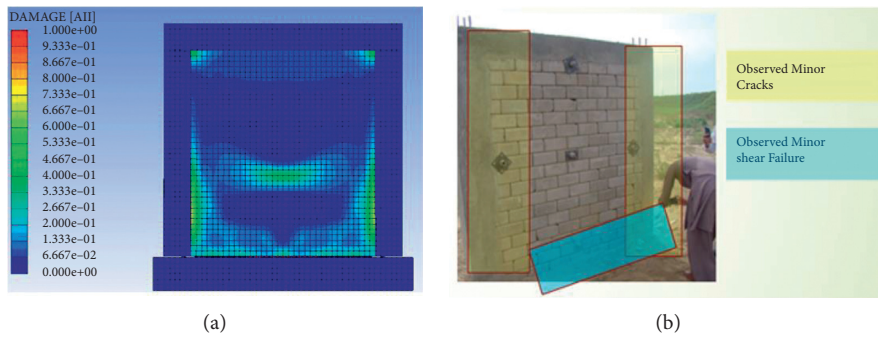


FIGURE 12: Damage pattern comparison for 8 kg Wabox Blast: (a) numerical results; (b) experimental results.

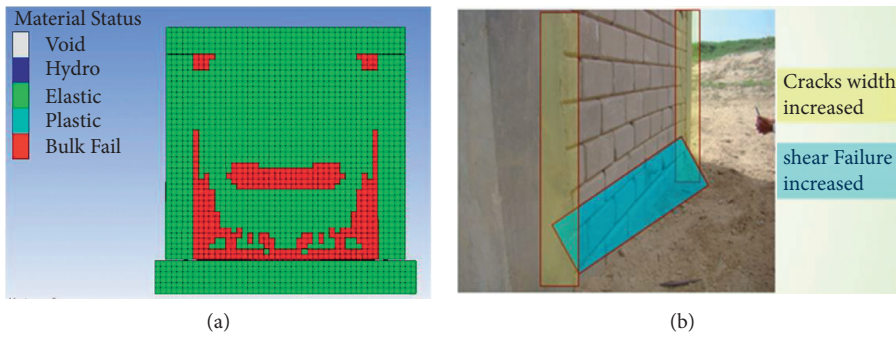


FIGURE 13: Damage pattern comparison for 12 kg Wabox Blast: (a) numerical results; (b) experimental results.

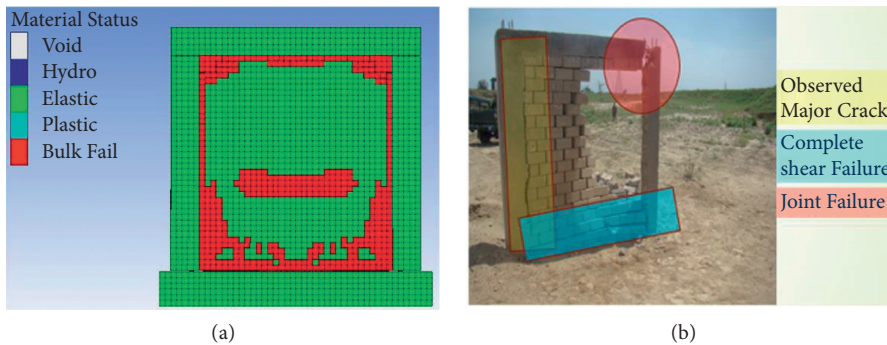


FIGURE 14: Damage pattern comparison for 16 kg Wabox Blast: (a) numerical results; (b) experimental results.

9. Conclusion

Four different test cases of explosive charge detonation and blast wave propagation in open space on CDSM wall were investigated numerically using ANSYS-Autodyn software. From this numerical simulation study, the following were concluded.

- (i) The complex wave structure of blasts was analysed and pressure-time history records on walls were described and compared with experimental records which shows good agreement.
- (ii) The incident overpressure and arrival time values obtained from pressure-time history records were compared with experimental data and empirical models for calibration. The numerical model output values show good correlation with experimental and empirical models.
- (iii) The numerical analysis is able to predict damage pattern with reasonable accuracy. Thus, the obtained damage patterns for each test were compared with experimental damage map which shows good correlation. Therefore, this numerical model can also be employed for parametric study on CDSM walls.
- (iv) It is observed from the results of numerical analysis that the out-of-plane flexure capacity of CDSM walls against blast loads has been increased by providing proper confining elements. This also confirms the response of CDSM walls observed in the experimental tests conducted in the field.

Data Availability

The simulation data used to support the findings of this study are included within the article.

Conflicts of Interest

The authors declare that there are no conflicts of interest regarding the publication of this study.

Acknowledgments

The work was financially supported by the Higher Education Commission, Islamabad, Pakistan (Project code: TDF-(02-038)), for executing scientific activities in the country. The authors are grateful to ECO Enterprises for providing the concrete blocks and financial support.

References

- [1] A. Ismail and S. Amjad, "Determinants of terrorism in Pakistan: an empirical investigation," *Economic Modelling*, vol. 37, pp. 320–331, 2014.
- [2] S. Yao, D. Zhang, X. Chen, F. Lu, and W. Wang, "Experimental and numerical study on the dynamic response of RC slabs under blast loading," *Engineering Failure Analysis*, vol. 66, pp. 120–129, 2016.
- [3] Century Dynamics Inc, "Autodyn," 2011.
- [4] K. Lin, Y. Totoev, H. Liu, and C. Wei, "Experimental characteristics of dry stack masonry under compression and shear loading," *Materials*, vol. 8, no. 12, pp. 8731–8744, 2015.
- [5] I. G. Castro, P. T. Laursen, D. C. Jansen, and B. Qu, "Performance of interlocking compressed earth block infill in confined masonry construction," in *Proceedings of the National Conference on Earthquake Engineering Frontiers of Earthquake Engineering*, Anchorage, AK, USA, July 2014.
- [6] H. C. Uzoegbo, "Dry-stack and compressed stabilised earth-block construction," *Nonconventional and Vernacular Construction Materials*, Woodhead Publishing, Sawston, UK, pp. 205–249, 2016.
- [7] K. Lin, Y. Z. Totoev, H. J. Liu, and A. W. Page, "Modeling of dry-stacked masonry panel confined by reinforced concrete frame," *Archives of Civil and Mechanical Engineering*, vol. 14, no. 3, pp. 497–509, 2014.
- [8] B. M. Luccioni, R. D. Ambrosini, and R. F. Danesi, "Analysis of building collapse under blast loads," *Engineering Structures*, vol. 26, no. 1, pp. 63–71, 2004.
- [9] B. Luccioni, D. Ambrosini, and R. Danesi, "Blast load assessment using hydrocodes," *Engineering Structures*, vol. 28, no. 12, pp. 1736–1744, 2006.
- [10] M. D. Theobald and G. N. Nurick, "Experimental and numerical analysis of tube-core claddings under blast loads," *International Journal of Impact Engineering*, vol. 37, no. 3, pp. 333–348, 2010.
- [11] G. Thiagarajan, A. V. Kadambi, S. Robert, and C. F. Johnson, "Experimental and finite element analysis of doubly reinforced concrete slabs subjected to blast loads," *International Journal of Impact Engineering*, vol. 75, pp. 162–173, 2015.
- [12] C. Wu, H. Hao, and Y. Lu, "Dynamic response and damage analysis of masonry structures and masonry infilled RC frames to blast ground motion," *Engineering Structures*, vol. 27, no. 3, pp. 323–333, 2005.
- [13] M. Ghaderi, V. A. Maleki, and K. Andalibi, "Retrofitting of unreinforced masonry walls under blast loading by FRP and spray on polyurea," *Cumhuriyet Science Journal*, vol. 36, pp. 462–477, 2015.
- [14] B. Hopkinson, *British Ordnance Board Minutes 13565*, Vol. 11, The National Archives, Kew, UK, 1915.
- [15] S. H. Alsayed, H. M. Elsanadedy, Z. M. Al-Zaheri, Y. A. Al-Salloum, and H. Abbas, "Blast response of GFRP-strengthened infill masonry walls," *Construction and Building Materials*, vol. 115, pp. 438–451, 2016.
- [16] I. E. Edri and D. Z. Yankelevsky, "Analytical model for the dynamic response of blast-loaded arching masonry walls," *Engineering Structures*, vol. 176, pp. 49–63, 2018.
- [17] G. Michaloudis and N. Gebbeken, "Modeling masonry walls under far-field and contact detonations," *International Journal of Impact Engineering*, vol. 123, pp. 84–97, 2019.
- [18] A. Ullah, *Capacity Assessment of Confined Block Masonry Buildings against Blast Loading*, UET, Peshawar, Pakistan, 2019.
- [19] J. Hafeez, *Evaluation of Mechanical Properties of Dry-Stack Block Masonry*, UET, Peshawar, Pakistan, 2017.
- [20] E. L. Lee, H. C. Hornig, and J. W. Kury, *Adiabatic Expansion of High Explosive Detonation Products*, University of California Radiation Laboratory, Livermore, CA, USA, 1968.
- [21] A. Abbas, M. Adil, N. Ahmad, and I. Ahmad, "Behavior of reinforced concrete sandwiched panels (RCSPs) under blast load," *Engineering Structures*, vol. 181, pp. 476–490, 2019.
- [22] W. Riedel, K. Thoma, and S. Hiermaier, "Penetration of reinforced concrete by BETA-B-500 numerical analysis using a new macroscopic concrete model for hydrocodes," in

- Proceedings of the 9th International Symposium on Interaction of the Effect of Munitions with Structures*, pp. 315–322, Berlin, Germany, 1999.
- [23] W. Herrmann, “Constitutive equation for the dynamic compaction of ductile porous materials,” *Journal of Applied Physics*, vol. 40, no. 6, pp. 2490–2499, 1969.
- [24] M. Wang, H. Hao, Y. Ding, and Z.-X. Li, “Prediction of fragment size and ejection distance of masonry wall under blast load using homogenized masonry material properties,” *International Journal of Impact Engineering*, vol. 36, no. 6, pp. 808–820, 2009.
- [25] X. Wei and H. Hao, “Numerical derivation of homogenized dynamic masonry material properties with strain rate effects,” *International Journal of Impact Engineering*, vol. 36, no. 3, pp. 522–536, 2009.
- [26] G. N. Pande, J. X. Liang, and J. Middleton, “Equivalent elastic moduli for brick masonry,” *Computers and Geotechnics*, vol. 8, no. 3, pp. 243–265, 1989.
- [27] P. D. Buhan and G. D. Felice, “A homogenization approach to the ultimate strength of brick masonry,” *Journal of the Mechanics and Physics of Solids*, vol. 45, no. 7, pp. 1085–1104, 1997.
- [28] F. Cluni and V. Gusella, “Homogenization of non-periodic masonry structures,” *International Journal of Solids and Structures*, vol. 41, no. 7, pp. 1911–1923, 2004.
- [29] G. Ma, H. Hao, and Y. Lu, “Homogenization of masonry using numerical simulations,” *Journal of Engineering Mechanics*, vol. 127, pp. 421–431, 2001, <https://doi.org/10.1061/>.
- [30] H. M. Elsanadedy, T. H. Almusallam, S. H. Alsayed, and Y. A. Al-Salloum, “Flexural strengthening of RC beams using textile reinforced mortar-experimental and numerical study,” *Composite Structures*, vol. 97, pp. 40–55, 2013.
- [31] J. Silfwerbrand, “Shear bond strength in repaired concrete structures,” *Materials and Structures*, vol. 36, no. 260, pp. 419–424, 2003.
- [32] H. M. Elsanadedy, T. H. Almusallam, H. Abbas, Y. A. Al-Salloum, and S. H. Alsayed, “Effect of blast loading on CFRP-retrofitted RC columns-a numerical study,” *Latin American Journal of Solids and Structures*, vol. 8, no. 1, pp. 55–81, 2011.
- [33] S. Lan and J. E. Crawford Kbm, “Design of reinforced concrete columns to resist the effects of suitcase bombs,” in *Proceedings of the 6th International Conference on Shock and Impact Loads on Structures*, pp. 5–10, Australia, Perth, May 2005.
- [34] R. A. Izadifard, “Blastwave parameters assessment at different altitude using numerical simulation,” *Turkish Journal of Engineering and Environmental Sciences*, vol. 34, pp. 25–41, 2010.
- [35] P. Sherkar, “Modeling the effects of detonations of high explosives to inform blast-resistant design,” MS Thesis, State University of New York, Albany, NY, USA, 2010.
- [36] C. N. K. Bulmash, “Air blast parameters from tnt spherical air burst and hemi-spherical surface burst,” 1984.

Research Article

Generalized Ulam–Hyers–Rassias Stability Results of Solution for Nonlinear Fractional Differential Problem with Boundary Conditions

A. Naimi,¹ B. Tellab,¹ Y. Altayeb ,² and A. Moumen³

¹Laboratory of Applied Mathematics, Kasdi Merbah University, B. P. 511, 30000 Ouargla, Algeria

²Department of Mathematics, College of Sciences and Arts, Qassim University, Ar-Rass, Saudi Arabia

³Department of Mathematics, Faculty of Science, University of Hail, Hail 55425, Saudi Arabia

Correspondence should be addressed to Y. Altayeb; y.hassan@qu.edu.sa

Received 9 September 2021; Accepted 3 November 2021; Published 23 November 2021

Academic Editor: Adel Ouannas

Copyright © 2021 A. Naimi et al. This is an open access article distributed under the Creative Commons Attribution License, which permits unrestricted use, distribution, and reproduction in any medium, provided the original work is properly cited.

The problem of existence and generalized Ulam–Hyers–Rassias stability results for fractional differential equation with boundary conditions on unbounded interval is considered. Based on Schauder's fixed point theorem, the existence and generalized Ulam–Hyers–Rassias stability results are proved, and then some examples are given to illustrate our main results.

1. Introduction and Position of Problem

There are various, not equivalent, definitions of fractional derivatives according to Grunwald Letnikov, Weil, Caputo, and Riemann–Liouville, etc. Ordinary and partial differential order equations (with fractional derivatives of Caputo and Riemann–Liouville) have awakened in recent years with considerable interest both in mathematics and in applications. Let us describe the abstract Cauchy problem:

$$D_t^\gamma u(t) = Au(t), \quad m-1 < \gamma \leq m \in \mathbb{N},$$
$$\frac{d^\kappa}{dt^\kappa} u(0) = \xi_\kappa, \quad \kappa = 0, \dots, m-1, \quad (1)$$

where the corresponding solutions are represented through the Mittag–Leffler function. In mathematical papers on fractional differential equations, the Riemann–Liouville approach to the concept of a fractional order derivative $\gamma \geq 0$ is usually used as follows:

$$D^\gamma u(t) = \left(\frac{d}{dt}\right)^m \frac{1}{\Gamma(m-\gamma)} \int_0^t (t-r)^{m-\gamma-1} u(r) dr, \quad (2)$$

$$m-1 < \gamma \leq m \in \mathbb{N}.$$

The fractional Riemann–Liouville derivative is the left inverse to the corresponding fractional integral, which is a natural generalization of the Cauchy formula for the anti-derivative function $u(t)$. The initial conditions, of the initial value problem for ordinary differential equations of fractional order γ with fractional derivatives in the Riemann–Liouville form, are given in terms of fractional integrals:

$$\frac{1}{\Gamma(m-\kappa-\gamma)} \int_0^{0+} (0_+ - r)^{m-\kappa-\gamma-1} u^{(\kappa)}(r) dr, \quad (3)$$

$$\kappa = 0, \dots, m-1.$$

To satisfy the physical requirements, Caputo introduced an alternative definition of the fractional differential derivative. It was adopted by Caputo and Mainardi as

$${}^c D_t^\gamma u(t) = \frac{1}{\Gamma(m-\gamma)} \int_0^t (t-r)^{m-\gamma-1} u^{(m)}(r) dr, \quad (4)$$

$$m-1 < \gamma \leq m.$$

The advantage of this definition is a more natural solution for the problem of initial conditions for solving integro-differential equations of noninteger orders.

The cases of Caputo derivative for $0 < \gamma < 1$ was called the regularized fractional derivative of order γ .

This paper concerns the existence with Ulam stability for the following equation:

$$D_{0+}^\beta u(t) + f(t, u(t)) + \theta(t)g(u(t)) = 0, \quad t \geq 0. \quad (5)$$

For a continuous function $u(t)$ together with boundary conditions,

$$\begin{aligned} u(0) &= 0, \\ u'(0) &= 0, \\ D_{0+}^{\beta-1} u(+\infty) &= bu(\xi) + \lambda \int_0^\sigma u(s) ds, \end{aligned} \quad (6)$$

where $2 < \beta \leq 3, 0 \leq \lambda, b < \infty$, we fix $0 \leq \xi < \sigma < \infty$, the functions $f: \mathbb{R}_+ \times \mathbb{R} \rightarrow \mathbb{R}$ and $g: \mathbb{R} \rightarrow \mathbb{R}$ are continuous and θ is a continuous decreasing positive function such that $0 < \theta(t) \leq 1$, for all $t \in [0, +\infty)$. D_{0+}^β is the standard Riemann–Liouville fractional derivative of order β .

2. Literature Overview

Fractional differential equations, which are often encountered in mathematical modeling of various processes in natural and technical sciences, play an important role in describing many phenomena in physics, bioengineering, and engineering applications. The properties of such equations were investigated in many reviews (among them, we refer [1–6]).

Regarding the existence, we mention the work by Zhao and Ge [7], where the authors used the well-known Leray Schauder nonlinear alternative theorem to prove the existence of positive solutions to the problem

$$\begin{cases} D_{0+}^\alpha u(t) + f(t, u(t)) = 0, & t \in [0, +\infty), 1 < \alpha \leq 2, \\ u(0) = 0, & D_{0+}^{\alpha-1} u(+\infty) = \beta u(\xi), \end{cases} \quad (7)$$

where $f \in C([0, +\infty) \times \mathbb{R}, [0, +\infty))$, $0 \leq \xi, \beta < +\infty$. Next, Wang et al. [8] extended the above results and discussed the question of existence for solutions of (7) with condition:

$$D_{0+}^{\alpha-1} u(+\infty) = \lambda \int_0^\tau u(s) ds, \quad (8)$$

where $0 \leq \lambda, \tau < +\infty$. Shen et al. [9] considered the existence of solution for boundary value problem of nonlinear multipoint fractional differential equation:

$$\begin{cases} D_{0+}^\gamma u(t) = f(t, u(t), D_{0+}^\gamma u(t)), & t \in [0, +\infty), \\ u(0) = 0, u'(0) = 0, & D_{0+}^{\gamma-1} u(+\infty) = \sum_{i=1}^{m-2} \beta_i u(\xi_i), \end{cases} \quad (9)$$

where

$$\begin{aligned} 2 < \gamma &\leq 3, \\ f &\in C(\mathbb{R}_+ \times \mathbb{R} \times \mathbb{R}, \mathbb{R}), \\ \Gamma(\beta) &= \sum_{i=1}^{m-2} \beta_i \xi_i^{\gamma-1}. \end{aligned} \quad (10)$$

SM Ulam in 1940 was the first to raise the question of stability for functional equations. After his lecture, this question became popular for many specialists in mathematical analysis. It became an area of in-depth research (see for more details [10–12]). Next, many mathematicians turned in their studies to two types of stability—according to Ulam–Hyers and according to Ulam–Hyers–Rassias. This kind of study has become one of the central and most important in the fields of fractional differential equations. Details of recent advances in Ulam–Hyers sustainability and according to Ulam–Hyers for differential equations can be found in [13, 14] and in articles [15–17]. However, as far as we know, most authors discussed Ulam stability of some fractional differential problem on bounded/unbounded intervals, while the present paper discusses the existence of solutions and stability in the sense of Ulam–Hyers–Rassias for nonlinear fractional differential equations boundary conditions, for which research is just beginning, please see [18–23].

3. Preliminaries

Here, we present some notations, definitions, auxiliary lemmas concerning fractional calculus, fixed point theorems, and some preliminary concepts of fractional calculus.

Definition 1 (see [4, 24]). The Riemann–Liouville fractional integral of order β for a function f is defined as

$$I_{0+}^\beta f(t) = \frac{1}{\Gamma(\beta)} \int_0^t (t-s)^{\beta-1} f(s) ds, \quad (11)$$

provided the right side is pointwise defined on $(0; +\infty)$.

Lemma 1 (see [25]). *Let $U \subset X$ be a bounded set. U is said to be relatively compact in a space E if*

- (i) $\forall u \in U$, the function $u(t)/(1+t^{\beta-1})$ is equicontinuous on any compact subinterval of J .
- (ii) $\forall \varepsilon > 0$, there exists a constant $T = T(\varepsilon) > 0$ such that

$$\left| \frac{u(t_2)}{1+t_2^{\beta-1}} - \frac{u(t_1)}{1+t_1^{\beta-1}} \right| < \varepsilon, \quad t_1, t_2 \geq T \text{ and } u \in U. \quad (12)$$

Lemma 2 (see [4, 24]). Assume that $x \in C(J) \cap L^1(J)$ with a fractional derivative of order $\beta > 0$. Then,

$$I_{0^+}^\beta D_{0^+}^\beta x(t) = x(t) - C_1 t^{\beta-1} - C_2 t^{\beta-2} - \dots - C_n t^{\beta-n}, \tag{13}$$

where $C_1, C_2, \dots, C_N \in \mathbb{R}$ with $n = [\beta] + 1$.

Lemma 3. Let us define the following space:

$$E = \left\{ u \in C[0, +\infty): \sup_{t \geq 0} \frac{|u(t)|}{1 + t^{\beta-1}} < +\infty \right\}, \tag{14}$$

equipped with the norm

$$\|u\|_E = \sup_{t \geq 0} \frac{|u(t)|}{1 + t^{\beta-1}}. \tag{15}$$

Then, clearly $(E, \|\cdot\|_E)$ is a Banach space.

Lemma 4. u is a solution of the problem (5)-(6) if and only if u satisfies the following integral equation:

$$u(t) = \int_0^{+\infty} H(t, s) [f(s, u(s)) + \theta(s)g(u(s))] ds, \tag{16}$$

where

$$H(t, s) = \begin{cases} -\frac{(t-s)^{\beta-1}}{\Gamma(\beta)} + \frac{[\Gamma(\beta+1) - b\beta(\xi-s)^{\beta-1} - \lambda(\sigma-s)^\beta] t^{\beta-1}}{\Gamma(\beta)[\Gamma(\beta+1) - \lambda\sigma^\beta - b\beta\xi^{\beta-1}]}, & s \leq t, s \leq \xi, \\ \frac{[\Gamma(\beta+1) - b\beta(\xi-s)^{\beta-1} - \lambda(\sigma-s)^\beta] t^{\beta-1}}{\Gamma(\beta)[\Gamma(\beta+1) - \lambda\sigma^\beta - b\beta\xi^{\beta-1}]}, & t \leq s \leq \xi \leq \sigma, \\ -\frac{(t-s)^{\beta-1}}{\Gamma(\beta)} + \frac{[\Gamma(\beta+1) - \lambda(\sigma-s)^\beta] t^{\beta-1}}{\Gamma(\beta)[\Gamma(\beta+1) - \lambda\sigma^\beta - b\beta\xi^{\beta-1}]}, & \xi \leq s \leq t, s \leq \sigma, \\ \frac{[\Gamma(\beta+1) - \lambda(\sigma-s)^\beta] t^{\beta-1}}{\Gamma(\beta)[\Gamma(\beta+1) - \lambda\sigma^\beta - b\beta\xi^{\beta-1}]}, & \xi \leq s < \sigma, \quad t \leq s \\ -\frac{(t-s)^{\beta-1}}{\Gamma(\beta)} + \frac{\Gamma(\beta+1)t^{\beta-1}}{\Gamma(\beta)[\Gamma(\beta+1) - \lambda\sigma^\beta - b\beta\xi^{\beta-1}]}, & \xi \leq \sigma \leq s \leq t, \\ \frac{\beta t^{\beta-1}}{\Gamma(\beta+1) - \lambda\sigma^\beta - b\beta\xi^{\beta-1}}, & s \geq t, s \geq \sigma. \end{cases} \tag{17}$$

Proof. Using Lemma 2, we have

$$u(t) = -I_{0^+}^\beta [f(t, u(t)) + \theta(t)g(u(t))] + c_1 t^{\beta-1} + c_2 t^{\beta-2} + c_3 t^{\beta-3}. \tag{18}$$

By the first and second conditions, we get

$$\begin{aligned} c_3 &= 0, \\ c_2 &= 0. \end{aligned} \tag{19}$$

Consequently,

$$u(t) = -I_{0^+}^\beta [f(t, u(t)) + \theta(t)g(u(t))] + c_1 t^{\beta-1}. \tag{20}$$

From the third boundary condition, it follows that

$$\begin{aligned} D_{0^+}^{\beta-1} u(t) &= -I_{0^+}^{\beta-\beta+1} [f(t, u(t)) + \theta(t)g(u(t))] + c_1 \Gamma(\beta) \\ &= -\int_0^t [f(s, u(s)) + \theta(s)g(u(s))] ds + c_1 \Gamma(\beta). \end{aligned} \tag{21}$$

On the other hand, we have

$$\begin{aligned}
 bu(\xi) + \lambda \int_0^\sigma u(s)ds &= -bI_{0^+}^\beta [f(\xi, u(\xi)) + \theta(\xi)g(u(\xi))] + c_1 b\xi^{\beta-1} \\
 &\quad - \lambda \int_0^\sigma I_{0^+}^\beta [f(s, u(s)) + \theta(s)g(u(s))]ds + \lambda \int_0^\sigma c_1 s^{\beta-1} ds \\
 &= -bI_{0^+}^\beta [f(\xi, u(\xi)) + \theta(\xi)g(u(\xi))] + c_1 b\xi^{\beta-1} \\
 &\quad - \lambda I_{0^+}^{\beta+1} [f(\sigma, u(\sigma)) + \theta(\sigma)g(u(\sigma))] + \frac{\lambda\sigma^\beta}{\beta} c_1.
 \end{aligned}
 \tag{22}$$

Then, we deduce

$$\begin{aligned}
 c_1 &= \frac{\beta}{\Gamma(\beta + 1) - \lambda\sigma^\beta - b\beta\xi^{\beta-1}} \left[\int_0^{+\infty} [f(s, u(s)) + \theta(s)g(u(s))]ds \right. \\
 &\quad \left. - bI_{0^+}^\beta [f(\xi, u(\xi)) + g(u(\xi))] - \lambda I_{0^+}^{\beta+1} [f(\sigma, u(\sigma)) + \theta(\sigma)g(u(\sigma))] \right].
 \end{aligned}
 \tag{23}$$

By substituting the values of $c_1, c_2,$ and c_3 in (18), we get the following integral equation:

$$\begin{aligned}
 u(t) &= - \int_0^t \frac{(t-s)^{\beta-1}}{\Gamma(\beta)} [f(s, u(s)) + \theta(s)g(u(s))]ds \\
 &\quad + \frac{\beta t^{\beta-1}}{\Gamma(\beta + 1) - \lambda\sigma^\beta - b\beta\xi^{\beta-1}} \int_0^{+\infty} [f(s, u(s)) + \theta(s)g(u(s))]ds \\
 &\quad - \frac{b\beta t^{\beta-1}}{\Gamma(\beta + 1) - \lambda\sigma^\beta - b\beta\xi^{\beta-1}} \int_0^\xi \frac{(\xi-s)^{\beta-1}}{\Gamma(\beta)} [f(s, u(s)) + \theta(s)g(u(s))]ds \\
 &\quad - \frac{\lambda\beta t^{\beta-1}}{\Gamma(\beta + 1) - \lambda\sigma^\beta - b\beta\xi^{\beta-1}} \int_0^\sigma \frac{(\sigma-s)^\beta}{\Gamma(\beta + 1)} [f(s, u(s)) + \theta(s)g(u(s))]ds.
 \end{aligned}
 \tag{24}$$

Then, we get (16).

Conversely, suppose that (16) is satisfied. To get (5), we use the following appropriate relationships:

$$\begin{aligned}
 D_{0^+}^\beta I_{0^+}^\beta [f(t, u(t)) + \theta(t)g(u(t))] &= f(t, u(t)) + \theta(t)g(u(t)), \\
 D_{0^+}^\beta t^{\beta-1} &= 0.
 \end{aligned}
 \tag{25}$$

The present paper is organized as follows. In Section 4, we prove the existence of the solution for problem (5)-(6) in the Banach space. The generalized Ulam–Hyers stable is stated and proved in Section 5. Finally, an illustrative example is given. \square

4. Existence Result

In order to prove the existence of the solution for problem (5)-(6), we transform problem (5)-(6) into the fixed point problem $Pu = u$, where P is an operator defined on

$$\mathfrak{B}(r) = \{u \in E, \|u\|_E \leq r\},
 \tag{26}$$

by

$$Pu(t) = \int_0^{+\infty} H(t, s)[f(s, u(s)) + \theta(s)g(u(s))]ds.
 \tag{27}$$

Theorem 1. *Let $f: [0, +\infty) \times \mathbb{R} \rightarrow \mathbb{R}$ and $g: \mathbb{R} \rightarrow \mathbb{R}$ are two functions such that*

$$(A_1) \Gamma(\beta + 1) > \lambda\sigma^\beta + b\beta\xi^{\beta-1}.$$

(A₂) There exist a nonnegative measurable function ψ_1 defined on $[0, +\infty)$ and a real constant $L > 0$ such that:

$$|f(t, u(t)) - f(t, v(t))| \leq \psi_1(t)|u(t) - v(t)|, \quad u, v \in \mathbb{R},$$

$$|g(u(t)) - g(v(t))| \leq L|u(t) - v(t)|, \quad u, v \in \mathbb{R},$$

$$\beta \int_0^{+\infty} (1 + t^{\beta-1})[\psi_1(t) + \psi_2(t)]dt < \Gamma(\beta + 1) - \lambda\sigma^\beta - b\beta\xi^{\beta-1} \tag{28}$$

with

$$\psi_2(t) = \theta(t)L, \quad \text{for each } t \in [0, +\infty). \tag{29}$$

(A₃) Let $\phi_1(t) = |f(t, 0)|$ and $\phi_2(t) = \theta(t)|g(0)|$, $t \in [0, +\infty)$ such that

$$\int_0^{+\infty} [\phi_1(t) + \phi_2(t)]dt < +\infty. \tag{30}$$

Then, problem (5)-(6) has at least one solution in $[0, +\infty)$.

Lemma 5. If (A₁) holds, then the Green function $H(t, s)$ satisfies for all $\xi, \sigma, s, t \in [0, +\infty)$, we have

$$\frac{H(t, s)}{1 + t^{\beta-1}} \leq \frac{\beta}{\Gamma(\beta + 1) - \lambda\sigma^\beta - b\beta\xi^{\beta-1}}. \tag{31}$$

Proof. If $s \leq t$, and $s \leq \xi$, we get

$$\begin{aligned} \frac{H(t, s)}{1 + t^{\beta-1}} &= -\frac{(t-s)^{\beta-1}}{(1+t^{\beta-1})\Gamma(\beta)} \\ &+ \frac{[\Gamma(\beta + 1) - b\beta(\xi-s)^{\beta-1} - \lambda(\sigma-s)^\beta]t^{\beta-1}}{\Gamma(\beta)[\Gamma(\beta + 1) - \lambda\sigma^\beta - b\beta\xi^{\beta-1}](1+t^{\beta-1})} \\ &\leq \frac{\Gamma(\beta + 1)t^{\beta-1}}{\Gamma(\beta)[\Gamma(\beta + 1) - \lambda\sigma^\beta - b\beta\xi^{\beta-1}](1+t^{\beta-1})} \\ &\leq \frac{\beta}{\Gamma(\beta + 1) - \lambda\sigma^\beta - b\beta\xi^{\beta-1}}. \end{aligned} \tag{32}$$

All other cases of $H(t, s)$ are simple. This completes the proof of Lemma 5. \square

Proof. of Theorem 1. We shall use Schauder's fixed point theorem, which is divided into three steps. \square

Step 1. Let $r > 0$ such that

$$r \geq \frac{\beta \int_0^{+\infty} [\phi_1(p) + \phi_2(p)]dp}{\Gamma(\beta + 1) - \lambda\sigma^\beta - b\beta\xi^{\beta-1} - \beta \int_0^{+\infty} (1 + p^{\beta-1})[\psi_1(p) + \psi_2(p)]dp}. \tag{33}$$

If u is a continuous function on J , then $Pu \in C(J)$. In order to show $P(\mathfrak{B}_r) \subset \mathfrak{B}_r$, let $u \in \mathfrak{B}_r, t \in \mathbb{R}^+$. Then,

$$\begin{aligned} \left| \frac{Pu(t)}{1 + t^{\beta-1}} \right| &= \left| \int_0^{+\infty} \frac{H(t, s)}{1 + t^{\beta-1}} [f(s, u(s)) + \theta(s)g(u(s))]ds \right| \\ &\leq \frac{\beta}{\Gamma(\beta + 1) - \lambda\sigma^\beta - b\beta\xi^{\beta-1}} \left| \int_0^{+\infty} [f(s, u(s)) + \theta(s)g(u(s))]ds \right| \\ &\leq \frac{\beta}{\Gamma(\beta + 1) - \lambda\sigma^\beta - b\beta\xi^{\beta-1}} \times \\ &\quad \cdot \int_0^{+\infty} [|f(s, u(s)) - f(s, 0)| + \theta(s)|g(u(s)) - g(0)| + |f(s, 0)| + |\theta(s)g(0)|]ds \\ &\leq \frac{\beta}{\Gamma(\beta + 1) - \lambda\sigma^\beta - b\beta\xi^{\beta-1}} \int_0^{+\infty} [\psi_1(s)|u(s)| + \theta(s)L|u(s)| + \phi_1(s) + \phi_2(s)]ds \\ &\leq \frac{\beta}{\Gamma(\beta + 1) - \lambda\sigma^\beta - b\beta\xi^{\beta-1}} \int_0^{+\infty} [\phi_1(s) + \phi_2(s)]ds \\ &\quad + \frac{\beta\|u\|_E}{\Gamma(\beta + 1) - \lambda\sigma^\beta - b\beta\xi^{\beta-1}} \int_0^{+\infty} (1 + s^{\beta-1})[\psi_1(s) + \psi_2(s)]ds \\ &\leq \frac{\beta}{\Gamma(\beta + 1) - \lambda\sigma^\beta - b\beta\xi^{\beta-1}} \int_0^{+\infty} [\phi_1(s) + \phi_2(s)]ds \\ &\quad + \frac{\beta r}{\Gamma(\beta + 1) - \lambda\sigma^\beta - b\beta\xi^{\beta-1}} \int_0^{+\infty} (1 + s^{\beta-1})[\psi_1(s) + \psi_2(s)]ds \\ &\leq r. \end{aligned} \tag{34}$$

Therefore, $\|P\|_E \leq r$; thus, $P(\mathfrak{B}_r) \in \mathfrak{B}_r$.

Step 2. $P: \mathfrak{B}_r \rightarrow \mathfrak{B}_r$ is continuous. Let $\{u_n\}$ be a sequence which converges to u in \mathfrak{B}_r . Then, for all $t \in [0, +\infty)$,

$$\begin{aligned}
 & \left| \frac{Pu_n(t) - Pu(t)}{1 + t^{\beta-1}} \right| \\
 &= \left| \int_0^{+\infty} \frac{H(t,s)}{1 + t^{\beta-1}} [(f(s, u_n(s)) - f(s, u(s))) + t\theta n(s)q(g(u_n(s)) - g(u(s)))] ds \right| \\
 &\leq \frac{\beta}{\Gamma(\beta+1) - \lambda\sigma^\beta - b\beta\xi^{\beta-1}} \int_0^{+\infty} |(f(s, u_n(s)) - f(s, u(s))) + t\theta n(s)q(g(u_n(s)) - g(u(s)))| ds \\
 &\leq \frac{\beta}{\Gamma(\beta+1) - \lambda\sigma^\beta - b\beta\xi^{\beta-1}} \int_0^{+\infty} [f(s, u_n(s)) - f(s, u(s)) + \theta g(u_n(s)) - g(u(s))] ds \\
 &\leq \frac{\beta \|u_n - u\|_E}{\Gamma(\beta+1) - \lambda\sigma^\beta - b\beta\xi^{\beta-1}} \int_0^{+\infty} [\psi_1(s) + \psi_2(s)] (1 + s^{\beta-1}) ds \\
 &< \|u_n - u\|_E.
 \end{aligned} \tag{35}$$

So, we conclude that $\|Pu_n - Pu\|_E \rightarrow 0$ as $n \rightarrow +\infty$. Hence, P is a continuous operator on E .

Step 3. We have two claims to verify that $P(\mathfrak{B}_r)$ is a relatively compact set.

First claim: let $I \subset J$ be a compact interval, $t_1, t_2 \in I$ with $t_1 < t_2$. Then, for any $u \in \mathfrak{B}_r$, we have

$$\begin{aligned}
 & \left| \frac{Pu(t_2)}{1 + t_2^{\beta-1}} - \frac{Pu(t_1)}{1 + t_1^{\beta-1}} \right| \\
 &\leq \int_0^{+\infty} \left| \frac{H(t_2, s)}{1 + t_2^{\beta-1}} - \frac{H(t_1, s)}{1 + t_1^{\beta-1}} \right| |f(s, u(s)) + \theta(s)g(u(s))| ds \\
 &\leq \int_0^{+\infty} \left| \frac{H(t_2, s)}{1 + t_2^{\beta-1}} - \frac{H(t_1, s)}{1 + t_1^{\beta-1}} \right| [[\psi_1(s) + \psi_2(s)] (1 + s^{\beta-1}) \|u\|_E + \phi_1(s) + \phi_2(s)] ds.
 \end{aligned} \tag{36}$$

Since it is continuous on $J \times J$, we have that $H(t, s)/(1 + t^{\beta-1})$ is a uniformly continuous function on the compact set $I \times I$.

For $s \geq t$, the function depends only on t , then it is uniformly continuous on $I \times (J/I)$. Therefore, we have $\forall s \in J$ and $t_1, t_2 \in I$; the next property holds.

$\forall \varepsilon > 0$, there is $\delta(\varepsilon) > 0$ such that, if $|t_1 - t_2| < \delta$, then

$$\left| \frac{H(t_2, s)}{1 + t_2^{\beta-1}} - \frac{H(t_1, s)}{1 + t_1^{\beta-1}} \right| \leq \varepsilon. \tag{37}$$

This property, together with (36) and the fact that

$$\int_0^{+\infty} [(1 + s^{\beta-1}) [\psi_1(s) + \psi_2(s)] r + \phi_1(s) + \phi_2(s)] ds < \infty, \tag{38}$$

means that $Pu(t)/(1 + t^{\beta-1})$ is equicontinuous on I .

Second claim: in order to achieve (ii) of Lemma 1, we use

$$\lim_{t \rightarrow +\infty} \frac{H(t, s)}{1 + t^{\beta-1}} = \frac{1}{\Gamma(\beta) [\Gamma(\beta + 1) - \lambda\sigma^\beta - b\beta\xi^{\beta-1}]} \times \begin{cases} \lambda[\sigma^\beta - (\sigma - s)^\beta] + b\beta[\xi^{\beta-1} - (\xi - s)^{\beta-1}], & s \leq t, s \leq \xi, \\ \Gamma(\beta + 1) - b\beta(\xi - s)^{\beta-1} - \lambda(\sigma - s)^\beta, & t \leq s \leq \xi \leq \sigma, \\ \lambda[\sigma^\beta - (\sigma - s)^\beta] + b\beta\xi^{\beta-1}, & \xi \leq s \leq \sigma, \\ \Gamma(\beta + 1) - \lambda(\sigma - s)^\beta, & \xi \leq t, s < \sigma, \\ \lambda\sigma^\beta + b\beta\xi^{\beta-1}, & \xi \leq \sigma \leq s \leq t, \\ \beta\Gamma(\beta), & s \geq \sigma, s \geq t. \end{cases} \quad (39)$$

From (39), it is not hard to see, $\forall \varepsilon > 0$, there exists a dependent constant $T = T(\varepsilon) > 0$ such that, for $t_1, t_2 \geq T$ and $s \in J$, we have

$$\left| \frac{H(t_2, s)}{1 + t_2^{\beta-1}} - \frac{H(t_1, s)}{1 + t_1^{\beta-1}} \right| \leq \varepsilon. \quad (40)$$

Now, from (36) and (38), the same property holds for $Pu(t)/(1 + t^{\beta-1})$, uniformly for $u \in \mathfrak{B}_r$. Then, $P(\mathfrak{B}_r)$ is equiconvergent at ∞ .

Thus, Lemma 1 implies that $P(\mathfrak{B}_r)$ is relatively compact.

Therefore, the operator P has a fixed point on \mathfrak{B}_r . Then, from Schauder's fixed point theorem, we conclude that problem (5)-(6) has at least one solution.

5. Stability Result

Before stating and proving our main stability results, let us consider the following integration formula:

$$v(t) = \int_0^{+\infty} H(t, s)[f(s, v(s)) + \theta(s)g(v(s))]ds, \quad (41)$$

for continuous function H, θ . Here, we suppose that $v \in C([0, +\infty), E)$ has a fractional derivative of order β , where $2 < \beta \leq 3$, $f: [0, +\infty) \times E \rightarrow \mathbb{R}$ and $g: E \rightarrow \mathbb{R}$ are two continuous functions, and let us define the following nonlinear continuous operator:

$$\begin{aligned} \mathcal{F}: [0, +\infty) \times E &\rightarrow \mathbb{R}, \\ \mathcal{F}v(t) &= D_{0^+}^\beta v(t) + f(t, v(t)) + \theta(t)g(v(t)), \end{aligned} \quad (42)$$

Definition 2 (see [26, 27]). For any $\varepsilon > 0$ and for each solution v of (5)-(6), such that

$$\|\mathcal{F}v\|_E \leq \varepsilon, \quad (43)$$

problem (5)-(6) is said to be Ulam-Hyers stable, if we can find a positive real number $C_f > 0$ and a solution $u \in C([0, +\infty), E)$ of (5)-(6) satisfying the inequality

$$\|u - v\|_E \leq \varepsilon C_f. \quad (44)$$

Definition 3 (see [26, 27]). Let $C_f \in C(\mathbb{R}^+, \mathbb{R}^+)$ with $\xi(0) = 0$, for each solution v of (5)-(6), we can find a solution $u \in C([0, +\infty), E)$ of (5)-(6) such that

$$\|u - v\|_E \leq C_f(\varepsilon). \quad (45)$$

Then, problem (5)-(6), is called generalized Ulam-Hyers stable.

Definition 4 (see [26, 27]). For any $\varepsilon > 0$ for each solution v of (5)-(6), problem (5)-(6) is called Ulam-Hyers-Rassias stable with respect to $\Phi \in C([0, +\infty), \mathbb{R}^+)$ if

$$\|\mathcal{F}v\|_E \leq \varepsilon\Phi(t) \quad t \in [0, +\infty), \quad (46)$$

and there exists a real number $C_{f,\Phi} > 0$ and a solution $u \in C([0, +\infty), E)$ of (5)-(6) such that

$$\|u - v\|_E \leq \varepsilon C_{f,\Phi}\Phi(t), \quad t \in [0, +\infty). \quad (47)$$

Definition 5 (see [26, 27]). For any $\varepsilon > 0$ and for each solution v of (5)-(6), problem (5)-(6) is called generalized Ulam-Hyers-Rassias stable with respect to $\Phi \in C([0, +\infty), \mathbb{R}^+)$ if

$$\|\mathcal{F}v\|_E \leq \Phi(t) \quad t \in [0, +\infty), \quad (48)$$

and there exists $C_{f,\Phi} > 0$ and a solution $u \in C([0, +\infty), E)$ of (5)-(6) such that

$$\|u - v\|_E \leq C_{f,\Phi}\Phi(t), \quad t \in [0, +\infty). \quad (49)$$

Theorem 2. *If the assumptions (A_1) and (A_2) hold, then problems (5)-(6) are generalized Ulam-Hyers stable.*

Proof. By the equivalence between the operators $(I d - P)$ and \mathcal{F} and the assumptions $(A_1), (A_2)$, we find

$$\begin{aligned}
 |v(t) - u(t)| &\leq |v(t) - Pv(t)| + |Pv(t) - u(t)| \\
 &= |(I - P)v(t)| + |Pv(t) - Pu(t)| \\
 &= |\mathcal{F}v(t)| + \left| \int_0^{+\infty} H(t, s)[f(s, v(s)) - f(s, u(s))]ds, \right. \\
 &\quad \left. - \int_0^{+\infty} H(t, s)\theta(s)[g(v(s)) - g(u(s))]ds \right| \tag{50} \\
 &\leq |\mathcal{F}v(t)| + \left| \int_0^{+\infty} H(t, s)[f(s, v(s)) - f(s, u(s))]ds \right| \\
 &\quad + \left| \int_0^{+\infty} H(t, s)\theta(s)[g(v(s)) - g(u(s))]ds \right|.
 \end{aligned}$$

Then,

$$\begin{aligned}
 \|v - u\|_E &\leq \|\mathcal{F}v\|_E + \frac{\beta\|v - u\|_E}{\Gamma(\beta + 1) - \lambda\sigma^\beta - b\beta\xi^{\beta-1}} \times \\
 &\quad \cdot \int_0^{+\infty} [\psi_1(s) + \psi_2(s)](1 + s^{1-\beta})ds \\
 &\leq \epsilon + \frac{\beta\|v - u\|_E}{\Gamma(\beta + 1) - \lambda\sigma^\beta - b\beta\xi^{\beta-1}} \times \\
 &\quad \cdot \int_0^{+\infty} [\psi_1(s) + \psi_2(s)](1 + s^{1-\beta})ds. \tag{51}
 \end{aligned}$$

Consequently,

$$\begin{aligned}
 \|v - u\|_E &\leq \frac{\Gamma(\beta + 1) - \lambda\sigma^\beta - b\beta\xi^{\beta-1}}{\Gamma(\beta + 1) - \lambda\sigma^\beta - b\beta\xi^{\beta-1} - \beta \int_0^{+\infty} [\psi_1(s) + \psi_2(s)](1 + s^{\beta-1})ds} \epsilon. \tag{52}
 \end{aligned}$$

Thus, we get the Ulam–Hyers stability of (5)–(6). Then, if we take $C_f(\epsilon)$ equal to the right hand side of (52), we obtain the generalized Ulam–Hyers stability of (5)–(6). \square

Theorem 3. Assume that the hypotheses (A_1) and (A_2) hold. In addition, the following hypotheses hold:

(A_4) There exist two positive constants p and q such that

$$\begin{aligned}
 \psi_1(t) &\leq \frac{p}{\|v - u\|_E} \Phi(t), \\
 \psi_2(t) &\leq \frac{q}{\|v - u\|_E} \Phi(t). \tag{53}
 \end{aligned}$$

(A_5) There exists a positive real number C_Φ such that, for each $t \in [0, +\infty)$, we have

$$\Phi(t) \leq \int_0^{+\infty} (1 + s^{\beta-1})\Phi(s)ds \leq C_\Phi \Phi(t). \tag{54}$$

Then, problems (5) and (6) are generalized Ulam–Hyers–Rassias stable.

Proof. By exploiting the assumptions (A_2) , (A_3) , (A_4) , and (A_5) , then we get

$$\begin{aligned}
 |v(t) - u(t)| &\leq |v(t) - Pv(t)| + |Pv(t) - u(t)| \\
 &\leq |\mathcal{F}v(t)| + |Pv(t) - Pu(t)| \\
 &\leq |\mathcal{F}v(t)| \\
 &\quad + \left| \int_0^{+\infty} H(t, s)[f(s, v(s)) - f(s, u(s))]ds \right| \\
 &\quad + \left| \int_0^{+\infty} H(t, s)\theta(s)[g(v(s)) - g(u(s))]ds \right|. \tag{55}
 \end{aligned}$$

Then,

$$\begin{aligned}
 \|u - v\|_E &\leq \|\mathcal{F}v\|_E + \left| \int_0^{+\infty} \frac{H(t, s)}{1 + t^{1-\beta}} [f(s, v(s)) - f(s, u(s))]ds \right| \\
 &\quad + \left| \int_0^{+\infty} \frac{H(t, s)}{1 + t^{1-\beta}} \theta(s)[g(v(s)) - g(u(s))]ds \right| \\
 &\leq \Phi(t) + \frac{\beta}{\Gamma(\beta + 1) - \lambda\sigma^\beta - b\beta\xi^{\beta-1}} \int_0^{+\infty} |f(s, v(s)) - f(s, u(s))|ds \\
 &\quad + \frac{\beta}{\Gamma(\beta + 1) - \lambda\sigma^\beta - b\beta\xi^{\beta-1}} \int_0^{+\infty} \theta(s)|g(v(s)) - g(u(s))|ds
 \end{aligned}$$

$$\begin{aligned}
 &\leq \int_0^\infty (1+s^{\beta-1})\Phi(s)ds + \frac{\beta}{\Gamma(\beta+1)-\lambda\sigma^\beta-b\beta\xi^{\beta-1}} \int_0^{+\infty} |f(s, v(s)) - f(s, u(s))|ds \\
 &\quad + \frac{\beta}{\Gamma(\beta+1)-\lambda\sigma^\beta-b\beta\xi^{\beta-1}} \int_0^{+\infty} \theta(s)|g(v(s)) - g(u(s))|ds \\
 &\leq C_\Phi\Phi(t) + \frac{\beta(p+q)}{\Gamma(\beta+1)-\lambda\sigma^\beta-b\beta\xi^{\beta-1}} \int_0^{+\infty} (1+s)^{1-\beta}\Phi(s)ds \\
 &\leq \left(1 + \frac{\beta(p+q)}{\Gamma(\beta+1)-\lambda\sigma^\beta-b\beta\xi^{\beta-1}}\right)C_\Phi\Phi(t) \\
 &= C_{f,\Phi}\Phi(t).
 \end{aligned} \tag{56}$$

Hence, problems (5) and (6) are generalized Ulam–Hyers–Rassias stable. Example 1. \square

$$\begin{cases} D_{0^+}^{5/2}u(t) = \frac{e^{-t} + \sin(u(t))}{100(1+t^2)(1+t^{3/2})} + \frac{1 + \sin(u(t))}{100(1+t)^2(1+t^{3/2})} & t \in [0, +\infty), \\ u(0) = 0, u'(0) = 0, & D_{0^+}^{3/2}u(+\infty) = bu(1) + \lambda \int_0^2 u(s)ds. \end{cases} \tag{57}$$

In this example, we have

$$\begin{aligned}
 f(t, u(t)) &= \frac{e^{-t} + \sin(u(t))}{100(1+t^2)(1+t)}, \\
 g(u(t)) &= 1 + \sin(u(t)), \\
 |f(t, u(t)) - f(t, v(t))| &\leq \frac{1}{100(1+t^2)(1+t^{3/2})} |u(t) - v(t)|, \\
 |g(u(t)) - g(v(t))| &\leq |u(t) - v(t)|, \\
 L &= 1,
 \end{aligned} \tag{58}$$

$$\begin{aligned}
 \theta(t) &= \frac{1}{100(1+t)^2(1+t^{3/2})}, \\
 \psi_1(t) &= \frac{1}{100(1+t^2)(1+t^{3/2})}, \\
 \psi_2(t) &= \frac{1}{100(1+t)^2(1+t^{3/2})}.
 \end{aligned}$$

Since ξ and σ are fixed, then λ and b are chosen so that hypothesis (A_1) is satisfied. So, we have

$$\left\{ \begin{array}{l} b < \frac{\Gamma(\beta + 1) - \lambda\sigma^\beta}{\beta\xi^{\beta-1}}, \\ \lambda < \frac{\Gamma(\beta + 1)}{\sigma^\beta}. \end{array} \right. \quad (59)$$

$$\left\{ \begin{array}{l} b < \frac{2(\Gamma(7/2) - 4\sqrt{2})}{5} \approx 0.19, \\ \lambda < \frac{\Gamma(7/2)}{4\sqrt{2}} \approx 0.58. \end{array} \right. \quad (60)$$

In our example, we have $\beta = (5/2)$, $\xi = 1$, $\sigma = 2$. Then,

So, we can choose $\lambda = 1/2$ and $b = 1/10$.
By simple computation, we get

$$\begin{aligned} \beta \int_0^{+\infty} (1 + t^{\beta-1}) [\psi_1(t) + \psi_2(t)] dt &= \frac{5}{200} \int_0^{+\infty} \frac{dt}{1 + t^2} + \frac{5}{200} \int_0^{+\infty} \frac{dt}{(1 + t)^2} \\ &= \frac{5}{200} \left[\arctan(t) - \frac{1}{1 + t} \right]_0^{+\infty} \\ &= \frac{5}{200} \left(\frac{\pi}{2} + 1 \right) \approx 0.06, \end{aligned} \quad (61)$$

$$\Gamma(\beta + 1) - \lambda\sigma^\beta - b\beta\xi^{\beta-1} \approx 0.25.$$

Thus, (A_2) is satisfied.

Now, it remains to verify (A_3) . We have

$$\begin{aligned} \int_0^{+\infty} [\phi_1(t) + \phi_2(t)] dt &\leq \int_0^{+\infty} \left(\frac{1}{(1 + t^2)} + \frac{1}{(1 + t)^2} \right) dt \\ &= \frac{\pi}{2} + 1 < +\infty. \end{aligned} \quad (62)$$

All hypotheses of Theorem 1 are satisfied. Therefore, boundary value problems (5)-(6) has at least one solution in \mathbb{R} .

Data Availability

No data were used in this study.

Conflicts of Interest

The authors declare that they have no conflicts of interest.

Authors' Contributions

The authors contributed equally and significantly in writing this paper. All authors read and approved the final manuscript.





References

- [1] B. Azzaoui, B. Tellab, and K. Zennir, "Positive solutions for integral nonlinear boundary value problem in fractional sobolev spaces," *Mathematical Methods in the Applied Sciences*, pp. 1–18, 2021.
- [2] A. Boulfoul, B. Tellab, N. Abdellouahab, and K. Zennir, "Existence and uniqueness results for initial value problem of nonlinear fractional integro-differential equation on an unbounded domain in a weighted Banach space," *Mathematical Methods in the Applied Sciences*, vol. 44, no. 5, pp. 3509–3520, 2021.
- [3] R. Hilfer, *Applications of Fractional Calculus in Physics*, World Scientific Publishing Co., Inc., River Edge, NJ, USA, 2000.
- [4] A. A. Kilbas, H. M. Srivastava, and J. J. Trujillo, *Theory and Applications of Fractional Differential Equations*, p. 539, Elsevier, Amsterdam, Netherlands, 2006.
- [5] I. Podlubny, "Fractional differential equations," *Mathematics in Science and Engineering*, vol. 198, 1999.
- [6] V. E. Tarasov, *Fractional Dynamics, Nonlinear Physical Science*, Springer, Heidelberg, Germany, 2010.
- [7] X. Zhao and W. Ge, "Unbounded solutions for a fractional boundary value problems on the infinite interval," *Acta Applicandae Mathematica*, vol. 109, no. 2, pp. 495–505, 2010.
- [8] G. Wang, A. Cabada, and L. Zhang, "An integral boundary value problem for nonlinear differential equation of fractional order on an unbounded domain," *Journal of Integral Equations*, vol. 26, no. 1, 2014.
- [9] C. Shen, H. Zhou, and L. Yang, "On the existence of solutions to a boundary value problem of fractional differential equation on the infinite interval," *Boundary Value Problems*, vol. 2015, Article ID 241, 2015.
- [10] D. H. Hyers, "On the stability of the linear functional equation," *Proceedings of the National Academy of Sciences*, vol. 27, no. 4, pp. 222–224, 1941.
- [11] T. M. Rassias, "On the stability of the linear mapping in Banach spaces," *Proceedings of the American Mathematical Society*, vol. 72, no. 2, pp. 297–300, 1978.
- [12] S. M. Ulam, "A collection of mathematical problems," in *Interscience Tracts in Pure and Applied Mathematics*, p. 150, Interscience Publishers, London, UK, 1960.
- [13] D. H. Hyers, G. Isac, and T. M. Rassias, "Stability of functional equations in several variables," *Progress in Nonlinear Differential Equations and Their Applications*, vol. 34, p. 313, 1998.
- [14] S.-M. Jung, *Hyers-Ulam-Rassias Stability of Functional Equations in Mathematical Analysis*, p. 256, Hadronic Press, Inc., Palm Harbor, FL, USA, 2001.
- [15] M. R. Abdollahpour, R. Aghayari, and M. T. Rassias, "Hyers-Ulam stability of associated Laguerre differential equations in

- a subclass of analytic functions,” *Journal of Mathematical Analysis and Applications*, vol. 437, no. 1, pp. 605–612, 2016.
- [16] S.-M. Jung, “Hyers-Ulam stability of linear differential equations of first order,” *Applied Mathematics Letters*, vol. 17, no. 10, pp. 1135–1140, 2004.
- [17] T. Miura, S. Miyajima, and S.-E. Takahasi, “A characterization of Hyers-Ulam stability of first order linear differential operators,” *Journal of Mathematical Analysis and Applications*, vol. 286, no. 1, pp. 136–146, 2003.
- [18] S. Abbas, M. Benchohra, J. Lagreg, A. Alsaedi, and Y. Zhou, “Existence and Ulam stability for fractional differential equations of Hilfer-Hadamard type,” *Advances in Difference Equations*, vol. 2017, no. 1, Article ID 180, 2017.
- [19] N. Abdellouahab, B. Tellab, and K. Zennir, “Existence and stability results of A nonlinear fractional integro-differential equation with integral boundary conditions,” *Kragujevac Journal of Mathematics*, vol. 46, no. 5, pp. 685–699, 2022.
- [20] A. Naimi, T. Brahim, and K. Zennir, “Existence and Stability results for the solution of Neutral fractional integro-differential equation with nonlocal conditions,” *Tamkang Journal of Mathematics*, vol. 53, pp. 1–22, 2021.
- [21] W. Wei, X. Li, and X. Li, “New stability results for fractional integral equation,” *Computers & Mathematics with Applications*, vol. 64, no. 10, pp. 3468–3476, 2012.
- [22] X.-J. Yang, *General Fractional Derivatives: Theory, Methods and Applications*, CRC Press, New York, NY, USA, 2019.
- [23] X.-J. Yang, F. Gao, and Y. Ju, *General Fractional Derivatives with Applications in Viscoelasticity*, Academic Press, Cambridge, MA, USA, 2020.
- [24] Y. Zhou, *Basic Theory of Fractional Differential Equations*, World Scientific, Singapore, Singapore, 2014.
- [25] Y. Liu, “Existence and unboundedness of positive solutions for singular boundary value problems on half-line,” *Applied Mathematics and Computation*, vol. 144, no. 2-3, pp. 543–556, 2003.
- [26] S. Abbas, M. Benchohra, and G. M. N. Guerekata, *Topics in Fractional Differential Equations*, Springer, New York, NY, USA, 2012.
- [27] I. A. Rus, “Ulam stability of ordinary differential equations,” *Studia Univ. “Bases, -Bolyai”, Mathematica*, vol. LIV, no. 4, pp. 125–133, 2009.

Research Article

Four-Scroll Hyperchaotic Attractor in a Five-Dimensional Memristive Wien Bridge Oscillator: Analysis and Digital Electronic Implementation

Gabin Jeatsa Kitio,^{1,2} Cyrille Ainamon,³ Karthikeyan Rajagopal ⁴,
Léandre Kamdjeu Kengne ^{1,2}, Sifeu Takougang Kingni ⁵,
and Justin Roger Mboupda Pone ²

¹Research Unit of Condensed Matter, Electronics and Signal Processing (RU-MACETS), Department of Physics, Faculty of Science, University of Dschang, P.O. Box 67, Dschang, Cameroon

²Research Unit of Automation and Applied Computer (RU-AIA), Electrical Engineering Department of IUT-FV of Bandjoun, University of Dschang, P.O. Box 134, Bandjoun, Dschang, Cameroon

³Institut de Mathématiques et de Sciences Physiques, Université d'Abomey-Calavi, B.P. 613, Porto Novo, Benin

⁴Center for Nonlinear Systems, Chennai Institute of Technology, Chennai, India

⁵Department of Mechanical, Petroleum and Gas Engineering, Faculty of Mines and Petroleum Industries, University of Maroua, P.O. Box 46, Maroua, Cameroon

Correspondence should be addressed to Justin Roger Mboupda Pone; pone00@yahoo.com

Received 24 July 2021; Accepted 1 October 2021; Published 19 October 2021

Academic Editor: Giuseppe Grassi

Copyright © 2021 Gabin Jeatsa Kitio et al. This is an open access article distributed under the Creative Commons Attribution License, which permits unrestricted use, distribution, and reproduction in any medium, provided the original work is properly cited.

An electronic implementation of a novel Wien bridge oscillation with antiparallel diodes is proposed in this paper. As a result, we show by using classical nonlinear dynamic tools like bifurcation diagrams, Lyapunov exponent plots, phase portraits, power density spectra graphs, time series, and basin of attraction that the oscillator transition to chaos is operated by intermittency and interior crisis. Some interesting behaviors are found, namely, multistability, hyperchaos, transient chaos, and bursting oscillations. In comparison with some memristor-based oscillators, the plethora of dynamics found in this circuit with current-voltage ($i-v$) characteristic of diodes mounted in the antiparallel direction represents a major advance in the knowledge of the behavior of this circuit. A suitable microcontroller based design is built to support the numerical findings as these experimental results are in good agreement.

1. Introduction

An evidence fact in the research community is that the electronic circuits containing nonlinear elements exhibit rich dynamic behavior and it has been described in numerous books [1–4]. The research of chaotic memristive circuits is a hot topic of academic research in these recent years [5–8] due to their tremendous engineering applications. We can cite the field applications of communication systems, neural networks, image security, and so on. Memristor-based circuits are famous for displaying a rich variety of behaviors, including multiperiodic, quasiperiodic, and chaotic oscillations as well as self-pulsing and the

coexistence of multiple attractors and hidden attractors [9–14]. The Wien bridge oscillator among many types of memristor-based oscillators appears to be one of the most studied recently with good standing papers published [15–17]. Memristor-based circuits are famous for displaying a rich variety of behaviors. These striking scenarios are defined as follows.

- (i) Multistability is a critical property of nonlinear dynamical systems, where a variety of behaviors such as coexisting attractors can appear for the same parameters, but different initial conditions. The flexibility in the system's performance can be

achieved without changing parameters. This striking scenario has been witnessed in numerous fields of engineering ranging across physics [18], biology [19], chemistry [20], electronics [21–23], and mechanics, as well as reported applications in oscillators and secure communications.

- (ii) Quasiperiodicity is the property of a system that displays irregular periodicity [24]. Quasiperiodic behavior is a pattern of recurrence with a component of unpredictability that does not lend itself to precise measurement. It has been witnessed in rare systems such as the acoustic field [25], laser [26], and neural network [27].
- (iii) Hyperchaotic scenario in the dynamical system is defined as a chaotic system with more than one positive Lyapunov exponent; this implies that its chaotic dynamics extend in several different directions simultaneously [24]. Therefore, comparing with the traditional chaotic system, the hyperchaotic system has more complex dynamical behaviors which can be used to enhance the security of the chaotic communication system [28]. Consequently, the topic of theoretical design and circuitry realization of various hyperchaotic systems has recently become a hotspot in the nonlinear research field. Hyperchaos has been found numerically and experimentally such as Chua's circuit [29], Chen system [30], or Lorenz equation [31].
- (iv) Bursting oscillations are defined as complex oscillations consisting of spiking (cluster of spikes or rapid oscillations) separated by periods of relative quiescence [32]. They have been observed in many practical systems and found a multitude of applications in areas such as electromechanics [33], electronics [34], biology [35], and bioengineering of artificial organs [36]. They have been discovered in many fields, magnetohydrodynamics [37], plasma confinement [25], and X-ray pulsar emission [26]. In biological neurons and cells electrophysiology, bursting oscillations play an important role in information processing. Moreover, in biological neurons, bursting oscillations are important for motor pattern generation and synchronization.
- (v) Transient chaos is a dynamical behavior that displays the existence of chaotic behavior on finite time [38]. Generally, the phenomenon of transient chaos can be observed in dynamical system with boundary crisis [39] and also in families of the logistic and Hénon maps.

Zhijun and Yicheng [40] employed a piecewise linear memristor to construct a fourth-order memristor-based Wien bridge circuit with hyperchaotic dynamics. Wu et al. [41] constructed an active generalized memristor, in which a fourth-order Wien bridge chaotic oscillator was designed further. In recent years, the electronic research team focused on the infinitely differentiable characteristic

equation of the diode component in electronic chaotic circuits replacing nonsmooth ones. The synthesis are well presented in [42, 43] just to name some well-standing papers. Some rare and interesting dynamics are found, namely, coexisting hidden attractors, quasi periodicity with anti-monotonicity, and hyperchaos. As we recall, finding chaotic circuits, (i) which modeled some important unsolved problems in nature, (ii) shed insight on that problems, and (iii) exhibited some behavior previously unobserved [44], is still a major interest. For this purpose, we explore the 5D Wien bridge memristive oscillator with antiparallel diodes with smooth (i–v) characteristics not yet explored in this circuit with interesting dynamics discover:

- (i) Intermittency route to chaos
- (ii) Transient chaos
- (iii) Hyperchaos with offset boosting and partial amplitude control
- (iv) Multistability
- (v) Bursting oscillations
- (vi) The successful microcontroller implementation

The (i–v) characteristic model without approximations of the behavior of the nonlinear element diodes connected in antiparallel direction, therefore, constitutes an advance in the field of research for this Wien bridge oscillator.

The rest of this paper is organized as follows. In Section 2, the model and analysis of a memristive Wien bridge oscillator are presented. It is followed in Section 3 by the numerical analyses highlighting transitions to chaos. Then, in Section 4, some complex dynamics are discovered in this oscillator. We then continue with the microcontroller implementation in Section 5 to verify the numerical findings. The paper ends with some concluding remarks.

2. Modelling and Analysis of a Memristive Wien Bridge Oscillator

The schematic diagram of a memristive circuit based on the 5D Wien bridge oscillator is presented in Figure 1.

2.1. The Model of the Circuit. The circuit of Figure 1 consists of three capacitors C_1, C_2, C_3 ; an inductor L_1 with its internal resistor R_1 ; an operational amplifier; two antiparallel diodes D_1, D_2 ; three resistors R_2, R_3, R_4 ; and a flux-controlled memristor $\omega(\varphi)$. The authors in [16, 45] used a piecewise linear function to describe the voltage-current characteristics of two antiparallel diodes. The exponent of the internal state of the flux-controlled memristor was set to first order as in [46]. In this work, the current-voltage characteristic of two antiparallel diodes D_1 and D_2 is described without any approximation:

$$i_d = i_S (e^{\rho(u_1 - u_3)} - 1) - i_S (e^{-\rho(u_1 - u_3)} - 1) = 2i_S \sinh(\rho(u_1 - u_3)),$$
 where $\rho = 1/(\eta V_T)$, the parameters $i_S = 2.682$ nA, and $V_T = 26$ mV stand for the reverse saturation current, ideality factor, and the thermal voltage of the diodes, respectively. The exponent of the internal state of the memristor here is set to second order as in [47]. The five dynamic

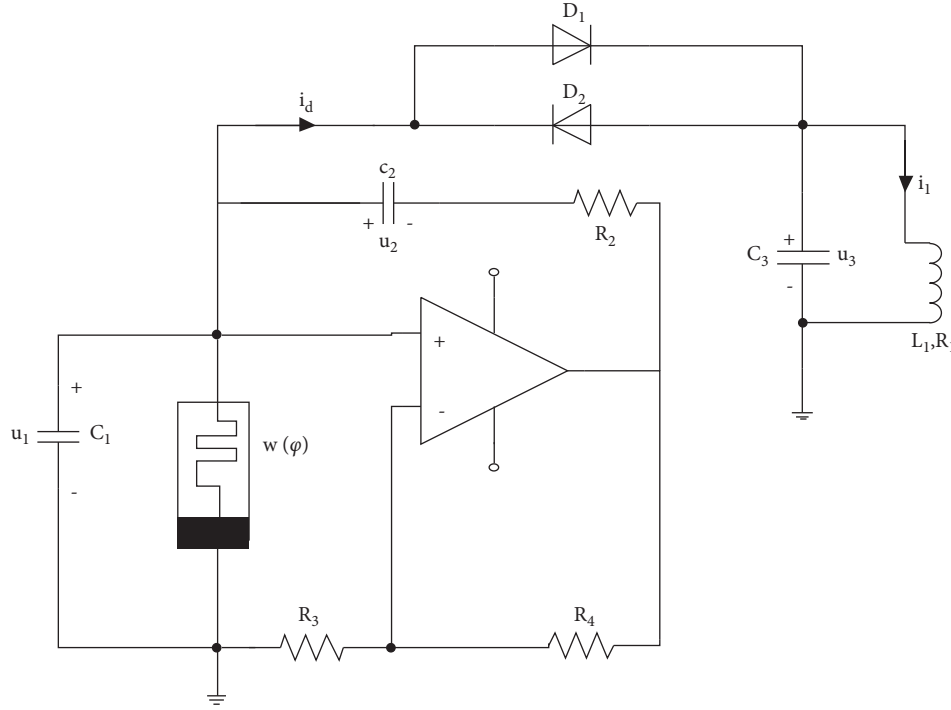


FIGURE 1: The memristive Wien bridge circuit.

elements C_1 , C_2 , C_3 , L , and memristor correspond to each state variable u_1 , u_2 , u_3 , i_1 , and ϕ , respectively. For analysis of the circuit, Kirchoff's law is applied to the circuit of Figure 1 to reveal five sets of first-order differential equations:

$$C_1 \frac{du_1}{dt'} = \frac{R_4}{R_2 R_3} u_1 - w(\phi) u_1 - \frac{1}{R_2} u_2 - 2i_s \sinh(\rho(u_1 - u_3)), \quad (1a)$$

$$C_2 \frac{du_2}{dt'} = \frac{R_4}{R_2 R_3} u_1 - \frac{1}{R_2} u_2, \quad (1b)$$

$$C_3 \frac{du_3}{dt'} = 2i_s \sinh(\rho(u_1 - u_3)) - i_1, \quad (1c)$$

$$L_1 \frac{di_1}{dt'} = u_3 - R_L i_1, \quad (1d)$$

$$\frac{d\phi}{dt'} = -u_1 - \alpha \phi + u_1^2 \phi, \quad (1e)$$

where the parameter α is associated with the memristor and $w(\phi) = (a + 3b'\phi^2)$ is the memristance. Let us define

$x = u_1/\rho$, $y = u_2/\rho$, $z = u_3/\rho$, $w = i_1 \sqrt{R_2 R_3}/\rho$, $v = \phi/(\rho C_1 \sqrt{R_2 R_3})t = t'/C_1 \sqrt{R_2 R_3}$, $b = R_2 R_3 (C_1 \rho)^2 b'$, $c = R_4/\sqrt{R_2 R_3}$, $d = \sqrt{R_3/R_2}$, $e = \sqrt{R_2 R_3} f = \rho C_1$, $g = 2i_s/\rho$, $k = R_2 R_3 C_1/L$, $\delta = \rho^2$, $C_1 = C_2 = C_3$ by inserting the normalized parameters in the set of equations (1a)–(1e); the dimensionless set of equations (1a)–(1e) is given by equations (2a)–(2e) suitable for numerical studies:

$$\frac{dx}{dt} = [c - e(a + 3bv^2)]x - dy - eg \sinh(x - z), \quad (2a)$$

$$\frac{dy}{dt} = cx - dy, \quad (2b)$$

$$\frac{dz}{dt} = eg \sinh(x - z) - w, \quad (2c)$$

$$\frac{dw}{dt} = kz, \quad (2d)$$

$$\frac{dv}{dt} = -x + ef(-\alpha + \delta x^2)v. \quad (2e)$$

2.2. Mathematical Analysis. System (2a)–(2e) is invariant under the transformation: $S(x, y, z, w, v) \rightarrow S(-x, -y, -z, -w, -v)$; therefore, system (2a)–(2e) is symmetry about the origin. The origin of the state space is a trivial equilibrium point $E(0, 0, 0, 0, 0)$ meaning that the solution shows twin symmetric around the origin. The other equilibrium points of system (2a)–(2e) are obtained by solving $dx/dt = 0$, $dy/dt = 0$, $dz/dt = 0$, $dw/dt = 0$, $dv/dt = 0$, which gives

$$z^* = 0, \quad (3a)$$

$$y^* = \frac{cx^*}{d}, \quad (3b)$$

$$w^* = eg \sinh(x^*), \quad (3c)$$

$$\left[a + \frac{3b(x^*)^2}{(ef)^2[-\alpha + \delta(x^*)^2]^2} \right] x^* + g \sinh(x^*) = 0. \quad (3d)$$

Equation (3d) cannot be solved analytically. Then, the Newton–Raphson method [48] is used to find the value of x^*

$$Jac = \begin{pmatrix} [c - e(a + 3bv^2)] - eg \cosh(x - z) & -d & eg \cosh(x - z) & 0 & -6ebvx \\ c & -d & 0 & 0 & 0 \\ eg \cosh(x - z) & 0 & -eg \cosh(x - z) & -1 & 0 \\ 0 & 0 & k & 0 & 0 \\ (-1 + 2ef\delta xv) & 0 & 0 & 0 & ef(-\alpha + \delta x^2) \end{pmatrix}, \quad (4)$$

where Jac is the Jacobian matrix. Thus, the stability of E can be determined by solving the characteristic equation $\det(M_j - \lambda I_5) = 0$, where I_5 represents the 5×5 identity matrix. Table 1 illustrates the eigenvalues obtained by the Newton–Raphson method.

The screening parameter α is kept in the range $1.4 < \alpha < 2$ while the other parameters of the model are the ones defined previously.

We can conclude that, for α belonging to the interval, the system can develop self-excited attractors.

The overview of the stability of system (2a)–(2e) is performed by plotting the stability diagram versus parameters a and α .

In Figure 2, we can notice that the unstable area is limited to the stable area at a critical value of a around 0.75; this helps to choose the value of the parameter for numerical analyses.

3. Numerical Analysis

3.1. 2D Bifurcation Diagrams. Numerical analyses of the dynamical system can be obtained by plotting the 2-D MLE when varying simultaneously two parameters to provide global information about the dynamic behavior of the system under investigation [49].

The colors on these diagrams of the model of our oscillator vary according to the value of the MLE computed using the well-known method of Wolf et al. [50]. In these figures, the light green, cyan, and magenta characterize a chaotic motion while the dark-green yellow and dark red represent periodic or quasiperiodic motion. It is therefore visible that parameters c , d , and g provide many diverse dynamics in contrary to the parameter e that is monotone. For these reasons, we choose them in their interesting interval to study the scenario toward chaos (Figure 3).

3.2. Transitions to Chaos. In this section, intensive numerical analyses are performed by monitoring the bifurcation parameter α and initial states. We plot the local maxima of the coordinate $x(x_{\max})$ and record the Lyapunov spectra. We noticed sparse chaotic windows alternating with periodic ones while increasing or decreasing the bifurcation

for the chosen value $a = 0.05$, $b = 0.03$, $f = 1$, $g = 1$, $\alpha = 2$, $\delta = 1$, $e = 2$, and the method yield $x^* = -3.08e - 18$ resulting in the trivial E . By linearizing system (2a)–(2e) around E , we obtain

parameter α . The red curve is obtained during the increasing path of α while the red one is during the decreasing path.

In this manner, the hysteresis firstly discovered in dynamical systems by Berglund [51] occurs in Figure 4(a) while the red and black curve does not overlap. It is used here to discover symmetric or multiple attractors.

The chaos behavior is obtained as we can see by the intermittency route. We note that this phenomenon is rarely found in dynamical system interring chaotic dynamics [52]. It is described as a scenario involving several frequencies and spontaneously becomes chaotic while varying the bifurcation parameter. The sudden changes in the quality behavior (competition between several frequencies and chaos) are revealed in detail in Figure 5 where some phase portraits with corresponding power density spectra are plotted.

According to Figure 5, we can reveal to the reader the transition to chaos (in forward and in the reversed directions of the bifurcation parameter α) from Figure 5(j) € Figure 5(k). We can observe a periodic behavior suddenly followed by chaotic dynamics by a tiny variation of α .

In this numerical research, it is usually during the intermittency route to encounter the same scenario while time elapsed. In this situation, chaos can appear and disappear to become periodic: this scenario is called transient chaos and it is very rare in dynamical systems.

3.2.1. Transient Chaos Behavior. The findings of transients' chaos are of great interest since they are believed to be the culprit for disastrous such as voltage collapse in electric power systems [53] and species extinction in ecology. We choose the set of system parameters $a = 0.05$, $b = 0.03$, $c = 6$, $d = 3$, $e = 2$, $f = 1$, $g = 1$, $k = 2$, $\alpha = 1.3$, $\delta = 1$ and plot the time trace of the dynamical system in Figure 6.

In Figure 6, one can notice that starting the system at $t = 0$, the behavior of the system is chaotic until $t = 600$ s. This description is revealed by the chaotic attractor in (b) with the corresponding power density spectra. Passing the critical time 600 s, the system becomes regular as shown in Figure 6(d). This phenomenon is also reported in memristive systems [54] including Chua's [55] and Duffing oscillators [56] and deserves to be shared.

TABLE 1: Eigenvalues and stability nature of the equilibrium point E computed for some discrete values of the parameter α .

α	λ_1	λ_2	λ_3	λ_4	λ_5	Stability nature of E
2	-4.0000	$0.8727 + 1.3475i$	$0.8727 - 1.3475i$	$-1.4227 + 1.6926i$	$-1.4227 - 1.6926i$	Instable
2.5	-5.0000	$0.8727 + 1.3475i$	$0.8727 - 1.3475i$	$-1.4227 + 1.6926i$	$-1.4227 - 1.6926i$	Instable
2.8	-5.6000	$0.8727 + 1.3475i$	$0.8727 - 1.3475i$	$-1.4227 + 1.6926i$	$-1.4227 - 1.6926i$	Instable
3	-6.0000	$0.8727 + 1.3475i$	$0.8727 - 1.3475i$	$-1.4227 + 1.6926i$	$-1.4227 - 1.6926i$	Instable
3.2	-6.4000	$0.8727 + 1.3475i$	$0.8727 - 1.3475i$	$-1.4227 + 1.6926i$	$-1.4227 - 1.6926i$	Instable
3.3	-6.6000	$0.8727 + 1.3475i$	$0.8727 - 1.3475i$	$-1.4227 + 1.6926i$	$-1.4227 - 1.6926i$	Instable
1	-2.0000	$0.8727 + 1.3475i$	$0.8727 - 1.3475i$	$-1.4227 + 1.6926i$	$-1.4227 - 1.6926i$	Instable
1.2	-2.4000	$0.8727 + 1.3475i$	$0.8727 - 1.3475i$	$-1.4227 + 1.6926i$	$-1.4227 - 1.6926i$	Instable
1.4	-2.8000	$0.8727 + 1.3475i$	$0.8727 - 1.3475i$	$-1.4227 + 1.6926i$	$-1.4227 - 1.6926i$	Instable

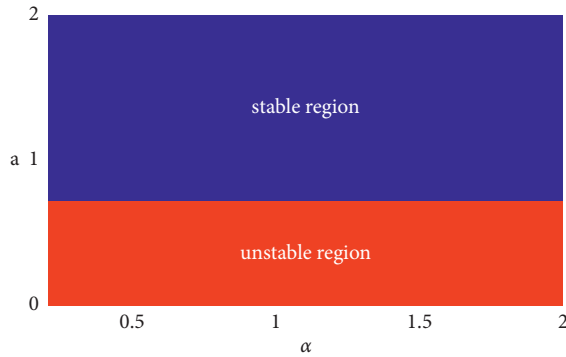


FIGURE 2: Stability diagram of the Wien bridge oscillator in the plane (α, a) highlighting the stable regions (blue) and unstable regions (red) of system (1a)–(1e).

3.2.2. *Intermittency Route to Chaos during Symmetric Interior Crisis.* Another interesting dynamic found in this system is the interior crisis. It describes the bifurcation events in which a chaotic attractor suddenly expands in size. It was initially observed by Grebori et al. [57].

In Figure 7, when the control parameter is varied, we noticed the expansion in size of the red and black attractors until they merged to form a unique huge attractor in Figure 7(f). This striking phenomenon is shown with the time traces of the black and red attractors in the right column of Figure 7.

The description of the multiple routes to chaos observed in system (2a)–(2e) rise to a very interesting and complex behavior as we revealed in the next section.

3.3. Complex Dynamics of the Oscillator

3.3.1. *Multistability.* The famous and interesting behavior of multistability in the dynamical system was shown in the optical chain by [58] and in the isolation of a new defect in n -type silicon [59, 60]. It was recently encountered in well-known systems such as Chua ([61]) and Sprott [62], jerk system [63]. A simple technique to detect this property is to scan the bifurcation diagram upward and downward using the same control parameter (see Figure 4). In the light of this technique, one can observe in Figure 4(a) some windows where the black curve and the red curve do not overlap showing the multistability phenomenon. We draw a zoom in the interesting interval of the control parameter to share this scenario, Figure 8(a).

In Figures 8(b1) and (b2), one can see that the 4 attractors coexist for the same set of system parameters. The red ones are obtained with positive initial conditions while black attractors are obtained with negative initial conditions. The basin of attraction showing the space of initial conditions resulting from each coexisting steady state is plotted in Figure 9. Recall that the basin of attraction associated with attractors red or black is the closure of the set of initial points that, taken as initial conditions, converge to red or black attractors when time increases to infinity. This subset-plane of initial points are determined using the computation of maximum Lyapunov Exponent (MLE) using the well-known algorithm by Wolf et al. [50]. For the 5D system under study, we fixed the initial points $x_2(0) = x_3(0) = x_4(0) = 1$. The system parameters are set in the caption of Figure 9 and remain unchanged during the computation. For any couple of starting points.

$-4 < x_1(0) < 4$ and $-10 < x_5(0) < 10$, the long-term behavior of system (1a)–(1e) is computed using the Runge–Kutta algorithm, and the MLE is determined using the Wolf et al.’s method. Then, it is saved. If:

- (a) $MLE > 0$, we plot on the substate space the point with magenta color for positive chaotic attractors while the blue color area is for negative ones.
- (b) $MLE \leq 0$, we plot on the substate space the point with black color (for negative limit cycles) and red color (for positive limit cycles) for initial conditions that led to periodic attractors.

In Figure 9, the reader can discover the fractal form of the substate space resulting in the complexity of system (1a)–(1e). Note that other planes are not plotted for simplicity purposes.

3.3.2. *Hyperchaos.* The new memristive Wien Bridge oscillator, as in Figure 1, generates hyperchaotic attractor with two positive Lyapunov exponents. In Table 2, Lyapunov exponents and dynamics of system (1a)–(1e) for different values of α are given.

Figure 10 displays the phase portraits of the hyperchaotic attractors.

As we can see, the spiraling trajectories are much denser than those in the chaotic ones, showing to the reader the striking phenomenon of hyperchaos. In Table 2, there are two Lyapunov exponents greater than zero.

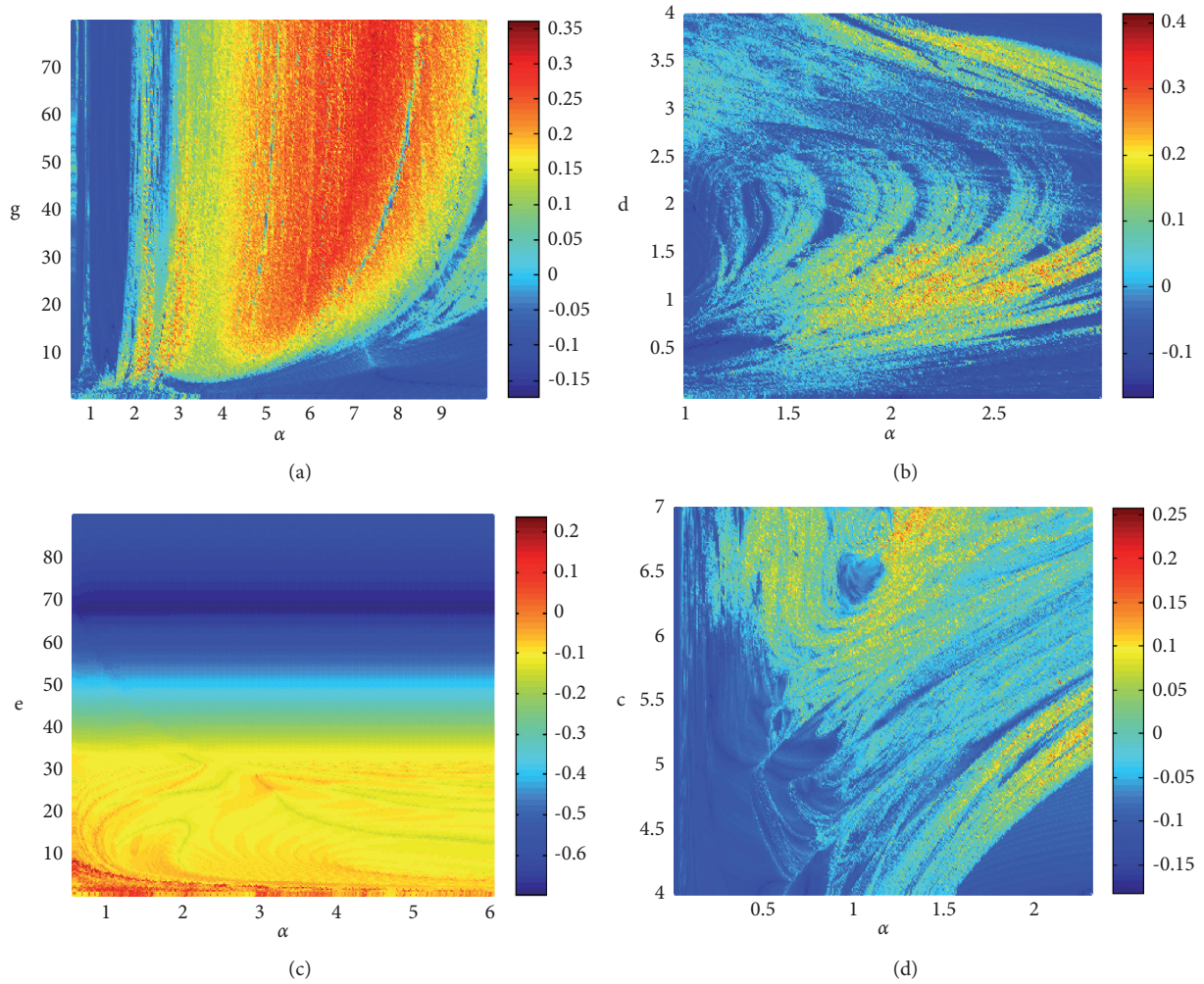


FIGURE 3: 2D maximum Lyapunov exponent (MLE) bifurcation diagrams in the plane: (a) (g, α) ; (b) (d, α) ; (c) (d, c) ; and (d) (α, c) depicting the region of complex dynamics of system (2a)–(2e) with respect to the MLE (right column bar); the system parameters are: $a = 0.05$; $b = 0.03$; $c = 6$; $d = 3$; $e = 2$; $g = 1$; $k = 2$. Initial conditions are $(x_0; y_0; z_0; w_0; v_0) = (1; 1; 1; 0.1; 1)$ (color figure online).

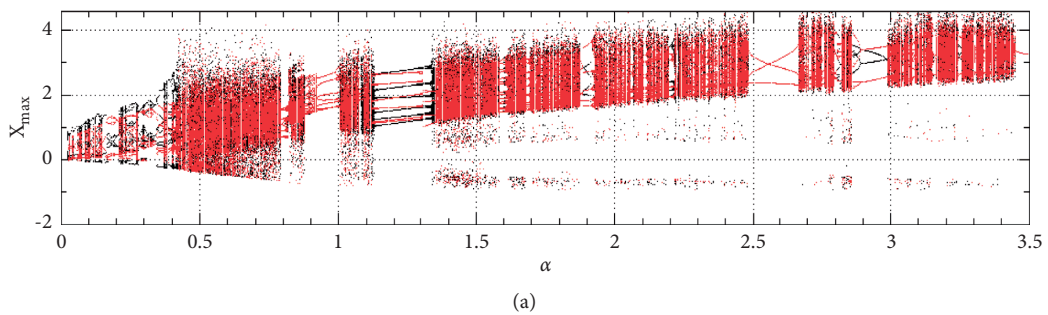


FIGURE 4: Continued.

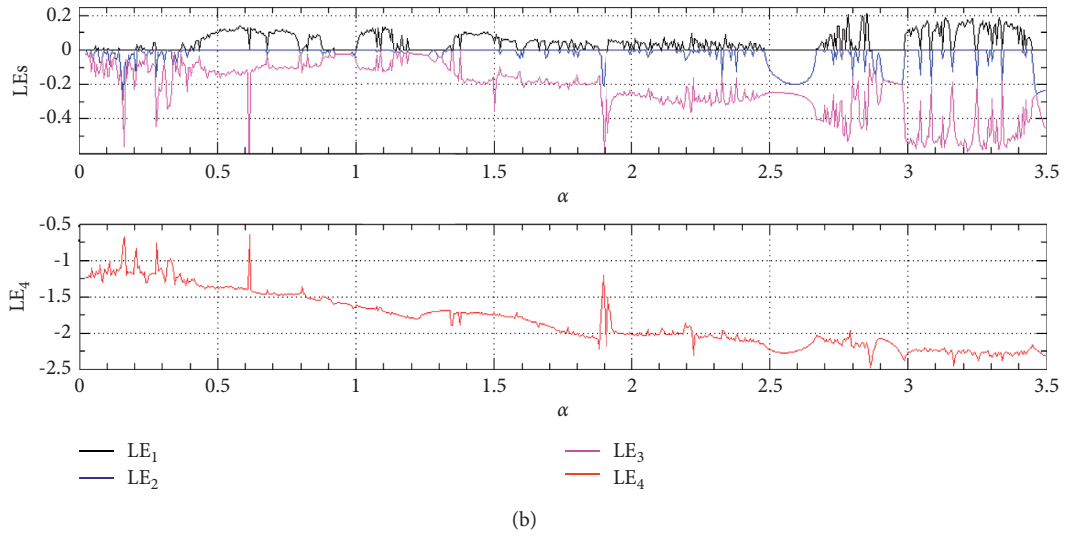


FIGURE 4: Bifurcation (2a)–(2e) of the system showing local maxima of the coordinate x_{\max} versus the parameter α black curve for increasing parameter α and red for decreasing parameter α . (b): the corresponding graphs of Lyapunov exponent spectra. The system parameters are $a=0.05$, $b=0.03$, $c=6$, $d=3$, $e=2$, $g=1$, $k=2$, and $f=1$. Initial conditions are $(x_0; y_0; z_0; w_0; v_0) = (1; 1; 1; 0.1; 1)$ (color figure online).

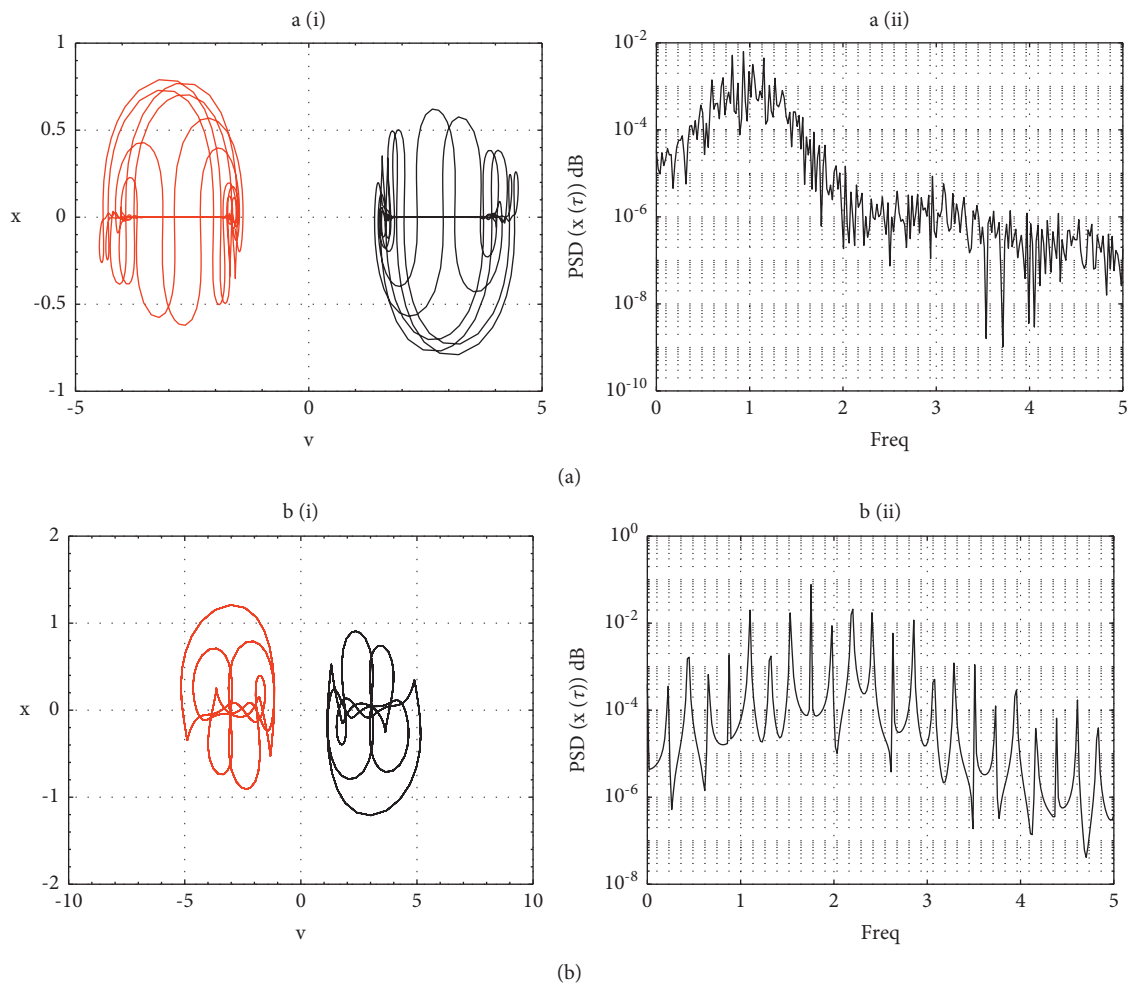


FIGURE 5: Continued.

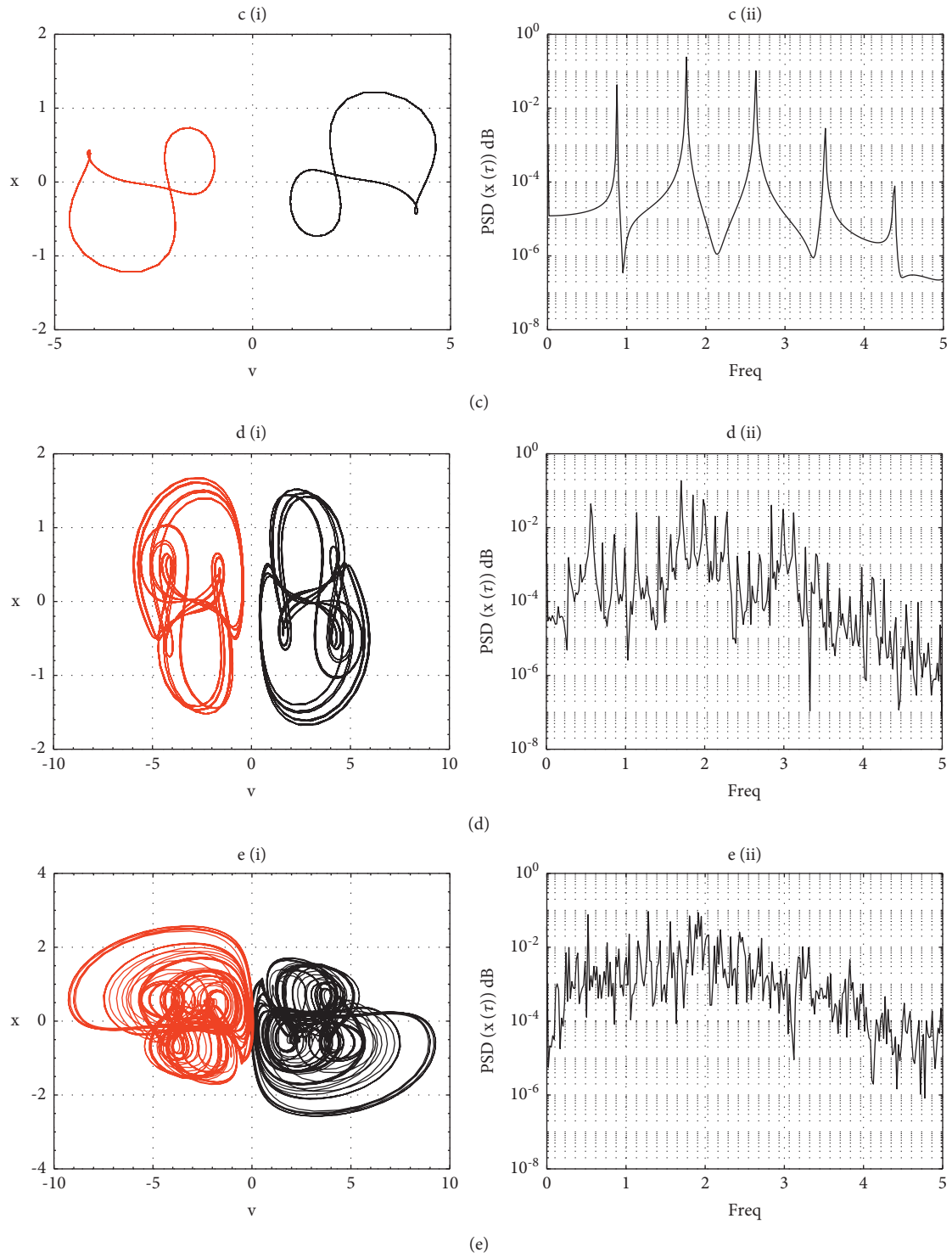


FIGURE 5: Continued.

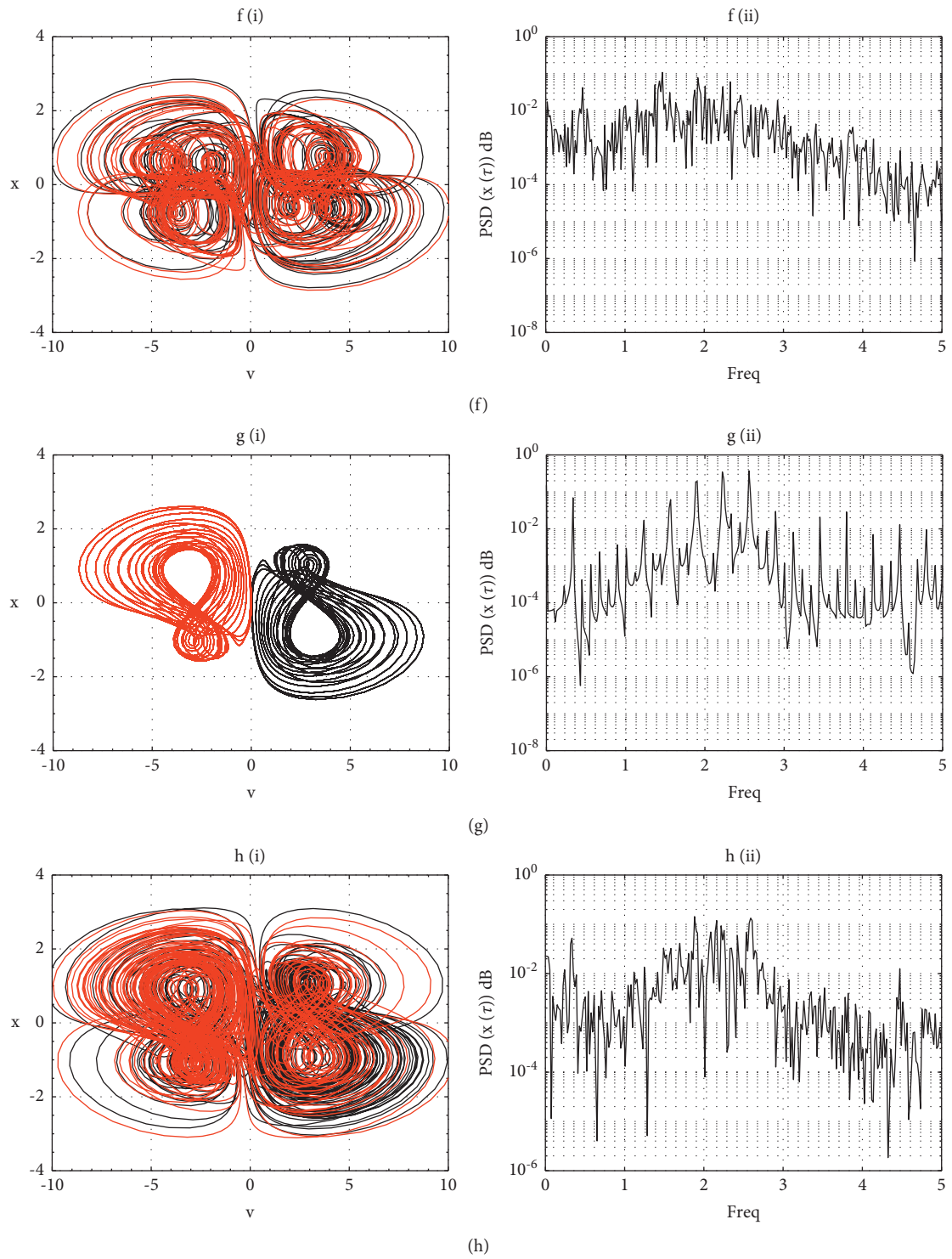


FIGURE 5: Continued.

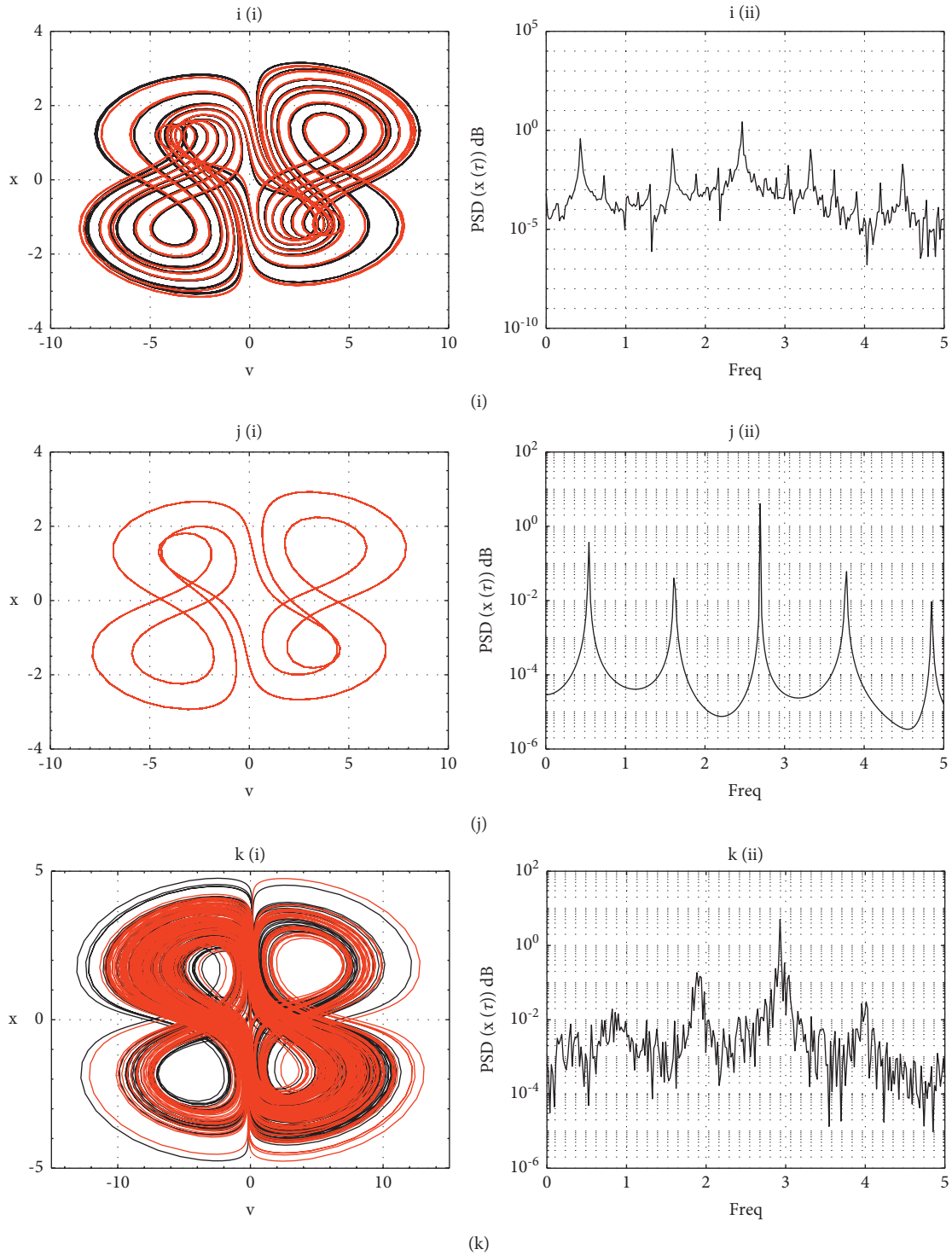


FIGURE 5: Phased portrait revealing the transition to chaos in column (i) with their corresponding power density spectra in column (ii): (a) the pair of chaotic attractors with $\alpha = 0.01$; (b) symmetric attractor period-8 with $\alpha = 0.1$; (c) symmetric attractor period-2 with $\alpha = 0.2$; (d) symmetric attractor period-15 with $\alpha = 0.3$; (e) two-wing symmetric chaotic attractor with $\alpha = 0.4$; (f) four-wing symmetric chaotic attractor with $\alpha = 0.5$; (g) two-wing symmetric period-20 attractor with $\alpha = 0.9$; (h) two-wing symmetric full chaotic attractor with $\alpha = 1$; (i) four-wing period-9 attractor with $\alpha = 1.6$; (j) four-wing period-2 attractor with $\alpha = 1.9$; (k) four-wing merge chaotic attractor with $\alpha = 3.2$. Initial conditions: $(1, 1, 1, 0.1, \pm 1)$.

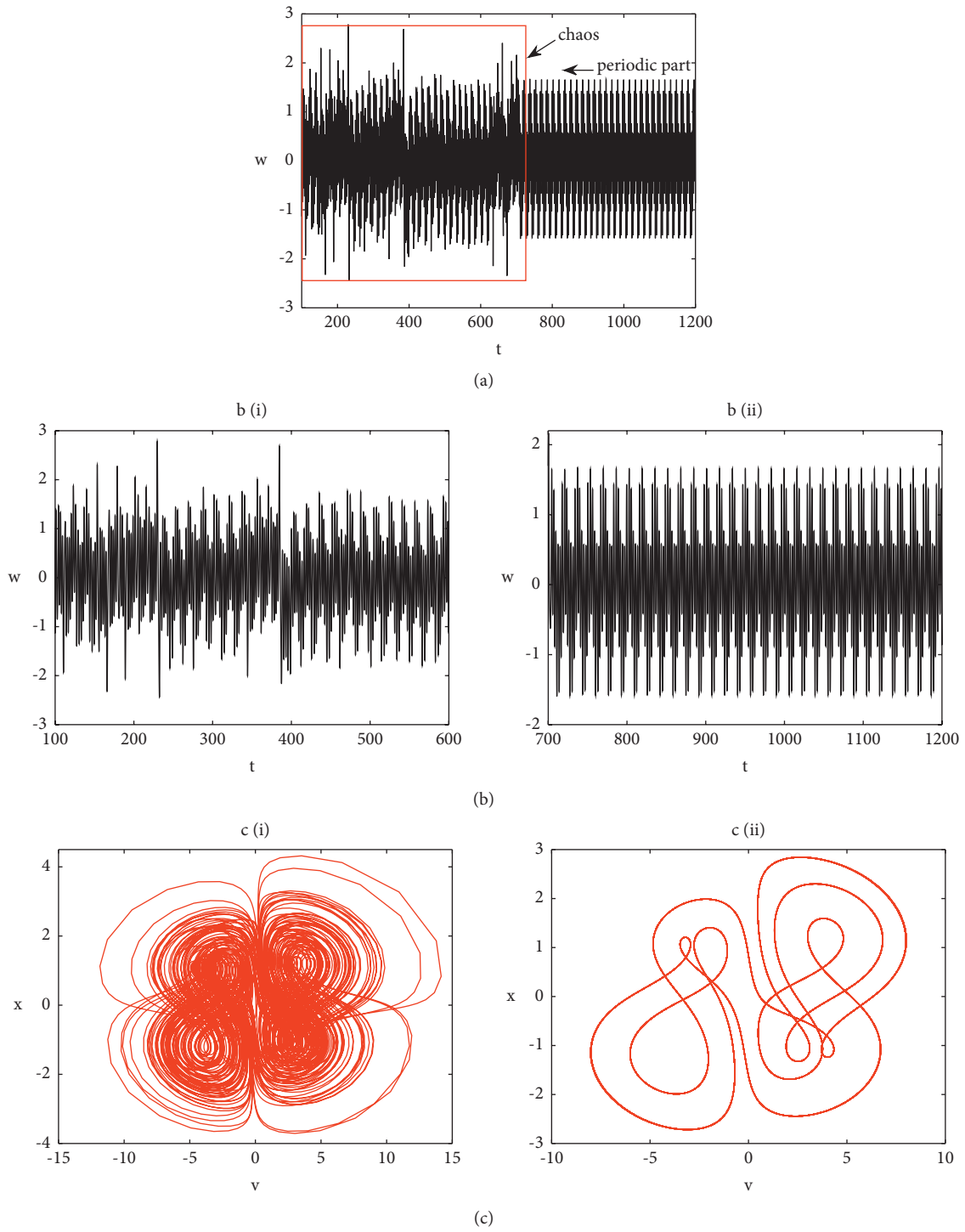


FIGURE 6: Continued.

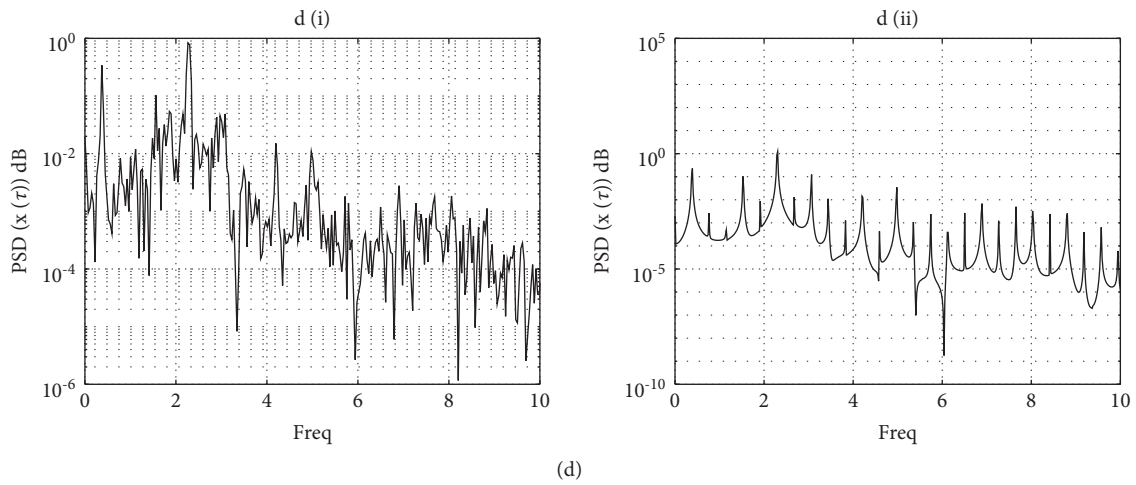


FIGURE 6: (a) Time trace of the state variable x of the system while time elapsed. (b) Division of the interval of monotone dynamics: b(i) chaotic; b(ii) periodic. (c) Corresponding chaotic phase portrait: during time $t < 600$ s c(i) and c(ii) periodic phase portrait during regular motion $t > 600$ s (system parameters: $a = 0.05$, $b = 0.03$, $c = 6$, $d = 3$, $e = 2$, $f = 1$, $g = 1$, $k = 2$, $\alpha = 1.3$, $\delta = 1$; initial state: $(x_0; y_0; z_0; w_0; v_0) = (1; 1; 1; 0.1; 1)$).

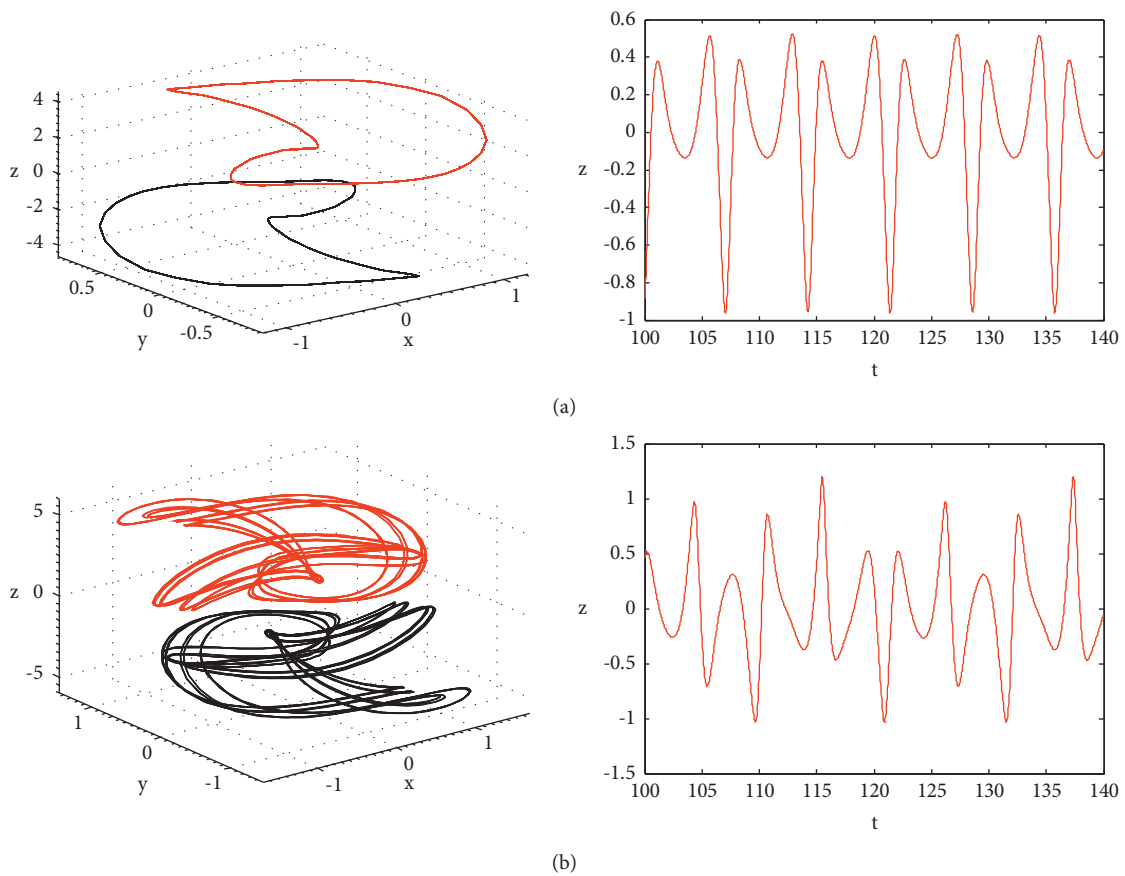
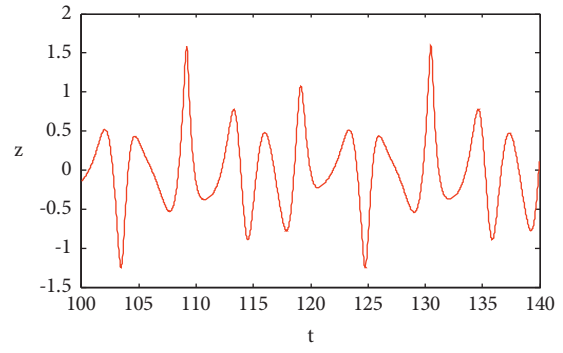
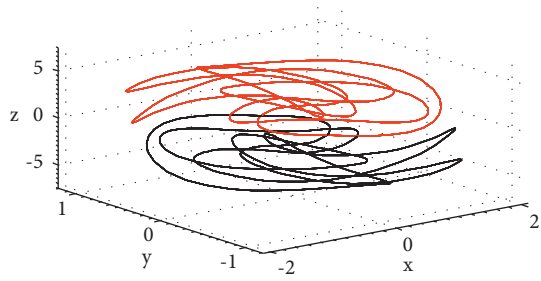
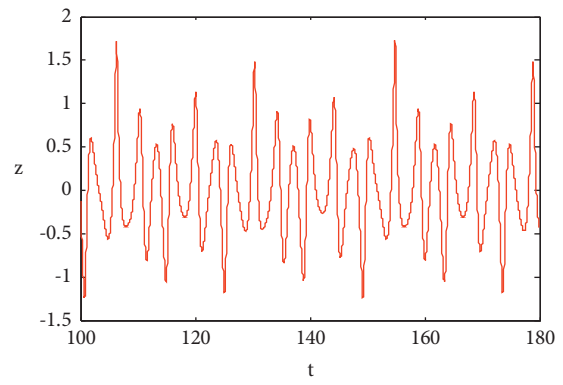
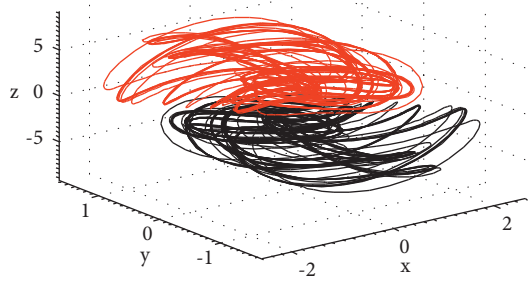


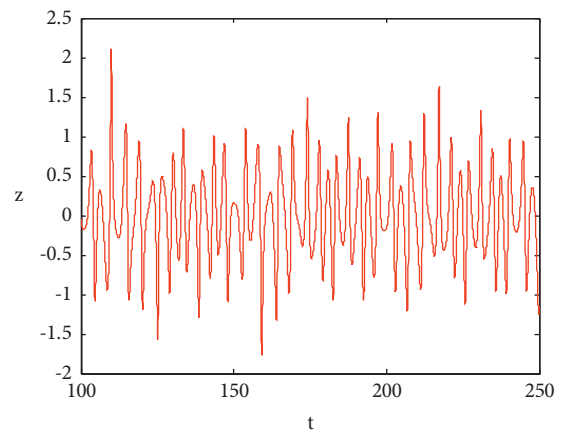
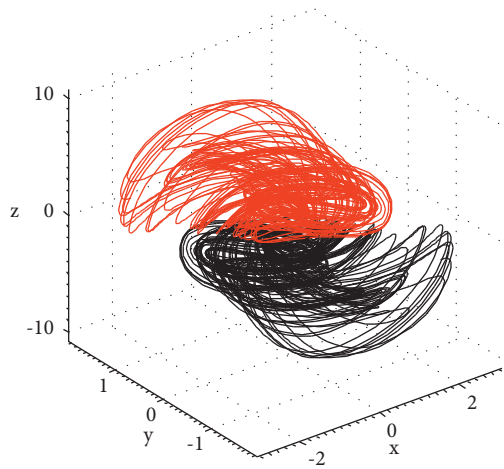
FIGURE 7: Continued.



(c)



(d)



(e)

FIGURE 7: Continued.

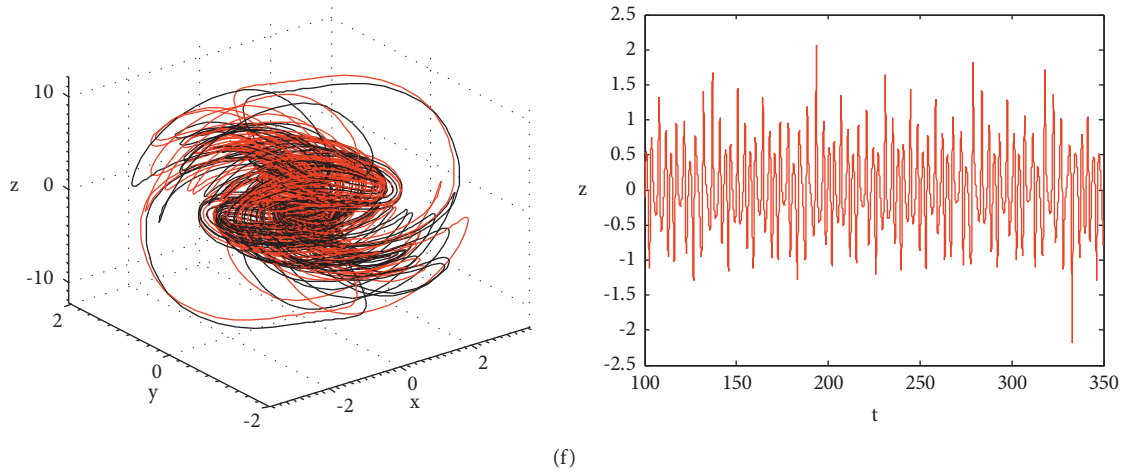


FIGURE 7: 3D projection of the attractors of system (3a)–(3d) in the (x, y, z) plane (i) and the corresponding time traces (ii) illustrating crisis transitions: the transition from (e) \Rightarrow (f) indicates the interior crisis behavior while α is varied. Initial conditions $(1; 1; 1; 0.01)$: (a) period-2 for $\alpha = 0.2$, (b) period-6 for $\alpha = 0.3$, (c) period-5 for $\alpha = 0.35$, (d) symmetric chaotic attractors for $\alpha = 0.4$, (e) $\alpha = 0.42$, and (f) chaotic single band for $\alpha = 0.43$.

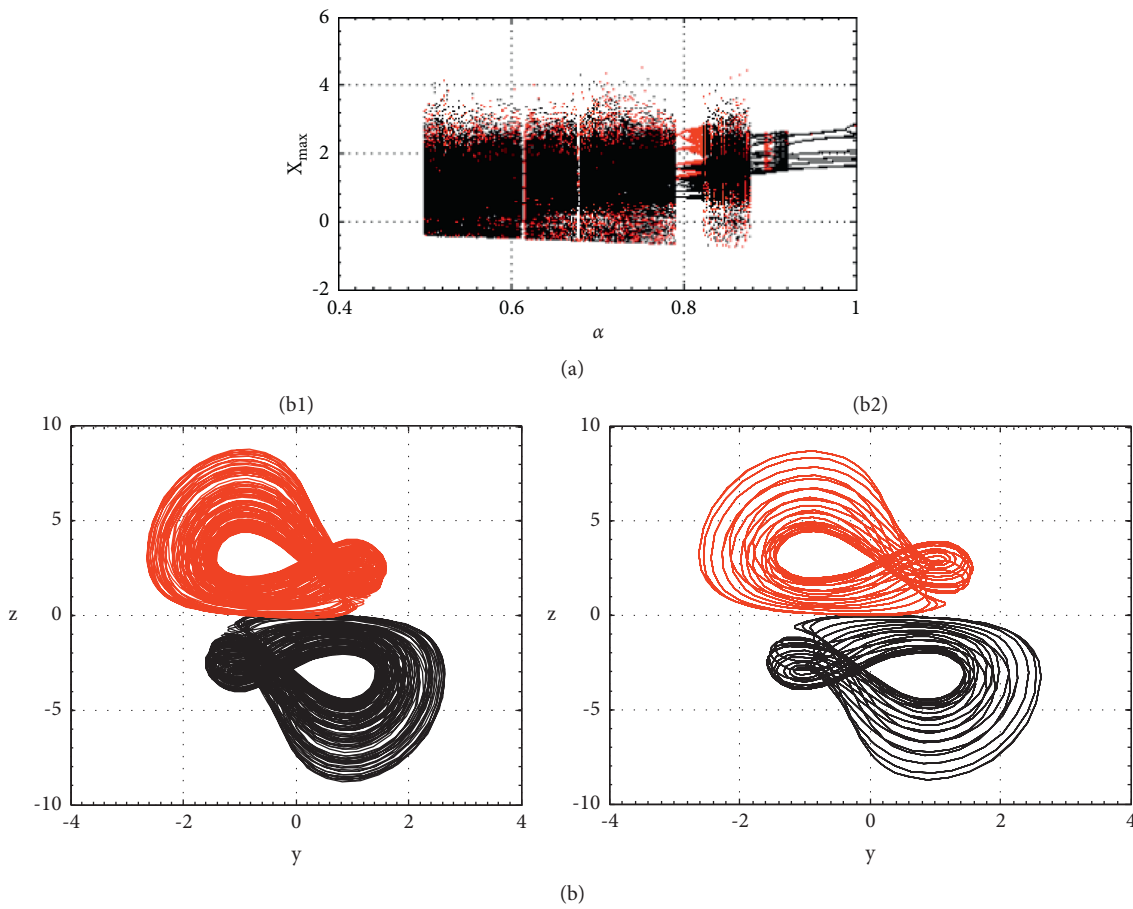


FIGURE 8: Zoom in the bifurcation diagram (a) and the corresponding discovery of coexistence of 4 attractors (2 symmetric chaotic and 2 symmetric periodic attractors) for the same set of parameters $\alpha = 0.9, a = 0.05, b = 0.03, c = 6, d = 3, e = 2, f = 1, g = 1, k = 2, \alpha = 1.3, \delta = 1$. Initial conditions are $(x_0; y_0; z_0; w_0; v_0) = (\pm 1; \pm 1; \pm 1; \pm 0.1; \pm 1)$.

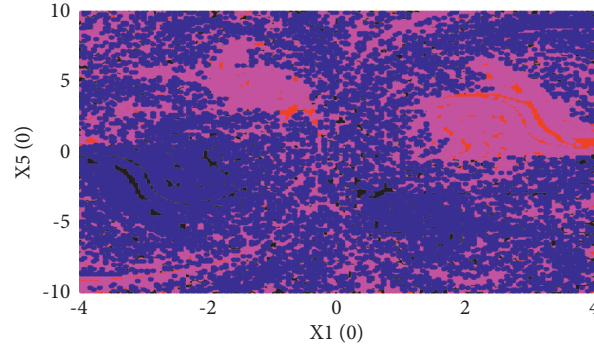


FIGURE 9: Basin of attraction plotted in the plane $(x_1(0), x_5(0))$ showing the initial conditions that lead to each coexisting steady state: the orange area is for positive chaotic attractor while the blue area is for negative ones. The black and red zones are for initial conditions that led to periodic attractors. System parameters are $a = 0.05, b = 0.03, c = 6, d = 3, e = 2, f = 1, g = 1, k = 2, \alpha = 1.3, \delta = 1$. The other initial conditions are $X_2(0) = 1, X_3(0) = 1, X_4(0) = 1$ (color version online).

TABLE 2: Lyapunov exponents and dynamics of system (2a)–(2e) with parameter alpha varying.

α	LE_1	LE_2	LE_3	LE_4	LE_5	Dynamics	Figure
0.525	0.119	0.00107	-0.156	-1.368	-1.5	Hyperchaos	Figure 10
0.69	0.107	0.001	-0.105	-1.462	-1.612	Hyperchaos	

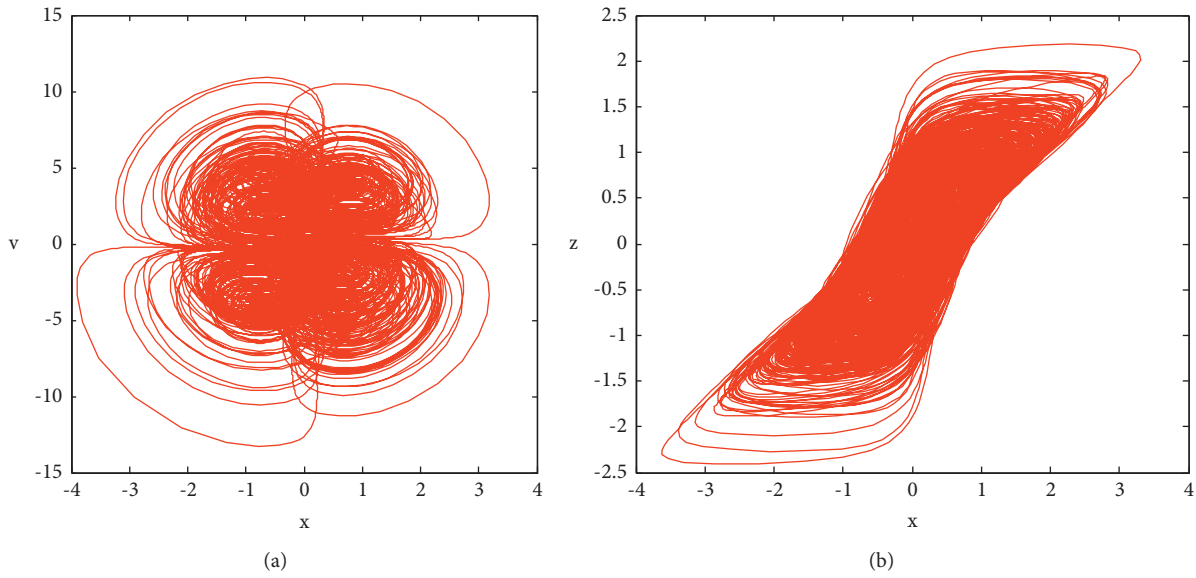


FIGURE 10: Phase portraits of the four-scroll hyperchaotic attractor for (a) $\alpha = 0.525$ ($LE_1 = 0.119381$ and $LE_2 = 0.00107263$) and (b) $\alpha = 0.69$ ($LE_1 = 0.107339$ and $LE_2 = 0.001000881$) initial conditions $(x_0; y_0; z_0; w_0; v_0) = (1; 1; 1; 0.1; 1)$.

3.3.3. *Offset Boosting.* The flexibility of the Wien Bridge oscillator can be used as a chaotic encoding circuit by means of varying parameters. For this purpose, we exploit the rescaling factor k to illustrate the displaced attractor on the w axis as follows: $w \rightarrow w + \mu$. System (2a)–(2e) is written as follows:

$$\frac{dx}{dt} = [c - e(a + 3bv^2)]x - dy - eg \sinh(x - z), \quad (5a)$$

$$\frac{dy}{dt} = cx - dy, \quad (5b)$$

$$\frac{dz}{dt} = eg \sinh(x - z) - (w + \mu), \quad (5c)$$

$$\frac{dw}{dt} = kz, \quad (5d)$$

$$\frac{dv}{dt} = -x - ef(-\alpha + \delta x^2)v. \quad (5e)$$

In Figure 11, the attractor moved in the z -axis in accordance with the offset variable μ .

3.3.4. *Amplitude Control.* In this section, we show that the amplitude of the attractor of the oscillator can be varied by means of the scaling factor m . In Figure 12, one can see that the dimension attractor can be shrunk or expanded in accordance with the amplitude control factor m .

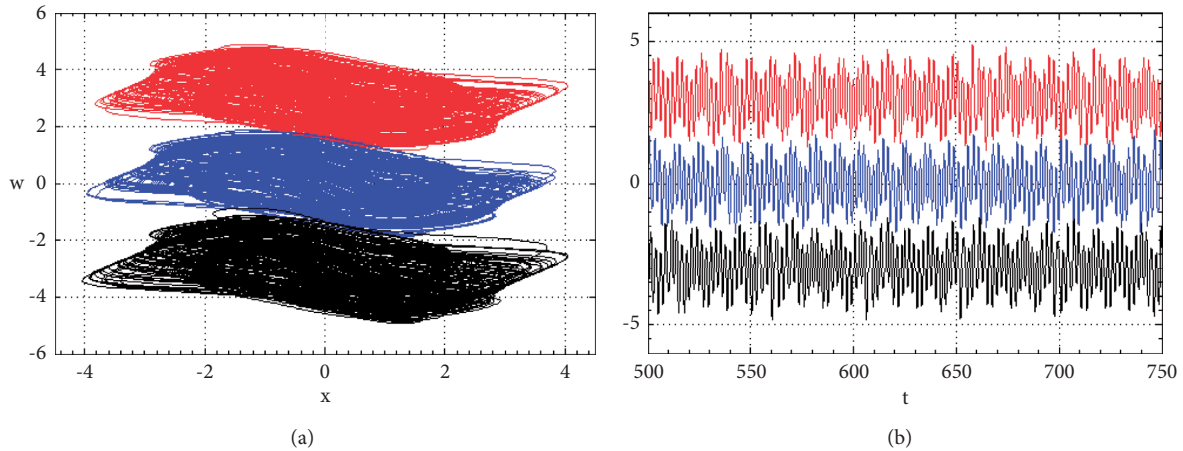


FIGURE 11: Offset boosting dynamics in w axis (i.e., $w = w + \mu$): (a) phase portraits in (w, x) plane and (b) the time series of $w(t)$ for discrete values of the boosted parameter μ : $\mu = -3$ red; $\mu = 0$ blue; $\mu = +3$ green. Initial conditions: $x(0) = 1, y(0) = 1, z(0) = 1, w(0) = 1, v(0) = 0.01$. The rest of the system (2a)–(2e) parameters are in Figure 2.

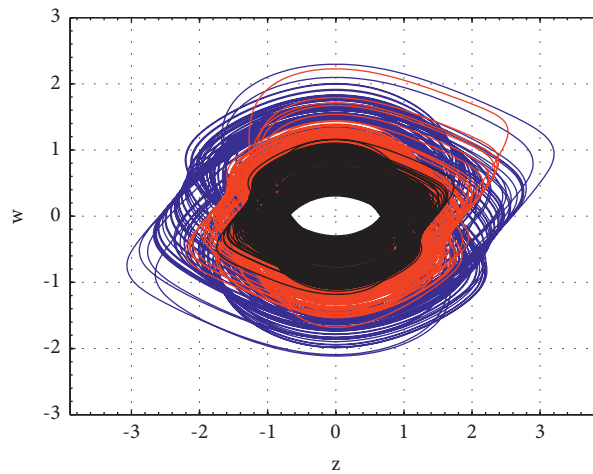


FIGURE 12: Total amplitude control dynamics by substitution of state variables $x \rightarrow x/m, y$ by $y/m, z$ by $z/m, w$ by w/m , and v by v/m shown by means of (a) phase portraits in (z, w) plane and (b) (x, z) plane for discrete values of the amplitude parameter m : $m = 0.5$ red; $m = 0.2$ blue; $m = 30$ black. The rest of the system (3a)–(3d) parameters are in Figure 2; t is the dimensionless time.

As we can see, the striking amplitude behavior can be exploited in engineering instrumentation.

3.3.5. Bursting Oscillations. By selecting some discrete values of the parameter $\alpha = 0.01$, the time series and phase portraits of y versus x and z versus y are displayed in Figures 13(iii) and (iv) illustrating the periodic bursting oscillations. According to these figures, one can observe that sometimes, the system is fast while other times, it is slow in regular space by a constant period, $T = 50$ s.

4. Electronic Implementation of a Memristive Wien Bridge Oscillator

In this section, the objective of the study is to verify some interesting behaviors found during the numerical simulation of the model of the Wien bridge oscillator with real anti-parallel diodes.

It is important to note that recently, numerous advantages of digital components like FPGA, FPAA, DSP, and SOC have made them suitable for the implementation of chaotic systems just to name a few compared to the analog electronics component. Among them, the microcontrollers offer more flexibility for setting control parameters and initial conditions accurately, reducing the system to a portable source code, and realizing complicated mathematical operations or algorithms without needing special tools. These features increase the number of realizable chaotic systems and simplify the implementation process [64–67].

For this purpose, the experimental setup is drawn in Figure 14.

The experimental setup is composed of an Arduino MEGA board powered by a 9 V DC battery. The computer is connected to the USB port of the Arduino card built with an ATMEGA2560 microprocessor. It is connected to the computer to display data from the Arduino MEGA interface.

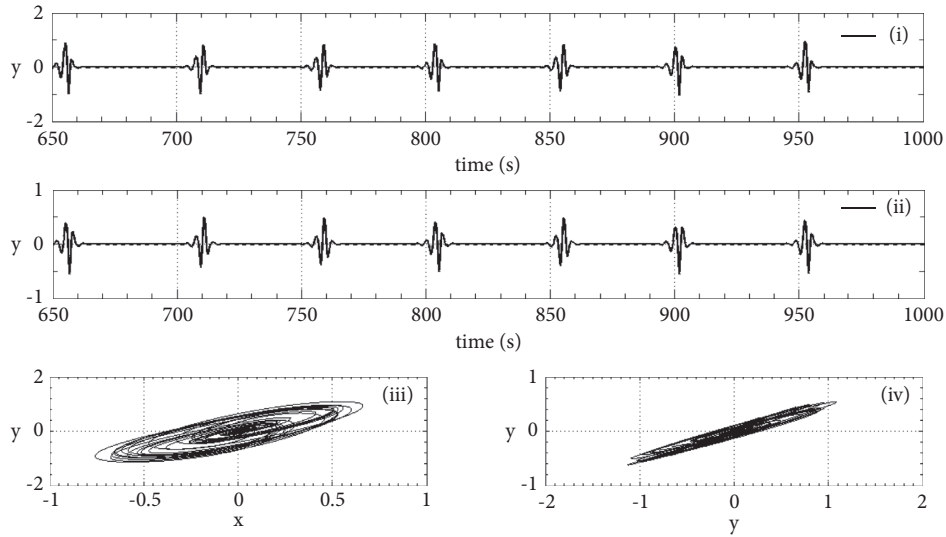


FIGURE 13: Periodic bursting oscillations of the Wien Bridge Oscillator: (i) + (ii) time traces of y and z ; (iii) + (iv) 2D phase portraits. Parameters of the system are $\alpha = 0.01$; the other ones are in Figure 8.

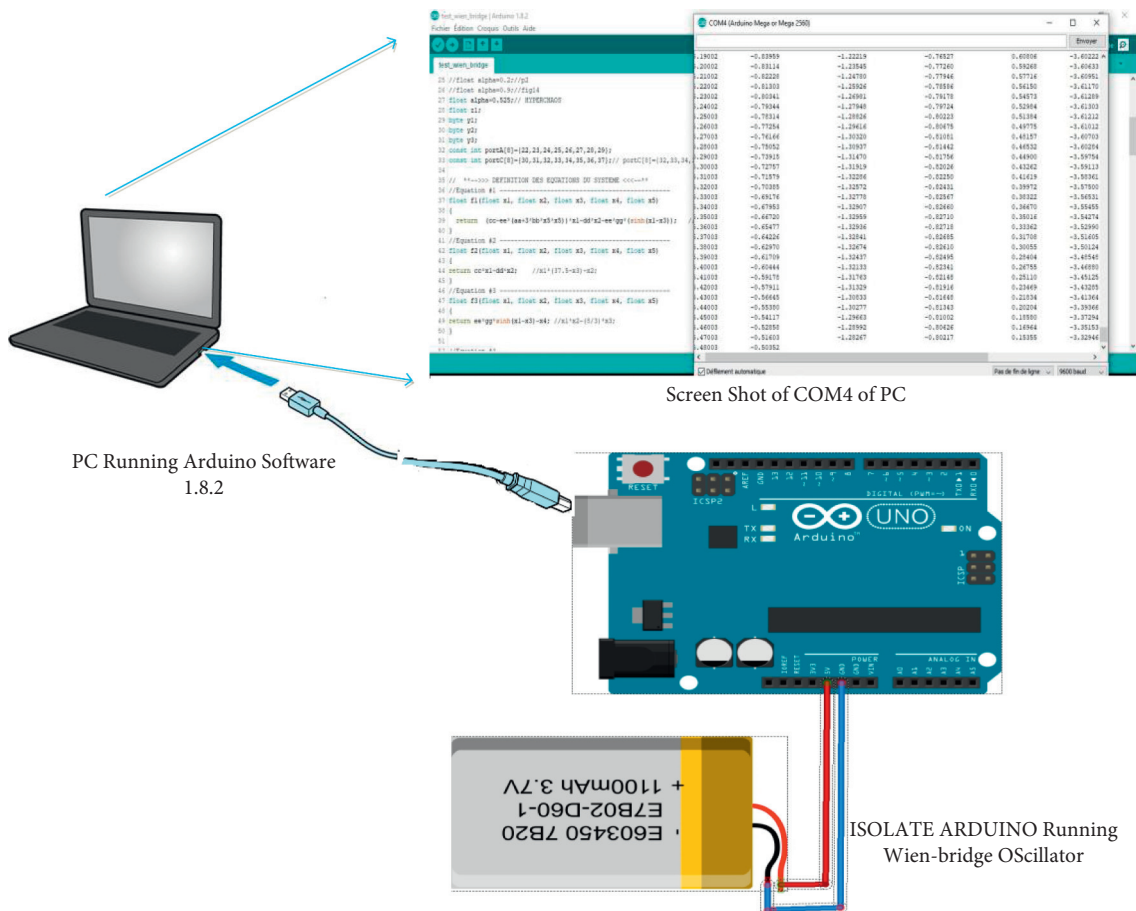


FIGURE 14: Microcontroller experiment workbench of the Wien bridge oscillator.

The memristive Wien bridge oscillator described by system (1a)–(1e) is transformed in numerical form by means of the 4th order Runge–Kutta numerical method with a tiny step time of 0.005 s, typed in the Arduino software, and

downloaded in the Arduino MEGA. The resulting real state variables x, y, z, w, v are sent to the serial monitor of the software from the analog signal. Figures 15 and 16 show the phase planes obtained from the microcontroller.

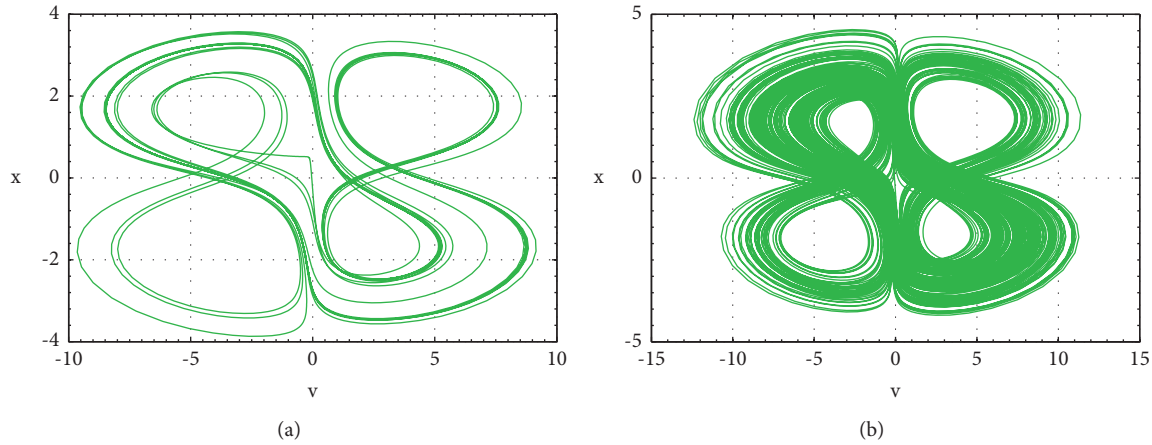


FIGURE 15: Four-wing phased portraits of the Arduino-based implementation of the Wien bridge oscillator confirming the intermittency chaotic scenario for external input A_0 . (a) $A_0 = 2.95$ period-2 and (b) $A_0 = 3.2$ chaotic; this figure reassembles Figure 8(m), (n).

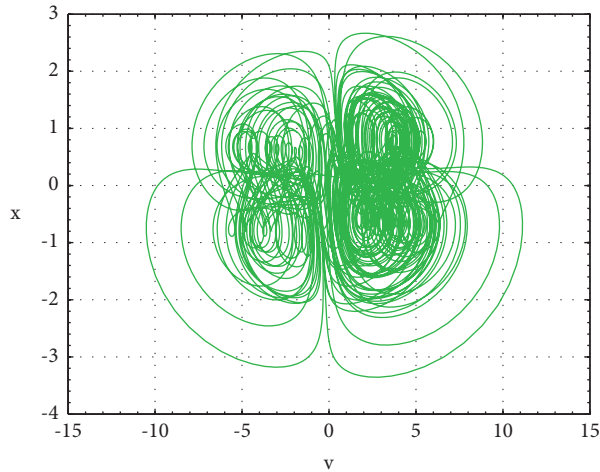


FIGURE 16: Experimental phase portraits of the four-scroll hyperchaotic attractor: (a) $\alpha = 0.525$ starting points are (1; 1; 1; 3.1; 1).

As the reader can see, the experimental design produces on the screen of the computer data that are captured and plotted in MATLAB software for comparison purposes and similar results are recovered.

4.1. Intermittency Route to Chaos with Symmetry Crisis Verification

4.2. *Hyperchaotic Behavior.* As we can see, Figure 15 reproduces the intermittency scenario and Figure 16 the hyperchaotic dynamic of the real component.

5. Conclusion

In this contribution, a new Wien bridge oscillator was introduced and analyzed. The investigations show that some additional behavior found apart from those already revealed in this oscillator was discovered, namely,

intermittency route to chaos, transient chaos, hyperchaos with offset boosting, partial amplitude control, and bursting oscillations. The route to chaos is intermittent, transient chaos with some multistability characterized by the coexistence of up to 4 attractors for the same set of parameters. A basin of attraction is the plot to highlight this scenario. Experiment results based on an isolated Arduino card-built ATMEGA2560 processor producing a digital output of each state variable of the Wien bridge oscillator are consistent with theoretical and numerical predictions. With the research on fracmemristor [68, 69] increasing with high interest, the outlook of this paper is to propose the fractional version of the circuit in Figure 1 with fracmemristor to increase the complexity of the nonlinear Wien bridge oscillator because it can increase the number of disconnected attractors of the Wien bridge. The dimension of the system under scrutinizing is 5D greater than the ones in the literature, but the presence of 4-wing hyperchaotic attractors is an important metric for the system to be used as an image encryption oscillator embedded on an Arduino microcontroller. Therefore, we are planning in the nearest future to experiment with this fascinating application.

Data Availability

No data were used to support this study.

Conflicts of Interest

The authors declare they have no conflicts of interest.

Acknowledgments

The authors sincerely thank Serdar ÇIÇEK of Vocational School of Hacibektaş, Nevşehir Hacı Bektaş Veli University, 50800 Hacibektaş, Nevşehir, Turkey, for fruitful discussion on arduino based implementation. Karthikeyan Rajagopal was partially supported by the Institute of

Research and Development, Defence University, Ethiopia (Grant no. CND/DEC/2018-10).

References

- [1] W.-K. Ling, *Control of Chaos in Nonlinear Circuits and Systems*, Vol. 64, World Scientific, Singapore, 2009.
- [2] I. Nagy, "Nonlinear phenomena in power electronics," *Automatika-Zagreb*, vol. 42, no. 3/4, pp. 117–132, 2001.
- [3] T. L. Carroll and L. M. Pecora, *Nonlinear Dynamics in Circuits*, World Scientific, Singapore, 1995.
- [4] G. Chen and T. Ueta, "Chaos in circuits and systems," vol. 11, Singapore, World Scientific, 2002.
- [5] M. E. Sahin, Z. G. C. Taskiran, H. Guler, and S. E. Hamamci, "Application and modeling of a novel 4D memristive chaotic system for communication systems," *Circuits, Systems, and Signal Processing*, vol. 39, no. 7, pp. 3320–3349, 2020.
- [6] B. Karakaya, A. Gülten, and M. Frasca, "A true random bit generator based on a memristive chaotic circuit: analysis, design and FPGA implementation," *Chaos, Solitons & Fractals*, vol. 119, pp. 143–149, 2019.
- [7] M. Wang, Y. Deng, X. Liao, Z. Li, M. Ma, and Y. Zeng, "Dynamics and circuit implementation of a four-wing memristive chaotic system with attractor rotation," *International Journal of Non-linear Mechanics*, vol. 111, pp. 149–159, 2019.
- [8] M. E. Sahin, Z. G. Cam Taskiran, H. Guler, and S. E. Hamamci, "Simulation and implementation of memristive chaotic system and its application for communication systems," *Sensors and Actuators A: Physical*, vol. 290, pp. 107–118, 2019.
- [9] V. T. Pham, S. Jafari, S. Vaidyanathan, C. Volos, and X. Wang, "A novel memristive neural network with hidden attractors and its circuitry implementation," *Science China Technological Sciences*, vol. 59, no. 3, pp. 358–363, 2016.
- [10] J. Kengne, Z. Njitacke Tabekoueng, V. Kamdoum Tamba, and A. Nguomkam Negou, "Periodicity, chaos, and multiple attractors in a memristor-based Shinriki's circuit," *Chaos: An Interdisciplinary Journal of Nonlinear Science*, vol. 25, no. 10, Article ID 103126, 2015.
- [11] Z. T. Njitacke, J. kengne, H. B. Fotsin, A. N. Negou, and D. Tchiotop, "Coexistence of multiple attractors and crisis route to chaos in a novel memristive diode bridge-based Jerk circuit," *Chaos, Solitons & Fractals*, vol. 91, pp. 180–197, 2016.
- [12] Q. Xu, Q. L. Zhang, H. Qian, H. G. Wu, and B. C. Bao, "Crisis-induced coexisting multiple attractors in a second-order nonautonomous memristive diode bridge-based circuit," *International Journal of Circuit Theory and Applications*, vol. 46, no. 10, pp. 1917–1927, 2018.
- [13] B. C. Bao, H. Bao, N. Wang, M. Chen, and Q. Xu, "Hidden extreme multistability in memristive hyperchaotic system," *Chaos, Solitons & Fractals*, vol. 94, pp. 102–111, 2017.
- [14] J. R. M. Pone, F. Momo, G. Honore Kom, I. Ornela Lowe Kombou, S. Takougang Kingni, and A. Tiedeu, "Extreme multistability, hidden chaotic attractors and amplitude controls in an absolute memristor Van der Pol–duffing circuit: dynamical analysis and electronic implementation." in *In Mem-Elements for Neuromorphic Circuits with Artificial Intelligence Applications*, pp. 165–181, Academic Press, Cambridge, MA, USA, 2021.
- [15] B. C. Bao, P. Y. Wu, H. Bao, H. G. Wu, X. Zhang, and M. Chen, "Symmetric periodic bursting behavior and bifurcation mechanism in a third-order memristive diode bridge-based oscillator," *Chaos, Solitons & Fractals*, vol. 109, pp. 146–153, 2018.
- [16] X. Ye, J. Mou, C. Luo, and Z. Wang, "Dynamics analysis of Wien-bridge hyperchaotic memristive circuit system," *Nonlinear Dynamics*, vol. 92, no. 3, pp. 923–933, 2018.
- [17] Y. Song, F. Yuan, and Y. Li, "Coexisting attractors and multistability in a simple memristive Wien-bridge chaotic circuit," *Entropy*, vol. 21, no. 7, p. 678, 2019.
- [18] A. Jhangeer, M. Muddassar, Z. Ur Rehman, J. Awrejcewicz, and M. B. Riaz, "Multistability and dynamic behavior of nonlinear wave solutions for analytical kink periodic and quasi-periodic wave structures in plasma physics," *Results in Physics*, vol. 29, Article ID 104735, 2021.
- [19] S. He, H. Natiq, and S. Mukherjee, "Multistability and chaos in a noise-induced blood flow," *The European Physical Journal-Special Topics*, vol. 230, no. 5, pp. 1525–1533, 2021.
- [20] M. Morozov, "Adsorption inhibition by swollen micelles may cause multistability in active droplets," *Soft Matter*, vol. 16, no. 24, pp. 5624–5632, 2020.
- [21] A. Sambas, S. Vaidyanathan, E. Tlelo-Cuautle et al., "A 3-D multi-stable system with a peanut-shaped equilibrium curve: circuit design, FPGA realization, and an application to image encryption," *IEEE Access*, vol. 8, pp. 137116–137132, 2020.
- [22] A. Sambas, S. Vaidyanathan, S. Zhang, Y. Zeng, M. A. Mohamed, and M. Mamat, "A new double-wing chaotic system with coexisting attractors and line equilibrium: bifurcation analysis and electronic circuit simulation," *IEEE Access*, vol. 7, pp. 115454–115462, 2019.
- [23] A. Sambas, S. Vaidyanathan, E. Tlelo-Cuautle et al., "A novel chaotic system with two circles of equilibrium points: multistability, electronic circuit and FPGA realization," *Electronics*, vol. 8, no. 11, p. 1211, 2019.
- [24] R. C. Hilborn, *Chaos and Nonlinear Dynamics: An Introduction for Scientists and Engineers*, Oxford University Press on Demand, Oxford, UK, 2000.
- [25] S. Mondal, S. A. Pawar, and R. I. Sujith, "Synchronous behaviour of two interacting oscillatory systems undergoing quasiperiodic route to chaos," *Chaos: An Interdisciplinary Journal of Nonlinear Science*, vol. 27, no. 10, Article ID 103119, 2017.
- [26] M. Gupta and M. Ruzzene, "Dynamics of quasiperiodic beams," *Crystals*, vol. 10, no. 12, p. 1144, 2020.
- [27] N. Ichinose, "Quasiperiodic-chaotic neural networks and short-term analog memory," *International Journal of Bifurcation and Chaos*, vol. 31, no. 1, Article ID 2130003, 2021.
- [28] X. Wu, H. Wang, and H. Lu, "Modified generalized projective synchronization of a new fractional-order hyperchaotic system and its application to secure communication," *Nonlinear Analysis: Real World Applications*, vol. 13, no. 3, pp. 1441–1450, 2012.
- [29] A. Ishaq Ahamed and M. Lakshmanan, "Nonsmooth bifurcations, transient hyperchaos and hyperchaotic beats in a memristive Murali-Lakshmanan-Chua circuit," *International Journal of Bifurcation and Chaos*, vol. 23, no. 6, Article ID 1350098, 2013.
- [30] A. S. Hegazi and A. E. Matouk, "Dynamical behaviors and synchronization in the fractional order hyperchaotic Chen system," *Applied Mathematics Letters*, vol. 24, no. 11, pp. 1938–1944, 2011.
- [31] Z. Cao and L. Wang, "A secure video watermarking technique based on hyperchaotic Lorentz system," *Multimedia Tools and Applications*, vol. 78, no. 18, pp. 26089–26109, 2019.
- [32] L. Holden and T. Erneux, "Understanding bursting oscillations as periodic slow passages through bifurcation and limit

- points,” *Journal of Mathematical Biology*, vol. 31, no. 4, pp. 351–365, 1993.
- [33] S. T. Kingni, B. Nana, G. S. Mbouna Ngueuteu, P. Wofo, and J. Danckaert, “Bursting oscillations in a 3D system with asymmetrically distributed equilibria: mechanism, electronic implementation and fractional derivation effect,” *Chaos, Solitons & Fractals*, vol. 71, pp. 29–40, 2015.
- [34] S. T. Kingni, L. Keuninckx, P. Wofo, G. V. D. Sande, and J. Danckaert, “Dissipative chaos, Shilnikov chaos and bursting oscillations in a three-dimensional autonomous system: theory and electronic implementation,” *Nonlinear Dynamics*, vol. 73, no. 1, pp. 1111–1123, 2013.
- [35] E. M. Izhikevich, “Neural excitability, spiking and bursting,” *International Journal of Bifurcation and Chaos*, vol. 10, no. 6, pp. 1171–1266, 2000.
- [36] J. Jerrelind and A. Stensson, “Nonlinear dynamics of parts in engineering systems,” *Chaos, Solitons & Fractals*, vol. 11, no. 15, pp. 2413–2428, 2000.
- [37] A. Kadivar and K. Niayesh, “Simulation of free burning arcs and arcs inside Cylindrical Tubes initiated by exploding wires,” in *Proceedings of the 2019 5th International Conference on Electric Power Equipment-Switching Technology (ICEPEST)*, October 2019.
- [38] C. Grebogi, E. Ott, and J. A. Yorke, “Crises, sudden changes in chaotic attractors, and transient chaos,” *Physica D: Nonlinear Phenomena*, vol. 7, no. 1–3, pp. 181–200, 1983.
- [39] H. M. Osinga and U. Feudel, “Boundary crisis in quasi periodically forced systems,” *Physica D: Nonlinear Phenomena*, vol. 141, no. 1–2, pp. 54–64, 2000.
- [40] L. Zhi-Jun and Z. Yi-Cheng, “A memristor chaotic circuit based on Wien-bridge oscillator,” *Journal of Electronics and Information Technology*, vol. 36, no. 1, pp. 88–93, 2014.
- [41] H. Wu, B. Bao, Z. Liu, Q. Xu, and P. Jiang, “Chaotic and periodic bursting phenomena in a memristive Wien-bridge oscillator,” *Nonlinear Dynamics*, vol. 83, no. 1, pp. 893–903, 2016.
- [42] J. R. Mboupda Pone, S. Çiçek, S. Takougang Kingni, A. Tiedeu, and M. Kom, “Passive-active integrators chaotic oscillator with anti-parallel diodes: analysis and its chaos-based encryption application to protect electrocardiogram signals,” *Analog Integrated Circuits and Signal Processing*, vol. 103, no. 1, pp. 1–15, 2019.
- [43] L. Kamdjeu Kengne, H. T. Kamdem Tagne, A. N. Kengnou Telem, J. R. Mboupda Pone, and J. Kengne, “A broken symmetry approach for the modeling and analysis of anti-parallel diodes-based chaotic circuits: a case study,” *Analog Integrated Circuits and Signal Processing*, vol. 104, no. 2, pp. 205–227, 2020.
- [44] J. C. Sprott, “A proposed standard for the publication of new chaotic systems,” *International Journal of Bifurcation and Chaos*, vol. 21, no. 9, pp. 2391–2394, 2011.
- [45] X. Ye, X. Wang, J. Mou, X. Yan, and Y. Xian, “Characteristic analysis of the fractional-order hyperchaotic memristive circuit based on the Wien bridge oscillator,” *The European Physical Journal Plus*, vol. 133, no. 12, p. 516, 2018.
- [46] B. Muthuswamy and L. O. Chua, “Simplest chaotic circuit,” *International Journal of Bifurcation and Chaos*, vol. 20, no. 05, pp. 1567–1580, 2010.
- [47] L. Teng, H. C. I. Herbert, X. Wang, and X. Wang, “Chaotic behavior in fractional-order memristor-based simplest chaotic circuit using fourth degree polynomial,” *Nonlinear Dynamics*, vol. 77, no. 1, pp. 231–241, 2014.
- [48] W. H. Press et al., *Numerical Recipes*, Vol. 818, Cambridge University Press, Cambridge, 1986.
- [49] W. Marszalek, H. Podhaisky, and J. Sadecki, “Computing two-parameter bifurcation diagrams for oscillating circuits and systems,” *IEEE Access*, vol. 7, pp. 115829–115835, 2019.
- [50] A. Wolf, J. B. Swift, H. L. Swinney, and J. A. Vastano, “Determining Lyapunov exponents from a time series,” *Physica D: Nonlinear Phenomena*, vol. 16, no. 3, pp. 285–317, 1985.
- [51] N. Berglund, *Adiabatic Dynamical Systems and Hysteresis*, EPFL, Berglund, Nils, 1998.
- [52] R. Benzi, G. Paladin, G. Parisi, and A. Vulpiani, “Characterisation of intermittency in chaotic systems,” *Journal of Physics A: Mathematical and General*, vol. 18, no. 12, pp. 2157–2165, 1985.
- [53] T. Tél and Y.-C. Lai, “Chaotic transients in spatially extended systems,” *Physics Reports*, vol. 460, no. 6, pp. 245–275, 2008.
- [54] N. H. Alombah, H. Fotsin, and K. Romanic, “Coexistence of multiple attractors, metastable chaos and bursting oscillations in a multiscroll memristive chaotic circuit,” *International Journal of Bifurcation and Chaos*, vol. 27, no. 5, Article ID 1750067, 2017.
- [55] B. Bo-Cheng, L. Zhong, and X. Jian-Ping, “Transient chaos in smooth memristor oscillator,” *Chinese Physics B*, vol. 19, no. 3, Article ID 030510, 2010.
- [56] S. Sabarathinam, C. K. Volos, and K. Thamilaran, “Implementation and study of the nonlinear dynamics of a memristor-based Duffing oscillator,” *Nonlinear Dynamics*, vol. 87, no. 1, pp. 37–49, 2017.
- [57] C. Grebogi, E. Ott, and J. A. Yorke, “Chaotic attractors in crisis,” *Physical Review Letters*, vol. 48, no. 22, pp. 1507–1510, 1982.
- [58] K. Otsuka, “Chaotic itinerancy in a coupled-element multistable optical chain,” *Physical Review A*, vol. 43, no. 1, pp. 618–621, 1991.
- [59] A. Chantre and L. C. Kimerling, “Configurational multistable defect in silicon,” *Applied Physics Letters*, vol. 48, no. 15, pp. 1000–1002, 1986.
- [60] N. Wang, G. Zhang, N. V. Kuznetsov, and H. Bao, “Hidden attractors and multistability in a modified Chua’s circuit,” *Communications in Nonlinear Science and Numerical Simulation*, vol. 92, Article ID 105494, 2021.
- [61] Y.-Z. Cheng, F.-H. Min, Z. Rui, and L. Zhang, “A heterogeneous dual memristive circuit: multistability, symmetry and FPGA implementation,” *Chinese Physics B*, 2021.
- [62] M. A. Al-hayali and F. S. Al-Azzawi, “A 4D hyperchaotic Sprott S system with multistability and hidden attractors,” *Journal of Physics: Conference Series*, vol. 1879, no. 3, Article ID 032031, 2021.
- [63] Q. Xu, S. Cheng, Z. Ju, M. Chen, and H. Wu, “Asymmetric coexisting bifurcations and multi-stability in an asymmetric memristive diode-bridge-based Jerk circuit,” *Chinese Journal of Physics*, vol. 70, pp. 69–81, 2021.
- [64] F. Yu, L. Liu, H. Shen et al., “Multistability analysis, coexisting multiple attractors, and FPGA implementation of Yu-Wang Four-Wing chaotic system,” *Mathematical Problems in Engineering*, vol. 2020, Article ID 7530976, 16 pages, 2020.
- [65] K. Altun, “FPAA implementations of fractional-order chaotic systems,” *Journal of Circuits, Systems, and Computers*, Article ID 2150271, 2021.
- [66] T. Liu, H. Yan, S. Banerjee, and J. Mou, “A fractional-order chaotic system with hidden attractor and self-excited attractor and its DSP implementation,” *Chaos, Solitons & Fractals*, vol. 145, Article ID 110791, 2021.
- [67] Q. Lai, Z. Wan, P. D. Kamdem Kuate, and H. Fotsin, “Coexisting attractors, circuit implementation and synchronization control of a new chaotic system evolved from the

- simplest memristor chaotic circuit,” *Communications in Nonlinear Science and Numerical Simulation*, vol. 89, Article ID 105341, 2020.
- [68] Y. Peng, S. He, and K. Sun, “A higher dimensional chaotic map with discrete memristor,” *AEU-International Journal of Electronics and Communications*, vol. 129, Article ID 153539, 2021.
- [69] S. He, K. Sun, Y. Peng, and L. Wang, “Modeling of discrete fracmemristor and its application,” *AIP Advances*, vol. 10, no. 1, Article ID 015332, 2020.

Research Article

Numerical Analysis of Stratified and Slug Flows

Saliha Nouri,^{1,2} Zouhaier Hafsia^{1,3}, Salah Mahmoud Boulaaras^{1,4,5}, Ali Allahem^{1,6}, Salem Alkhalaf,⁷ and Baowei Feng⁸

¹Department of Physics, College of Science and Arts at ArRass, Qassim University, Buraydah, Saudi Arabia

²Department of Physics, University of Tunis, Tunis, Tunisia

³Department of Physics, University of Tunis El-Manar, Tunis, Tunisia

⁴Department of Mathematics, College of Science and Arts at ArRass, Qassim University, Buraydah, Saudi Arabia

⁵Laboratory of Fundamental and Applied Mathematics of Oran (LMFAO), University of Oran 1, Oran 31000, Algeria

⁶Department of Mathematics, College of Science, Qassim University, Buraydah, Saudi Arabia

⁷Department of Computer Science, College of Science and Arts at ArRass, Qassim University, Buraydah, Saudi Arabia

⁸Department Economic Mathematics, Southwestern University of Finance and Economics, Chengdu, China

Correspondence should be addressed to Zouhaier Hafsia; hafsia.zouhaier@gmail.com

Received 21 September 2021; Accepted 9 October 2021; Published 19 October 2021

Academic Editor: Sundarapandian Vaidyanathan

Copyright © 2021 Saliha Nouri et al. This is an open access article distributed under the Creative Commons Attribution License, which permits unrestricted use, distribution, and reproduction in any medium, provided the original work is properly cited.

The main purpose of this study is to compare two-dimensional (2D) and three-dimensional (3D) two-phase models for both stratified and slug flows. These two flow regimes interest mainly the petroleum and chemical industries. The volume of fluid (VOF) approach is used to predict the interface between the two-phase flows. The stratified turbulent flow corresponds to the oil-water phases through a cylindrical pipe. To simulate the turbulent stratified flow, the $k-\omega$ turbulence model is used. The slug laminar flow concerns the kerosene-water phases through a rectangular microchannel. The simulated results are validated using the previous experimental results available in the literature. For the stratified flow, the axial velocity and the water volume fraction profiles obtained by 2D and 3D models approximate the measurement profiles at the same test section. Also, the T-junction in a 2D model affects only the inlet vicinity. For downstream, the 2D and 3D models lead to the same axial velocity and water volume distribution. For the slug flow, the simulated results show that the 3D model predicts the thin film wall contrary to the 2D model. Moreover, the 2D model underestimates the slug length.

1. Introduction

The stratified and the slug flows are particular two-phase phenomena existing in many applications such as petroleum transportation and chemical microreactors (see Desir et al. [1] and Santos et al. [2]). Using the slug flow, the transfer distance is reduced and the mixing process is enhanced along a microchannel. In the production pipelines, the pressure drop has a great effect on the operational costs and depends on the phase flow rates, the pipe diameter, and fluid properties (surface tension, density, and viscosity).

The two-phase flow can be divided into two kinds: the gas-liquid flow and the liquid-liquid flow. The gas-liquid flow regimes are the most studied regimes numerically and

experimentally [3]. Since the pioneer experimental study of a liquid-liquid flow regime conducted by Charles et al. in [4], many other investigations have been conducted. Following the experimental investigation of Angeli and Hewitt in [5], different flow characteristics of two-phase immiscible fluids are measured including phase distribution and phase holdup of oil and water in horizontal pipe. Based on the experimental study conducted by Elseth in [6], the stratified flow occurs under low mixture velocity, and when the mixture velocity increases, the dispersed regime is observed. The contribution of the wall film associated with the slug flow on the mass transfer was demonstrated experimentally by Arsenjuk et al. in [7]. The available analytical solution is limited to a particular flow pattern. In the literature, different

formulations for the determination of the pressure drop are available for core-annular flow with a laminar core and turbulent annulus [8].

The recent advances in computational fluid dynamics (CFD) have led to various numerical studies of the complex unsteady two-phase flow, overcoming the lack of laboratory information in some operating conditions. Al-Jadidi in [9] investigated a three-dimensional (3D) two-phase model with a large eddy simulation (LES) to better reproduce the turbulent structure to simulate the heavy oil and water flow regimes. The primary annular flow is identified and distinguished into three configurations: sudden contraction or sudden expansion and horizontal channel orifice. Carlos in [10] developed a numerical model of oil and water flow in horizontal pipes in order to study the transition between semidispersed and fully dispersed flows. The T-junction geometry in 2D and 3D models is the most used method to investigate the CAF and stratified and slug flows [11, 12]. Senapati and Dewangan in [13] used a 2D T-junction model to study the stratified flow with three different approaches to capture the interface between the oil and water phase. The coupled level set and volume of fluid (CLSVOF) can better reproduce the flow characteristics. For all these simulations, the $k-\omega$ turbulence model was adopted. 3D Reynolds Average Navier–Stokes (RANS) equations combined with the VOF method were used by Al-Yaari and Abu-Sharkh in [14] to simulate the oil and water stratified flow. The oil enters perpendicular to the water inlet along a T-junction configuration. After a comparative study between the different $k-\varepsilon$ turbulence variants, the re-normalization group (RNG) $k-\varepsilon$ is chosen. The pressure drop associated to the slug flow was investigated experimentally by Kashid and Agar in [15] using a Y-junction as inlet configuration of the oil and water fluids. Desamala et al. in [16] conducted an experimental study to identify the transition of various flow regimes: plug to slug flow, slug to stratified wavy flow, and stratified wavy to stratified mixed flow. Based on 2D T-junction inlet configuration, the different transition flow patterns were validated. The RANS coupled with the VOF model and the $k-\varepsilon$ turbulence model were used.

The majority of numerical studies focused on the effects of the mixture velocity, the water-cut, the fluid properties, and the wetting properties on the flow regime. The two and three-dimensional flow nature is rarely analyzed. In this study, the numerical results of 2D and 3D models are compared for both turbulent stratified and laminar slug

flows. This comparative study permits to identify the effect of the lateral dimension on the prediction of the interface interaction for oil-water stratified flow and kerosene-water slug flows.

2. Problem Description

In order to validate and examine the stratified and slug flows in 2D and 3D, we consider the following geometric configurations previously studied experimentally. Figure 1 illustrates the T-junction adopted to study the water and oil stratified flow regime using a 2D model. The flow direction is along the z -axis. The diameter of the pipe is the same as in the experimental study conducted by Elseth in [6] and is equal to $D = 0.05575$ m. The length of the main pipe is $L_1 = 5$ m, and the branch pipe dimensions are as follows: $D_1 = 0.76 D$, $B_1 = 2.26 D$, $B_2 = 0.72 D$, and $B_3 = 1.45 D$. The stratified flow is simulated for the mixture velocity $U_m = 0.68$ m/s and the water-cut $C_w = 0.5$, which corresponds to the following inlet velocities of water and oil imposed, respectively, at boundaries (1) and (2): $U_{w,in} = U_{o,in} = (U_m/2) \times (D/D_1) = 0.45$ m/s. In the present 3D model, we suppose that the stratified flow is axisymmetric. Hence, the computational domain is composed of only the half cylinder as shown in Figure 2.

The geometric configuration of T-junction to simulate the 2D slug flow is illustrated in Figure 3. The same configuration was investigated experimentally by Cherlo et al. in [17]. The main and the branch microchannels meet at a right angle. The diameter of the microchannel is $D = 590 \mu\text{m}$. The water and kerosene inlets have the following length: $B_4 = 5 D$. The length of the main channel $L = 17 D$. For the 3D slug flow model, the dimension of the rectangular pipe in the x -direction is equal to $h = 500 \mu\text{m}$. The inlet for water and kerosene at boundaries (1) and (2) is $U_{w,in} = U_{k,in} = 10$ ml/h.

3. Mathematical Model

3.1. Governing Transport Equations. For turbulent flow, the transport equations for the two immiscible phases are the Reynolds Average Navier–Stokes (RANS) equations written in terms of the mixture properties. These equations concern the average mass conservation equation and the average momentum conservation equations and can be written in the following form [11]:

$$\begin{aligned} \frac{\partial \rho}{\partial t} + \frac{\partial}{\partial x_j} (\rho U_j) &= 0, \quad j = 1, 2, 3, \\ \frac{\partial}{\partial t} (\rho U_i) + \frac{\partial}{\partial x_j} (\rho U_j U_i) &= -\frac{\partial P}{\partial x_i} + \frac{\partial}{\partial x_j} \left[(\mu + \mu_t) \frac{\partial U_i}{\partial x_j} \right] + g_i + F_i, \quad i, j = 1, 2, 3, \end{aligned} \quad (1)$$

where ρ is the density of the mixture and μ is the dynamic molecular viscosity of the mixture defined by

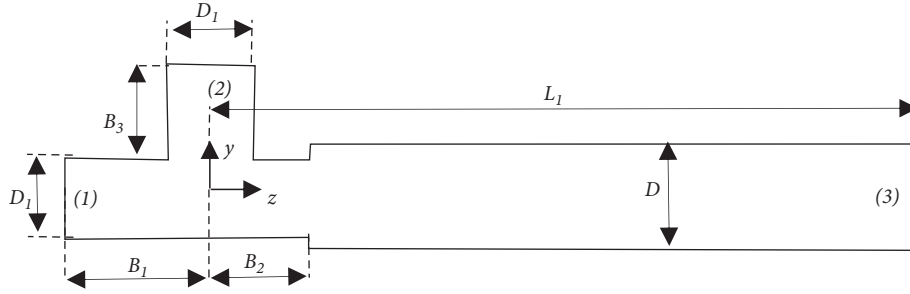


FIGURE 1: Sketch of 2D geometry of the T-junction adopted to simulate the stratified flow.

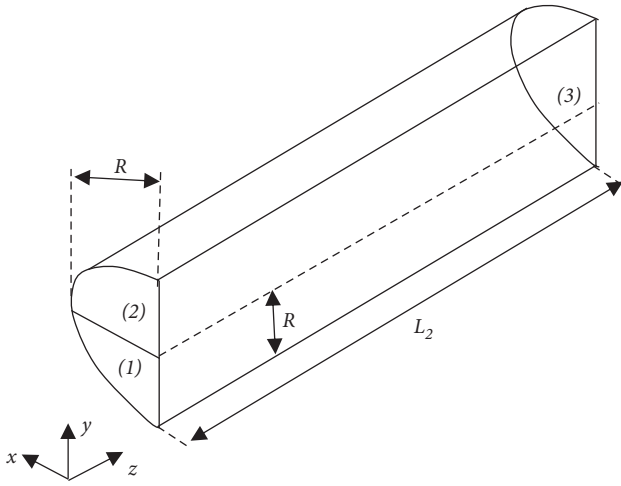


FIGURE 2: Sketch of 3D half cylinder adopted to simulate the stratified flow.

$$\begin{aligned}\rho &= \rho_1 \alpha_1 + \rho_2 \alpha_2, \\ \mu &= \mu_1 \alpha_1 + \mu_2 \alpha_2,\end{aligned}\quad (2)$$

where ρ_1 and ρ_2 are, respectively, the densities of phases 1 and 2; μ_1 and μ_2 are, respectively, the dynamic viscosities of phases 1 and 2; α_1 and α_2 are the volume fractions of each phase such that $\alpha_1 + \alpha_2 = 1$; U_i are the mean velocity components; P is the mean pressure; μ_t is the dynamic turbulent viscosity ($\mu_t = 0$ for the laminar slug flow); g_i is the gravity acceleration field; and F_i are the components of external force per unit volume associated to the interfacial tension.

Depending on the flow configuration, the better closure turbulent model can be chosen. In the present study, the $k-\omega$ model with shear stress transport (SST) is adopted as indicated by Shi et al. in [11]. Following this model, the turbulent viscosity μ_t is defined as follows [18]:

$$\mu_t = f_\mu \frac{\rho k}{\omega}. \quad (3)$$

Two added transport equations are needed to compute μ_t : for the turbulent kinetic energy, k , and for the specific dissipation rate, ω :

$$\begin{aligned}\frac{\partial}{\partial t}(\rho k) + \frac{\partial}{\partial x_j}(\rho k U_j) &= \frac{\partial}{\partial x_j} \left[\left(\mu + \frac{\mu_t}{\sigma_k} \right) \frac{\partial k}{\partial x_j} \right] + \rho (P_k - f_2 \varepsilon), \\ \frac{\partial}{\partial t}(\rho \omega) + \frac{\partial}{\partial x_j}(\rho \omega U_j) &= \frac{\partial}{\partial x_j} \left[\left(\mu + \frac{\mu_t}{\sigma_\omega} \right) \frac{\partial \omega}{\partial x_j} \right] + \rho \omega \left(f_1 C_{1\omega} \frac{P_k}{k} - C_{2\omega} \omega \right),\end{aligned}\quad (4)$$

where P_k is the volumetric production rate of k :

$$P_k = \frac{\mu_t}{\rho} \left(\frac{\partial U_i}{\partial x_j} + \frac{\partial U_j}{\partial x_i} \right) \frac{\partial U_i}{\partial x_j}, \quad (5)$$

where f_μ , f_1 , and f_2 are low Reynolds damping functions. The turbulent dissipation rate is given by

$$\varepsilon = C_D \omega k. \quad (6)$$

The following constants are commonly used:

$$\begin{aligned}\sigma_k &= 2.0, \\ \sigma_\omega &= 2, \\ C_D &= 0.09, \\ C_{1\omega} &= \frac{5}{9}, \\ C_{2\omega} &= \frac{3}{40}.\end{aligned}\quad (7)$$

At high Reynolds numbers, the damping functions are set to unity and given by

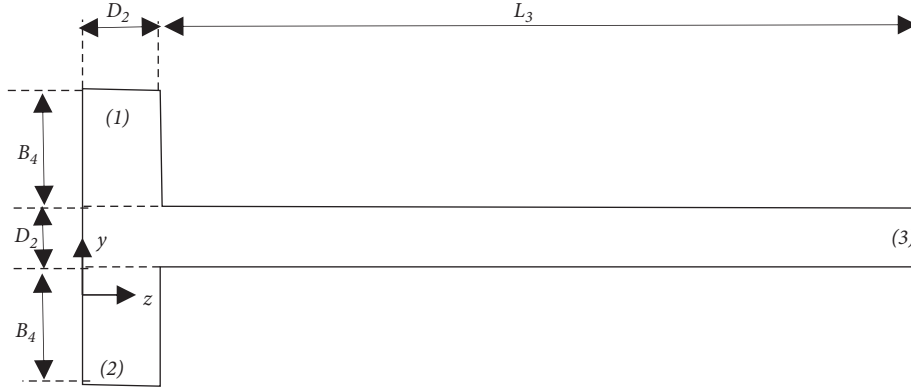


FIGURE 3: Side view of the computational domain adopted to simulate the slug flow.

$$f_{\mu} = \frac{1/40 + R_{e,t}/R_k}{1 + R_{e,t}/R_k}, \quad R_k = 6.0,$$

$$f_1 = \frac{1}{f_{\mu}} \frac{0.1 + R_{e,t}/R_{\omega}}{1 + R_{e,t}/R_{\omega}}, \quad R_{\omega} = 2.7, \quad (8)$$

$$f_2 = \frac{5/18 + (R_{e,t}/R_B)^4}{1 + (R_{e,t}/R_B)^4}, \quad R_B = 8.0,$$

where $R_{e,t}$ is the turbulent Reynolds number defined as

$$R_{e,t} = \frac{\rho k}{\mu \omega}. \quad (9)$$

At high Reynolds numbers, the damping functions f_{μ} , f_1 , and f_2 tend to unity.

The surface tension at the interface between the two phases (the oil-water for stratified flow and the kerosene-water for the slug flow) can be transformed to a continuum surface force (CSF) as indicated by Brackbill et al. [19]. Following this model, the surface tension force is proportional to the curvature κ :

$$\vec{F} = \sigma \kappa \frac{\rho \vec{\nabla} \alpha_1}{1/2(\rho_1 + \rho_2)}, \quad (10)$$

where κ is the interface curvature computed by the divergence of the unit normal as

$$\kappa = \vec{\nabla} \cdot \left(\frac{\vec{n}}{|\vec{n}|} \right). \quad (11)$$

The surface normal is given by the gradient of the volume fraction of the first phase:

$$\vec{n} = \vec{\nabla} \alpha_1. \quad (12)$$

For the stratified flow, investigated experimentally by Elseth in [6], the surface tension between the oil and water phases is $\sigma = 0.043 \text{ N/m}$. For the slug flow, investigated experimentally by Cherlo et al. in [17], the surface tension between the kerosene and water phases is $\sigma = 0.045 \text{ N/m}$ and the contact angle $\theta = 1^\circ$. These flow regimes are investigated through an academic version of a computational fluid

dynamics code. The following fluid properties are used in the simulations:

- (a) For the stratified flow, the fluid density and dynamic viscosity of each phase are as follows.

The first phase (oil): $\rho_1 = 790 \text{ kg/m}^3$
and $\mu_1 = 0.00164 \text{ Pa}\cdot\text{s}$.

The second phase (water): $\rho_2 = 1000 \text{ kg/m}^3$
and $\mu_2 = 0.00102 \text{ Pa}\cdot\text{s}$.

- (b) For the slug flow, the fluid density and dynamic viscosity of each phase are as follows.

The first phase (kerosene): $\rho_1 = 780 \text{ kg/m}^3$
and $\mu_1 = 0.001 \text{ Pa}\cdot\text{s}$.

The second phase (water): $\rho_2 = 998 \text{ kg/m}^3$
and $\mu_2 = 0.001 \text{ Pa}\cdot\text{s}$.

3.2. Initial and Boundary Conditions. For the stratified flow, the horizontal pipe is filled with water at the initial time of simulation ($t = 0 \text{ s}$). In the case of the slug flow, the rectangular cross section channel is filled with the kerosene phase. For all simulated cases, at the pipe wall, a no-slip boundary condition is considered. At the outlet, denoted as (3) as indicated in Figures 1–3, zero pressure is specified. For the turbulent stratified flow, the turbulent kinetic energy and the specific dissipation rate at the inlet are calculated by the following equations:

$$k = (IU)^2,$$

$$\omega = \frac{\varepsilon}{C_D k}, \quad (13)$$

$$\varepsilon = \frac{C_D^{3/4} k^{3/2}}{0.1H},$$

where H is a characteristic inlet dimension as the hydraulic radius.

3.3. Numerical Methods. For the stratified flow, the computational domain contains 17,640 cells for 2D geometry and 495,000 cells for the half-cylinder geometry. The first cell layer in the cross section of the pipe is located at 0.2 mm in

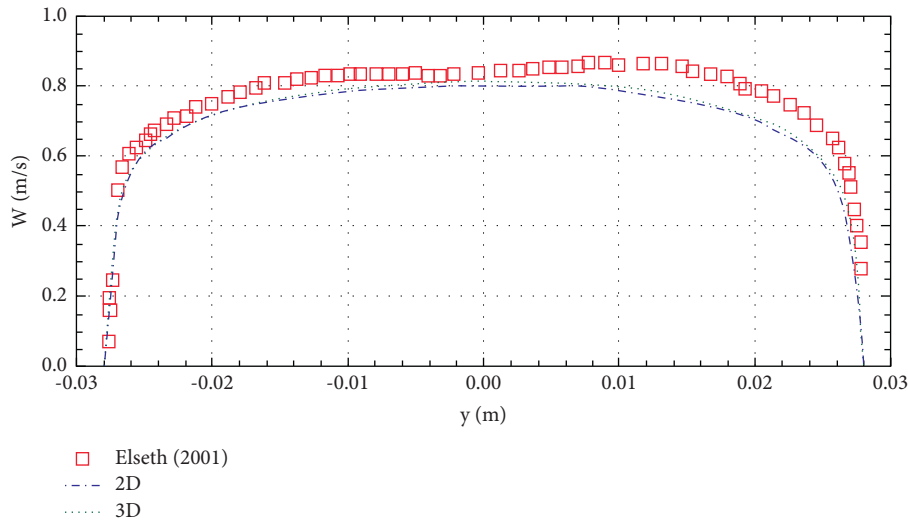


FIGURE 4: Comparison between the simulated axial velocity profile and the experimental results conducted by Elseth in [6] for a stratified flow.

order to satisfy that $y^+ < 5$. For the laminar slug flow, a local grid refinement is needed to well predict the velocity gradient near the wall. The grid numbers are 5100 and 71,400, respectively, for 2D and 3D T-junction geometries. The velocity-pressure coupling is solved by the PISO algorithm (pressure implicit with splitting of operator). For all solved variables, the residual is fixed to 10^{-5} . The geometric reconstruction (piecewise-linear) method is chosen to accurately capture the interface variation between the two immiscible phases. The same method was adopted by Shi et al. in [20]. A variable time step is chosen with initial time step $\Delta t = 10^{-5}$ s. For all simulated cases, the fully developed flow (FDF) is attained if the maximum axial velocity is unchanged with time.

4. Validation of the Numerical Results

4.1. Stratified Flow. The main differences between stratigraphic simulations by 2D and 3D models will be analyzed in terms of axial mixture velocity and water volume fraction. The simulated 2D stratified flow characteristics are compared to the experimental results of Elseth in [6] when the fully developed flow is attained. The axial velocities at the pipe axis and at $z = 72D = 4$ m are represented in Figure 4. There is a satisfactory agreement, but the faster flow in the oil region is not well reproduced. Figure 5 shows the predicted and measured water volume fractions. The sharp interface is correctly simulated. However, the existing waves at the oil and water interface cannot be predicted by the VOF model. To compare the effect of the inlet configuration, Figure 6 presents the water volume fraction in the axial plane of the pipe. The effect of the T-junction in the 2D model is only limited to the vicinity of the junction. The recirculation zone induced by the junction and by the expansion creates a water droplet having a dimension around twice the pipe diameter. There is no difference between these profiles far downstream.

4.2. Slug Flow. The slug flow is validated using the time evolution water volume distribution and the static pressure profiles for the 2D and 3D models. As confirmed by Cherlo et al. in [17], the mechanism of the slug formation can be explained through the following three stages (Figures 7(a)–7(e)).

- (a) The water phase enters into the top microchannel: for the 2D model, this stage continues until the water stream blocks almost the entire cross section of the main channel (Figures 7(a), 7(b), 7(f), and 7(g)). For the 3D model, the water phase is separated from the wall at the junction (Figure 7(g)) and a thinner water interface at the main channel.
- (b) For the 2D model, the water phase progresses in the main channel with a continuous oil entering from the low inlet channel. The shear stress and the pressure gradients exerted by the oil phase distorted the water stream at the end of the water inlet channel. A thin water layer connecting the two water streams is formed. The oil phase flows through the space between the wall and the water phase with high velocity (Figure 7(c)). For the 3D model, the water slug breaks up before the instant $t = 0.50$ s and a thin kerosene layer adjacent to the wall is observed contrary to the 2D model.
- (c) The thickness of the water layer is extremely reduced and breaks up to form a separate slug along the main channel (Figures 7(d) and 7(i)).

The formed slug progresses downstream, and a new droplet is formed when the break-up of the water layer at the junction occurs (Figures 7(e) and 7(j)). Experimentally, the slug length in the same operating conditions taken in the present simulation is equal to $L_s = 2.5$ mm. The length, L_s , is the measured distance between the upstream and downstream points along the plug interface at the developed regime flow. The calculated slug lengths are 2.0 mm and

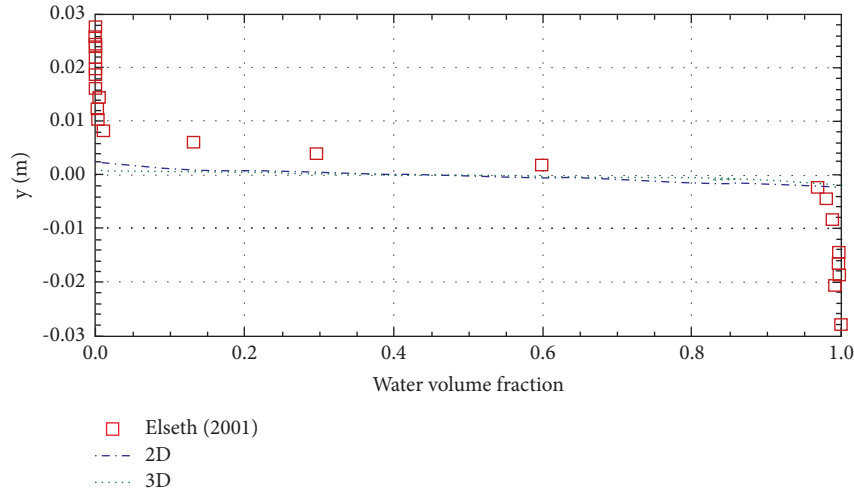


FIGURE 5: Comparison between the simulated water volume fraction profile and the experimental results conducted by Elseth in [6] for a stratified flow.

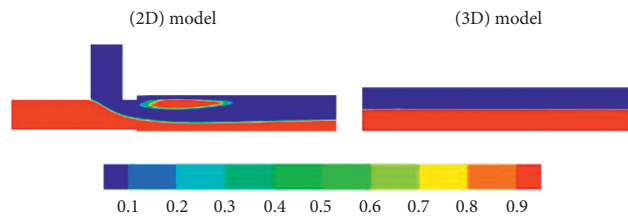


FIGURE 6: Water volume fraction at yz -plane simulated by 2D and 3D models for the fully developed stratified flow.

2.2 mm, respectively, for 2D and 3D models. It seems that the 2D model underestimates the slug length.

In order to validate the pressure drop in the 3D model, the computed static pressure will be compared to the Young–Laplace value. The variation of the static pressure along the axis of the microchannels at the instant $t = 0.80$ s is represented in Figure 8. The computed static pressure is higher in the dispersed phase (water) compared to the continuous phase (oil), and the increase of the pressure at the junction is due to the decrease of the velocity. The simulated pressure drop is around 310 Pa which approximates the Young–Laplace value calculated by the following equation:

$$\Delta p = \frac{2\sigma \cos \theta}{R_2} = 305 \text{ Pa}, \quad (14)$$

where σ is the surface tension ($\sigma = 0.045 \text{ N/m}$); θ is the contact angle ($\theta = 1^\circ$); and R is the radius of the curvature equal to half width of the channel ($R_2 = D_2/2 = 0.295 \text{ mm}$).

The 3D model takes into account the two radii of curvature. Hence, the pressure drop for this model is approximately twice the simulated value for the 2D model which is around 147 Pa (Figure 8). In the latest model, only one radius of curvature contributes to the pressure drop and the second radius is infinity.

To show the effect of the surface tension on the slug regime, we consider the extreme case where $\sigma = 0 \text{ N/m}$. Figure 9 illustrates the water volume fraction at two different instants simulated by the 2D model. Compared to the simulated case shown in Figure 7(e), the slug regime disappeared.

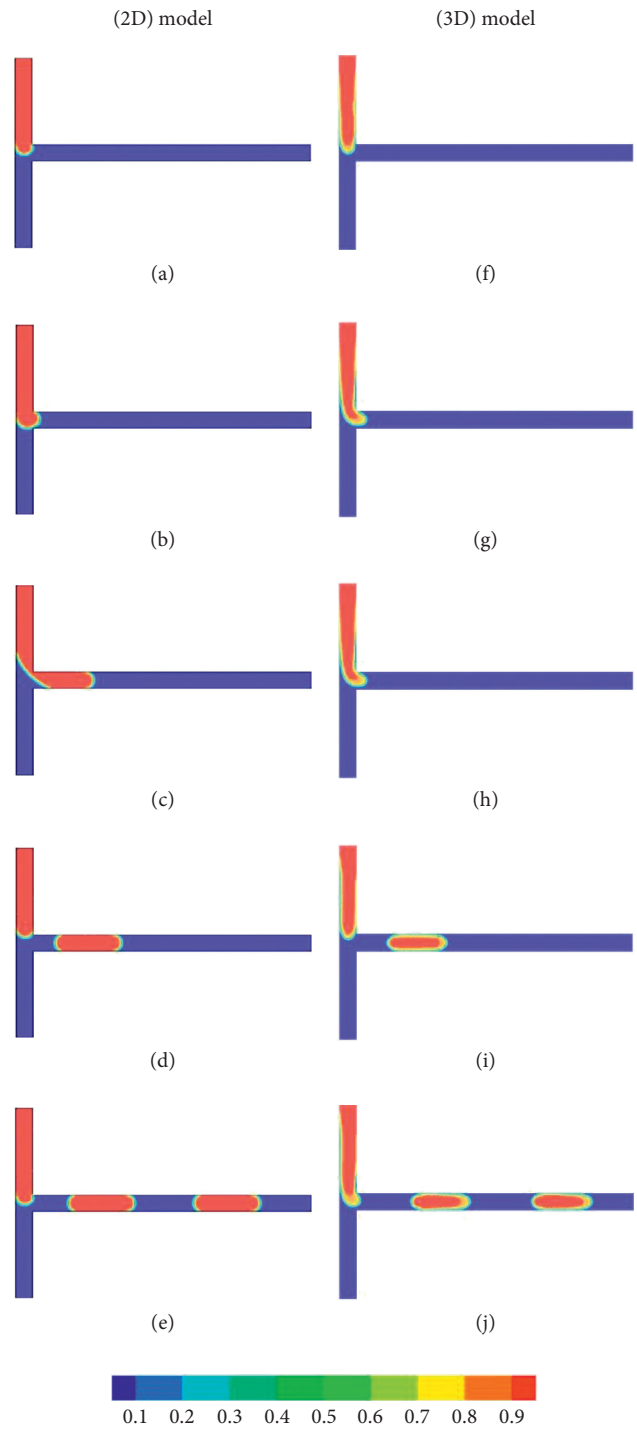


FIGURE 7: Water volume fraction simulated by 2D and 3D models at different times for the slug flow $\sigma=0.045$ N/m. (a) $t = 0.35$ s. (b) $t = 0.39$ s. (c) $t = 0.50$ s. (d) $t = 0.55$ s. (e) $t = 0.80$ s. (f) $t = 0.35$ s. (g) $t = 0.39$ s. (h) $t = 0.50$ s. (i) $t = 0.55$ s. (j) $t = 0.80$ s.

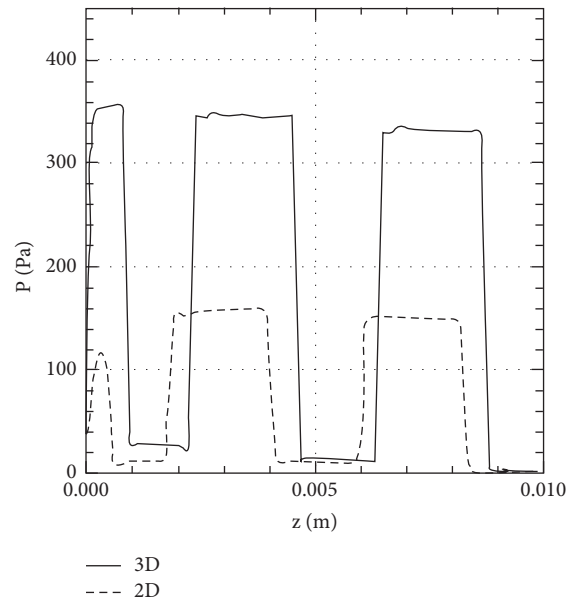


FIGURE 8: Pressure profile along the pipe length simulated by 2D and 3D models for the slug flow at $t = 0.8$ s.

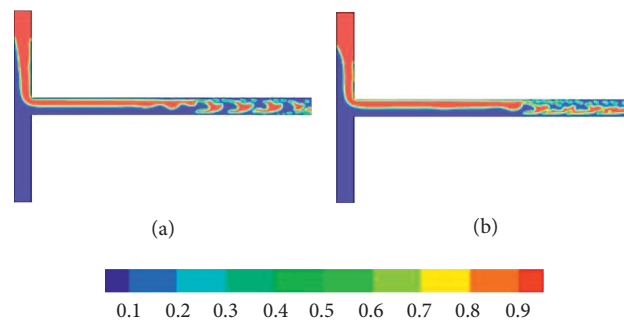


FIGURE 9: Water volume fraction simulated by 2D and 3D models at different times for the slug flow without surface tension. (a) $t = 0.80$ s. (b) $t = 1.19$ s.

5. Conclusions and Perspectives

The present two-phase flow model is based on RANS equations coupled with the VOF model and $k-\omega$ for turbulent flow. This model can predict the stratified flow characteristics by the 2D and 3D models. As expected, the surface tension has a crucial effect on the flow pattern. Without surface tension, the slug regime disappeared. The slug length obtained by the 2D model is slightly different from the 3D model; however, the thin film is not predicted by the 2D model.

As perspectives of this study, we can illustrate the following aspects:

- (1) Investigation of the slug flow for multiple ducts.
- (2) Development of a two-phase model taking into account the phase transfer.
- (3) The effect of other inlet configurations such as Y-junction can be tested.

- (4) The extension of this proposed model to study the effects of the air injection flow rate on the oil, water, and gas flow regimes and pressure drop through horizontal pipelines.
- (5) Analysis of the effect of the microchannel inclination on the flow regimes.

Data Availability

No data were used in this study.

Conflicts of Interest

The authors declare that they have no conflicts of interest.

Acknowledgments

The authors gratefully acknowledge Qassim University, represented by the Deanship of Scientific Research, for the

financial support (10133-cos-2020-1-3-I) during the academic year 1442 AH/2020 AD.

References

- [1] P. Desir, T.-Y. Chen, M. Bracconi, B. Saha, M. Maestri, and D. G. Vlachos, "Experiments and computations of microfluidic liquid-liquid flow patterns," *Reaction Chemistry and Engineering*, vol. 5, no. 1, pp. 39–50, 2020.
- [2] D. S. Santos, P. M. Faia, F. A. P. Garcia, and M. G. Rasteiro, "Oil/water stratified flow in a horizontal pipe: simulated and experimental studies using EIT," *Journal of Petroleum Science and Engineering*, vol. 174, pp. 1179–1193, 2019.
- [3] S. Ban, W. Pao, and M. S. Nasif, "Numerical simulation of two-phase flow regime in horizontal pipeline and its validation," *International Journal of Numerical Methods for Heat and Fluid Flow*, vol. 28, no. 6, pp. 1279–1314, 2018.
- [4] M. E. Charles, G. W. Govier, and G. W. Hodgson, "The horizontal pipeline flow of equal density oil-water mixtures," *Canadian Journal of Chemical Engineering*, vol. 39, no. 1, pp. 27–36, 1961.
- [5] P. Angeli and G. F. Hewitt, "Flow structure in horizontal oil-water flow," *International Journal of Multiphase Flow*, vol. 26, no. 7, pp. 1117–1140, 2000.
- [6] G. Elseth, *An experimental study of oil/water flow in horizontal pipes*, PhD thesis, Norwegian University of Science and Technology, Trondheim, Norway, 2001.
- [7] L. Arsenjuk, F. Kaske, J. Franzke, and D. W. Agar, "Experimental investigation of wall film renewal in liquid-liquid slug flow," *International Journal of Multiphase Flow*, vol. 85, pp. 177–185, 2016.
- [8] A. P. A. Kurban, *Stratified liquid-liquid flow*, PhD thesis, Imperial College of Science, London, UK, 1997.
- [9] S. Al-Jadidi, *Lubricated transport of heavy oil investigated by CFD*, PhD Thesis, University of Leicester, Leicester, UK, 2017.
- [10] F. T.-M. Carlos, *Modeling of oil-water in horizontal and near horizontal pipes*, PhD Thesis, University of Tulsa, Tulsa, OK, USA, 2006.
- [11] J. Shi, M. Gourma, and H. Yeung, "CFD simulation of horizontal oil-water flow with matched density and medium viscosity ratio in different flow regimes," *Journal of Petroleum Science and Engineering*, vol. 151, pp. 373–383, 2017.
- [12] Y. Zhao, G. Chen, and Q. Yuan, "Liquid-Liquid two-phase flow patterns in a rectangular microchannel," *American Institute of Chemical Engineers*, vol. 52, no. 12, pp. 4052–4060, 2006.
- [13] S. K. Senapati and S. K. Dewangan, "Comparison of performance of different multiphase models in predicting stratified flow," *Computational Thermal Sciences: International Journal*, vol. 9, no. 6, pp. 529–539, 2017.
- [14] M. A. Al-Yaari and B. F. Abu-Sharkh, "CFD prediction of stratified oil-water flow in a horizontal pipe," *Asian Transactions on Engineering*, vol. 1, no. 5, pp. 68–75, 2011.
- [15] M. N. Kashid and D. W. Agar, "Hydrodynamics of liquid-liquid slug flow capillary microreactor: flow regimes, slug size and pressure drop," *Chemical Engineering Journal*, vol. 131, no. 1–3, pp. 1–13, 2007.
- [16] A. B. Desamala, V. Vijayan, A. Dasari, A. K. Dasmahapatra, and T. K. Mandal, "Prediction of oil-water flow patterns, radial distribution of volume fraction, pressure and velocity during separated flows in horizontal pipe," *Journal of Hydrodynamics*, vol. 28, no. 4, pp. 658–668, 2016.
- [17] S. K. R. Cherlo, S. Kariveti, and S. Pushpavanam, "Experimental and numerical investigations of two-phase (Liquid–Liquid) flow behavior in rectangular microchannels," *Industrial & Engineering Chemistry Research*, vol. 49, no. 2, pp. 893–899, 2010.
- [18] D. C. Wilcox, "Formulation of the $k - \omega$ turbulence model revisited," *AIAA Journal*, vol. 46, no. 11, pp. 2823–2838, 2008.
- [19] J. U. Brackbill, D. B. Kothe, and C. Zemach, "A continuum method for modeling surface tension," *Journal of Computational Physics*, vol. 100, no. 2, pp. 335–354, 1992.
- [20] J. Shi, *A study on high-viscosity oil-water two-phase flow in horizontal pipes*, PhD thesis, Cranfield University, Bedford, UK, 2015.

Research Article

On Behavior of the Periodic Orbits of a Hamiltonian System of Bifurcation of Limit Cycles

Amor Menaceur,¹ Mohamed Abdalla ,^{2,3} Sahar Ahmed Idris ,^{4,5} and Ibrahim Mekawy⁶

¹Laboratory of Analysis and Control of Differential Equations “ACED”, Department of Mathematics, University of Guelma, P.O. Box 401, Guelma 24000, Algeria

²Department of Mathematics, College of Science, King Khalid University, P.O. Box 9004, 61413 Abha, Saudi Arabia

³Mathematics Department, Faculty of Science, South Valley University, Qena 83523, Egypt

⁴College of Industrial Engineering, King Khalid University, Abha, Saudi Arabia

⁵Department of Mathematics, Faculty of Science, Juba University-Khartoum, Juba, Sudan

⁶Department of Mathematics, College of Sciences and Arts, ArRas, Qassim University, Saudi Arabia

Correspondence should be addressed to Sahar Ahmed Idris; sa6044690@gmail.com

Received 28 August 2021; Accepted 15 September 2021; Published 30 September 2021

Academic Editor: Sundarapandian Vaidyanathan

Copyright © 2021 Amor Menaceur et al. This is an open access article distributed under the Creative Commons Attribution License, which permits unrestricted use, distribution, and reproduction in any medium, provided the original work is properly cited.

In light of the previous recent studies by Jaume Llibre et al. that dealt with the finite cycles of generalized differential Kukles polynomial systems using the first- and second-order mean theorem such as (Nonlinear Anal., 74, 1261–1271, 2011) and (J. Dyn. Control Syst., vol. 21, 189–192, 2015), in this work, we provide upper bounds for the maximum number of limit cycles bifurcating from the periodic orbits of Hamiltonian system using the averaging theory of first order.

1. Introduction

Among the many interesting problems in the qualitative theory of planar polynomial differential systems is the study of their limit cycles (see [1, 2]). In particular, concerning Kukles differential system of the form,

$$\begin{cases} \dot{x} = -y, \\ \dot{y} = f(x, y), \end{cases} \quad (1)$$

has a long history, where $f(x, y)$ is a polynomial with real coefficients of degree n . Since it was first introduced in Kukles 1944, many researchers have concentrated on its maximum number of limit cycles and their location. See, for example, [3–5].

In [6], Llibre and Mereu studied the maximum number of limit cycles using the averaging theory as follows:

$$\begin{cases} \dot{x} = y, \\ \dot{y} = -x - \sum_{k \geq 1} \varepsilon^k (f_k(x) + g_k(x)y + h_k(x)y^2 + d_k y^3), \end{cases} \quad (2)$$

where, for every k , the polynomials $f_k(x)$, $g_k(x)$, and $h_k(x)$ have degree n_1, n_2 , and n_3 , respectively. $d_0^k \neq 0$ is a real number and ε is a small parameter.

Also, Makhoul and Menaceur [7] studied the maximum number for the more generalized polynomial Kukles differential systems in the form

$$\begin{cases} \dot{x} = y, \\ \dot{y} = -x - \sum_{k \geq 1} \varepsilon^k (f_k(x) + g_k(x)y + h_k(x)y^2 + g_k(x)y^3). \end{cases} \quad (3)$$

The number of limit cycles bifurcating from the center $\dot{x} = -y^{2p-1}$ and $\dot{y} = x^{2q-1}$, where p, q are positive integers, for the following two kinds of polynomial differential systems,

$$\begin{cases} \dot{x} = -y^{2p-1}, \\ \dot{y} = x^{2q-1} - \varepsilon f(x)y^{2n-1}, \\ \dot{x} = -y^{2p-1} - \varepsilon pxf(x, y), \\ \dot{y} = x^{2q-1} - \varepsilon qyf(x, y), \end{cases} \quad (4)$$

were investigated in the works [8, 9], respectively. In the current study, we discuss the maximum number of limit cycles of the following differential system:

$$\begin{cases} \dot{x} = -y^{2p-1}, \\ \dot{y} = x^{2q-1} - \varepsilon(f(x) + g(x)y^{2n-1} + h(x)y^{2n} + l(x)y^{2n+1}), \end{cases} \quad (5)$$

where p, q , and n are positive integers, the polynomials $f(x), g(x), h(x)$, and $l(x)$ have degree n_1, n_2, n_3 , and n_4 , respectively, and ε is a small positive parameter. Clearly, system (5) with $\varepsilon = 0$ is an Hamiltonian system with

$$H(x, y) = \frac{1}{2q}x^{2q} + \frac{1}{2p}y^{2p}. \quad (6)$$

Our main theorems are given as follows.

Theorem 1. For the sufficiently small $|\varepsilon|$, system (5), using averaging theory of first order, has at most

$$\max\left\{\left[\frac{n_2}{2}\right]p, \left[\frac{n_4}{2}\right]p + q\right\}, \quad (7)$$

The limit cycles bifurcating from the periodic orbits of the center are $\dot{x} = -y^{2p-1}$ and $\dot{y} = x^{2q-1}$, where $[\cdot]$ denotes the integer part function.

The proof of Theorem 1 is given in Section 3.

Theorem 2. Consider system (5) with $q = lp$, l is a positive integer, and $|\varepsilon|$ sufficiently small; let $H(n_i, l)$ denote the maximum number of limit cycles of the polynomial differential system (5) bifurcating from the periodic orbits of the center $\dot{x} = -y^{2p-1}$ and $\dot{y} = x^{2l p-1}$ using the averaging theory of first order; then,

$$\begin{aligned} (a) \quad & H(n_i, l) = \left[\frac{n_2}{2}\right] + \left[\frac{n_4}{2}\right] + 1, \quad \text{if } \left[\frac{n_2}{2}\right] < l, \\ (b) \quad & H(n_i, l) = \left[\frac{n_4}{2}\right] + l + 1, \quad \text{if } l \leq \left[\frac{n_2}{2}\right] \leq l + \left[\frac{n_4}{2}\right], \\ (c) \quad & H(n_i, l) = \left[\frac{n_2}{2}\right], \quad \text{if } l + \left[\frac{n_4}{2}\right] < \left[\frac{n_2}{2}\right]. \end{aligned} \quad (8)$$

The proof of Theorem 2 is given Section 4.

2. First-Order Averaging Method

The averaging theory is an interesting method to research the limit cycles. Here, some specific function, associated to the initial system, is stated.

Theorem 3. The two initial value problems are as follows:

$$\dot{x} = \varepsilon R(t, x) + \varepsilon^2 G(t, x, \varepsilon), \quad x(0) = x_0, \quad (9)$$

$$\dot{y} = \varepsilon f^0(y), \quad y(0) = x_0, \quad (10)$$

where x, y and $x_0 \in D$ which is an open domain of \mathbb{R} , $t \in [0, \infty)$, $\varepsilon \in (0, \varepsilon_0]$, R and G are periodic functions with their period T with its variable t , and $f^0(y)$ is the average function of $R(t, y)$ with respect to t , i.e.,

$$f^0(y) = \frac{1}{T} \int_0^T R(t, y) dt. \quad (11)$$

Assume that

- (i) $R, \partial R/\partial x, \partial^2 R/\partial x^2, G$, and $\partial G/\partial x$ are well defined, continuous, and bounded by a constant independent by $\varepsilon \in (0, \varepsilon_0]$ in $[0, \infty) \times D$.
- (ii) T is a constant independent of ε .
- (iii) $y(t)$ belongs to D on the time scale $1/\varepsilon$. Then, the following statements hold:

- (i) On the time scale $1/\varepsilon$, we have

$$x(t) - y(t) = O(\varepsilon), \text{ as } \varepsilon \rightarrow 0. \quad (12)$$

- (ii) If p is an equilibrium point of the averaged system (10), such that

$$\frac{\partial f^0}{\partial y} \Big|_{y=p} \neq 0, \quad (13)$$

then system (9) has a T -periodic solution $\phi(t, \varepsilon) \rightarrow p$ as $\varepsilon \rightarrow 0$.

- (iii) If (11) is a negative, therefore, the corresponding periodic solution $\phi(t, \varepsilon)$ of equation (9) according to (t, x) is asymptotically stable, for all ε sufficiently small; if (11) is a positive, then it is unstable.

For more information about the averaging theory, see [10–12].

3. Proof of Theorem 1

Here, we need to transform system (5) to the canonical form (9). Doing the change of (p, q) -polar coordinates $x = r^p C s \theta$ and $y = r^q S n \theta$ (see Appendix) and taking θ as an independent variable, then system (5) can be written as

$$\begin{cases} \dot{r} = -\varepsilon r^{-q+1} (Sn\theta)^{2p-1} \begin{bmatrix} f(r^p Cs\theta) + g(r^p Cs\theta) (Sn\theta)^{2n-1} r^{q(2n-1)} \\ +h(r^p Cs\theta) (Sn\theta)^{2n} \\ r^{2qn} + l(r^p Cs\theta) (Sn\theta)^{2n+1} r^{q(2n+1)} \end{bmatrix}, \\ \dot{\theta} = r^{pq-p-q} - \varepsilon pr^{-q} Cs\theta \begin{bmatrix} f(r^p Cs\theta) + g(r^p Cs\theta) (Sn\theta)^{2n-1} r^{q(2n-1)} \\ +h(r^p Cs\theta) (Sn\theta)^{2n} r^{2qn} \\ +l(r^p Cs\theta) (Sn\theta)^{2n+1} r^{q(2n+1)} \end{bmatrix}. \end{cases} \quad (14)$$

If we write

then system (14) becomes

$$\begin{aligned} f(x) &= \sum_{k=0}^{n_1} a_k x^k, \\ g(x) &= \sum_{k=0}^{n_2} b_k x^k, \\ h(x) &= \sum_{k=0}^{n_3} c_k x^k, \\ l(x) &= \sum_{k=0}^{n_4} d_k x^k, \end{aligned} \quad (15)$$

$$\begin{cases} \dot{r} = -\varepsilon r^{-q+1} \left[\sum_{k=0}^{n_1} a_k (Cs\theta)^k (Sn\theta)^{2p-1} r^{pk} + \sum_{k=0}^{n_2} b_k (Cs\theta)^k (Sn\theta)^{2(p+n-1)} r^{pk+q(2n-1)} \right. \\ \left. + \sum_{k=0}^{n_3} c_k (Cs\theta)^k (Sn\theta)^{2(p+n)-1} r^{pk+2qn} + \sum_{k=0}^{n_4} d_k (Cs\theta)^k (Sn\theta)^{2(p+n)} r^{pk+q(2n+1)} \right], \\ \dot{\theta} = r^{pq-p-q} - \varepsilon pr^{-q} \left[\sum_{k=0}^{n_1} a_k (Cs\theta)^{k+1} r^{pk} + \sum_{k=0}^{n_2} b_k (Cs\theta)^{k+1} (Sn\theta)^{2n-1} r^{pk+q(2n-1)} \right. \\ \left. + \sum_{k=0}^{n_3} c_k (Cs\theta)^{k+1} (Sn\theta)^{2n} r^{pk+2qn} + \sum_{k=0}^{n_4} d_k (Cs\theta)^{k+1} (Sn\theta)^{2n+1} r^{pk+q(2n+1)} \right]. \end{cases} \quad (16)$$

where θ is the independent variable we get from system (16).
From

$$\frac{dr}{d\theta} = \varepsilon R(r, \theta) + O(\varepsilon^2), \quad (17)$$

where

$$R(r, \theta) = -r^{-pq+p+1} \left[\sum_{k=0}^{n_1} a_k (Cs\theta)^k (Sn\theta)^{2p-1} r^{pk} + \sum_{k=0}^{n_2} b_k (Cs\theta)^k (Sn\theta)^{2(p+n-1)} r^{pk+q(2n-1)} \right. \\ \left. + \sum_{k=0}^{n_3} c_k (Cs\theta)^k (Sn\theta)^{2(p+n)-1} r^{pk+2qn} + \sum_{k=0}^{n_4} d_k (Cs\theta)^k (Sn\theta)^{2(p+n)} r^{pk+q(2n+1)} \right]. \quad (18)$$

According to the notation introduced in Section 2, we have

$$f^0(r) = \frac{r^{-pq+p+1}}{T} \left[\begin{aligned} & \sum_{k=0}^{n_1} a_k r^{pk} \int_0^T (Cs\theta)^k (Sn\theta)^{2p-1} d\theta \\ & + \sum_{k=0}^{n_2} b_k r^{pk+q(2n-1)} \int_0^T (Cs\theta)^k (Sn\theta)^{2(p+n-1)} d\theta \\ & + \sum_{k=0}^{n_3} c_k r^{pk+2qn} \int_0^T (Cs\theta)^k (Sn\theta)^{2(p+n)-1} d\theta \\ & + \sum_{k=0}^{n_4} d_k r^{pk+q(2n+1)} \int_0^T (Cs\theta)^k (Sn\theta)^{2(p+n)} d\theta \end{aligned} \right], \tag{19}$$

and we write

$$f^0(r) = \frac{r^{-pq+p+1}}{T} \left[\begin{aligned} & \sum_{k=0}^{n_1} a_k I_{k,2p-1} r^{pk} + \sum_{k=0}^{n_2} b_k I_{k,2(p+n-1)} r^{pk+q(2n-1)} \\ & + \sum_{k=0}^{n_3} c_k I_{k,2(p+n)-1} r^{pk+2qn} + \sum_{k=0}^{n_4} d_k I_{k,2(p+n)} r^{pk+q(2n+1)} \end{aligned} \right], \tag{20}$$

where

$$I_{i,j} = \int_0^T Cs^i \theta Sn^j \theta d\theta. \tag{21}$$

It is known that

$$\begin{aligned} I_{i,j} &= 0, \text{ if } i \text{ or } j \text{ is odd,} \\ I_{i,j} &> 0, \text{ if } i \text{ and } j \text{ are even.} \end{aligned} \tag{22}$$

Hence,

$$f^0(r) = \frac{r^{q(2n-p-1)+p+1}}{T} \left[\sum_{\substack{k=0 \\ k \text{ even}}}^{n_2} n_2 b_k I_{k,2(p+n-1)} r^{pk} + \sum_{\substack{k=0 \\ k \text{ even}}}^{n_4} n_4 d_k I_{k,2(p+n)} r^{pk+2q} \right], \tag{23}$$

we obtain

$$f^0(r) = \frac{r^{q(2n-p-1)+p+1}}{T} \left[\sum_{s=0}^{\lfloor n_2/2 \rfloor} b_{2s} I_{2s,2(p+n-1)} r^{2ps} + \sum_{s=0}^{\lfloor n_4/2 \rfloor} d_{2s} I_{2s,2(p+n)} r^{2(ps+q)} \right]. \tag{24}$$

For the simplicity of calculation, let $B_s = b_{2s} I_{2s,2(p+n-1)}$ and $D_s = d_{2s} I_{2s,2(p+n)}$; therefore, (24) can be reduced to

$$f^0(r) = \frac{r^{q(2n-p-1)+p+1}}{T} \left[\sum_{s=0}^{\lfloor n_2/2 \rfloor} B_s r^{2ps} + \sum_{s=0}^{\lfloor n_4/2 \rfloor} D_s r^{2(ps+q)} \right]. \tag{25}$$

As we all know, the number of positive roots of $f^0(r)$ is equal to that of

$$N(r) = \sum_{s=0}^{\lfloor n_2/2 \rfloor} B_s r^{2ps} + \sum_{s=0}^{\lfloor n_4/2 \rfloor} D_s r^{2(ps+q)}. \tag{26}$$

Then, to find the real positive roots of $N(r)$, we must find the zeros of a polynomial in the variable $\rho = r^2$:

$$M(\rho) = \sum_{s=0}^{\lfloor n_2/2 \rfloor} B_s \rho^{ps} + \sum_{s=0}^{\lfloor n_4/2 \rfloor} D_s \rho^{ps+q}. \tag{27}$$

So, the degree of $M(\rho)$ is bounded by $\mu = \max\{\lfloor n_2/2 \rfloor p, \lfloor n_4/2 \rfloor p + q\}$, we conclude that $f^0(r)$ has at most μ positive root r . Hence, Theorem 1 is proved.

4. Proof of Theorem 2

Consider the polynomial differential system (5) with $q = lp$; from equation (25) we obtain

$$f^0(r) = -\frac{r^{lp(2n-p-1)+p+1}}{T} \left[\sum_{s=0}^{[n_2/2]} B_s r^{2ps} + \sum_{s=0}^{[n_4/2]} D_s r^{2p(s+l)} \right]. \quad (28)$$

As we all know, the number of positive roots of $f^0(r)$ is equal to that of

$$G(r) = B_0 + B_1 r^{2p} + B_2 r^{4p} + \dots + B_{[n_2/2]} r^{2p[n_2/2]} + D_0 r^{2pl} + D_1 r^{2p(l+1)} + D_2 r^{2p(l+2)} + \dots + D_{[n_4/2]} r^{2p(l+[n_4/2])}. \quad (29)$$

To find the number of positive roots of polynomials $G(r)$, we distinguish 3 cases.

$$f^0(r) = -\frac{r^{6n-4}}{T} (B_0 + B_1 r^2 + B_2 r^4 + D_0 r^6 + D_1 r^8 + D_2 r^{10}), \quad (33)$$

where $B_s = b_{2s} I_{2s,2}$ and $D_s = d_{2s} I_{2s,4}$. Using (A.3) of the Appendix, we obtain

$$\begin{aligned} I_{0,2} &= 2.1033, \\ I_{2,2} &= 0.60460, \\ I_{4,2} &= 0.32339, \\ I_{0,4} &= 0.63098, \\ I_{2,4} &= 0.15115, \\ I_{4,4} &= 6.9298 \times 10^{-2}. \end{aligned} \quad (34)$$

Case 1. For $[n_2/2] < l$, the number terms in polynomial (29) is $[n_2/2] + [n_4/2] + 2$. Now, we shall apply the Descartes theorem of the Appendix, we can choose the appropriate coefficients B_i and D_j so that the simple positive roots' number of $G(r)$ is at most $[n_2/2] + [n_4/2] + 1$. Hence, (a) of Theorem 2 is proved.

Case 2. For $l \leq [n_2/2] \leq l + [n_4/2]$, the number terms in polynomial (29) is

$$\left[\frac{n_2}{2} \right] + \left[\frac{n_4}{2} \right] + 2 - \left(\left[\frac{n_2}{2} \right] - l + 1 \right) = \left[\frac{n_4}{2} \right] + l + 1. \quad (30)$$

By Descartes Theorem, we can choose the appropriate coefficients B_i and D_j so that the simple positive roots' number of $G(r)$ is at most $[n_4/2] + l$. Hence, (b) of Theorem 2 is proved.

Case 3. For $l + [n_4/2] < [n_2/2]$, the number terms in polynomial (29) is $[n_2/2] + 1$; by Descartes Theorem, we can choose the appropriate coefficients B_i and D_j so that the simple positive roots number of $G(r)$ is at most $[n_2/2]$. Hence, (c) of Theorem 2 is proved.

Example 1. We consider system (5), with $p = 1, q = 3, n = 1$, and

$$\begin{aligned} f(x) &= \sum_{k=0}^2 a_k x^k, \\ g(x) &= \sum_{k=0}^4 b_k x^k, \\ h(x) &= \sum_{k=0}^2 c_k x^k, \\ l(x) &= \sum_{k=0}^4 d_k x^k, \end{aligned} \quad (31)$$

where

$$\begin{aligned} a_0 &= 1, \\ a_1 &= 2.3, \\ a_2 &= 4.7, \\ b_0 &= -0.5, \\ b_1 &= 1.1, \\ b_2 &= 6.3, \\ b_3 &= 2.5, \\ b_4 &= -15.32, \\ c_0 &= 2.2, \\ c_1 &= -6.4, \\ c_2 &= 7.3, \\ d_0 &= 4.65, \\ d_1 &= 3.4, \\ d_2 &= -5.24, \\ d_3 &= 6.4, \\ d_4 &= 1.13. \end{aligned} \quad (32)$$

In this case, $Cs\theta$ and $Sn\theta$ are T-periodic function with period $T = 8.4131$. From equation (28), we obtain

So,

$$f^0(r) = -\frac{r^2}{T} \left[\begin{array}{c} -1.0517 + 3.8083r^2 - 4.9553r^4 \\ +2.9320r^6 - 0.79257r^8 + 7.8473 \times 10^{-2}r^{10} \end{array} \right]. \quad (35)$$

This polynomial has four positive real roots: $r_1 = 0.6, r_2 = 0.8, r_3 = 1.1, r_4 = 1.3$, and $r_5 = 2$. According to statement (a) of Theorem 2, the system has exactly 5 limit cycles bifurcating from the periodic orbits of the center $\dot{x} = -y$ and $\dot{y} = x^5$, using the averaging theory of first order.

5. Conclusion

In this work, by using averaging theory of the first order, we have proved upper bounds for the maximum number of limit cycles bifurcating from the periodic orbits of the Hamiltonian system. In addition, in the next work, a new

condition with a new method will be used to prove our main result in this study.

Appendix

1- p, q)-Polar Coordinates

Following Lyapunov [13], we introduce the (p, q) -trigonometric functions $u(\theta) = Cs\theta$ and $v(\theta) = Sn\theta$ as the solution of the following initial value problem:

$$\begin{aligned} \dot{u} &= -v^{2p-1}, \\ \dot{v} &= u^{2q-1}, \\ u(0) &= \sqrt[2q]{\frac{1}{p}}, \\ v(0) &= 0. \end{aligned} \quad (\text{A.1})$$

Moreover, they satisfy the following properties:

(i) The functions $Cs\theta$ and $Sn\theta$ are T -periodic with

$$T = 2p^{-1/2q} q^{-1/2p} \frac{\Gamma(1/2p)\Gamma(1/2q)}{\Gamma((1/2p) + (1/2q))}, \quad (\text{A.2})$$

where Γ is the gamma function.

(ii) For $p = q = 1$, we have $Cs\theta = \cos \theta$ and $Sn\theta = \sin \theta$.

(iii) $pCs^{2p}\theta + qSn^{2q}\theta = 1$.

(iv) Let $Cs\theta$ and $Sn\theta$ be the $(1, q)$ -trigonometrical functions, for i and j are both even (see [1]):

$$I_{i,j} = \int_0^T Cs^i \theta Sn^j \theta d\theta = 2q^{-(j+1/2)} \frac{\Gamma(i + 1/2q)\Gamma(j + 1/2)}{\Gamma((i + 1/2q) + (j + 1/2))}. \quad (\text{A.3})$$

2-Descartes Theorem

The purpose of the Descartes theorem is to provide an insight on how many real roots a polynomial $P(x)$ may have.

Theorem A.1 (see [14]). *Consider the real polynomial*

$$p(x) = a_{l_1}x_{l_1} + a_{l_2}x_{l_2} + \dots + a_{l_k}x_{l_k}, \quad (\text{A.4})$$

with $0 \leq l_1 < l_2 < \dots < l_k$ and $a_{l_i} \neq 0$ real constants, for $i \in \{1, 2, 3, \dots, k\}$. When $a_{l_i}a_{l_{i+1}} < 0$, we say that a_{l_i} and $a_{l_{i+1}}$ have a variation of sign. If the number of variations of signs is n , then $p(x)$ has at most n positive real roots. Moreover, it is always possible to choose the coefficients of $p(x)$ in such a way that $p(x)$ has exactly $k - 1$ positive real roots.

Data Availability

No data were used to support the study.

Conflicts of Interest

The authors declare that they have no conflicts of interest.

Acknowledgments

The third author extends appreciation to the Deanship of Scientific Research at King Khalid University for funding this work through Research Group Project, under Grant no. R.G.P-2/53/42.

References

- [1] A. Gasull and J. Torregrosa, "A new algorithm for the computation of the Lyapunov constants for some degenerated critical points," *Nonlinear Analysis: Theory, Methods & Applications*, vol. 47, no. 7, pp. 4479–4490, 2001.
- [2] D. Hilbert, "Mathematische problems. lecture in: second international congress of mathematicians-Paris, France Nachrichten von der gesellschaft der wissenschaften zu göttingen, mathematisch-physikalische klasse," *English Translation*, vol. 5, pp. 253–297, 1900.
- [3] J. Chavarriga, I. A. García, E. Szántó, and I. Szant o., "Limit cycles in Kukles systems of arbitrary degree with invariant ellipse," *Nonlinear Analysis: Theory, Methods & Applications*, vol. 67, no. 4, pp. 1005–1014, 2007.
- [4] J. M. Hill, N. G. Lloyd, and J. M. Pearson, "Centres and limit cycles for an extended Kukles system," *The Electronic Journal of Differential Equations*, vol. 119, pp. 1–23, 2007.
- [5] A. Menaceur, S. Boulaaras, S. Alkhalaf, and S. Jain, "Limit cycles of a class of polynomial differential systems bifurcating from the periodic orbits of a linear center," *Symmetry*, vol. 12, no. 8, p. 15, 2020.
- [6] J. Llibre and A. C. Mereu, "Limit cycles for generalized Kukles polynomial differential systems," *Nonlinear Analysis: Theory, Methods & Applications*, vol. 74, no. 4, pp. 1261–1271, 2011.
- [7] A. Makhlof and A. Menaceur, "On the limit cycles of a class of generalized Kukles polynomial differential systems via averaging theory," *International Journal of Differential Equations*, vol. 2015, Article ID 325102, 10 pages, 2015.
- [8] J. Llibre and A. Makhlof, "Limit cycles of a class of generalized liénard polynomial equations," *Journal of Dynamical and Control Systems*, vol. 21, no. 2, pp. 189–192, 2015.
- [9] A. Menaceur, S. Boulaaras, A. Makhlof, K. Rajagobal, and M. Abdalla, "Limit cycles of a class of perturbed differential systems via the first-order averaging method," *Complexity*, vol. 2021, Article ID 5581423, 6 pages, 2021.
- [10] A. Buică and J. Llibre, "Averaging methods for finding periodic orbits vai Brouwer degree," *Bulletin des Sciences Mathematiques*, vol. 128, pp. 7–22, 2004.
- [11] J. A. Sanders and F. Verhulst, "Averaging methods in nonlinear dynamical systems," *Applied Mathematical Science*, Vol. 59, Springer-Verlag, New York, NY, USA, 1985.
- [12] F. Verhulst, *Nonlinear Differential Equations and Dynamical Systems*. Universitex, Springer-Verlag, Berlin, 1996.
- [13] A. M. Liapunov, "Stability of motion. with a contribution by V. A. Pliss and an introduction by V. P. Basov," *Mathematics in Science and Engineering*, Vol. 30, Academic Press, New York, London, 1966.
- [14] I. S. Berezin and N. P. Zhidkov, *Computing Methods*, Pergamon, Oxford, UK, 1964.

Research Article

A Note on Small Amplitude Limit Cycles of Liénard Equations Theory

Yassine Bouattia,¹ Djalil Boudjehem ,² Ammar Makhlof,³ Sulima Ahmed Zubair ,⁴
and Sahar Ahmed Idris ⁵

¹Department of Mathematics, College of Sciences, Université 8 Mai 1945 Guelma, Box 401, Guelma 24000, Algeria

²Department of Electronics and Telecommunication, College of Sciences and Technology, University of Guelma, 8 Mai 1945Box 401, Guelma 24000, Algeria

³Department of Mathematics, College of Sciences, Annaba University, Annaba 23000, Algeria

⁴Department of Mathematics, College of Sciences and Arts, ArRass, Qassim University, Buraydah, Saudi Arabia

⁵College of Industrial Engineering, King Khalid University, Abha, Saudi Arabia

Correspondence should be addressed to Sulima Ahmed Zubair; sulimaa2021@gmail.com

Received 3 August 2021; Accepted 13 September 2021; Published 29 September 2021

Academic Editor: Sundarapandian Vaidyanathan

Copyright © 2021 Yassine Bouattia et al. This is an open access article distributed under the Creative Commons Attribution License, which permits unrestricted use, distribution, and reproduction in any medium, provided the original work is properly cited.

In this paper, we demonstrate using a counterexample for a theorem of the small amplitude limit cycles in some Liénard systems and show that there will be no solutions unless we add an extra condition. A new condition is derived for some specific Liénard systems where a violation of the small amplitude limit cycles theorem takes place.

1. Introduction

A lot of previous works consider studies on a limit cycles' existence for Liénard systems [1–3]. It represents a very important class of nonlinear systems due to its appearance in some branches of science and engineering as well as in some ecological models, planar physical models, and even in some chemical models, where using a suitable transformation can change these systems into nonlinear Liénard systems. However, an extensive attention has been also devoted to the question of its uniqueness [4–6]; this uniqueness can be verified using different ways of methods based on Poincaré–Bendixson theorem. In [4], Zhou *et al.* proposed a set of theorems for the limit cycles' uniqueness for the Liénard systems; the proposed theorems represent a guarantee to complete the proof of some previous works' propositions. In [7], Sabatini and Gabriele studied the uniqueness of limit cycles for a class of planar dynamical systems taking into account those which are equivalent to Liénard systems, and they have also proved a theorem for limit cycles of a class of plane differential systems. In the paper proposed by Li and

Llibre [8], the authors proved that for any classical Liénard differential equation of degree four, there exists at most one hyperbolic limit cycle. In [9], a sufficient condition for the existence and the uniqueness of limit cycles for Liénard systems has been proposed for some applications.

In the theory of small amplitude limit cycles, Liénard systems have n solutions, However, in this paper, we use a counterexample to demonstrate that the existence of n solutions for some systems is not true unless we add an extra new condition.

We consider in our study the systems given by the following form:

$$\begin{cases} \dot{x} = y - F(x), \\ \dot{y} = -g(x), \end{cases} \quad (1)$$

where F and g are polynomials of order n of x and y . For several classes of such systems and in cases where the critical point is under perturbation of the coefficients in F and g , the maximum number of limit cycles that can bifurcate out can be formulated in terms of the degree of F and g [10–12].

2. Bendixon Criterion

We consider the following autonomous system:

$$\begin{cases} \dot{x} = P(x, y), \\ \dot{y} = Q(x, y). \end{cases} \quad (2)$$

Let $X = (P, Q)$ be the vector field and $\text{div } X = \partial P/\partial x + \partial Q/\partial y$.

Theorem 1. *Let D be a simply connected open subset of \mathbb{R}^2 . If $\text{div } X = \partial P/\partial x + \partial Q/\partial y$ is of constant sign and not identically zero in D , then the system defined by 2 has no periodic orbit lying entirely in the region D .*

Proof. If γ is a periodic orbit in D , then $\int_{\gamma} P(x, y)dy - Q(x, y)dx = 0$ on γ . Since the interior U of γ is simply connected, we can apply Green's theorem to obtain the following:

$$0 = \oint_{\gamma} (P(x, y)dy - Q(x, y)dx) = \iint_U \left(\frac{\partial P}{\partial x}(x, y) + \frac{\partial Q}{\partial y}(x, y) \right) dx dy. \quad (3)$$

This is a contradiction since our hypothesis implies that the integral on the right cannot be zero. \square

Proof. If we suppose that the system given by 2 has a periodic solution of a period T , then it has a closed orbit Γ in D . Let G be the interior of Γ , we can apply Green's theorem to obtain the following:

$$\begin{aligned} I &= \iint_G \left(\frac{\partial P}{\partial x}(x, y) + \frac{\partial Q}{\partial y}(x, y) \right) dx dy \\ &= \oint_{\Gamma} P(x, y)dy - Q(x, y)dx, \\ &= \int_0^T \left(P(x(t), y(t)) \frac{dy}{dt} - Q(x(t), y(t)) \frac{dx}{dt} \right) dt \quad (4) \\ &= \int_0^T (P(x(t), y(t))Q(x(t), y(t)) \\ &\quad - Q(x(t), y(t))P(x(t), y(t))) dt = 0. \end{aligned}$$

Since $\text{div } X$ is either >0 or <0 , then $\iint_G \text{div } X \, dx dy$ will not be zero; therefore, there are no periodic solutions. \square

3. A Note on Liénard Equations Theory

We consider the following system:

$$\begin{cases} \dot{x} = (y + c_2 y^2 + \dots + c_L y^L) - (a_1 x + a_3 x^3 + \dots + a_{2n+1} x^{2n+1}), \\ \dot{y} = -(x + b_2 x^2 + \dots + b_N x^N), \end{cases} \quad (5)$$

where $c_2, c_3, \dots, c_L, a_1, a_3, \dots, a_{2n+1}, b_2, b_3, \dots$ and b_N are real coefficients.

Theorem 2 (see [1]). *For the system of form (2), there are at most n small-amplitudes limit cycles. If $a_1, a_3, \dots, a_{2n+1}$ are so chosen that*

$$\begin{aligned} |a_1| &\ll |a_3| \ll \dots \ll |a_{2n+1}|, \\ a_{2j-1} a_{2j+1} &< 0 \quad (j = 1, \dots, n), \end{aligned} \quad (6)$$

then there are exactly n small-amplitudes limit cycles.

Proof. (counterexample).

We suppose the following system:

$$\begin{cases} \dot{x} = X = \phi(y) - F(x), \\ \dot{y} = Y = -g(x), \end{cases} \quad (7)$$

where

$$\begin{aligned} F(x) &= \sum_{j=0}^n \frac{(-1)^j}{(2j+1)10^{10(n-j)}} x^{2j+1}, \quad n = 2m, \\ g(x) &= x + b_2 x^2 + \dots + b_N x^N, \end{aligned} \quad (8)$$

$$\phi(y) = y + c_2 y^2 + \dots + c_L y^L.$$

By putting $a_{2j+1} = (-1)^j / (2j+1)10^{10(n-j)}$, we obtain

$$\left| \frac{a_{2j-1}}{a_{2j+1}} \right| = \frac{1/(2j-1)10^{10(n-j+1)}}{1/(2j+1)10^{10(n-j)}} = \frac{2j+1}{2j-1} 10^{-10}. \quad (9)$$

As

$$\left| \frac{a_{2j-1}}{a_{2j+1}} \right| = \frac{2j+1}{2j-1} 10^{-10} \leq 3 \times 10^{-10} \ll 1, \quad \text{for } j = 1, \dots, n, \quad (10)$$

then

$$\begin{aligned} |a_1| &\ll |a_3| \ll \dots \ll |a_{2n+1}|, \\ a_{2j-1} a_{2j+1} &< 0, \quad \text{for } j = 1, \dots, n. \end{aligned} \quad (11)$$

However,

$$\begin{aligned} \text{div}(X, Y) &= \frac{\partial(\phi(y) - \sum_{j=0}^n a_{2j+1} x^{2j+1})}{\partial x} + \frac{\partial(-g(x))}{\partial y}, \\ &= - \sum_{j=0}^n \frac{(-1)^j}{10^{10(n-j)}} x^{2j} \\ &= - \prod_{j=0}^{n/2-1} \left(\left(x^2 - \frac{1}{10^{10}} \cos \frac{2j+1}{n+1} \pi \right)^2 + \frac{1}{10^{20}} \sin^2 \frac{2j+1}{n+1} \pi \right) < 0, \end{aligned} \quad (12)$$

because

$$\begin{aligned}
 f(x) &= \sum_{j=0}^n \frac{(-1)^j}{10^{10(n-j)}} x^{2j}, \\
 &= \prod_{j=0}^{n/2-1} (x - 10^{-5} e^{i(2j+1)\pi/2n+2})(x - 10^{-5} e^{-i(2j+1)\pi/2n+2})(x + 10^{-5} e^{i(2j+1)\pi/2n+2})(x + 10^{-5} e^{-i(2j+1)\pi/2n+2}) \quad (13) \\
 &= \prod_{j=0}^{n/2-1} \left(\left(x^2 - \frac{1}{10^{10}} \cos \frac{2j+1}{n+1} \pi \right)^2 + \frac{1}{10^{20}} \sin^2 \frac{2j+1}{n+1} \pi \right).
 \end{aligned}$$

□

Theorem 3 (see [2]). *We consider the following equation:*

$$\dot{r} = r(v_0 + v_1 r^2 + v_2 r^4 + \dots + v_n r^{2n}). \quad (14)$$

If the focus values v_j given in equation (3) satisfy the following conditions:

$$v_j v_{j+1} < 0, \text{ and } |v_j| \ll |v_{j+1}| \ll 1, \text{ for } j = 0, 1, 2, \dots, n-1, \quad (15)$$

then the polynomial equation given by $\dot{r} = 0$ in equation (3) has n positive real roots for r^2 .

Proof. (counterexample).

We consider the following equation:

$$\dot{r} = f(r) = r \sum_{j=0}^n \frac{(-1)^j}{10^{10(n-j)+10}} r^{2j}. \quad (16)$$

By putting $v_j = (-1)^j / 10^{10(n-j)+10}$, we obtain

$$v_j v_{j+1} < 0, \text{ and } |v_j| \ll |v_{j+1}| \ll 1, \text{ for } j = 0, 1, 2, \dots, n-1, \quad (17)$$

because

$$\frac{v_j}{v_{j+1}} = \frac{10^{10(n-j-1)+10}}{10^{10(n-j)+10}} = 10^{-10} \ll 1, \text{ for } j = 0, 1, 2, \dots, n-1, \text{ and } |v_n| = 10^{-10} \ll 1. \quad (18)$$

However,

$$\begin{aligned}
 \frac{f(r)}{r} &= \sum_{j=0}^n \frac{(-1)^j}{10^{10(n-j)+10}} r^{2j} \\
 &= 10^{-10} \prod_{j=0}^{n/2-1} \left(\left(r^2 - \frac{1}{10^{10}} \cos \frac{2j+1}{n+1} \pi \right)^2 + \frac{1}{10^{20}} \sin^2 \frac{2j+1}{n+1} \pi \right) \neq 0, \quad \forall r \in \mathbb{R}.
 \end{aligned} \quad (19)$$

□

4. Examples

In this section, by using the counterexample, we can demonstrate that Theorems 2 and 3 are not true. However, the previous theorems will be true if we add the following condition: $a_0/a_2 \ll a_2/a_4 \ll a_4/a_6 \ll a_6/a_8 \ll \dots \ll a_{2j-2}/a_{2j}$, $j = 1, \dots, n$.

Example 1. We consider the following equation:

$$\dot{r} = f(r),$$

or

$$f(r) = \sum_{j=0}^4 v_j r^{2j+1} = r \left(\frac{1}{10^{50}} - \frac{1}{10^{40}} r^2 + \frac{1}{10^{30}} r^4 - \frac{1}{10^{20}} r^6 + \frac{1}{10^{10}} r^8 \right). \quad (20)$$

We have

$$v_j v_{j+1} < 0, \text{ and } |v_j| \ll |v_{j+1}| \ll 1, \text{ for } j = 0, 1, \dots, 3, \quad (21)$$

because

$$\frac{v_j}{v_{j+1}} = 10^{-10} \ll 1, \text{ for } j = 0, 1, \dots, 3, \text{ and } |v_4| = 10^{-10} \ll 1. \quad (22)$$

However,

$$\begin{aligned} \frac{f(r)}{r} &= 10^{-10} \left(r - \frac{1}{10^5} \left(\cos \frac{\pi}{10} + i \sin \frac{\pi}{10} \right) \right) \left(r - \frac{1}{10^5} \left(\cos \frac{3\pi}{10} + i \sin \frac{3\pi}{10} \right) \right), \\ &\left(r - \frac{1}{10^5} \left(\cos \frac{7\pi}{10} + i \sin \frac{7\pi}{10} \right) \right) \left(r - \frac{1}{10^5} \left(\cos \frac{9\pi}{10} + i \sin \frac{9\pi}{10} \right) \right) \\ &\left(r - \frac{1}{10^5} \left(\cos \frac{11\pi}{10} + i \sin \frac{11\pi}{10} \right) \right) \left(r - \frac{1}{10^5} \left(\cos \frac{13\pi}{10} + i \sin \frac{13\pi}{10} \right) \right) \\ &\left(r - \frac{1}{10^5} \left(\cos \frac{17\pi}{10} + i \sin \frac{17\pi}{10} \right) \right) \left(r - \frac{1}{10^5} \left(\cos \frac{19\pi}{10} + i \sin \frac{19\pi}{10} \right) \right) \neq 0, \quad \forall r \in \mathbb{R}, \end{aligned} \quad (23)$$

where the system roots are given by

$$\begin{aligned} r_1 &= \frac{1}{10^5} \left(\cos \frac{\pi}{10} + i \sin \frac{\pi}{10} \right) = 9.5106 \times 10^{-6} + 3.0902 \times 10^{-6} i, \\ r_2 &= \frac{1}{10^5} \left(\cos \frac{3\pi}{10} + i \sin \frac{3\pi}{10} \right) = 5.8779 \times 10^{-6} + 8.0902 \times 10^{-6} i, \\ r_3 &= \frac{1}{10^5} \left(\cos \frac{7\pi}{10} + i \sin \frac{7\pi}{10} \right) = -5.8779 \times 10^{-6} + 8.0902 \times 10^{-6} i, \\ r_4 &= \frac{1}{10^5} \left(\cos \frac{9\pi}{10} + i \sin \frac{9\pi}{10} \right) = -9.5106 \times 10^{-6} + 3.0902 \times 10^{-6} i, \\ r_5 &= \frac{1}{10^5} \left(\cos \frac{11\pi}{10} + i \sin \frac{11\pi}{10} \right) = -9.5106 \times 10^{-6} - 3.0902 \times 10^{-6} i, \\ r_6 &= \frac{1}{10^5} \left(\cos \frac{13\pi}{10} + i \sin \frac{13\pi}{10} \right) = -5.8779 \times 10^{-6} - 8.0902 \times 10^{-6} i, \\ r_7 &= \frac{1}{10^5} \left(\cos \frac{17\pi}{10} + i \sin \frac{17\pi}{10} \right) = 5.8779 \times 10^{-6} - 8.0902 \times 10^{-6} i, \\ r_8 &= \frac{1}{10^5} \left(\cos \frac{19\pi}{10} + i \sin \frac{19\pi}{10} \right) = 9.5106 \times 10^{-6} - 3.0902 \times 10^{-6} i. \end{aligned} \quad (24)$$

Example 2. Let us consider now the following system:

$$\dot{r} = f(r) = r \sum_{j=0}^4 \frac{(-1)^j}{10^{4(4-j)+1}} r^{2j} = r \left(\frac{1}{10^{1024}} - \frac{1}{10^{256}} r^2 + \frac{1}{10^{64}} r^4 - \frac{1}{10^{16}} r^6 + \frac{1}{10^4} r^8 \right), \quad (25)$$

with positive roots such as

$$\begin{pmatrix} r_1 = 10^{-6} \\ r_2 = 10^{-24} \\ r_3 = 10^{-96} \\ r_4 = 10^{-384} \end{pmatrix}, \quad (26)$$

$$v_j v_{j+1} < 0, \quad \text{and } |v_j| \ll |v_{j+1}| \ll 1, \text{ for } j = 0, 1, \dots, 3,$$

$$\frac{v_j}{v_{j+1}} \ll \frac{v_{j+1}}{v_{j+2}} \ll 1, \quad \text{for } j = 0, \dots, 2. \quad (27)$$

because

Example 3. We suppose the following system:

$$\begin{cases} \dot{x} = y - \varepsilon(b_1 x + b_3 x^3 + b_5 x^5 + b_7 x^7 + b_9 x^9), \\ \dot{y} = -x, \end{cases}$$

or

$$b_1 = 2(10^{-196}),$$

$$b_3 = -\frac{8}{3}(10^{-192} + 10^{-152} + 10^{-132} + 10^{-112}), \quad (28)$$

$$b_5 = \frac{16}{5}(10^{-148} + 10^{-128} + 10^{-110} + 10^{-88} + 10^{-68} + 10^{-48}),$$

$$b_7 = -\frac{128}{35}(10^{-4} + 10^{-44} + 10^{-64} + 10^{-84}),$$

$$b_9 = \frac{256}{63}.$$

By putting $a_{2j+1} = \varepsilon b_{2j+1}$, $j = \overline{0, 4}$, we obtain

$$\begin{cases} \dot{x} = y - (a_1 x + a_3 x^3 + a_5 x^5 + a_7 x^7 + a_9 x^9), \\ \dot{y} = -x, \end{cases} \quad (29)$$

and by applying the first-order averaging method [13, 14] on (14), we obtain

$$f^0(r) = r \left\{ r^8 - (10^{-4} + 10^{-44} + 10^{-64} + 10^{-84}) r^6 + (10^{-148} + 10^{-128} + 10^{-110} + 10^{-88} + 10^{-68} + 10^{-48}) r^4 - (10^{-192} + 10^{-152} + 10^{-132} + 10^{-112}) r^2 + 10^{-196} \right\}. \quad (30)$$

$f^0(r) = 0$ implied $r_1 = 10^{-2}$, $r_2 = 10^{-22}$, $r_3 = 10^{-32}$, and $r_4 = 10^{-42}$, then there are exactly 4 small-amplitudes limit cycles r_i , $i = \overline{1, 4}$

Note that $a_{2j+1}/a_{2j+3} = b_{2j+1}/b_{2j+3} \ll 1$ for $j = 0, \dots, 3$ and $b_{2j+1}/b_{2j+3} \ll b_{2j+3}/b_{2j+5}$ for $j = 0, \dots, 2$.

5. Conclusion

In this work, by using a counterexample for a theorem of the small amplitude limit cycles in some Liénard systems, we have shown that that there will be no solutions unless an

extra condition is added. In addition, a new condition is derived for some specific Liénard systems where a violation of the small amplitude limit cycles theorem takes place. However, these theorems will be true if we add the following condition: $a_0/a_2 \ll a_2/a_4 \ll a_4/a_6 \ll a_6/a_8 \ll \dots \ll a_{2j-2}/a_{2j}$, $j = 1, \dots, n$.

Data Availability

No data were used to support this study.

Conflicts of Interest

The authors declare that they have no conflicts of interest.

Acknowledgments

The authors extend their appreciation to the Deanship of Scientific Research at King Khalid University for funding this work through Research Group Project under Grant no. (R.G.P-2/53/42).

References

- [1] J. Yang and W. Ding, "Limit cycles of a class of Liénard systems with restoring forces of seventh degree," *Applied Mathematics and Computation*, vol. 316, pp. 422–437, 2018.
- [2] H. Zhu, M. Wei, S. Yang, and C. Jiang, "Bifurcation of limit cycles from a Liénard system of degree 4," *Acta mathematica scientia, Series A*, vol. 41, no. 4, pp. 936–953, 2021.
- [3] F. Jiang, Z. Ji, and Y. Wang, "On the number of limit cycles of discontinuous Liénard polynomial differential systems," *International Journal of Bifurcation and Chaos*, vol. 28, no. 14, Article ID 1850175, 2018.
- [4] Y. Zhou, C. Wang, and D. Blackmore, "The uniqueness of limit cycles for Liénard system," *Journal of Mathematical Analysis and Applications*, vol. 304, no. 2, pp. 473–489, 2005.
- [5] Z. Daoxiang and P. Yan, "On the uniqueness of limit cycles in a generalized Liénard system," *Qualitative theory of dynamical systems*, vol. 18, no. 3, pp. 1191–1199, 2019.
- [6] G. Villari and F. Zanolin, "On the uniqueness of the limit cycle for the Liénard equation with $f(x)$ not sign-definite," *Applied Mathematics Letters*, vol. 76, pp. 208–214, 2018.
- [7] M. Sabatini and G. Villari, "Limit cycle uniqueness for a class of planar dynamical systems," *Applied Mathematics Letters*, vol. 19, no. 11, pp. 1180–1184, 2006.
- [8] C. Li and J. Llibre, "Uniqueness of limit cycles for Liénard differential equations of degree four," *Journal of Differential Equations*, vol. 252, no. 4, pp. 3142–3162, 2012.
- [9] T. Carletti and G. Villari, "A note on existence and uniqueness of limit cycles for Liénard systems," *Journal of Mathematical Analysis and Applications*, vol. 307, no. 2, pp. 763–773, 2005.
- [10] S. Lynch, "Liénard systems and the second part of Hilbert's sixteenth problem," *Nonlinear Analysis: Theory, Methods & Applications*, vol. 30, no. 3, pp. 1395–1403, 1997.
- [11] P. Yu and M. Han, "Limit cycles in generalized Liénard systems," *Chaos, Solitons & Fractals*, vol. 30, no. 5, pp. 1048–1068, 2006.
- [12] N. G. Lloyd and S. Lynch, "Small-amplitude limit cycles of certain Liénard systems," *Proceedings of the Royal Society of London. A. Mathematical and Physical Sciences*, vol. 418, no. 1854, pp. 199–208, 1988.
- [13] J. Llibre and A. Makhlouf, "Limit cycles of a class of generalized Liénard polynomial equations," *Journal of Dynamical and Control Systems*, vol. 21, no. 2, pp. 189–192, 2015.
- [14] A. Menaceur, S. M. Boulaaras, A. Makhlouf, K. Rajagopal, and M. Abdalla, "Limit cycles of a class of perturbed differential systems via the first-order averaging method," *Dynamic Analysis, Learning, and Robust Control of Complex Systems*, vol. 2021, Article ID 5581423, 6 pages, 2021.

Research Article

FPGA Realization and Lyapunov–Krasovskii Analysis for a Master-Slave Synchronization Scheme Involving Chaotic Systems and Time-Delay Neural Networks

J. Perez-Padron , C. Posadas-Castillo , J. Paz-Perez , E. Zambrano-Serrano ,
and M. A. Platas-Garza 

Universidad Autónoma de Nuevo León, Av. Pedro de Alba S/N, Cd. Universitaria, San Nicolás de los Garza
C.P. 66455, NL, Mexico

Correspondence should be addressed to M. A. Platas-Garza; miguel.platasgrz@uanl.edu.mx

Received 17 July 2021; Revised 5 September 2021; Accepted 8 September 2021; Published 23 September 2021

Academic Editor: Adel Ouannas

Copyright © 2021 J. Perez-Padron et al. This is an open access article distributed under the Creative Commons Attribution License, which permits unrestricted use, distribution, and reproduction in any medium, provided the original work is properly cited.

In this paper, the trajectory tracking control and the field programmable gate array (FPGA) implementation between a recurrent neural network with time delay and a chaotic system are presented. The tracking error is globally asymptotically stabilized by means of a control law generated from the Lyapunov–Krasovskii and Lur’e theory. The applicability of the approach is illustrated by considering two different chaotic systems: Liu chaotic system and Genesis–Tesi chaotic system. The numerical results have shown the effectiveness of obtained theoretical results. Finally, the theoretical results are implemented on an FPGA, confirming the feasibility of the synchronization scheme and showing that it is hardware realizable.

1. Introduction

Neural networks can be considered as nonlinear mathematical functions whose parameters are adjusted to describe the behavior of a static or dynamic system [1]. According to their structure, neural networks can be classified as static neural networks or dynamic neural networks. The static neural networks are capable of approximating any function using static mapping [2]. Meanwhile, dynamic neural networks, also called recurrent neural networks, have feedback connections that give them higher capability than static neural networks. For example, recurrent neural networks can reproduce the dynamic response of a dynamic system due to their feedback connection. They can also overcome many problems related to static neural networks, such as extreme global search, and consequently, have better approximation properties [3]. Recently, due to the richness of dynamic behaviors from recurrent neural networks, they have received much attention and been investigated in a wide variety of applications in diverse fields such as in associative memory [4], neurodynamic optimization problems

[5], pattern recognition [6], image processing [7], and so on [8, 9].

It is well known that the time-delay phenomenon is an inherent feature of many physical processes such as nuclear reactors, chemical processes, and biological systems. Usually, it is considered a source of oscillation and divergence, leading to system performance degradation or even generating instability [9]. A delayed neural network can generate complicated dynamic behaviors such as boundedness, periodicity, stability, chaos, and synchronization [10]. Synchronization is a fundamental behavior of recurrent neural networks. Hence, many researchers devote their effort to studying the delay effect on drive-response synchronization. Indeed, the drive-response synchronization of recurrent neural networks cannot be achieved individually, so external input signals should be considered in the neural network response. Many efficient control approaches have been designed to control or achieve the synchronized state in the literature, such as linear feedback control, active control, intermittent control, adaptive control, event-triggered control, pinning control, and impulsive control, among

others [11–13]. In particular, the Lyapunov–Krasovskii approach has demonstrated to be an efficient method to deal with the global asymptotic stability of recurrent neural networks with time delay. In [14], the global synchronization of multiple recurrent neural networks with time delays under a switching topology via impulsive interaction is given. An exponential H_∞ synchronization method for an uncertain drive and response neural networks with mixed time delays was presented based on a Lyapunov–Krasovskii functional and free-weighting matrices [15]. The synchronization of delayed neural networks with hybrid couplings by employing the Lyapunov functional method and the Kronecker product technique is used to guarantee the global synchronization in coupled networks [16]. In [17], the global asymptotic synchronization for a class of delayed neural networks is investigated. In [18], the pinning synchronization in an array of coupled delayed neural networks with both constant and delayed couplings is presented, showing that the network can be pinned to a homogenous state by applying adaptive feedback control. It is worth noting that the Lyapunov–Krasovskii approach has been demonstrated to be an efficient method to deal with the global asymptotic stability of a recurrent neural network with time delay [19, 20]. In [21], the stability of linear continuous-time systems with time delay by employing new Lyapunov–Krasovskii functionals is presented. New Lyapunov–Krasovskii functionals are proposed to achieve the synchronization behavior of delay neural networks with two time scales for the fixed and adaptive coupling schemes [22]. Some new Lyapunov–Krasovskii functionals are developed by nonuniformly dividing the delay interval into multiple segments and choosing proper functionals with different weighting matrices corresponding to different sections in the Lyapunov–Krasovskii functionals proposed in [23]. In [24], the global stability of a system composed by identical Hopfield neural networks with time-delayed connections is presented by constructing a Lyapunov–Krasovskii functional.

Inspired by all the above works, this paper focuses on the problem of tracking a given reference trajectory. It proposes a trajectory tracking scheme in which a time-delay neural network is forced to follow a chaotic system’s reference signal, achieving a drive-response synchronization state between the neural network and the chaotic system. The control law that guarantees the trajectory tracking problem solution is obtained by using the Lyapunov–Krasovskii and Lur’e approach. The pertinence of the approach is demonstrated by considering two numerical examples. In each example, synchronization with one chaotic oscillator is addressed, and the derived control laws are tested via numerical experimentation. The Genesis–Tesi and Liu systems are considered. Although the proposed scheme could be useful to follow other nonlinear systems, we decide to restrict this work using only these two chaotic systems because their tracking can be more challenging than other tracking problems such as the reproduction of the gait cycle in humanoids [25] or the trajectory tracking in different mechanical systems [26] and complex systems [27]. In all the former cases, the movement may be softer and periodic.

Additionally, the FPGA technology is used to implement the proposed scheme by using a NI c-RIO-9068 device with a Xilinx Zynq-7000 XC7Z020 FPGA. The hardware implementation results confirm the feasibility of the proposed scheme. We decided to implement the entire scheme on the same chip, i.e., the system to be tracked, the recurrent neural network with time delay, and the derived control law are implemented on the same FPGA chip.

This article is organized as follows. In Section 2, the construction of the mathematical model is given. The control law of delayed neural network and global asymptotic stability conditions are shown in Section 3. The numerical results showing the applicability of the theory are given in Section 4. Section 5 provides experimental results based on FPGA implementations. Finally, we conclude the paper in the last section.

2. Preliminaries

Consider the following time-delay neural network model:

$$\dot{x}(t) = Ax(t) + W\phi[x(t - \tau)] + u(t), \quad (1)$$

where $x(t) = [x_1(t), x_2(t), \dots, x_n(t)]^T \in \mathbb{R}^n$ is the state vector associated with the neurons; $A = \text{diag}(-\lambda_1, -\lambda_2, \dots, -\lambda_n)$ with λ_i with $i = 1, \dots, n$ being positive constants representing the rate with at which the neural network will reset its potential to the resting state when disconnected from the external input; $W = [w_{ij}] \in \mathbb{R}^n \times \mathbb{R}^n$ represents the delayed connection weight matrix; $\phi(x) = [\phi_1(x_1), \phi_2(x_2), \dots, \phi_n(x_n)]^T \in \mathbb{R}^n$ is the activation function; $\tau > 0$ is the transmission delay; and $u(t) = (u_1(t), u_2(t), \dots, u_n(t))^T \in \mathbb{R}^n$ is an external input vector.

The following properties are assumed for the activation function [28, 29]:

- (1) $\phi(x)$ is bounded and monotonically nondecreasing on \mathbb{R} .
- (2) The activation function $\phi(x)$ is Lipschitz continuous, that is, there exists constant $L_\phi > 0$ such that

$$|\phi(x) - \phi(y)| \leq L_\phi |x - y|, \quad \forall x, y \in \mathbb{R}. \quad (2)$$

The system to be tracked by the recurrent neural network with time delay (driving system) is defined as an autonomous n -dimensional dynamical system given by

$$\dot{x}_r(t) = f(x_r(t)), \quad (3)$$

where $x_r(t) = [x_{r_1}(t), x_{r_2}(t), \dots, x_{r_n}(t)]^T \in \mathbb{R}^n$ is a n -dimensional state vector, with $f(x_r(t))$ defining a vector field $f(x_r(t)): \mathbb{R}^n \rightarrow \mathbb{R}^n$. In this paper, (3) is a nonlinear system that generates chaotic behavior.

We continue by presenting the Lyapunov–Krasovskii approach. This method is the natural extension of the second Lyapunov approach associated with the stability analysis of functional differential equations [30]. It consists of considering functionals of the form $V(t; x_t)$ that are positive definite and decreasing along the trajectories of system

$\dot{x}(t) = f(t, x(t), x_t)$. The Lyapunov–Krasovskii theorem is expressed as follows.

Theorem 1 (see [30]). *Let u, v , and $w: \mathbb{R}^+ \rightarrow \mathbb{R}^+$ be nondecreasing functions such that $u(\theta)$ and $v(\theta)$ are strictly positive for all $\theta > 0$. Let $h \in \mathbb{R}^+$ and $\beta: \mathcal{C}[-h; 0] \rightarrow \mathbb{R}^n$. Assume that the vector field $f(\cdot)$ of $\dot{x}(t) = f(t, x(t), x_t)$ is bounded for bounded values of its arguments. If there exists a continuous and differentiable functional $V: \mathbb{R} \times \mathcal{C}[-h; 0] \rightarrow \mathbb{R}^+$ such that*

$$\begin{aligned} (a) \quad & u(\|\beta(0)\|) \leq V(t, \beta) \leq v(\|\beta\|) \\ (b) \quad & \dot{V}(t, \beta) \leq -w(\|\beta(0)\|) \quad \text{for all trajectories of} \\ & x(t) = f(t, x(t), x_t) \end{aligned}$$

$$V(t + \theta, \beta(t + \theta)) \leq V(t, \beta(t)), \quad \forall \theta \in [-h, 0], \quad (4)$$

then the solution $x_t = 0$ is uniformly stable for $\dot{x}(t) = f(t, x(t), x_t)$.

Finally, we add two definitions that will be used to analyze equilibrium points.

Definition 1. An equilibrium E_* is called a saddle point of index 1 if E_* has one eigenvalue with nonnegative real part (unstable).

Definition 2. An equilibrium E_* is called a saddle point of index 2 if E_* has two unstable eigenvalues.

3. Trajectory Tracking for a Recurrent Neural Network with Time Delay

While the main objective of the work is to present the proposed tracking scheme and its hardware implementation, the main objective of this section is to develop a control law such that the delayed neural network (1) tracks the solution of the dynamical system (3).

3.1. Dynamical Analysis Error. Define the tracking error as $e(t) = x(t) - x_r(t)$, where the respective error dynamics are

$$\dot{e}(t) = \dot{x}(t) - \dot{x}_r(t). \quad (5)$$

Substituting (1) and (3) in (5), the dynamics of the error are governed by the following equation:

$$\dot{e}(t) = Ax(t) + W\phi[x(t - \tau)] + u(t) - f(x_r(t)). \quad (6)$$

Adding and subtracting to (6) the terms $Ax_r(t)$, $W\phi[x_r(t - \tau)]$, and $\alpha(t)$, we have

$$\begin{aligned} \dot{e}(t) = & Ae(t) + W(\phi[x(t - \tau)] - \phi[x_r(t - \tau)]) \\ & + (u(t) - \alpha(t) + [Ax_r(t) + W\phi[x_r(t - \tau)] + \alpha(t)] \\ & - f(x_r(t)), \end{aligned} \quad (7)$$

where $\alpha(t)$ is the function to be determined. In order to guarantee that the neural network given in (1) can track the

reference trajectory of dynamical system (3), the following assumption has to be satisfied [31].

There exist functions $\rho(t)$ and $\alpha(t)$ such that

$$\begin{aligned} \dot{\rho}(t) &= A\rho(t) + W\phi[\rho(t - \tau)] + \alpha(t), \\ \rho(t) &= x_r(t). \end{aligned} \quad (8)$$

Therefore, from (3) and (8), we obtain that

$$Ax_r(t) + W\phi[x_r(t - \tau)] + \alpha(t) = f(x_r(t)), \quad (9)$$

and then

$$\alpha(t) = f(x_r(t)) - Ax_r(t) - W\phi[x_r(t - \tau)], \quad (10)$$

so that (7) becomes

$$\dot{e}(t) = Ae(t) + W\varphi_\phi(t - \tau) + \bar{u}(t), \quad (11)$$

with $W\varphi_\phi(t - \tau) = W(\phi[x(t - \tau)] - \phi[x_r(t - \tau)])$ and $\bar{u}(t) = (u(t) - \alpha(t))$. It is clear that $e(t) = 0$ is an equilibrium point of (11) when $\bar{u}(t) = 0$. In this way, the tracking problem can be expressed as a global asymptotic stabilization problem for system (11).

3.2. Error Stabilization and Control Design. In order to establish the convergence of (11) to $e(t) = 0$, a Lyapunov–Krasovskii functional is proposed ensuring the desired tracking. The Lyapunov–Krasovskii analysis is a Lyapunov-inspired method that consists of proposing a functional $V(t, x(t))$ of the state $x(t)$, which should be positive and decreasing definite along the trajectories of the system. This is essential for the design of a globally and asymptotically stabilizing control law for time-delay systems [20]. In this work, the following Lyapunov–Krasovskii functional is proposed as in [19, 32]:

$$V(e) = \sum_{i=1}^n \int_0^{e_i} \varphi(\xi, x_r) d\xi + \int_{t-\tau}^t (\varphi_\phi^T(s) W^T W \varphi_\phi(s)) ds, \quad (12)$$

where the expression $\sum_{i=1}^n \int_0^{e_i} \varphi(\xi, x_r) d\xi$ is proposed to analyze the stability related to error $\dot{e}(t)$, whereas the expression $\int_{t-\tau}^t (\varphi_\phi^T(s) W^T W \varphi_\phi(s)) ds$ is envisioned to analyze the effect of the delay τ ; note that this term vanishes as $\tau \rightarrow 0$.

In this manner, the time derivate of (12), along the trajectories of (11), was computed using the fundamental theorem of calculus as follows:

$$\begin{aligned} \dot{V}(e) = & \frac{\partial V(e)}{\partial e} \dot{e} = \varphi(e, x_r)^T \dot{e} + \varphi_\phi^T W^T W \varphi_\phi \\ & - \varphi_\phi^T(t - \tau) W^T W \varphi_\phi(t - \tau). \end{aligned} \quad (13)$$

Substituting (11) in (13), we get

$$\begin{aligned} \dot{V}(e) = & \varphi(e, x_r)^T Ae + \varphi(e, x_r)^T W(\phi[x(t - \tau)] \\ & - \phi[x_r(t - \tau)]) + \varphi(e, x_r)^T \bar{u} + \varphi_\phi^T W^T W \varphi_\phi \\ & - \varphi_\phi^T(t - \tau) W^T W \varphi_\phi(t - \tau). \end{aligned} \quad (14)$$

Regarding $\varphi_\phi(t - \tau) = (\phi[x(t - \tau)] - \phi[x_r(t - \tau)])$, equation (14) can be denoted as

$$\begin{aligned} \dot{V}(e) = & -\lambda\varphi(e, x_r)^T e + \varphi(e, x_r)^T W\varphi_\phi(t - \tau) + \varphi(e, x_r)^T \bar{u} \\ & + \varphi_\phi^T W^T W\varphi_\phi - \varphi_\phi^T(t - \tau)W^T W\varphi_\phi(t - \tau). \end{aligned} \quad (15)$$

Consider the inequality [19]:

$$P^T Q + Q^T P \leq P^T \Lambda P + Q^T \Lambda^{-1} Q, \quad (16)$$

which holds for all matrices $P, Q \in \mathbb{R}^{n \times k}$ and a positive definite matrix $\Lambda \in \mathbb{R}^{n \times n}$. To prove the inequality (16), we consider $F \equiv P^T \Lambda P + Q^T \Lambda^{-1} Q - P^T Q - Q^T P \geq 0$. Denoting $v_1 = \Lambda^{(1/2)} P v$ and $v_2 = \Lambda^{-(1/2)} Q v$, we obtain $F = v_1^T v_1 - v_2^T v_2 - 2v_1^T v_2 = \|v_1 - v_2\|^2 \geq 0$.

Applying (16) with $\Lambda = I$ to the term $\varphi(e, x_r)^T W\varphi_\phi(t - \tau)$, we get

$$\begin{aligned} \dot{V}(e) \leq & -\lambda\varphi(e, x_r)^T e + \frac{1}{2}\varphi(e, x_r)^T \varphi(e, x_r) \\ & + \frac{1}{2}\varphi_\phi^T(t - \tau)W^T W\varphi_\phi(t - \tau) + \varphi(e, x_r)^T \bar{u} \\ & + \varphi_\phi^T W^T W\varphi_\phi - \varphi_\phi^T(t - \tau)W^T W\varphi_\phi(t - \tau). \end{aligned} \quad (17)$$

Simplifying (17), the following is obtained:

$$\begin{aligned} \dot{V}(e) \leq & -\lambda\varphi(e, x_r)^T e + \frac{1}{2}\varphi(e, x_r)^T \varphi(e, x_r) \\ & - \frac{1}{2}\varphi_\phi^T(t - \tau)W^T W\varphi_\phi(t - \tau) + \varphi(e, x_r)^T \bar{u} \\ & + \varphi_\phi^T W^T W\varphi_\phi. \end{aligned} \quad (18)$$

Because $\varphi(e, x_r)$ is a sector function with respect to $e(t)$, there exist positive constants k_1 and k_2 such that $k_1 \|e\|^2 \leq \varphi(e, x_r)^T \varphi(e, x_r) \leq k_2 \|e\|^2$, where $\|\cdot\|$ is used to denote the Euclidean norm. From $\varphi_\phi(t) = (\phi(x(t)) - \phi(x_r(t)))$,

$$\begin{aligned} \|\varphi_\phi(t)\| & \|\phi(x(t)) - \phi(x_r(t))\| \\ & \leq L_\phi \|x(t) - x_r(t)\| \\ & = L_\phi \|e(t)\|. \end{aligned} \quad (19)$$

Then, there exists a positive constant L_ϕ such that $\varphi(e, x_r)^T \varphi(e, x_r) \leq L_\phi^2 \|e\|^2$. Henceforth, (18) can be written as follows:

$$\begin{aligned} \dot{V}(e) \leq & -\left[\lambda k_1 - \frac{1}{2}L_\phi^2\right] \|e\|^2 - \frac{1}{2}\varphi_\phi^T(t - \tau)W^T W\varphi_\phi(t - \tau) \\ & + \varphi(e, x_r)^T \bar{u} + \varphi_\phi^T W^T W\varphi_\phi. \end{aligned} \quad (20)$$

Simplifying (20), we have

$$\dot{V}(e) \leq -\left[\lambda k_1 - \frac{1}{2}L_\phi^2\right] \|e\|^2 + \varphi(e, x_r)^T \bar{u} + \varphi_\phi^T W^T W\varphi_\phi. \quad (21)$$

Since φ_ϕ is Lipschitz, we consider (20) applied to $\varphi_\phi^T W^T W\varphi_\phi$, obtaining

$$\varphi_\phi^T W^T W\varphi_\phi \leq \|\varphi_\phi^T W^T W\varphi_\phi\| \leq L_\phi^2 \|W\|^2 \|e\|^2, \quad (22)$$

with L_ϕ^2 being the Lipschitz constant of $\phi(\cdot)$.

Replacing (22) in equation (21), the following expression is obtained:

$$\dot{V}(e) \leq -\left[\lambda k_1 - \frac{1}{2}L_\phi^2\right] \|e\|^2 + L_\phi^2 \|W\|^2 \|e\|^2 + \varphi(e, x_r)^T \bar{u}. \quad (23)$$

Now we consider the control law given as follows:

$$\bar{u} = -\left(2 + 2L_\phi^2 \|W\|^2\right) \varphi(e, x_r). \quad (24)$$

Then, substituting (24) in (23), we obtain

$$\dot{V}(e) \leq -\left[\lambda + L_\phi^2 + L_\phi^2 \|W\|^2\right] \|e\|^2. \quad (25)$$

Then, $\dot{V}(e) < 0$ for all $e \neq 0$. This means that the proposed control law can globally and asymptotically stabilize the error system, thus ensuring the tracking of (1) by (3) achieving the synchronization, which means that $\lim_{t \rightarrow \infty} \|x(t) - x_r(t)\| = 0$ holds; moreover, this implies that the both systems have reached the synchrony state (synchronization).

Finally, the control action driving the recurrent neural network is given by

$$u = -\left(2 + 2L_\phi^2 \|W\|^2\right) \varphi(e, x_r) + f(x_r) - Ax_r - W\phi[x_r(t - \tau)]. \quad (26)$$

We summarize the developed analysis in the following theorem.

Theorem 2. *The control law defined as u in (26) ensures that the time-delay neural network established in (1) tracks the dynamical behavior generated by the reference system (chaotic system) (3).*

4. Numerical Simulations

In this section, computer simulations are presented to confirm the applicability of the results proposed previously, which are applied to two dynamical systems that generate chaotic behavior.

4.1. Synchronization between Delayed Neural Network and Genesio-Tesi System. In 1992, Genesio and Tesi proposed a chaotic system known as the Genesio-Tesi system [33]. It is described by the following simple three-dimensional autonomous system with only one quadratic nonlinear term:

$$\begin{aligned} \dot{x}_{r_1} &= x_{r_2}, \\ \dot{x}_{r_2} &= x_{r_3}, \\ \dot{x}_{r_3} &= -a_1 x_{r_1} - a_2 x_{r_2} - a_3 x_{r_3} + a_4 x_{r_1}^2, \end{aligned} \quad (27)$$

where $x_r = [x_{r_1}, x_{r_2}, x_{r_3}] \in \mathbb{R}^3$ is the vector state and a_i with $(i = 1, \dots, 4)$ are positive real parameters. System (27) has two equilibrium points $E_1(0, 0, 0)$ and $E_2(a_1/a_4, 0, 0)$. The parameters and initial conditions of (27) are chosen as $a_1 = 1$, $a_2 = 1.1$, $a_3 = 0.44$, $a_4 = 1$, and $[x_{r_1}(0), x_{r_2}(0), x_{r_3}(0)]^T = [0.1, 0.1, 0.1]^T$. The corresponding eigenvalues of equilibria E_1 , E_2 and their stability are described in Table 1. The Lyapunov exponents for system (27) are $LE_1 = 0.0818$, $LE_2 = 0$, $LE_3 = -0.5227$ which according to [34] make the system chaotic. The algorithm

employed for determining Lyapunov exponents was proposed in [35]. Its Kaplan–Yorke dimension is $D_{KY} = 2.1564$, and the phase plane of the chaotic system is displayed in Figure 1. In addition, the bifurcation diagrams of system (27) in terms of the parameters a_1 and a_3 are plotted in Figures 2(a) and 2(b), respectively. Moreover, the bifurcation diagrams are obtained by plotting the local maximal of the state variable x_{r_1} denoted as \hat{x} in Figures 2(a) and 2(b).

By considering the following delayed neural network defined as in equation (1), we get

$$\begin{bmatrix} \dot{x}_1 \\ \dot{x}_2 \\ \dot{x}_3 \end{bmatrix} = \begin{bmatrix} -1 & 0 & 0 \\ 0 & -1 & 0 \\ 0 & 0 & -1 \end{bmatrix} \begin{bmatrix} x_1 \\ x_2 \\ x_3 \end{bmatrix} + \begin{bmatrix} 0.3 & \frac{4}{5} & 0 \\ 0.3 & 0 & 0 \\ 0 & 0 & 1 \end{bmatrix} \begin{bmatrix} \tanh(x_1(t-\tau)) \\ \tanh(x_2(t-\tau)) \\ \tanh(x_2(t-\tau)) \end{bmatrix} + \begin{bmatrix} u_1 \\ u_2 \\ u_3 \end{bmatrix}, \quad (28)$$

where $u = [u_1, u_2, u_3]^T$ is the control action applied to the recurrent neural network defined as in (24) and defined by

$$\begin{bmatrix} u_1 \\ u_2 \\ u_3 \end{bmatrix} = -\psi \begin{bmatrix} x_1 - x_{r_1} \\ x_2 - x_{r_2} \\ x_3 - x_{r_3} \end{bmatrix} + \begin{bmatrix} x_{r_2} \\ x_{r_3} \\ -a_1 x_{r_1} - a_2 x_{r_2} - a_3 x_{r_3} + a_4 x_{r_1}^2 \end{bmatrix} - \begin{bmatrix} -1 & 0 & 0 \\ 0 & -1 & 0 \\ 0 & 0 & -1 \end{bmatrix} \begin{bmatrix} x_{r_1} \\ x_{r_2} \\ x_{r_3} \end{bmatrix} - \begin{bmatrix} 0.3 & \frac{4}{5} & 0 \\ \frac{2}{5} & 0.3 & 0 \\ 0 & 0 & 1 \end{bmatrix} \begin{bmatrix} \tanh(x_{r_1}(t-\tau)) \\ \tanh(x_{r_2}(t-\tau)) \\ \tanh(x_{r_3}(t-\tau)) \end{bmatrix}, \quad (29)$$

where ψ is a real constant defined as follows:

$$\psi = 2 + 2 \left[\sqrt{\sum_{i=1}^n \sum_{j=1}^n w_{ij}^2} \right]^2. \quad (30)$$

The initial values of the delayed neural network are taken as $(2, -1, -2)$; also, we consider a delay $\tau = 15$ s. In Figure 3, the results are shown.

Figure 3(a) shows the time evolution of the state variables x_r (purple line) and x (olive line) that corresponds to the chaotic system and delayed neural network, respectively, and we observe that both solutions evolve independently until $\tau = 15$ s, that is, when the control law begins to activate. In Figure 3(b), the error between the state variables x_{r_i} and x_i with $i = 1, 2, 3$ are given, respectively.

4.2. Synchronization between Delayed Neural Network and Liu System. Now, in this instance, we demonstrate the applicability of the discussed results considering the delayed neural network (1) described as in the previous example, i.e., equation (28), where the reference model to be tracked is the Liu system.

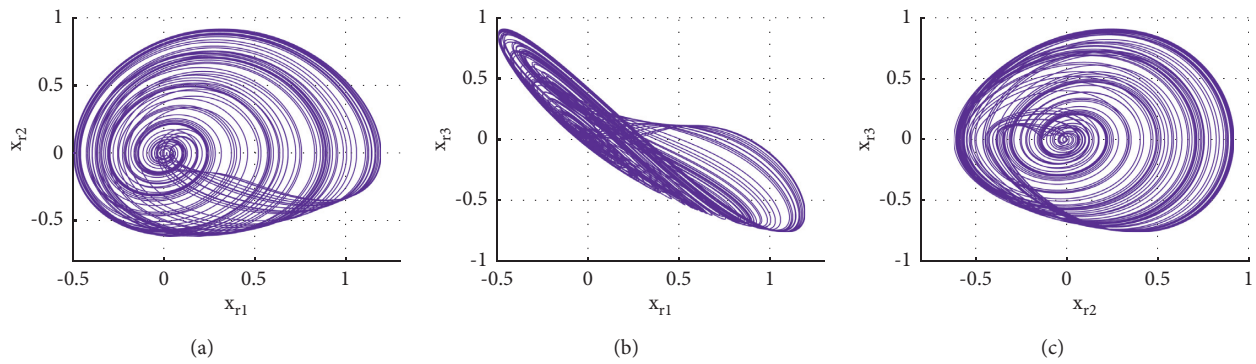
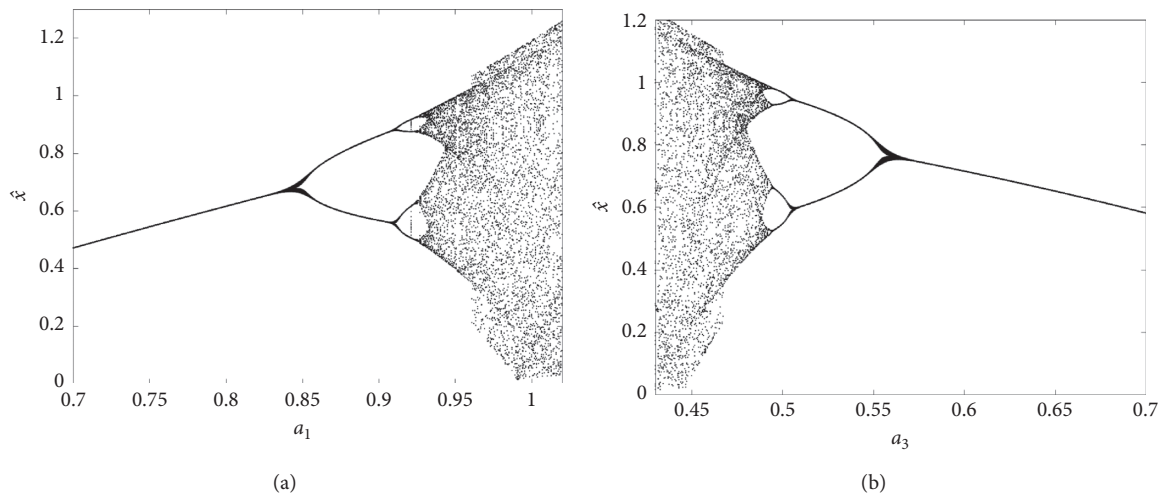
Liu et al. introduced in 2009 a three-dimensional autonomous chaotic system which is based on two multipliers and one quadratic term to introduce the nonlinearity necessary for folding trajectories [36]. The Liu chaotic oscillator is defined as follows:

$$\begin{aligned} \dot{x}_{r_1} &= -ax_{r_1} - m_1 x_{r_2}^2, \\ \dot{x}_{r_2} &= bx_{r_2} - m_2 x_{r_1} x_{r_3}, \\ \dot{x}_{r_3} &= -cx_{r_3} + m_3 x_{r_1} x_{r_2}, \end{aligned} \quad (31)$$

where $a, b, c, m_1, m_2, m_3 \in \mathbb{R}$. Its parameters are chosen as $a = m_1 = 1$, $b = 2.5$, $c = 5$, and $m_2 = m_3 = 4$. The equilibrium points, eigenvalues, and stability of the system are represented in Table 1. By considering the following initial conditions $[x_{r_1}(0), x_{r_2}(0), x_{r_3}(0)]^T = [-1, -0.5, 0.5]^T$, the Lyapunov exponents are $LE_1 = 0.4155$, $LE_2 = 0$, $LE_3 = -3.8586$, which according to [34] confirm that the Liu system is a chaotic oscillator. The algorithm employed for determining Lyapunov exponents was proposed in [35]. Its Kaplan–Yorke dimension is $D_{KY} = 2.1077$. The phase planes of Liu chaotic oscillator are displayed in Figure 4. In addition, the bifurcation diagrams of system (31) with the parameters b and c are displayed in Figures 5(a) and 5(b), respectively. Moreover, the bifurcation diagrams are obtained by plotting the local maximum of the state variable x_{r_1} denoted as \hat{x} in Figures 5(a) and 5(b).

TABLE 1: Stability of equilibrium points from Genesio–Tesi and Liu chaotic systems.

Chaotic system	Equilibria	Eigenvalues	Stability
Genesio–Tesi	$E_1 = (0, 0, 0)$	$\lambda_1 = -0.7503$ $\lambda_{2,3} = 0.1551 \pm 1.1440j$	Saddle point of index 2
	$E_2 = (1, 0, 0)$	$\lambda_1 = 0.5871$ $\lambda_{2,3} = -0.5136 \pm 1.1997j$	Saddle point of index 1
Liu	$E_1 = (0, 0, 0)$	$\lambda_1 = 2.5$ $\lambda_2 = -1; \lambda_3 = -5$	Saddle point
	$E_2 = (-0.8838, -0.9401, 0.6647)$	$\lambda_1 = -4.3878$ $\lambda_{2,3} = 0.4439 \pm 3.3464j$	Saddle point of index 2
	$E_3 = (-0.8838, 0.9401, -0.6647)$	$\lambda_1 = -4.3878$ $\lambda_{2,3} = 0.4439 \pm 3.3464j$	Saddle point of index 2

FIGURE 1: The Genesio–Tesi chaotic attractor in the phase plane with initial conditions $[x_{r_1}(0), x_{r_2}(0), x_{r_3}(0)]^T = [0.1, 0.1, 0.1]^T$. (a) $x_{r_1} - x_{r_2}$ phase plane. (b) $x_{r_1} - x_{r_3}$ phase plane. (c) $x_{r_2} - x_{r_3}$ phase plane.FIGURE 2: (a) Bifurcation diagram of Genesio–Tesi system with varying parameter a_1 . (b) Bifurcation diagram of Genesio–Tesi system with varying parameter a_3 .

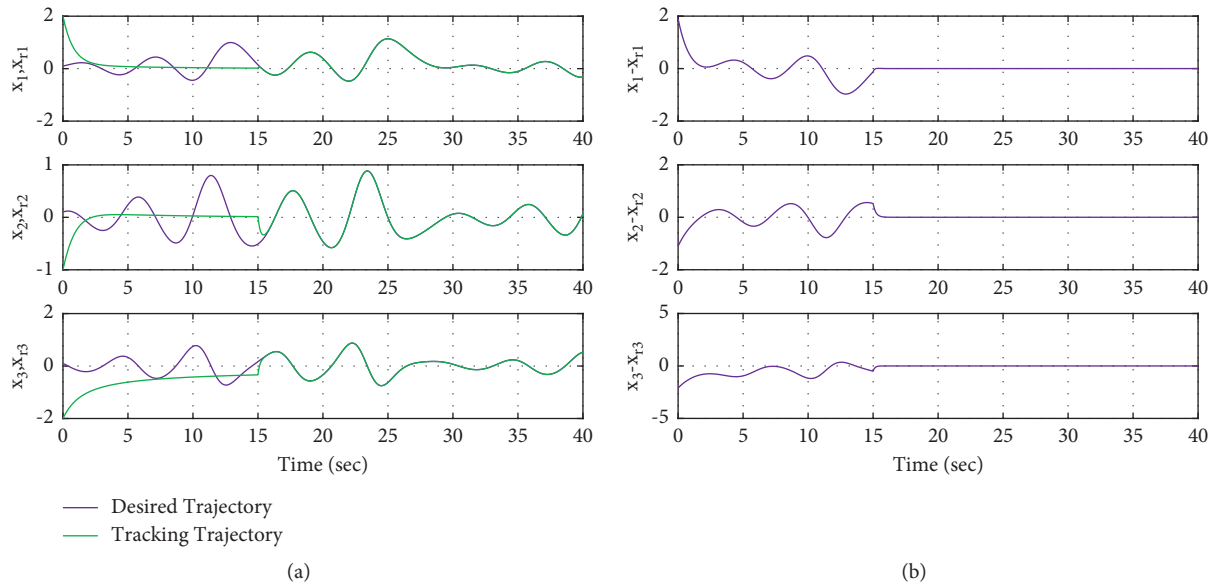


FIGURE 3: (a) Time evolution for the Genesio–Tesi reference states x_{r1} , x_{r2} , and x_{r3} with initial conditions $(0.1, 0.1, 0.1)$ (purple line) and time evolution for the neural network states x_1 , x_2 , and x_3 with initial conditions $(2, -1, -2)$ (green line). (b) Error between states $x_i - x_{r_i}$ with $i = 1, 2, 3$.

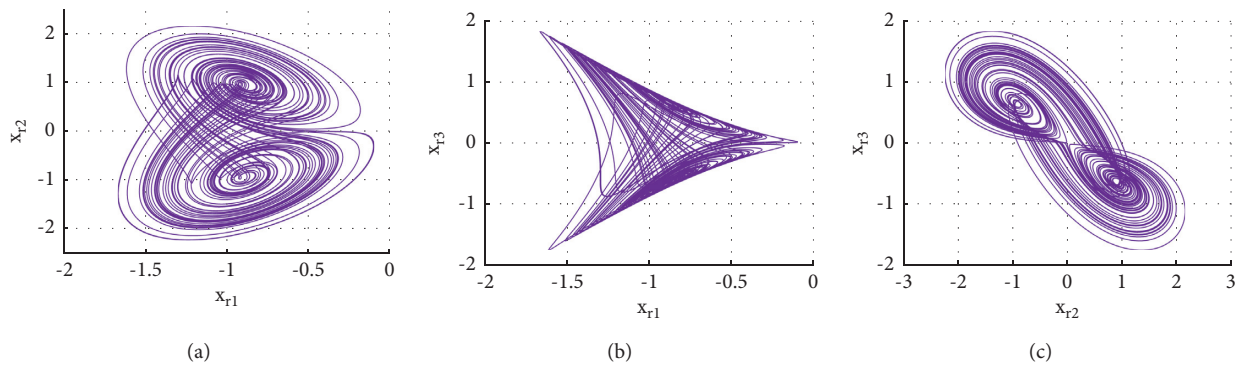


FIGURE 4: The Liu chaotic oscillator in the phase plane with initial conditions $[x_{r1}(0), x_{r2}(0), x_{r3}(0)]^T = [-1, -0.5, 0.5]^T$. (a) $x_{r1} - x_{r2}$ phase plane. (b) $x_{r1} - x_{r3}$ phase plane. (c) $x_{r2} - x_{r3}$ phase plane.

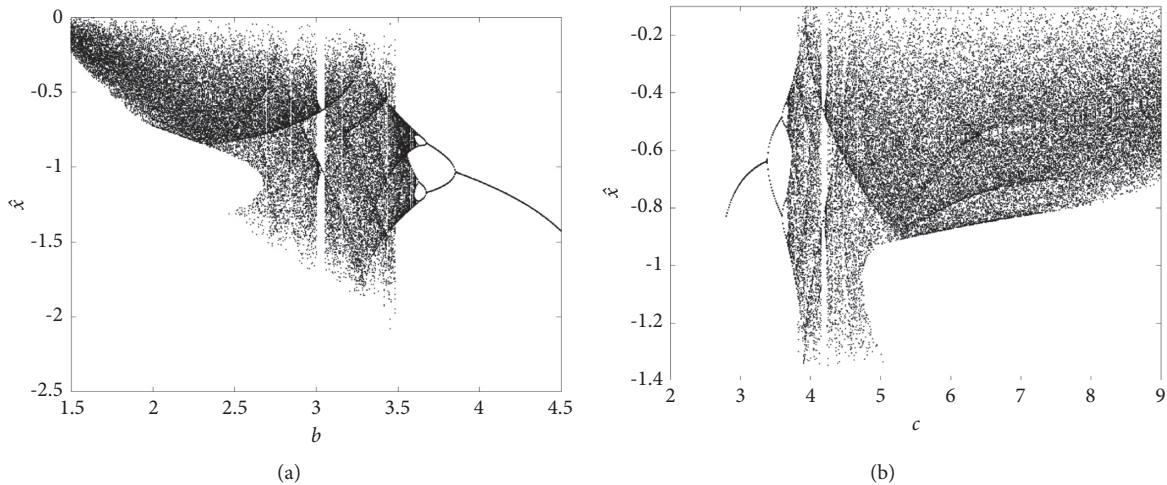


FIGURE 5: (a) Bifurcation diagram of Liu system with varying parameter b . (b) Bifurcation diagram of Liu system with varying parameter c .

The initial values of the delayed neural network are taken as $(0.1, 0.2, -0.1)$; also, we consider a delay $\tau = 15$ s. Simulation results are presented in Figure 6.

Here we consider the control law u defined as

$$\begin{bmatrix} u_1 \\ u_2 \\ u_3 \end{bmatrix} = -\psi \begin{bmatrix} x_1 - x_{r_1} \\ x_2 - x_{r_2} \\ x_3 - x_{r_3} \end{bmatrix} + \begin{bmatrix} -ax_{r_1} - m_1x_{r_2}^2 \\ bx_{r_2} - m_2x_{r_1}x_{r_3} \\ -cx_{r_3} + m_3x_{r_1}x_{r_2} \end{bmatrix}$$

$$- \begin{bmatrix} -1 & 0 & 0 \\ 0 & -1 & 0 \\ 0 & 0 & -1 \end{bmatrix} \begin{bmatrix} x_{r_1} \\ x_{r_2} \\ x_{r_3} \end{bmatrix} - \begin{bmatrix} 0.3 & \frac{4}{5} & 0 \\ \frac{2}{5} & 0.3 & 0 \\ 0 & 0 & 1 \end{bmatrix} \begin{bmatrix} \tanh(x_{r_1}(t - \tau)) \\ \tanh(x_{r_2}(t - \tau)) \\ \tanh(x_{r_3}(t - \tau)) \end{bmatrix}, \quad (32)$$

where ψ is a real constant given as in (30). Furthermore, Figure 6(a) presents the time-evolution of the delayed neural network (28) and the chaotic system (31), where they evolve independently until $\tau = 15$ seconds; at that time, the proposed control (32) law is incepted. Finally, in Figure 6(b), the error between $x_i - x_{r_i}$ states is displayed.

5. FPGA-Based Implementation

The digital implementations of chaotic systems have attracted increasing interest in the last few years [37, 38]. They provide certain advantages in comparison with analog-based systems, like accuracy and possible integration in embedded applications, especially in data encryption and secure communications, which exhibit various practical difficulties like the sensitivity of components to temperature, aging, etc. Recently, the digital-based chaotic implementations are realized considering different numerical circuit-based integrated systems like digital signal processors (DSPs), application specific integrated circuits (ASIC), and FPGA. But the FPGA implementation designs overcome the problems related to AISC and DSP-based applications; this is due to the excellent trade-off between computational power and the performance and reliability which it provides.

In this section, the FPGA realizations for the systems previously shown are addressed. We present two implementations: one of them implements the systems shown in Section 4.1 and the other implements those shown in Section 4.2. Both implementations were done into a Xilinx Zynq-7000 XC7Z020 FPGA chip. The LabVIEW FPGA compiler software and the National Instruments cRIO-9068 hardware were used. cRIO-9068 has attached the FPGA chip and the NI-9264 module. The NI-9264 module allows each design to have six analog outputs from 0 to 10 volts. Both designs use the states of the neural network and the chaotic system as outputs.

5.1. Description of the Designs. All the mathematical operations were done using fixed-point (FXP) arithmetic. FXP was chosen to reduce the hardware cost and achieve higher

speeds. We use 30 bits to represent each state of the neural network and the chaotic system; specifically, we use 7 bits for the integer part and 23 bits for the fractional part. In digital systems, the chaotic behavior may be affected by time discretization or low-resolution FXP arithmetic. In our case, we compute the maximum Lyapunov exponent (MLE) from the FXP sequences related to the implemented Liu and Genesio-Tesi systems by employing TISEAN package software [39]. The obtained values were as follows: MLE = 0.0664 for the Genesio-Tesi system and MLE = 0.0782 for the Liu system. The positive value for each MLE confirms chaotic behavior and validates the FXP resolution and the sampling time used.

5.1.1. Top Level. The top-level description of each implementation is shown in Figure 7, where k represents the sample index. In this work, the top-level description used allows to implement the tracker and the system to be tracked on the same chip, and is composed of the following modules: (a) the chaotic system to be tracked, (b) the delayed neural network, (c) the control law, and (e) the integration method. Note that the block diagram in Figure 7 applies to both designs.

5.1.2. Secondary Level. The dynamics of the chaotic system, which are represented in the dashed block labeled as (a) in Figure 7, are given by the time-discrete version of (27):

$$\begin{aligned} f_1[k] &= x_{r_2}[k], \\ f_2[k] &= x_{r_3}[k], \\ f_3[k] &= -x_{r_1}[k] - 1.1x_{r_2}[k] - 0.44x_{r_3}[k] + x_{r_1}^2[k], \end{aligned} \quad (33)$$

for the Genesio-Tesi case, and by the discrete version of (31):

$$\begin{aligned} f_1[k] &= -x_{r_1}[k] - x_{r_2}^2[k], \\ f_2[k] &= 2.5x_{r_2}[k] - 4x_{r_1}[k]x_{r_3}[k], \\ f_3[k] &= -5x_{r_3}[k] + 4x_{r_1}[k]x_{r_2}[k], \end{aligned} \quad (34)$$

for the Liu case. In both cases, FXP multipliers and adders were used to perform the arithmetic operations involved.

The dynamics of the delayed neural network, which are represented in the dashed block labeled as (b) in Figure 7, are given by the discrete version of (1):

$$\begin{aligned} \eta_1[k] &= -x_1[k] + \sum_{i=1}^3 w_{1,i} \tanh(x_i[k - m]) + u_1[k], \\ \eta_2[k] &= -x_2[k] + \sum_{i=1}^3 w_{2,i} \tanh(x_i[k - m]) + u_2[k], \\ \eta_3[k] &= -x_3[k] + \sum_{i=1}^3 w_{3,i} \tanh(x_i[k - m]) + u_3[k], \end{aligned} \quad (35)$$

where the $\tanh(\cdot)$ function was approximated by its fourth-order Taylor series, and FIFO buffers implemented on the block RAM of the device were used to perform the delay of m samples in the three states. Six FIFO registers were used,

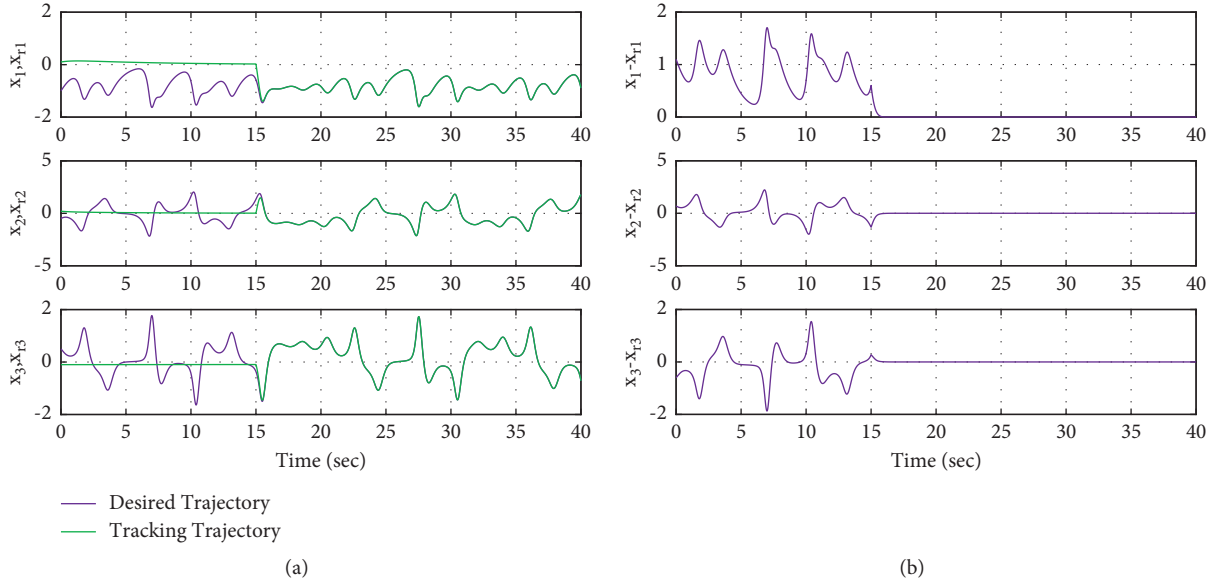


FIGURE 6: (a) Time evolution for the Liu reference states x_{r_1} , x_{r_2} , and x_{r_3} with initial values $(-1, -0.5, 0.5)$ (purple line) and time evolution for the neural network states x_1 , x_2 , and x_3 with initial condition $(0.1, 0.2, -0.1)$ (green line). (b) Error between states $x_i - x_{r_i}$ with $i = 1, 2, 3$.

each one with 16384 elements of 30 bits each. With this configuration, a delay of $m = 16384$ samples is generated in all the states.

The control law $\{u_1[k], u_2[k], u_3[k]\}$ applied to the neural network (35) is represented in the dashed block labeled as (c) in Figure 7. It was implemented as follows:

$$\begin{aligned} u_1[k] &= \psi e_1[k] + f_1[k] - x_{r_1}[k] - \sum_{i=1}^3 w_{1,i} \tanh(x_{r_i}[k - m]), \\ u_2[k] &= \psi e_2[k] + f_2[k] - x_{r_2}[k] - \sum_{i=1}^3 w_{2,i} \tanh(x_{r_i}[k - m]), \\ u_3[k] &= \psi e_3[k] + f_3[k] - x_{r_3}[k] - \sum_{i=1}^3 w_{3,i} \tanh(x_{r_i}[k - m]), \end{aligned} \quad (36)$$

where $e_j[k] = x_j[k] - x_{r_j}[k]$ for $j = 1, 2, 3$ denotes the error sequence.

Finally, shift registers were used to perform the numerical integration. In order to use an integration time of H seconds, a mod- M counter is inferred to derive an enable tick for all the registers each H seconds, where $M = 4560$ ticks. The Euler method is based on the definition of the derivative operator and was selected to perform the numerical integration in order to reduce the complexity of the design due to its maximum simplicity. The block description of this method is presented in the dashed block labeled as (d) in Figure 7, which is described as

$$\begin{aligned} x_{r_i}[k + 1] &= x_{r_i}[k] + H f_i[k], \\ x_i[k + 1] &= x_i[k] + H \eta_i[k], \end{aligned} \quad (37)$$

where $i = 1, 2, 3$.

5.2. Implementation Results. The resources used for each design are presented in Table 2. The total amount of resources employed was obtained from the NI-FPGA compiler report. The minimal amount of ticks $M = 4560$ needed to get a new valid sample was computed using the LabVIEW FPGA tick count function. Its value was the same for both designs addressed. The achieved latencies for both designs are expressed as $L = 114 \mu\text{s}$.

The states of the chaotic system and the neural network were scaled to six analog outputs of the NI-9264 module within the range of 0 to 10 volts. These outputs were monitored by a Tektronix TDS5104B digital oscilloscope. The results for the system implementation are given in Figures 8(a)–8(d). The phase portraits $\{x_{r_1}[k] - x_{r_3}[k]\}$, $\{x_{r_1}[k] - x_{r_2}[k]\}$, and $\{x_{r_2}[k] - x_{r_3}[k]\}$ are described in Figures 8(a)–8(c). The time evolution of $x_{r_1}[k]$, $x_{r_2}[k]$, and $x_{r_3}[k]$ is shown in Figure 8(d). Regarding the performance of the neural network, the phase portraits $\{x_{r_1}[k] - x_1[k]\}$, $\{x_{r_2}[k] - x_2[k]\}$, and $\{x_{r_3}[k] - x_3[k]\}$ are shown in Figures 9(a)–9(c). Note that each phase portrait evidences a 45° line, which is related to the correct tracking performed by the time-delay neural network. Additional evidence of the tracking is shown in Figure 9(d) where the time evolution of $x_{r_1}[k]$ and $x_1[k]$ and its error $e_1[k]$ is described.

In addition, similar results were achieved for the Liu system. The results for the Liu system are shown in Figures 10 and 11.

5.3. Comparison with Other Works. Synchronization is an emerging behavior in neural networks. It has received academic attention because of a wide variety of applications [3, 8]. Schemes that consider chaotic systems and delayed recurrent neural networks are of particular interest due to

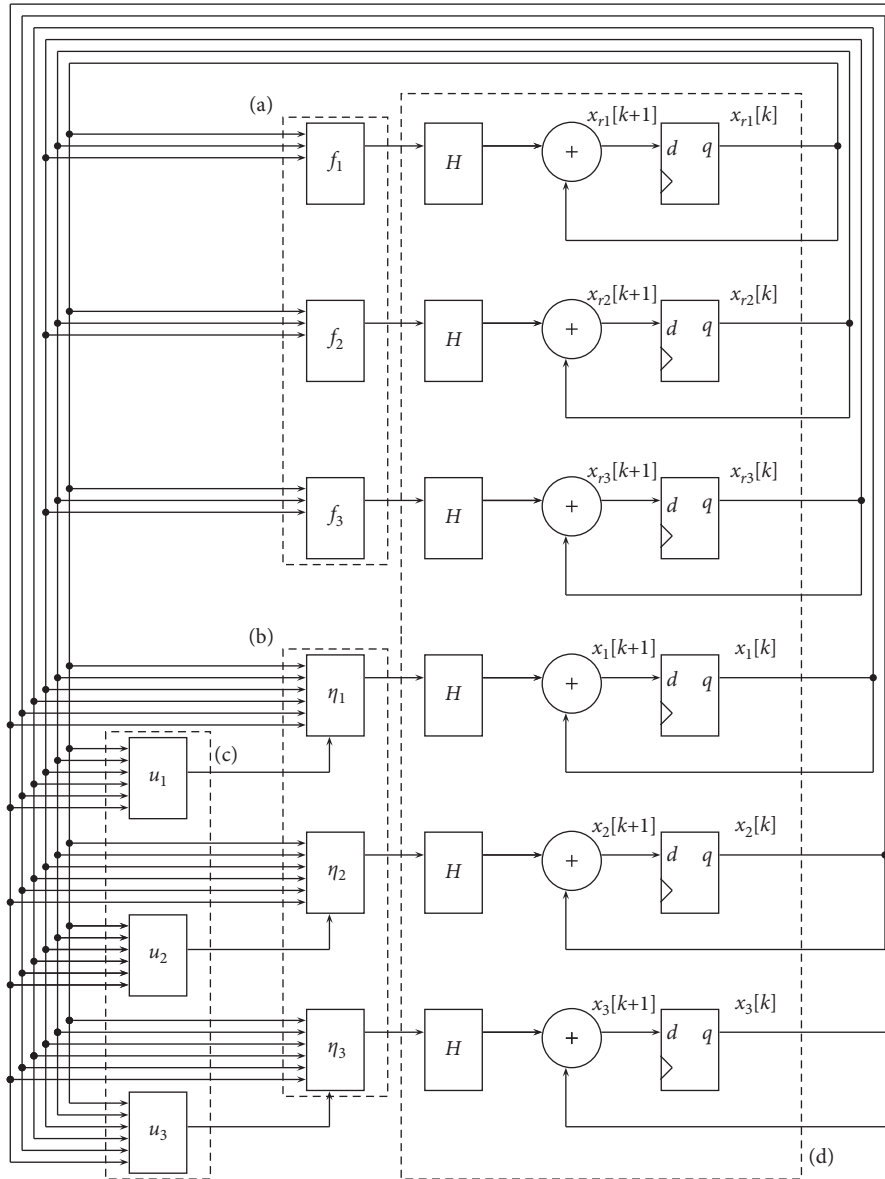


FIGURE 7: Block diagram describing the top-level description of the proposed implementation for the Genesis-Tesi and Liu trackers, where the dashed blocks represent (a) the chaotic system to be tracked given in (31) or (32), (b) the delayed neural network given in (33), (c) the control law given in (34), and (d) the Euler integration method (35).

TABLE 2: FPGA chip resource usage for the Xilinx Zynq-7000 XC7Z020 FPGA chip (the resources used for both implementations are shown in the table).

	Genesis-Tesi			Liu		
	Used	Total	Percent (%)	Used	Total	Percent (%)
Slice registers	24372	106400	22.9	24253	106400	22.8
Slice LUT	27543	53200	51.8	28550	53200	53.7
DSP48s	173	220	78.6	201	220	91.4
Block RAMs	103	140	73.6	103	140	73.6
Clock	40 MHz			40 MHz		

the high complexity depicted in their sensibility to initial conditions, parameters, and time delays. For that reason, synchronizing or controlling these schemes is challenging work; even more, the practical implementation is not a

trivial task. In this section, we perform a survey to demonstrate the pertinence of the proposed control method and the digital implementation. In Table 3, some synchronization schemes in a drive-response configuration are displayed

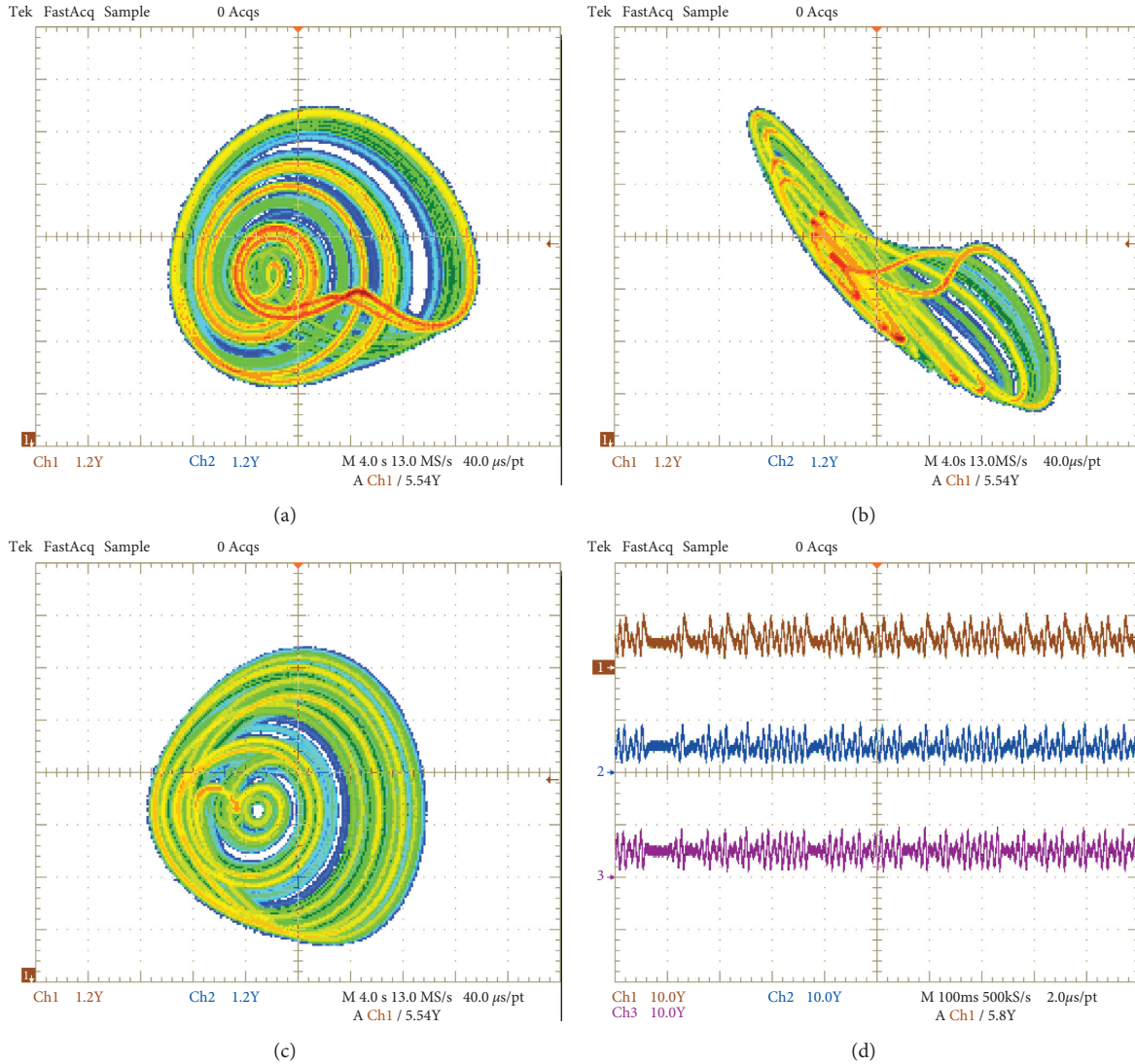


FIGURE 8: Response of the Genesio–Tesi chaotic oscillator implemented, with initial conditions $[x_{r_1}[0], x_{r_2}[0], x_{r_3}[0]]^T = [0.1, 0.1, 0.1]^T$. (a) $x_{r_1} - x_{r_2}$ phase plane. (b) $x_{r_1} - x_{r_3}$ phase plane. (c) $x_{r_2} - x_{r_3}$ phase plane. (d) Time evolution of x_{r_1} (brown line “CH1”), x_{r_2} (blue line “CH2”), and x_{r_3} (purple line “CH3”).

with their respective control approaches. From the information depicted in Table 3, reference [40] considers the implementation of a synchronization scheme on an Arduino chip while the rest of the references only consider numerical results. In this paper, we implement the chaotic system (27), the delayed recurrent neural network (28), and the control laws (29) and (30) in an FPGA.

Table 4 presents a brief review, including some FPGA-based implementations of chaotic systems over the last ten years. Table 4 does not include detailed characteristics like the chip resource usage and the achieved performance because these parameters are hardware dependent. Instead, it includes generalized details like a brief description of the application, the numerical representation, the integration method, and the hardware used.

From Table 4, it can be seen that the implementation of a single chaotic system is a common practice. However, recent works include a chaotic node as a module of a bigger scale

system, for example, a complex network in [38], an OFDM transmission system in [52], or a tracking scheme (this work).

It can also be seen that fixed-point (FXP) and floating-point (IEEE-754 FLP) implementations are equally used. The numerical representation selected in each work is related to a trade-off between accuracy and resource usage. It is evident that, in general, FXP representations require fewer resources and achieve better time performance, while an FLP representation has better numerical accuracy than FXP.

The integration method is used to implement a discrete version of the system. In Table 4, we found a prevalence of the following methods: fourth-order Runge–Kutta (RK4), forward Euler, and Heun. Note that the numerical integration method is not correlated to the date of the work, as we can see recent works using forward Euler and older works using a more complicated RK4 algorithm. Again, as the

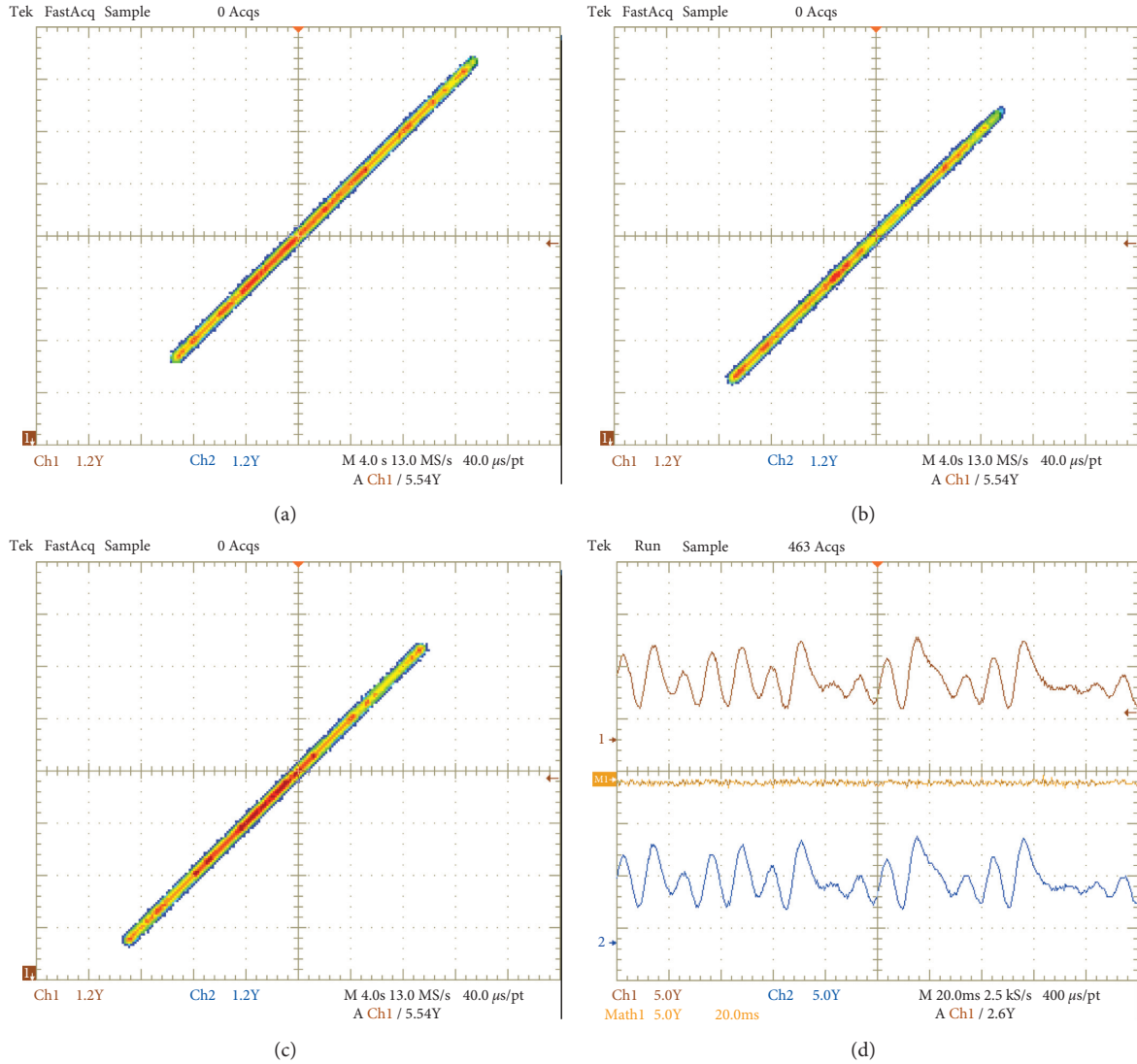


FIGURE 9: Synchronization of the time-delay neural network and the Genesio-Tesi oscillator, with initial conditions $[x_{r_1}[0], x_{r_2}[0], x_{r_3}[0]]^T = [0.1, 0.1, 0.1]^T$ and $[x_1[0], x_2[0], x_3[0]]^T = [1, 1, 1]^T$. (a) $x_{r_1} - x_1$ phase plane. (b) $x_{r_2} - x_2$ phase plane. (c) $x_{r_3} - x_3$ phase plane. (d) Time evolution of x_{r_1} (brown line “CH1”), x_1 (blue line “CH2”), and e_1 (orange line “Math1”).

numerical representation, the integration algorithm selection is based on a trade-off between the accuracy and complexity of the design.

There is a diversity of devices and software platforms used for the FPGA fast prototyping. Some devices are displayed in the last column of Table 4, while some examples of

the software platforms are the Matlab HDL Coder (used in [48]), the LabVIEW FPGA software (used in [46]), and Xilinx design suites like ISE and Vivado (used in [49, 52]). In this work, we use LabVIEW FPGA environment. This programming environment is well suited for the system-level design of prototypes.

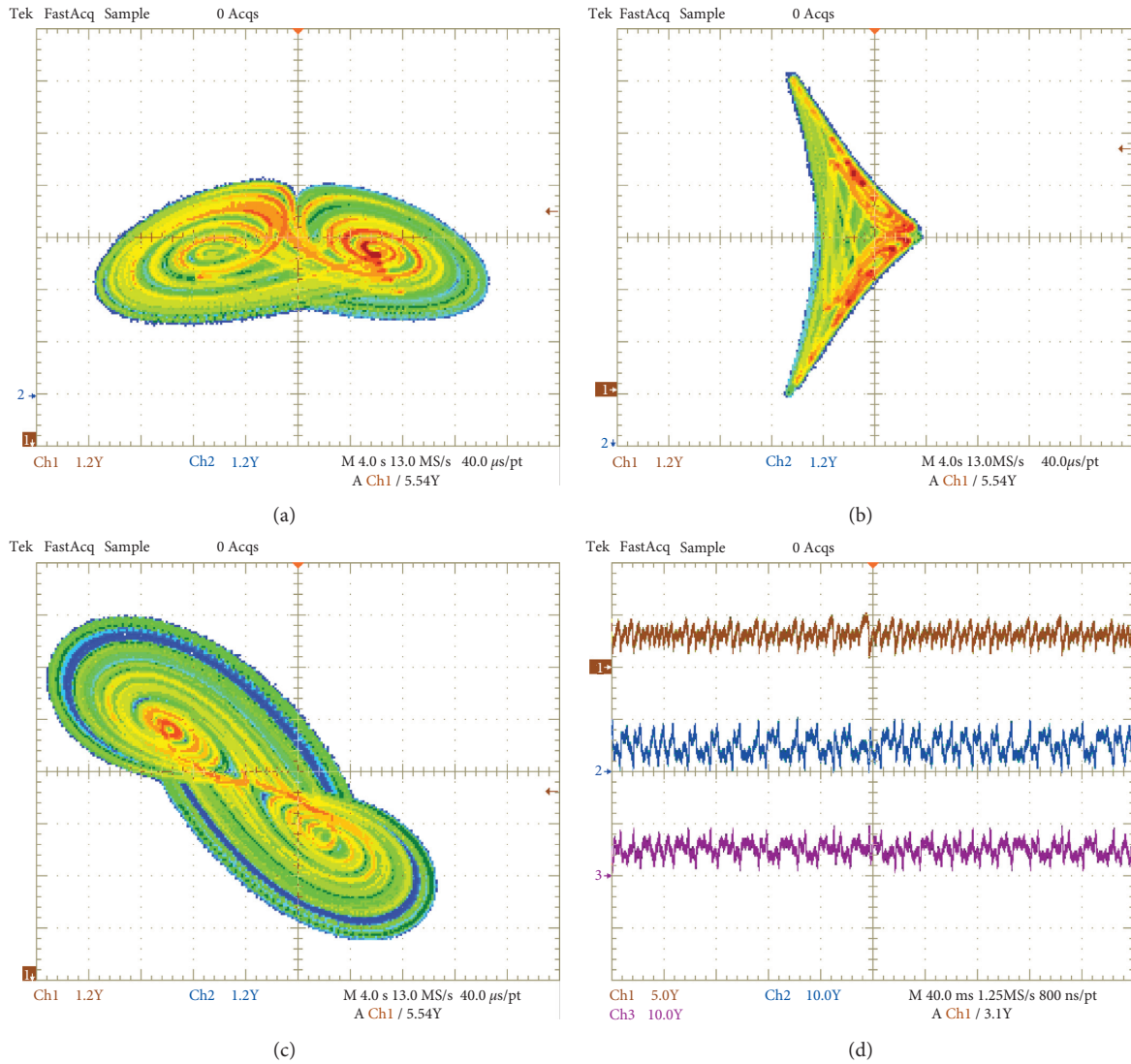


FIGURE 10: Response of the Liu chaotic oscillator implemented, with initial conditions $[x_{r_1}[0], x_{r_2}[0], x_{r_3}[0]]^T = [0.1, 0.1, 0.1]^T$. (a) $x_{r_2} - x_{r_1}$ phase plane. (b) $x_{r_1} - x_{r_3}$ phase plane. (c) $x_{r_2} - x_{r_3}$ phase plane. (d) Time evolution of x_{r_1} (brown line "CH1"), x_{r_2} (blue line "CH2"), and x_{r_3} (purple line "CH3").

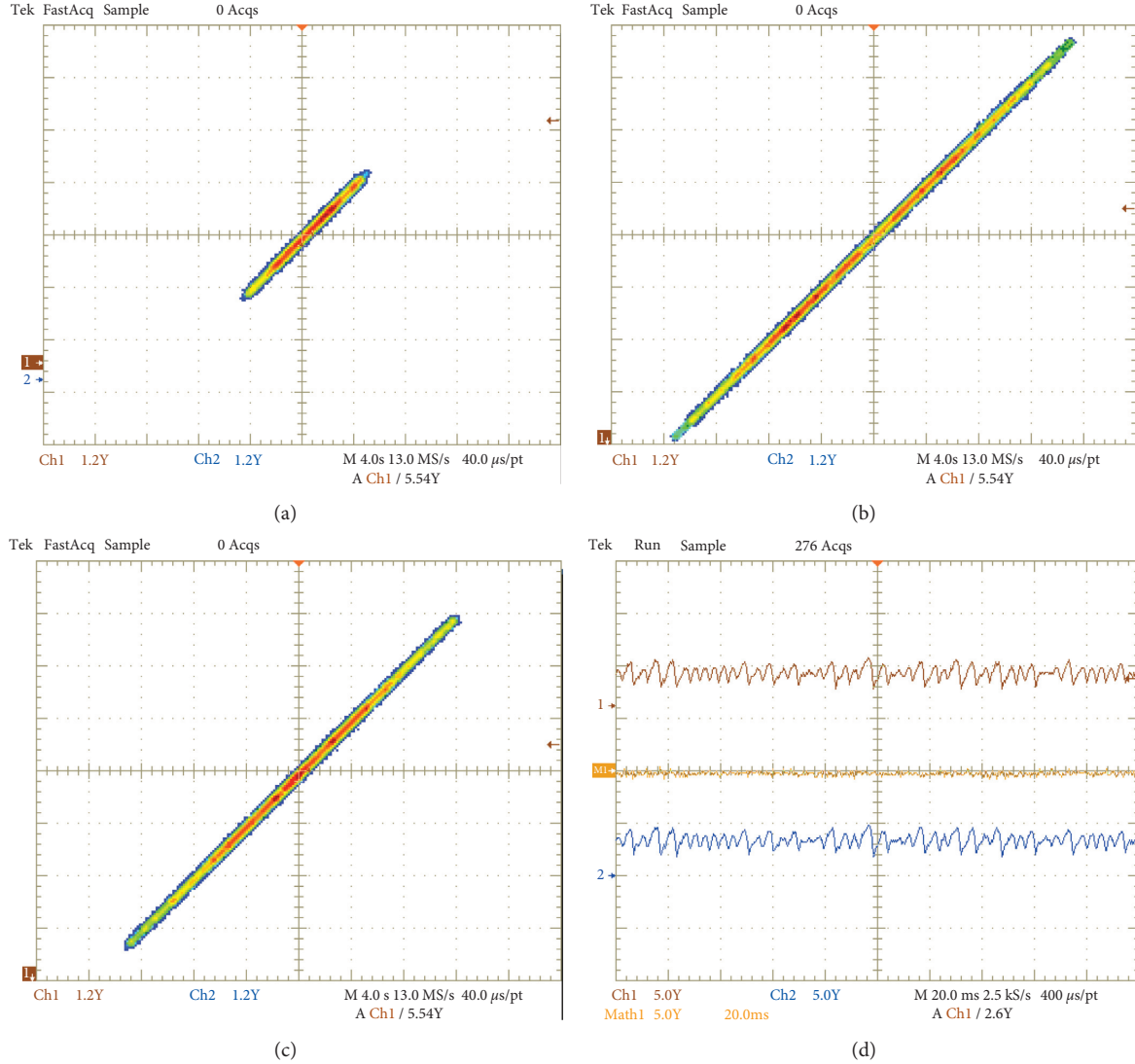


FIGURE 11: Synchronization of the time-delay neural network and the Liu oscillator, with initial conditions $[x_{r_1}[0], x_{r_2}[0], x_{r_3}[0]]^T = [0.1, 0.1, 0.1]^T$ and $[x_1[0], x_2[0], x_3[0]]^T = [1, 1, 1]^T$. (a) $x_{r_1} - x_1$ phase plane. (b) $x_{r_2} - x_{r_3}$ phase plane. (c) $x_{r_3} - x_3$ phase plane. (d) Time evolution of x_{r_1} (brown line “CH1”), x_1 (blue line “CH2”), and e_1 (orange line “Math1”).

TABLE 3: Some synchronization schemes proposed in the literature.

Reference	Approach	Synchronization scheme	Implementation
[40]	Extended Kalman filter	Drive-response between Genesio–Tesi multiscroll and recurrent neural network	Digital: Arduino uno microcontroller
[41]	Inverse optimality	Drive-response between chaotic time-delay recurrent neural networks	None
[19]	V-stability and Lyapunov theory	Drive-response between a delayed recurrent neural network and a complex dynamical network	None
[42]	Quantized sliding-mode control	Drive-response between delayed memristive neural networks	None
[43]	Adaptive intermittent control	Drive-response between chaotic systems with time-varying delay	None
Proposed	Lyapunov–Krasovskii and Lur’e theory	Drive-response between Liu-delayed recurrent neural network and Genesio–Tesi and delayed recurrent neural networks	Digital: FPGA Xilinx Zynq-7000 XC7Z020

TABLE 4: Some FPGA-based implementations of chaotic systems over the last decade.

Reference and year	Brief description	Numerical representation	Integration method	Device
[44], 2009	3D Chen chaotic system	IEEE-754 FLP 32 bits	RK4	Xilinx Virtex-II XCV1000FG456-4
[45], 2011	A new hyperchaotic 4D system	–	RK4	Xilinx Virtex-II Pro XC2VP30
[47], 2013	Switching 3D chaotic systems	FXP 32 bits 16I16Q	Euler	Xilinx Virtex-II FPGA 2VP30FFG896-7
[46], 2015	A 3D chaotic system	IEEE-754 FLP 32 bits	RK4	Xilinx Virtex-6 XC6VLX550T-2FF1759
[48], 2017	Fractional-order chaotic system	FXP 32 bits	Tustin	Altera Cyclone IV EP4CE11529C7N
[38], 2018	Fractional-order complex networks with chaotic nodes	FXP 24 bits 4I20Q	Grünwald–Letnikov	Xilinx Zynq-7000 XC7Z020
[49], 2019	Fractional-order chaotic system	FXP 32 bits	Grünwald–Letnikov	Altera Cyclone IV GX FPGA DE2I-150
[50], 2019	The Lü–Chen 2002 chaotic system	FXP 32 bits 16I16Q	Heun	Xilinx Virtex-6 XC6VLX75T-3FF484
[51], 2019	A new 3D chaotic system	FXP 32 bits 7I25Q	Euler and RK4	Xilinx Virtex-6 XC6VLX75T-3FF484
[52], 2019	OFDM system using chaos	FXP 128 bits	Euler	–
Proposed	A tracking scheme (master and slave)	FXP 30 bits 7I23Q	Euler	Xilinx Zynq-7000 XC7Z020

6. Conclusions

In this paper, the trajectory tracking for a nonlinear system with a time-delay neural network was obtained. In particular, neural networks are forced to follow reference signals generated by a chaotic system, thus achieving the synchronization state. The control law that guarantees trajectory tracking was obtained by considering the Lyapunov–Krasovskii and Lur’e theory. The applicability of the approach was illustrated by considering two different chaotic systems: Liu’s chaotic system and Genesio–Tesi chaotic system. Numerical simulations and FPGA implementations were presented to show the effectiveness of obtained theoretical results. The results obtained allowed us to demonstrate the successful implementation of these trajectory tracking examples on FPGA. Moreover, we confirm that the Lyapunov–Krasovskii theory is an efficient method to deal with the global asymptotic stability of a recurrent neural network with time delay. The synchronization of chaotic systems and the neural networks on different chips streamed through a physical channel could be addressed in a future continuation of this work. It should consider the channel and its properties, and it may be useful in the area of secure communications, where it is common to use the synchronization of chaotic systems as an encryption tool.

Data Availability

The data set used to support the findings of this study is available from the corresponding author upon request.

Conflicts of Interest

The authors declare that they have no potential conflicts of interest.

Acknowledgments

J. Perez-Padron and J. Paz-Perez acknowledge the academic group “Sistemas dinámicos” of “Facultad de Ciencias Físico-Matemáticas” at UANL. C. Posadas-Castillo, E. Zambrano-Serrano, and M.A. Platas-Garza acknowledge “Departamento de Electrónica y Automatización” from “Facultad de Ingeniería Mecánica y Eléctrica” at UANL. C. Posadas-Castillo and E. Zambrano-Serrano acknowledge CONACYT/Mexico (research grants no. 166654 A1-S-31628 and 350385). C. Posadas-Castillo and M.A. Platas-Garza acknowledge UANL (research grants IT1784-21 and IT1824-21).

References

- [1] S. Samarasinghe, *Neural Networks for Applied Sciences and Engineering: From Fundamentals to Complex Pattern Recognition*, Auerbach publications, Broken Sound Parkway, NW, USA, 2016.
- [2] R. Manivannan, S. Panda, K. T. Chong, and J. Cao, “An arcak-type state estimation design for time-delayed static neural networks with leakage term based on unified criteria,” *Neural Networks*, vol. 106, pp. 110–126, 2018.
- [3] Z. Xu, S. Li, X. Zhou, and T. Cheng, “Dynamic neural networks based adaptive admittance control for redundant manipulators with model uncertainties,” *Neurocomputing*, vol. 357, pp. 271–281, 2019.
- [4] T. Guo, L. Wang, M. Zhou, and S. Duan, “A multi-layer memristive recurrent neural network for solving static and dynamic image associative memory,” *Neurocomputing*, vol. 334, pp. 35–43, 2019.
- [5] Y. Jiang, C. Yang, J. Na, G. Li, Y. Li, and J. Zhong, “A brief review of neural networks based learning and control and their applications for robots,” *Complexity*, vol. 2017, Article ID 1895897, 14 pages, 2017.

- [6] Y. Li, W. Zheng, Z. Cui, and T. Zhang, "Face recognition based on recurrent regression neural network," *Neurocomputing*, vol. 297, pp. 50–58, 2018.
- [7] C. Qinetal, "Convolutional recurrent neural networks for dynamic MR image reconstruction," *IEEE Transactions on Medical Imaging*, vol. 38, no. 1, pp. 280–290, 2018.
- [8] K. Rajagopal, A. J. M. Khalaf, F. Parastesh, I. Moroz, A. Karthikeyan, and S. Jafari, "Dynamical behavior and network analysis of an extended Hindmarsh-Rose neuron model," *Nonlinear Dynamics*, vol. 98, no. 1, pp. 477–487, 2019.
- [9] J. Wang, F. Liu, and S. Qin, "Global exponential stability of uncertain memristor-based recurrent neural networks with mixed time delays," *International Journal of Machine Learning and Cybernetics*, vol. 10, no. 4, pp. 743–755, 2019.
- [10] G. Chen and Y. Yang, "New sufficient conditions for finite time stability of nonlinear time delay systems," *Asian Journal of Control*, vol. 21, no. 5, pp. 2321–2329, 2019.
- [11] E. Zambrano-Serrano and A. Anzo-Hernandez, "A novel antimonotonic hyperjerk system: analysis, synchronization and circuit design," *Physica D: Nonlinear Phenomena*, vol. 424, no. 1–8, p. 132927, 2021.
- [12] A. Taher Azar, F. E. Serrano, Q. Zhu et al., "Robust stabilization and synchronization of a novel chaotic system with input saturation constraints," *Entropy*, vol. 23, no. 3, p. 1110, 2021.
- [13] Y. Kan, J. Lu, J. Qiu, and J. Kurths, "Exponential synchronization of time-varying delayed complex-valued neural networks under hybrid impulsive controllers," *Neural Networks*, vol. 114, pp. 157–163, 2019.
- [14] S. Yang, Z. Guo, and J. Wang, "Global synchronization of multiple recurrent neural networks with time delays via impulsive interactions," *IEEE Transactions on Neural Networks and Learning Systems*, vol. 28, no. 7, pp. 1657–1667, 2016.
- [15] H. R. Karimi and H. Gao, "New delay-dependent exponential H_∞ synchronization for uncertain neural networks with mixed time delays," *IEEE Transactions on Systems, Man, and Cybernetics, Part B (Cybernetics)*, vol. 40, no. 1, pp. 173–185, 2009.
- [16] B. Huang, H. Zhang, D. Gong, and J. Wang, "Synchronization analysis for static neural networks with hybrid couplings and time delays," *Neurocomputing*, vol. 148, pp. 288–293, 2015.
- [17] Z. Zhang and L. Ren, "New sufficient conditions on global asymptotic synchronization of inertial delayed neural networks by using integrating inequality techniques," *Nonlinear Dynamics*, vol. 95, no. 2, pp. 905–917, 2019.
- [18] Q. Song, J. Cao, and F. Liu, "Pinning synchronization of linearly coupled delayed neural networks," *Mathematics and Computers in Simulation*, vol. 86, pp. 39–51, 2012.
- [19] J. P. Perez, J. P. Padron, A. F. Hemandez, and S. Arroyo, "Complex dynamical network control for trajectory tracking using delayed recurrent neural networks," *Mathematical Problems in Engineering*, vol. 2014, Article ID 162610, 7 pages, 2014.
- [20] X.-M. Zhang, Q.-L. Han, X. Ge, and D. Ding, "An overview of recent developments in Lyapunov-Krasovskii functionals and stability criteria for recurrent neural networks with time-varying delays," *Neurocomputing*, vol. 313, pp. 392–401, 2018.
- [21] J. Chen, J. H. Park, and S. Xu, "Stability analysis of continuous-time systems with time-varying delay using new Lyapunov-Krasovskii functionals," *Journal of the Franklin Institute*, vol. 355, no. 13, pp. 5957–5967, 2018.
- [22] W. Yang, Y.-W. Wang, Y. Shen, and L. Pan, "Cluster synchronization of coupled delayed competitive neural networks with two time scales," *Nonlinear Dynamics*, vol. 90, no. 4, pp. 2767–2782, 2017.
- [23] X.-M. Qing-Long Han and Q.-L. Han, "New Lyapunov-Krasovskii functionals for global asymptotic stability of delayed neural networks," *IEEE Transactions on Neural Networks*, vol. 20, no. 3, pp. 533–539, 2009.
- [24] A. Kundu, P. Das, and A. B. Roy, "Stability, bifurcations and synchronization in a delayed neural network model of n-identical neurons," *Mathematics and Computers in Simulation*, vol. 121, pp. 12–33, 2016.
- [25] J. Perez-Padron, J. P. Perez, C. F. Mendez-Barrios, and V. Ramírez-Rivera, "Trajectory tracking using adaptive fractional PID control of biped robots with time-delay feedback," in *Becoming Human with Humanoid from Physical Interaction to Social Intelligence*, A. Hoirul Basori, A. Leylavi Shoushtari, and A. V. T. IntechOpen, Eds., IntechOpen, London, UK, 2020.
- [26] J. Perez-Padron and J. P. Perez-Padron, "Trajectory tracking error between plant, reference and adaptive neural networks using two control law for two-link robot manipulator," in *Proceedings of the 2015 International Conference on Environmental Science and Sustainable Development (ICESSD)*, Bangkok, Thailand, October 2015.
- [27] J. Perez-Padron, J. P. Perez, C. F. Mendez Barrios, and E. J. González Galván, "Fractional complex dynamical systems for trajectory tracking using fractional neural network via fractional order PID control law," *Computación Y Sistemas*, vol. 24, no. 1, pp. 349–357, 2020.
- [28] J. Jun Wang and J. Wang, "Global asymptotic and robust stability of recurrent neural networks with time delays," *IEEE Transactions on Circuits and Systems I: Regular Papers*, vol. 52, no. 2, pp. 417–426, 2005.
- [29] J. Cao, Z. Wang, and Y. Sun, "Synchronization in an array of linearly stochastically coupled networks with time delays," *Physica A: Statistical Mechanics and Its Applications*, vol. 385, no. 2, pp. 718–728, 2007.
- [30] V. Kolmanovskii and A. Myshkis, *Applied Theory of Functional Differential Equations*, Springer Science & Business Media, Berlin, Germany, 1992.
- [31] M. Krstic and H. Deng, *Stabilization of Nonlinear Uncertain Systems*, Springer-Verlag, Berlin, Germany, 1998.
- [32] E. N. Sanchez, J. P. Perez, and G. Chen, "Using dynamic neural networks to generate chaos: an inverse optimal control approach," *International Journal of Bifurcation and Chaos*, vol. 11, no. 3, pp. 857–863, 2001.
- [33] R. Genesio and A. Tesi, "Harmonic balance methods for the analysis of chaotic dynamics in nonlinear systems," *Automatica*, vol. 28, no. 3, pp. 531–548, 1992.
- [34] J. C. Sprott, *Elegant Chaos: Algebraically Simple Chaotic Flows*, World Scientific, Singapore, 2010.
- [35] A. Wolf, J. B. Swift, H. L. Swinney, and J. A. Vastano, "Determining Lyapunov exponents from a time series," *Physica D: Nonlinear Phenomena*, vol. 16, no. 3, pp. 285–317, 1985.
- [36] C. Liu, L. Liu, and T. Liu, "A novel three-dimensional autonomous chaos system, Chaos," *Solitons & Fractals*, vol. 39, no. 4, pp. 1950–1958, 2009.
- [37] J. M. Munoz-Pacheco, C. Posadas-Castillo, and E. Zambrano-Serrano, "The effect of a non-local fractional operator in an asymmetrical glucose-insulin regulatory system: analysis, synchronization and electronic Implementation," *Symmetry*, vol. 12, no. 9, p. 1395, 2020.
- [38] A. G. Soriano-Sanchez, C. Posadas-Castillo, M. A. Platas-Garza, and A. Arellano-Delgado, "Synchronization and FPGA realization of complex networks with fractional-order Liu

- chaotic oscillators,” *Applied Mathematics and Computation*, vol. 332, pp. 250–262, 2018.
- [39] R. Hegger, H. Kantz, and T. Schreiber, “Practical implementation of nonlinear time series methods: the TISEAN package,” *Chaos: An Interdisciplinary Journal of Nonlinear Science*, vol. 9, no. 2, pp. 413–435, 1999.
- [40] C. E. Castañeda, D. López-Mancilla, R. Chiu et al., “Discrete-time neural synchronization between an arduino microcontroller and a compact development system using multi-scroll chaotic signals,” *Chaos, Solitons & Fractals*, vol. 119, pp. 269–275, 2019.
- [41] Z. Liu, “Design of nonlinear optimal control for chaotic synchronization of coupled stochastic neural networks via Hamilton-Jacobi-Bellman equation,” *Neural Networks*, vol. 99, pp. 166–177, 2018.
- [42] B. Sun, S. Wang, Y. Cao, Z. Guo, T. Huang, and S. Wena, “Exponential synchronization of memristive neural networks with time-varying delays via quantized sliding-mode control,” *Neural Networks*, vol. 126, pp. 163–169, 2020.
- [43] Y. Wang and L. Dong, “Adaptive synchronization of chaotic systems with time-varying delay via aperiodically intermittent control,” *Soft Computing*, vol. 24, pp. 12773–12780, 2020.
- [44] S. Sadoudi, M. Salah Azzaz, M. Djeddou, and M. Benssalah, “An FPGA real-time implementation of the Chen’s chaotic system for securing chaotic communications,” *International Journal of Nonlinear Science*, vol. 7, no. 4, pp. 467–474, 2009.
- [45] Z. Q. Chen, G. Q. Liang, and J. G. Tong, “The FPGA implementation of hyperchaotic system based upon VHDL design,” in *Proceedings of the 2011 Fourth International Workshop on Chaos-Fractals Theories and Applications*, pp. 47–51, Hangzhou, China, October 2011.
- [46] A. Akgul, H. Calgan, I. Koyuncu, I. Pehlivan, and A. Istanbulu, “Chaos-based engineering applications with a 3D chaotic system without equilibrium points,” *Nonlinear Dynamics*, vol. 84, no. 2, pp. 481–495, 2016.
- [47] M. Salah Azzaz, C. Tanougast, S. Sadoudi, R. Fellah, and A. Dandache, “A new auto-switched chaotic system and its FPGA implementation,” *Communications in Nonlinear Science and Numerical Simulation*, vol. 18, no. 7, pp. 1792–1804, 2013.
- [48] D. K. Shah, R. B. Chaurasiya, V. A. Vyawahare, K. Patil, and M. D. Patilb, “FPGA implementation of fractional-order chaotic systems,” *AEU-International Journal of Electronics and Communications*, vol. 78, pp. 245–257, 2017.
- [49] A. D. Pano-Azucena, B. Ovilla-Martinez, E. Tlelo-Cuautle, J. Manuel Muñoz-Pacheco, and L. G. de la Fraga, “FPGA-based implementation of different families of fractional-order chaotic oscillators applying Grünwald-Letnikov method,” *Communications in Nonlinear Science and Numerical Simulation*, vol. 72, pp. 516–527, 2019.
- [50] M. Tuna, M. Alçın, İ. Koyuncu, C. B. Fidan, and İ. Pehlivan, “High speed FPGA-based chaotic oscillator design,” *Microprocessors and Microsystems*, vol. 66, pp. 72–80, 2019.
- [51] A. Sambas, S. Vaidyanathan, E. Tlelo-Cuautle et al., “A novel chaotic system with two circles of equilibrium points: multistability, electronic circuit and FPGA realization,” *Electronics*, vol. 8, no. 11, p. 1211, 2019.
- [52] Y. Wang, Y. Xuelin, and W. Hu, “FPGA implementation of real-time secure OFDM transmission using digital chaos,” in *Proceedings of the 20th International Conference on Transparent Optical Networks ICTON*, July 2018.

Research Article

Circuit Implementation Synchronization between Two Modified Fractional-Order Lorenz Chaotic Systems via a Linear Resistor and Fractional-Order Capacitor in Parallel Coupling

Juan Liu,^{1,2,3} Xuefeng Cheng,^{3,4} and Ping Zhou ⁴

¹Chongqing University, Chongqing 400044, China

²Chongqing Institute of Green and Intelligent Technology, Chinese Academy of Sciences, Chongqing 400714, China

³Chongqing College, University of Chinese Academy of Sciences, Chongqing 400722, China

⁴School of Science, Chongqing University of Posts and Telecommunications, Chongqing 400065, China

Correspondence should be addressed to Ping Zhou; zhouping@cqupt.edu.cn

Received 12 July 2021; Accepted 10 August 2021; Published 19 August 2021

Academic Editor: Viet-Thanh Pham

Copyright © 2021 Juan Liu et al. This is an open access article distributed under the Creative Commons Attribution License, which permits unrestricted use, distribution, and reproduction in any medium, provided the original work is properly cited.

In this study, a modified fractional-order Lorenz chaotic system is proposed, and the chaotic attractors are obtained. Meanwhile, we construct one electronic circuit to realize the modified fractional-order Lorenz chaotic system. Most importantly, using a linear resistor and a fractional-order capacitor in parallel coupling, we suggested one chaos synchronization scheme for this modified fractional-order Lorenz chaotic system. The electronic circuit of chaos synchronization for modified fractional-order Lorenz chaotic has been given. The simulation results verify that synchronization scheme is viable.

1. Introduction

In the last twenty years, many fractional-order systems [1–9] have been used to discuss the dynamics, wave stability, initials, and boundary effect. Many real-world physical systems can be more accurately described by fractional-order differential equations (FODE) [3–6, 10, 11], e.g., diffusion-wave, super diffusion, heat conduction, dielectric polarization, viscoelasticity, and electromagnetic waves. The complex behavior such as chaos has been observed in many physical fractional-order systems, e.g., the fractional-order brushless DC motor chaotic system [6], the fractional-order Lorenz chaotic system [7], the fractional-order Chua's circuit [8], the fractional-order Duffing chaotic system [9], the fractional-order multistable locally active memristor [12], the fractional-order gyroscopes system [10], and the fractional-order microelectromechanical chaotic system [11]. Meanwhile, synchronization of chaotic systems has attracted extensive attention in recently years, and many synchronization strategies [10, 11, 13–15] have been

widely used in information processing, image encryption, network safety, secure communication, and machine learning.

On the other hand, many chaotic systems and synchronization strategies have been realized by electronic circuits [16–18]. So, synchronization between chaotic systems can be transferred to the synchronization between chaotic electronic circuits. Referring to synchronization between chaotic electronic circuits, the linear resistor coupling between two electronic circuits can realize the linear state variable coupling between chaotic systems, and the linear capacitive coupling or linear inductor coupling between two electronic circuits can realize the first derivative of state variable linear coupling. Up to now, many scholars [19–23] have proposed some synchronization approaches on integer-order chaotic electronic circuits by linear resistor coupling or linear capacitive coupling or a linear inductor coupling. However, to the best of our knowledge, there are little results on synchronization fractional-order chaotic electronic circuits coupled by a linear resistor or linear capacitive or linear inductor. Motivated by the

abovementioned discussion, we have studied the modified fractional-order Lorenz chaotic system based on the integer-order Lorenz chaotic system. Furthermore, using a linear resistor and a fractional-order capacitor in parallel coupling, the chaos synchronization of modified fractional-order Lorenz chaotic electronic circuits has been achieved, while the linear resistor, capacitor, or inductor coupling is usually used in the existing works.

The rest of this study is as follows. In Section 2, a modified fractional-order Lorenz chaotic system is proposed, and its chaotic electronic circuits is designed. In Section 3, chaos synchronization between two modified fractional-order Lorenz chaotic systems is realized via a linear resistor and a fractional-order capacitor in parallel coupling, and the circuit experiment is obtained. Conclusions are drawn in Section 4.

2. A Modified Fractional-Order Lorenz Chaotic System and Its Circuit Realization

A modified Lorenz chaotic system [24] is described as follows:

$$\begin{cases} \frac{dy_1}{dt} = 40(y_2 - y_1), \\ \frac{dy_2}{dt} = 10y_1 + 25y_2 - y_1y_3, \\ \frac{dy_3}{dt} = y_1y_2 - 3y_3. \end{cases} \quad (1)$$

Based on this integer-order Lorenz chaotic system (1), the modified fractional-order Lorenz chaotic system is obtained as follows:

$$\begin{cases} \frac{d^q y_1}{dt} = 40(y_2 - y_1), \\ \frac{d^q y_2}{dt} = 10y_1 + 25y_2 - y_1y_3, \\ \frac{d^q y_3}{dt} = y_1y_2 - 3y_3, \end{cases} \quad (2)$$

where $q = 0.95$ is the fractional order. Herein, the Caputo fractional-order derivatives are used. It is defined as

$$\frac{d^q f(t)}{dt} = \frac{1}{\Gamma(1-q)} \int_0^t \frac{f'(\tau)}{(t-\tau)^q} d\tau, \quad 0 < q < 1. \quad (3)$$

The Lyapunov exponents for this modified fractional-order Lorenz chaotic system (2) can be calculated by the numerical method [25, 26], and the Lyapunov exponents are (2.6245, -0.0461, -5.9568). The positive Lyapunov exponent indicates that chaotic attractors are emerged in system (2). Let $q = 0.95$, and the chaotic attractors of the fractional-order system (2) are shown in Figure 1.

Up to now, circuit implementation of chaotic systems has attracted more and more attentions. Many chaotic circuits have been reported. Now, we discuss the circuit implementation for the fractional-order chaotic system (2). Limited by the output of the operational amplifier, the amplitude of every variable in system (1) must be decreased, and we can choose $y_1 = 10x_1$, $y_2 = 10x_2$, and $y_3 = 10x_3$. So, system (2) can be changed as the following system:

$$\begin{cases} \frac{d^q x_1}{dt} = 40(x_2 - x_1), \\ \frac{d^q x_2}{dt} = 10x_1 + 25x_2 - 10x_1x_3, \\ \frac{d^q x_3}{dt} = 10x_1x_2 - 3x_3. \end{cases} \quad (4)$$

Recently, the guidelines to design circuits for fractional-order chaotic systems have been proposed in many studies [26–29]. To ordinary differential equation (ODE), we can use the linear capacitor C to realize the first-order differential unit (dy_i/dt), $i = 1, 2, 3$. Therefore, compared to the design of the first-order differential circuit unit in ODE, in order to realize the fractional-order differential unit ($d^q x_i/dt$), $i = 1, 2, 3$, we use the fractional-order capacitor F replacing the linear capacitor C in the first-order differential circuit unit in this study. According to [29], the fractional-order capacitor F is shown as Figure 2, and it can realize the operator (d^q/dt). In Figure 2, $C_1 = 3.616 \mu\text{F}$, $C_2 = 4.602 \mu\text{F}$, $C_3 = 1.267 \mu\text{F}$, $R_a = 15.1 \text{ k}\Omega$, $R_b = 1.51 \text{ M}\Omega$, $R_c = 692.9 \text{ M}\Omega$.

Based on the circuitry design method for fractional-order nonlinear systems in [25–29], the circuit diagram to realize the fractional-order nonlinear chaotic system (4) is presented as Figure 3.

In Figure 3, the operational amplifiers are the type of LF353N, the multipliers are the type of AD633, and the power is supplied by $\pm 15 \text{ V}$, and $R_1 = 10 \text{ k}\Omega$, $R_2 = 2.5 \text{ k}\Omega$, $R_3 = 4 \text{ k}\Omega$, and $R_4 = 33.3 \text{ k}\Omega$. Using electronics workbench (EWB), we can obtain the chaotic attractors in the fractional-order chaotic circuit, and the chaotic attractors are shown in Figure 4.

According to the results in Figures 1 and 4, the fractional-order Lorenz chaotic system (4) has been circuit implementation as Figure 3.

3. Synchronization of the Fractional-order Chaotic System (4) via a Linear Resistor and Fractional-Order Capacitor in Parallel Coupling

In this section, synchronization of the chaotic system (4) is discussed. Let system (4) as the driving system. The response system is as follows:

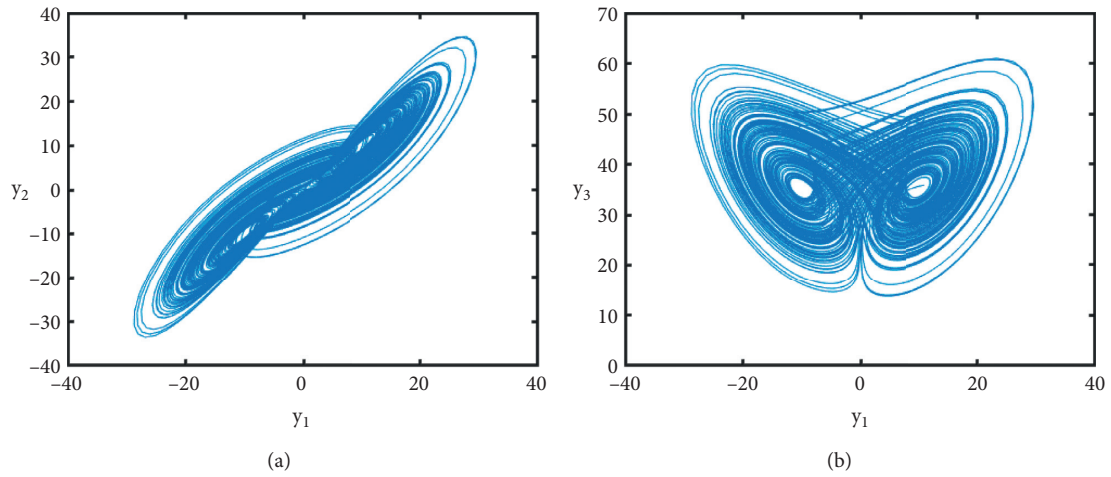


FIGURE 1: The chaotic attractors of the fractional-order system (2) for $q_1 = q_2 = q_3 = 0.95$. (a) The y_1y_2 phase diagram. (b) The y_1y_3 phase diagram.

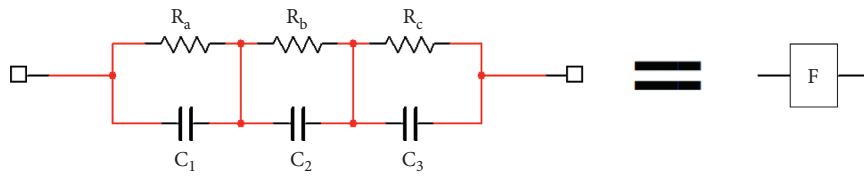


FIGURE 2: Circuit unit of the fractional-order capacitor F for $q = 0.95$.

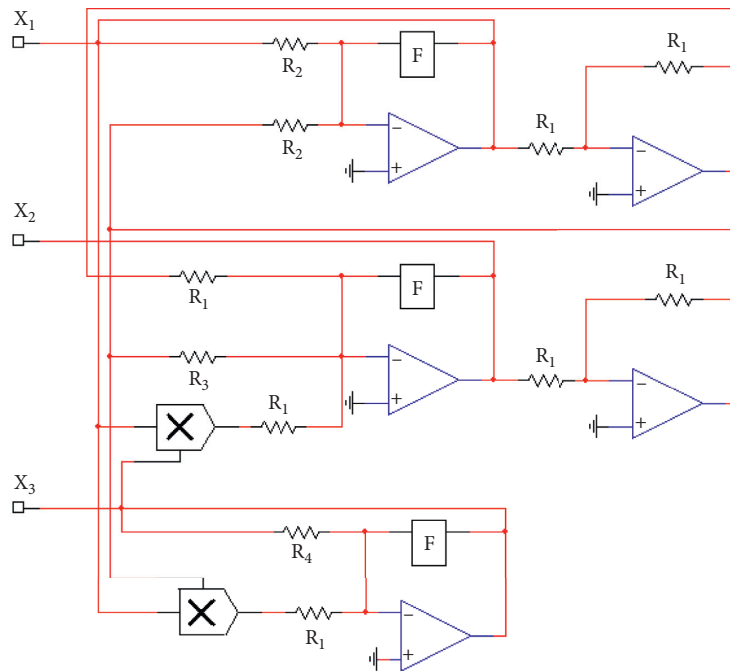


FIGURE 3: The circuit diagram to realize the fractional-order system (4) for $q = 0.95$.

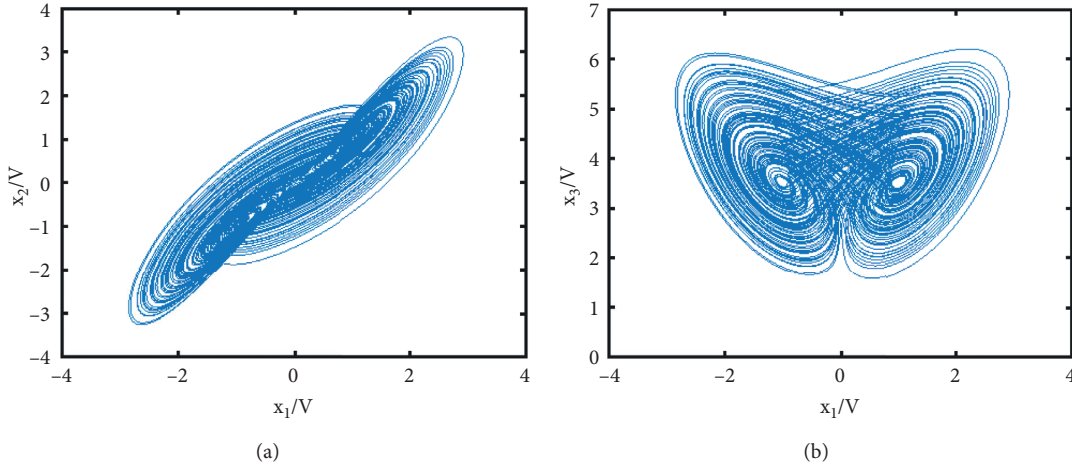


FIGURE 4: The circuit experiment phase portraits of the fractional-order chaotic system (4) for $q = 0.95$. (a) The x_1x_2 phase diagram. (b) The x_1x_3 phase diagram.

$$\begin{cases} \frac{d^q y_1}{dt} = 40(y_2 - y_1), \\ \frac{d^q y_2}{dt} = 10y_1 + 25y_2 - 10y_1y_3, \\ \frac{d^q y_3}{dt} = 10y_1y_2 - 3y_3. \end{cases} \quad (5)$$

According to Section 2, circuit implementation of the fractional-order chaotic system (5) is the same as Figure 3. Now, we discuss how to realize the chaos synchronization between the drive system (4) and response system (5) via

circuit implementation. In this study, the state variable x_2 in the driving system (4) and the state variable y_2 in the response system (5) are coupled via linear resistor R_k and fractional-order capacitor F in parallel, and its circuit diagram is shown in Figure 5. The green box in Figure 5 is the coupling part, and resistor $R_5 = 100 \text{ k}\Omega$.

According to Figure 5, one can obtain the following:

$$u = K_R(x_2 - y_2) + \left(\frac{d^q x_2}{dt} - \frac{d^q y_2}{dt} \right). \quad (6)$$

Here, variable $K_R = 100 \text{ k}\Omega/R_k$. Now, according to Figure 5, the coupled driving system and coupled response system are shown as follows:

$$\begin{cases} \frac{d^q x_1}{dt} = 40(x_2 - x_1), \\ \frac{d^q x_2}{dt} = 10x_1 + 25x_2 - 10x_1x_3 - K_R(x_2 - y_2) - \left(\frac{d^q x_2}{dt} - \frac{d^q y_2}{dt} \right), \\ \frac{d^q x_3}{dt} = 10x_1x_2 - 3x_3, \end{cases} \quad (7)$$

$$\begin{cases} \frac{d^q y_1}{dt} = 40(y_2 - y_1), \\ \frac{d^q y_2}{dt} = 10y_1 + 25y_2 - 10y_1y_3 + K_R(x_2 - y_2) + \left(\frac{d^q x_2}{dt} - \frac{d^q y_2}{dt} \right), \\ \frac{d^q y_3}{dt} = 10y_1y_2 - 3y_3. \end{cases} \quad (8)$$

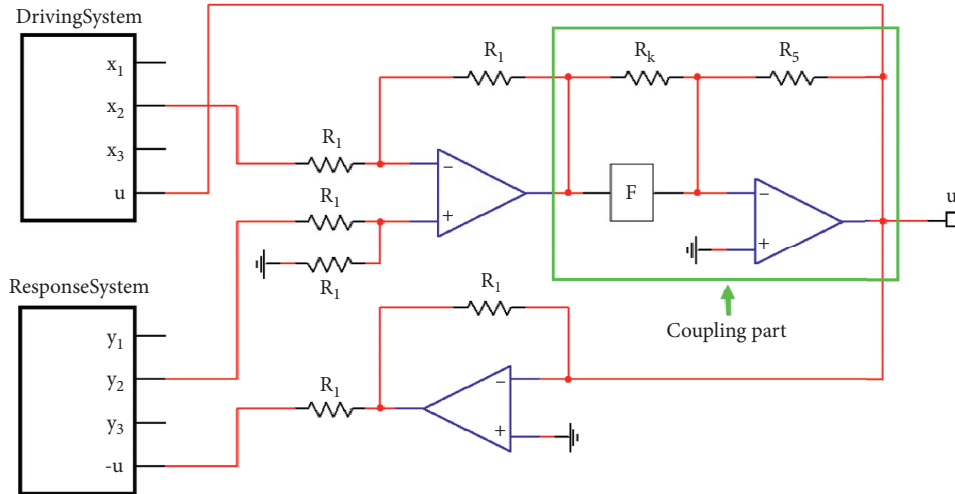


FIGURE 5: The circuit realization of chaos synchronization between the drive system (4) and response system (5).

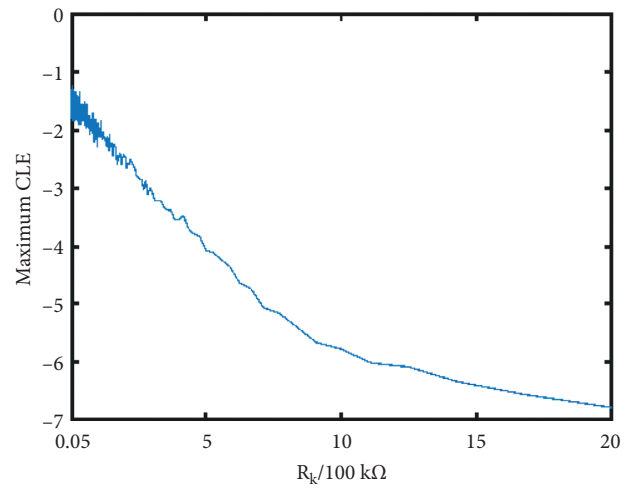
Next, we discuss how to realize chaos synchronization between the drive system (7) and response system (8) via linear resistor R_k or variable $K_R = 100 \text{ k}\Omega/R_k$. Let synchronization errors $e_i = x_i - y_i$ ($i = 1, 2, 3$), and we can obtain the error system as follows:

$$\begin{cases} \frac{d^q e_1}{dt} = 40(e_2 - e_1), \\ \frac{d^q e_2}{dt} = \frac{[10e_1 + (25 - 2K_R)e_2 + 10e_1e_3 - 10e_1x_3 - 10e_3x_1]}{3}, \\ \frac{d^q e_3}{dt} = -3e_3 - 10e_1e_2 + 10e_1x_2 + 10e_2x_1. \end{cases} \quad (9)$$

According to the error system (9), $e_i = 0$ ($i = 1, 2, 3$) is the equilibrium point of the error system (9). If the equilibrium point $e_i = 0$ ($i = 1, 2, 3$) is asymptotic stability, then chaotic synchronization between the driving system (7) and response system (8) can be achieved. This result indicates that the synchronization of the fractional-order chaotic system (4) can be realized via the linear resistor R_k and fractional-order capacitor F in parallel coupling. On the other hand, if all the Lyapunov exponents (LEs) in system (9) are negative, then chaos synchronization is achieved. In this study, the Lyapunov exponents (LEs) are used to check the chaos synchronization.

Now, MATLAB is used to study the QR decomposition to analyze the synchronization problem of variable parameter K_R . The Jacobi matrix of the error system (9) is as follows:

$$J = \begin{bmatrix} -40 & 40 & 0 \\ \frac{(10 + 10e_3 - 10x_3)}{3} & \frac{(25 - 2K_R)}{3} & \frac{(10e_1 - 10x_1)}{3} \\ -10e_2 + 10x_2 & -10e_1 + 10x_1 & 0 \end{bmatrix}. \quad (10)$$


 FIGURE 6: The maximum CLEs of error system (9) with variable $K_R = 100 \text{ k}\Omega/R_k$.

The maximum Lyapunov exponents (CLEs) [24, 25] related to R_k is shown in Figure 6. It can be seen that the maximum CLEs are negative if $K_R = 0.05 \sim 20$. So, choosing linear resistor $R_k = (20 \sim 0.05) \times 100 \text{ k}\Omega$, the chaos synchronization between the drive system (7) and response system (8) can be obtained.

Choose $K_R = 1$, then $R_k = 100 \text{ k}\Omega$. We can yield that all the CLEs of the error system (9) are $\lambda_1 = -2.4781$, $\lambda_2 = -3.2007$, and $\lambda_3 = -5.7004$. So, the chaos synchronization between the drive system (7) and response system (8) can be achieved. Take the initial driving signals $x = (2, 2, 2)$ and the initial response signals $y = (-2, -5, 5)$, and the synchronization results are shown in Figure 7.

Choose $K_R = 10$ and then $R_k = 10 \text{ k}\Omega$. According to Figure 6, the maximum CLEs of the error system (9) is negative. So, the chaos synchronization between the drive system (7) and response system (8) can be achieved. Taking the initial driving

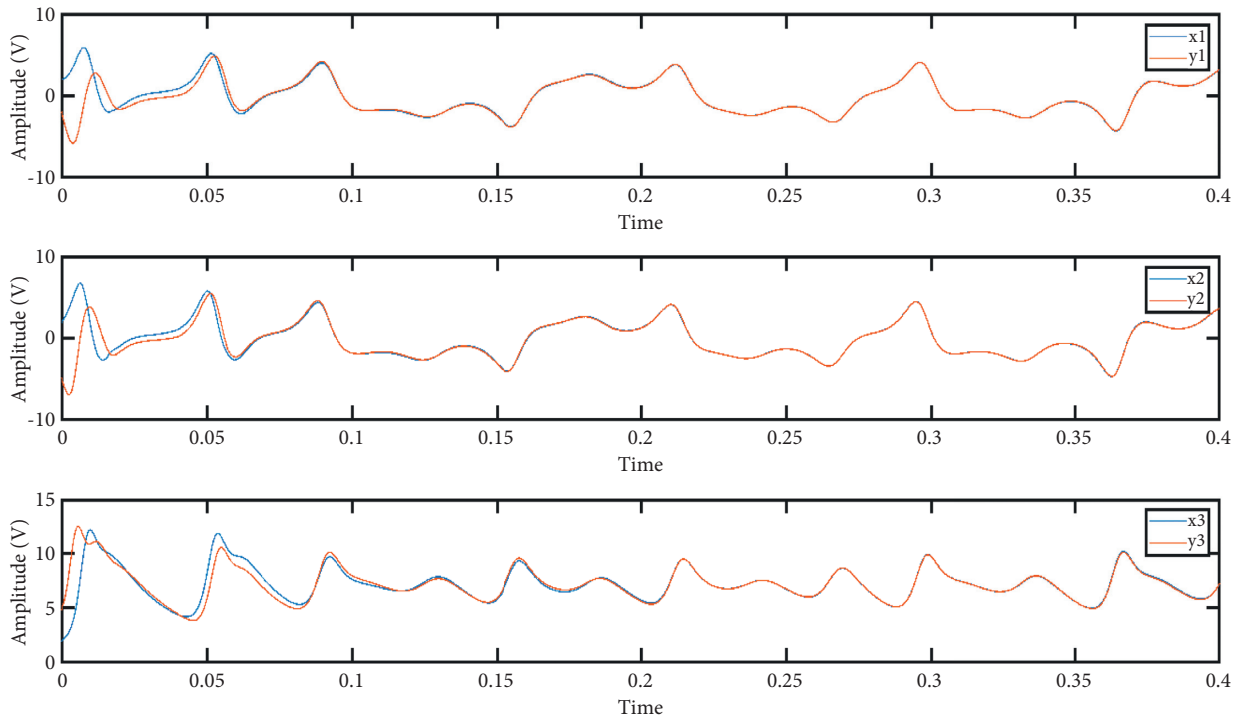


FIGURE 7: The synchronization process on $K_R = 1$.

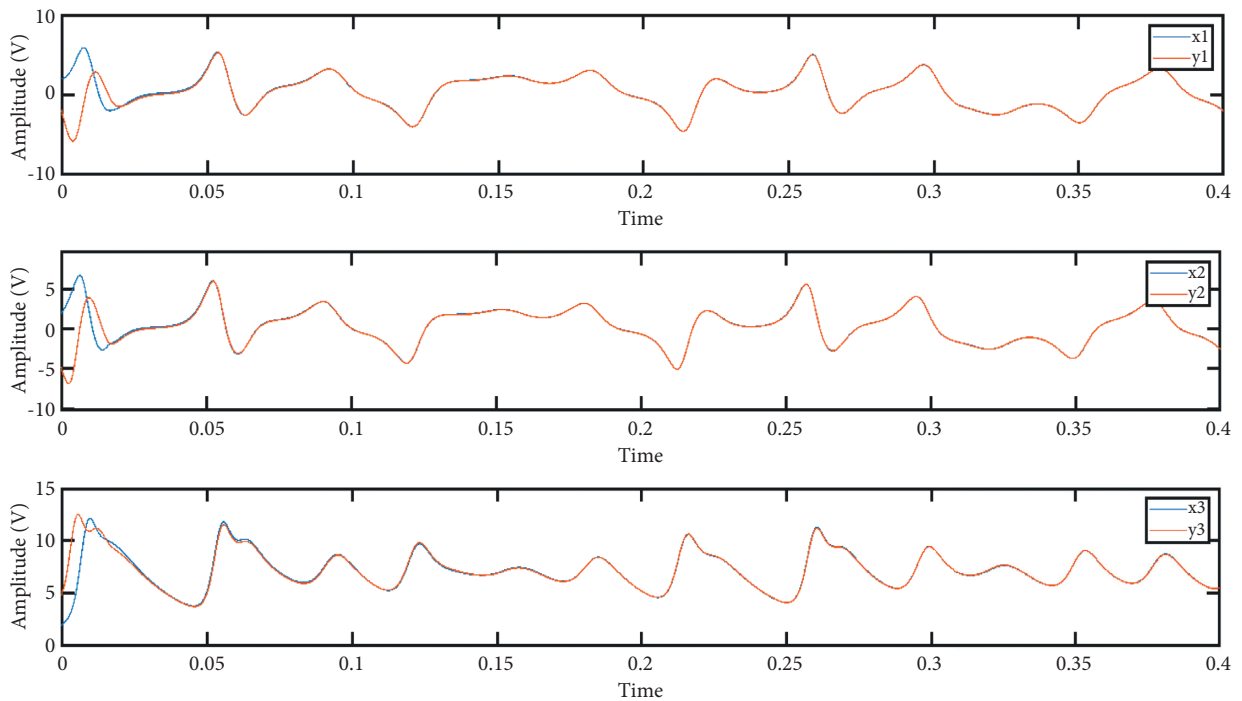


FIGURE 8: The synchronization process on $K_R = 10$.

signals $x = (2, 2, 2)$ and the initial response signals $y = (-2, -5, 5)$, the synchronization results are shown in Figure 8.

In summary, the chaos synchronization of the fractional-order chaotic system (4) can be realized via the linear resistor R_k and fractional-order capacitor F in parallel coupling, and the

maximum CLEs of the error system (9) with the linear resistor R_k are obtained. Furthermore, we find that chaotic synchronization cannot be reached via state variable x_1 and y_1 coupling or via state variable x_3 and y_3 coupling. In addition, we find that chaotic synchronization can be arrived via only linear resistor coupling or via only fractional-order capacitor coupling.

4. Conclusions

In this study, based on one modified Lorenz chaotic system, a modified fractional-order Lorenz chaotic system is suggested. We find that chaotic attractors are emerged in this modified fractional-order Lorenz chaotic system for $q = 0.95$. Furthermore, we discussed the circuit implementation for this fractional-order chaotic system, and the circuit diagram to realize the fractional-order nonlinear chaotic system (4) is presented. More importantly, a synchronization scheme is suggested to realize the chaos synchronization on this modified fractional-order Lorenz chaotic system for $q = 0.95$ via a linear resistor R_k and a fractional-order capacitor F in parallel coupling, which has not been used in the existing study. The electronic circuits for chaos synchronization of the modified fractional-order Lorenz chaotic system have been given. The simulation results verify that synchronization of the chaotic electronic circuit can be achieved. In the following study, whether inductive coupling can achieve synchronization is worth discussing.

Data Availability

The data used to support the findings of this study are available from the corresponding author upon request.

Conflicts of Interest

The authors declare that they have no conflicts of interest.

Acknowledgments

The authors thank Professor X. Luo for valuable suggestion.

References

- [1] C. Li and G. Peng, "Chaos in Chen's system with a fractional order," *Chaos, Solitons & Fractals*, vol. 22, no. 2, pp. 443–450, 2004.
- [2] M. S. Tavazoei and M. Haeri, "A necessary condition for double scroll attractor existence in fractional-order systems," *Physics Letters A*, vol. 367, no. 1, pp. 102–113, 2007.
- [3] R. Hilfer, *Applications of Fractional Calculus in Physics*, World Scientific, Singapore, 2000.
- [4] I. Podlubny, *Fractional Differential Equations*, Academic Press, San Diego, CA, USA, 1999.
- [5] P. Zhou, J. Ma, and J. Tang, "Clarify the physical process for fractional dynamical systems," *Nonlinear Dynamics*, vol. 100, no. 3, pp. 2353–2364, 2020.
- [6] P. Zhou, R. J. Bai, and J. M. Zheng, "Stabilization of a fractional-order chaotic brushless DC motor via a single input," *Nonlinear Dynamics*, vol. 82, no. 1-2, pp. 519–525, 2015.
- [7] I. Grigorenko and E. Grigorenko, "Chaotic dynamics of the fractional Lorenz system," *Physical Review Letters*, vol. 91, no. 3, pp. 34101–34104, 2003.
- [8] T. T. Hartley, C. F. Lorenzo, and H. Killory Qammer, "Chaos in a fractional order Chua's system," *IEEE Transactions on Circuits and Systems I: Fundamental Theory and Applications*, vol. 42, no. 8, pp. 485–490, 1995.
- [9] Z.-M. Ge and C.-Y. Ou, "Chaos in a fractional order modified duffing system," *Chaos, Solitons & Fractals*, vol. 34, no. 2, pp. 262–291, 2007.
- [10] M. P. Aghababa and H. P. Aghababa, "The rich dynamics of fractional-order gyros applying a fractional controller," *Proceedings of the Institution of Mechanical Engineers-Part I: Journal of Systems & Control Engineering*, vol. 227, no. 7, pp. 588–601, 2013.
- [11] M. P. Aghababa, "Chaos in a fractional-order micro-electromechanical resonator and its suppression," *Chinese Physics B*, vol. 21, no. 10, Article ID 100505, 2012.
- [12] W. Xie, C. Wang, and H. Lin, "A fractional-order multistable locally active memristor and its chaotic system with transient transition, state jump," *Nonlinear Dynamics*, vol. 104, no. 4, pp. 4523–4541, 2021.
- [13] P. Zhou, R. Ding, and Y.-X. Cao, "Multi drive-one response synchronization for fractional-order chaotic systems," *Nonlinear Dynamics*, vol. 70, no. 2, pp. 1263–1271, 2012.
- [14] P. Zhou and P. Zhu, "A practical synchronization approach for fractional-order chaotic systems," *Nonlinear Dynamics*, vol. 89, no. 3, pp. 1719–1726, 2017.
- [15] P. Muthukumar, P. Balasubramaniam, and K. Ratnavelu, "Synchronization of a novel fractional order stretch-twist-fold (STF) flow chaotic system and its application to a new authenticated encryption scheme (AES)," *Nonlinear Dynamics*, vol. 77, no. 4, pp. 1547–1559, 2014.
- [16] P. Zhou, Z. Yao, J. Ma, and Z. G. Zhu, "A piezoelectric sensing neuron and resonance synchronization between auditory neurons under stimulus," *Chaos, Solitons & Fractals*, vol. 145, no. 9, Article ID 110751, 2021.
- [17] V.-T. Pham, C. Volos, S. Jafari, and T. Kapitaniak, "Coexistence of hidden chaotic attractors in a novel no-equilibrium system," *Nonlinear Dynamics*, vol. 87, no. 3, pp. 2001–2010, 2017.
- [18] C. K. Volos, A. Akgul, V. T. Pham, and M. S. Baptista, "Antimonotonicity, crisis and multiple attractors in a simple memristive circuit," *Journal of Circuits, Systems, and Computers*, vol. 27, no. 2, Article ID 1850026, 2018.
- [19] X. K. Hu and P. Zhou, "Circuit realization of a 3D multistability chaotic system and its synchronization via linear resistor and linear capacitor in parallel coupling," *Complexity*, vol. 2020, Article ID 9846934, 10 pages, 2020.
- [20] Z. Liu, J. Ma, G. Zhang, and Y. Zhang, "Synchronization control between two Chua's circuits via capacitive coupling," *Applied Mathematics and Computation*, vol. 360, pp. 94–106, 2019.
- [21] Z. Liu, C. Wang, W. Jin, and J. Ma, "Capacitor coupling induces synchronization between neural circuits," *Nonlinear Dynamics*, vol. 97, no. 4, pp. 2661–2673, 2019.
- [22] Z. Yao, J. Ma, Y. Yao, and C. Wang, "Synchronization realization between two nonlinear circuits via an induction coil coupling," *Nonlinear Dynamics*, vol. 96, no. 1, pp. 205–217, 2019.
- [23] J. Ma, F. Wu, A. Alsaedi, and J. Tang, "Crack synchronization of chaotic circuits under field coupling," *Nonlinear Dynamics*, vol. 93, no. 4, pp. 2057–2069, 2018.
- [24] H. Y. Jia, Z. Q. Chen, and W. Xue, "Analysis and circuit implementation for the fractional-order Lorenz system," *Acta Physica Sinica*, vol. 62, no. 14, Article ID 140503, 2013.
- [25] W. Zhang, S. Zhou, X. Liao, H. Mai, and K. Xiao, "Estimate the largest Lyapunov exponent of fractional-order systems," in *Proceedings of the 2008 International Conference on Communications, Circuits and Systems*, pp. 1121–1124, Shanghai, China, May 2008.

- [26] P. Zhou and K. Huang, "A new 4-D non-equilibrium fractional-order chaotic system and its circuit implementation," *Communications in Nonlinear Science and Numerical Simulation*, vol. 19, no. 6, pp. 2005–2011, 2014.
- [27] P. Zhou, X. F. Cheng, and N. Y. Zhang, "One new fractional-order chaos system and its circuit simulation by electronic workbench," *Chinese Physics B*, vol. 17, no. 9, pp. 3252–3257, 2008.
- [28] Z. Xu and C. X. Liu, "Realization of fractional-order Liu chaotic system by a new circuit unit," *Chinese Physics B*, vol. 17, no. 11, pp. 4033–4038, 2008.
- [29] K. H. Sun, J. L. Yang, J. F. Ding, and L. Y. Sheng, "Circuit design and implementation of Lorenz chaotic system with one parameter," *Acta Physica Sinica*, vol. 59, no. 12, pp. 8385–8392, 2010.